

Additive manufacturing of high tensile strength steel for offshore & marine 3D complex joint applications

Wu, Wenjin

2020

Wu, W. (2020). Additive manufacturing of high tensile strength steel for offshore & marine 3D complex joint applications. Doctoral thesis, Nanyang Technological University, Singapore.

<https://hdl.handle.net/10356/146202>

<https://doi.org/10.32657/10356/146202>

This work is licensed under a Creative Commons Attribution-NonCommercial 4.0 International License (CC BY-NC 4.0).

Downloaded on 26 Aug 2022 23:54:39 SGT



**NANYANG
TECHNOLOGICAL
UNIVERSITY**

SINGAPORE

**ADDITIVE MANUFACTURING OF HIGH TENSILE
STRENGTH STEEL FOR OFFSHORE & MARINE 3D
COMPLEX JOINT APPLICATIONS**

WU WENJIN

SCHOOL OF MECHANICAL AND AEROSPACE ENGINEERING

2020

**Additive manufacturing of high tensile strength steel for offshore &
marine 3D complex joint applications**

Wu Wenjin

School of Mechanical and Aerospace Engineering

A thesis submitted to the Nanyang Technological University
in partial fulfillment of the requirement for the degree of
Doctor of Philosophy

2020

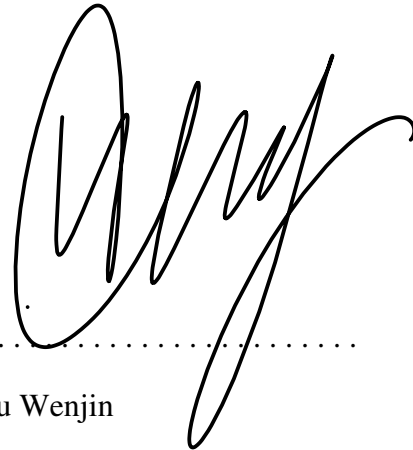
Statement of Originality

I hereby certify that the work embodied in this thesis is the result of original research, is free of plagiarised materials, and has not been submitted for a higher degree to any other University or Institution.

11 Jan 2020

.....

Date

A handwritten signature in black ink, consisting of a large, stylized 'W' followed by several loops and a long, sweeping tail that curves upwards and to the right. The signature is positioned above a horizontal dotted line.

Wu Wenjin

Supervisor Declaration Statement

I have reviewed the content and presentation style of this thesis and declare it is free of plagiarism and of sufficient grammatical clarity to be examined. To the best of my knowledge, the research and writing are those of the candidate except as acknowledged in the Author Attribution Statement. I confirm that the investigations were conducted in accord with the ethics policies and integrity standards of Nanyang Technological University and that the research data are presented honestly and without prejudice.

11 Jan 2020

.....

Date



.....

A/Prof Tor Shu Beng

Authorship Attribution Statement

Please select one of the following; *delete as appropriate:

~~*(A) This thesis **does not** contain any materials from papers published in peer-reviewed journals or from papers accepted at conferences in which I am listed as an author.~~

*(B) This thesis contains material from 2 paper(s) published in the following peer-reviewed journal(s) / from papers accepted at conferences in which I am listed as an author.

Chapter 3 is published as Wenjin Wu, Shu Beng Tor, Chee Kai Chua, Kah Fai Leong, and Aziz Amirali Merchant. "Investigation on processing of ASTM A131 Eh36 high tensile strength steel using selective laser melting." *Virtual and Physical Prototyping* 10, no. 4 (2015): 187-193.

The contributions of the co-authors are as follows:

- I prepared the manuscript drafts.
- All microscopy, including sample preparation, was conducted by me.
- I analysed the data.
- Prof Tor Shu Beng, Prof Chua Chee Kai, Prof Leong Kah Fai and Mr Aziz Amirali Merchant provided guidance in directions of the work.

Chapter 4 is partially published as Wenjin Wu, Shu Beng Tor, and Aziz Amirali Merchant. "Tensile Properties Of ASTM A131 EH36 Shipbuilding Steel Processed By Selective Laser Melting." In the proceedings of 3rd International Conference on Progress in Additive Manufacturing 2018. May 2018, Singapore..

The contributions of the co-authors are as follows:

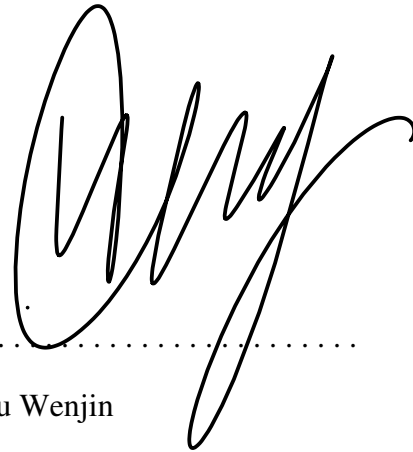
- I prepared the manuscript drafts.

- All sample preparation and tests were conducted by me.
- I analysed the data.
- Prof Tor Shu Beng and Mr Aziz Amirali Merchant provided guidance in directions of the work.

11 Jan 2020

.....

Date

A handwritten signature in black ink, appearing to be 'Wu Wenjin', written over a horizontal dotted line. The signature is stylized and cursive.

Wu Wenjin

Acknowledgements

The author wishes to express sincere gratitude and appreciation towards his supervisor, Associate Professor Tor Shu Beng for his advice, assistance and patience throughout his candidature. Prof Tor also provided an immense amount of guidance and mentorship in ensuring that the author progresses in the most appropriate manner. Prof Tor's appointment as his supervisor contributed the most towards the author's completion of the research work.

The author would also like to thank Keppel Technology and Innovation (KTI), Keppel Offshore & Marine Technology Centre (KOMtech), Energy Research Institute at Nanyang Technological University (ERI@N) and Singapore Centre for 3D Printing (SC3DP) for the research collaboration that led to this research opportunity. As part of this research collaboration, the author wants to thank KTI's industry supervisor, Dr Miguel Angel Moya Ramirez, KOMtech's industry supervisors, Dr Basil Lui and Mr Aziz Merchant, ERI@N's director Dr Narasimalu Srikanth and Professor Chua Chee Kai for their support. In support of this research, the author also expresses gratitude towards the support from Economic Development Board Singapore. The author also acknowledges the research funding received from these affiliations.

The author would also like to thank the following technical and research staff, and business associates for their assistance and guidance during his research work – Mr. Chia Yak Khoong, Mr. Soh Beng Choon, Mr. Mack Wong, Dr Alexander Liu, Dr Zhang Dan Qing, Dr Tan Xi Peng, Mr Sun Zhongji, Dr Sing Swee Leong, Dr An Jia, Ms Wang Jing Jing, Mr Daniel Yeo Yin Ping, Mr Justin Ong Lu Chen. The author would also like to express thanks to the other researchers and research students for all the assistance rendered.

On a personal basis, the author wishes to express his heartfelt gratitude to Mr Charles Foo, who had triggered the initial motivation for the author to embark on this research journey. The author also shares similar gratitude to his colleagues at Keppel Technology and Innovation, Mr Stanley Han, Mr Lee Yuan Hao, Ms Sharine Tan Ying Jia, for their understanding and support in his research journey.

Last but not the least, the author is especially thankful to his family, loved ones, and friends for their constant encouragement and understanding throughout the research

journey. Special thanks and appreciation go to the author's wife for her support and understanding, without which, the completion of the research will not be possible.

List of Publications

Throughout the course of this research, the author has written and contributed to several publications in international peer-reviewed journals and conference papers.

Peer-Reviewed Journal Papers

1. Jingjing Wang, **Wenjin Wu**, Meng Zhang, Bing Wang, Xipeng Tan, Guijun Bi, Hua Li, Shu Beng Tor, Erjia Liu. "Influence of surface porosity on fatigue life of additively manufactured ASTM A131 EH36 steel samples." *Journal of Materials Science and Technologies*. Under review.
2. Jingjing Wang, **Wenjin Wu**, You Xiang Chew, Wei Jing, Xipeng Tan, Sharine Ying Jia Tan, Yuan Hao Lee, Aziz Merchant, Shu Beng Tor, Kah Fai Leong, Chee Kai Chua, Guijun Bi, Erjia Liu. "Robust ASTM A131 EH36 steel samples printed in different orientations via laser aided additive manufacturing." *Materials Science and Engineering A*. Under review.
3. Jingjing Wang, **Wenjin Wu**, Wei Jing, Xipeng Tan, Guijun Bi, Shu Beng Tor, Kah Fai Leong, Chee Kai Chua, Erjia Liu. "Improvement of densification and microstructure of ASTM A131 EH36 steel samples additively manufactured via selective laser melting with varying laser scanning speed and hatch spacing." *Materials Science & Engineering A* 746 (2019): 300-313.
4. **Wenjin Wu**, Shu Beng Tor, Chee Kai Chua, Kah Fai Leong, and Aziz Amirali Merchant. "Investigation on processing of ASTM A131 Eh36 high tensile strength steel using selective laser melting." *Virtual and Physical Prototyping* 10, no. 4 (2015): 187-193.

Conference Papers

1. **Wenjin Wu**, Shu Beng Tor, and Aziz Amirali Merchant. "Tensile Properties Of ASTM A131 EH36 Shipbuilding Steel Processed By Selective Laser Melting." In the proceedings of 3rd International Conference on Progress in Additive Manufacturing 2018. May 2018, Singapore.
2. **Wenjin Wu**, Shu Beng Tor, Narasimalu Srikanth, Chee Kai Chua, and Aziz Amirali Merchant. " Introduction to Metal Additive Manufacturing and its Challenges in Offshore & Marine." In the proceedings of 3rd Asian Wave and Tidal Energy Conference 2016. Oct 2016, Singapore.

3. **Wenjin Wu**, Shu Beng Tor, Kah Fai Leong, Chee Kai Chua, and Aziz Amirali Merchant. "State Of The Art Review On Selective Laser Melting Of Stainless Steel For Future Applications In The Marine Industry." In the proceedings of 2nd International Conference on Progress in Additive Manufacturing 2016. May 2016, Singapore.
4. **Wenjin Wu**, Shu Beng Tor, Lui Onn Kit, Basil, and Aziz Merchant. "Study of Additive Manufacturing in Offshore & Marine." In the proceedings of Rapid 2014. Jun 2014, Detroit.

Contents

Acknowledgements	5
List of Publications	7
List of Figures	14
List of Tables	19
Abstract	21
Chapter One Introduction.....	23
1.1 Background	23
1.2 Research Motivation and Approach	30
1.3 Research Objectives	30
1.4 Thesis Outline	31
Chapter Two Literature Review	32
2.1 Materials.....	33
2.1.1 ASTM A131 Shipbuilding Material.....	33
2.1.1.1 Chemical Composition.....	36
2.1.1.2 Steel Transformation	41
2.1.1.3 Steel Processing.....	45
2.1.1.4 Selection of Grade of ASTM A131 Steel.....	48
2.2 Additive Manufacturing Technologies.....	50
2.2.1 Binder Jetting	54
2.2.2 Direct Energy Deposition.....	56
2.2.3 Material Extrusion.....	58

2.2.4	Material Jetting.....	61
2.2.5	Powder Bed Fusion	62
2.2.5.1	Selective Laser Sintering.....	63
2.2.5.2	Selective Laser Melting.....	64
2.2.5.3	Selective Heat Sintering	65
2.2.5.4	Electron Beam Melting	65
2.2.6	Sheet Lamination.....	70
2.2.7	Vat Photopolymerisation.....	71
2.2.8	Selection of Additive Manufacturing Technology.....	72
2.3	Part and Material Properties in SLM of Metals	76
2.3.1	Density	77
2.3.2	Surface Quality.....	83
2.3.3	Mechanical Properties	88
2.3.3.1	Toughness.....	88
2.3.3.2	Ductility.....	89
2.3.3.3	Tensile Strength.....	91
2.3.3.4	Fatigue	92
2.3.3.5	Hardness and Wear.....	94
2.3.4	Microstructure	97
2.4	Literature Review Summary	107
2.5	Research Objective and Scope	110

2.6	Proposed Research Roadmap	112
Chapter Three Preliminary Investigations.....		114
3.1	Material	114
3.2	SLM Machine and Process Parameters.....	117
3.3	Results	118
3.3.1	Density Test.....	120
3.3.2	X-Ray Diffraction	122
3.3.3	Light Optical Microscopy	123
3.3.4	Scanning Electron Microscopy	124
3.4	Discussion	126
3.5	Conclusion.....	127
Chapter Four Mechanical Tests.....		129
4.1	Experimental	129
4.2	Heat Treatment.....	132
4.3	Results	133
4.3.1	Tensile Strength.....	134
4.3.2	Elongation	140
4.3.3	Charpy V-Notched Impact Toughness.....	143
4.3.4	Vickers Hardness.....	148
4.4	Discussion	149
4.5	Conclusion.....	155

Chapter Five	Fracture Surface Morphology.....	156
5.1.	Procedure	156
5.2.	Results	156
5.3.	Discussion.....	158
5.3.1	Ductility.....	158
5.3.2	Density and Defects	159
5.4.	Conclusion	161
Chapter Six	Microstructure Characterisation.....	163
6.1.	Iron-Carbon Binary Phase Diagram	163
6.2.	Experimental.....	163
6.3.	Results	164
6.4.	Discussion.....	165
6.4.1	Effect of Heat Treatment.....	166
6.4.2	Grain Boundary Strengthening.....	169
6.4.3	Transformation of Microstructure.....	170
6.5.	Conclusion	171
Chapter Seven	Complex Joint Fabrication and Examination.....	173
7.1	Overview of Complex Joint	173
7.2	Microstructure Examination and SEM-Imaging.....	175
7.3	Vickers Hardness.....	177
7.4	Discussion	178

7.5 Conclusion.....	180
Chapter Eight Conclusion & Future Work.....	182
References	185
Appendix A – List of all data	196

List of Figures

Figure 2.1 - Iron-carbon phase diagram [25]	42
Figure 2.2 - Time-temperature transformation curves for (a) eutectoid, (b) hypo-eutectoid and (c) low-alloy (e.g. Ni/Cr/Mo) steels	44
Figure 2.3 - (a) TMCP diagram for 'conventional' vs 'unconventional' processing; (b) microstructural changes promoted by HOP [29]	47
Figure 2.4 - Industrial-Grade Metal Additive Manufacturing Processes [35]	52
Figure 2.5 - Industrial-Grade Metal Additive Manufacturing Machines [35]	53
Figure 2.6 - Schematic of binder jetting process [36].....	55
Figure 2.7 - Schematic of powdered based direct energy deposition process [39].....	57
Figure 2.8 - Schematic of material extrusion additive manufacturing (Fused Deposition Modelling) [43]	59
Figure 2.9 - Schematic of material jetting process (Polyjet from Objet Geometries) [36]	61
Figure 2.10 - Schematic of Selective Laser Sintering process [36]	64
Figure 2.11 - Schematic of Electron Beam Melting [36].....	66
Figure 2.12 - Schematic of ultrasonic additive manufacturing [36]	71
Figure 2.13 - Schematic of vat photopolymerisation [36]	72
Figure 2.14 - Relative density (a) and optical image (b) of SLM processed SS316L powder.....	78
Figure 2.15 - Material density versus preheating temperature of powder bed	79
Figure 2.16- (a) Effect of scanning strategy; (b) Different scanning strategies by Kruth et al. [54]	80
Figure 2.17 - Four scanning strategies investigated by Jhabvala et al. [69]	80
Figure 2.18 - Relative density values formed at differing island sizes in island scanning strategy [70]	81
Figure 2.19 - Optical microscopy images of SLM produced part without re-melting [54, 66]	82
Figure 2.20 - Optical microscopy images of SLM produced part with re-melting [54, 66]	83
Figure 2.21 - Surface quality enhancement with laser re-melting: (a) SLM without re-melting (b) Laser re-molten part [54].....	87
Figure 2.22 - SEM image of a SLM laser re-melted surface with no obvious edge-effect [54]	87

Figure 2.23 - SLM manufactured "truncheon" test part [81].....	87
Figure 2.24 - Charpy test results for SLM produced parts [54].....	89
Figure 2.25 - Elongation values for SLM built SS316L from Spierings et al. [84].....	90
Figure 2.26 - Fatigue results of SLM process stainless steel 316L [105].....	94
Figure 2.27 - Optical microscopy images showing characteristic microstructures of SLM-processed Ti parts at different processing parameters [112]	95
Figure 2.28 - Average macro hardness measured on cross-sections versus scan speed for different layer thicknesses with 95% confidence intervals [113]	97
Figure 2.29 - Micrographs after etching of cross-sections of Maraging Steel 300 from Yasa et al. [113]	97
Figure 2.30 - MPBs on the cross section parallel to the laser scanning direction [82].	98
Figure 2.31 - Morphology of the cross section perpendicular to the scanning direction [82]	99
Figure 2.32 - MPB boundary	99
Figure 2.33 - Tensile fracture morphologies of the sample fabricated along the direction (a) perpendicular to the laser scanning direction and (b) with an angle of 60° between the tensile loading direction and x-y plane [116].....	99
Figure 2.34 - Metallographic observation from the top view and from the side view of SLM-fabricated iron cubes at the laser power of 100W using different laser scanning speeds of: (a)–(b) 0.27m/s,(c)–(d) 0.33m/s and(e)–(f) 0.4m/s,respectively [90]	101
Figure 2.35 - Micrographs of SLM sample showing elongated grains along build direction [54].....	102
Figure 2.36 - Frontal section of a SLM part from AISI 316L stainless steel [54].....	102
Figure 2.37 - SEM image of the cross-section of SLM built AISI 316L part [54].....	103
Figure 2.38 - Influence of scanning speed on microstructure of SLM built parts, (a) side view, (b) front view [54]	105
Figure 2.39 - Micrographs of SLM built parts: (a) front view of an increased scan spacing, (b) influence of scan strategy on grain direction [54].....	105
Figure 2.40 - SEM pictures of AISI 316L stainless steel part when last layer was re-melted 10 times, (a) low magnification, (b) high magnification [54]....	106
Figure 3.1 - SEM image of ASTM A131 powder particles [129]	117
Figure 3.2 - SLM built test specimens [129]	119

Figure 3.3 - SLM built density cubes.....	119
Figure 3.4 - Graph of SLM built part density vs energy density [129]	121
Figure 3.5 - XRD of EH36 (a) powder sample, (b) SLM built specimen [129].....	122
Figure 3.6 - XRD of quenched commercial low carbon steel [131].....	123
Figure 3.7 - (a) Image of unetched SLM built specimen showing slight porosities, (b) etched sample showing microstructure and porosity indicating incomplete melting of powder particle [129].....	123
Figure 3.8 - SEM images of SLM built specimen showing (a) fine grains (Zone A) vs coarse grains (Zone B), (b) acicular martensitic structure [129]	124
Figure 3.9 - High magnification SEM image of SLM built specimen showing acicular martensitic structure	125
Figure 4.1 - Dimensions of SLM built test coupons (a) tensile test coupons, (b) Charpy test coupons	131
Figure 4.2 - SLM test coupon orientations (a) tensile test coupon, 45°; (b) tensile test coupon, vertical; (c) tensile test coupon, horizontal; (d) Charpy test coupon, notch facing up; (e) Charpy test coupon, notch facing side; (e) Charpy test coupon, notch facing 45°	131
Figure 4.3 - SLM built test coupons. (a) As-built on build plate; (b) Tensile test coupons following heat treatment; (c) Charpy test coupons following heat treatment	134
Figure 4.4 - Graph of tensile test results (Yield Strength) for SLM built samples.....	136
Figure 4.5 - Graph of tensile test results (Ultimate Tensile Strength) for SLM built samples	136
Figure 4.6 - Graph of Yield Strength (XY, Machined) with error bar.....	137
Figure 4.7 - Graph of Yield Strength (XY, As-built) with error bar	137
Figure 4.8 - Graph of Ultimate Tensile Strength (XY, Machined) with error bar.....	138
Figure 4.9 - Graph of Ultimate Tensile Strength (XY, As-built) with error bar.....	138
Figure 4.10- Graph of Yield Strength (Z) with error bar	139
Figure 4.11 - Graph of Yield Strength (45°) with error bar	139
Figure 4.12- Graph of Ultimate Tensile Strength (Z) with error bar	140
Figure 4.13 - Graph of Ultimate Yield Strength (45°) with error bar	140
Figure 4.14 - Graph of elongation results for SLM built samples	141
Figure 4.15 - Graph of elongation results (XY, machined) with error bar	142
Figure 4.16 - Graph of elongation results (XY, As-Built) with error bar.....	142

Figure 4.17 - Graph of elongation results (Z) with error bar	143
Figure 4.18 - Graph of elongation results (45°) with error bar	143
Figure 4.19 – Graph of Charpy test results for SLM built samples at 0°C	145
Figure 4.20 – Graph of Charpy test results for SLM built samples at -40°C	145
Figure 4.21 – Graph of Charpy test results (Notch Up) at 0°C with error bar	146
Figure 4.22 – Graph of Charpy test results (Notch Side) at 0°C with error bar.....	146
Figure 4.23 – Graph of Charpy test results (Notch 45°) at 0°C with error bar.....	147
Figure 4.24 – Graph of Charpy test results (Notch Up) at -40°C with error bar.....	147
Figure 4.25 – Graph of Charpy test results (Notch Side) at -40°C with error bar	148
Figure 4.26 – Graph of Charpy test results (Notch 45°) at -40°C with error bar	148
Figure 4.27 – Graph of Vickers hardness numbers (test coupons).....	149
Figure 4.28 - Hardness of tempered martensite in iron-carbon (Fe-C) steel [142].....	151
Figure 4.29 - Schematic diagram of molten pools during SLM process: (a) single molten pool; (b) “layer–layer” MPBs; (c) “track–track” MPBs. The arrows represent the grain orientations. [116]	153
Figure 4.30 - Schematic diagrams of MPBs on the stress cross sections of (a) the horizontal and (b) vertical specimens. [116].....	154
Figure 5.1 - SEM images of tensile coupons at 50x magnification (a) no heat treatment, (b) 205°C, (c) 315°C, (d) 425°C, (e) 540°C, (f) 650°C, (g) 800°C, (h) reference sample.....	157
Figure 5.2 - SEM images of tensile coupons at 1000x magnification (a) no heat treatment, (b) 205°C, (c) 315°C, (d) 425°C, (e) 540°C, (f) 650°C, (g) 800°C, (h) reference sample.....	157
Figure 5.3 - SEM images of Charpy coupons at 50x magnification (a) no heat treatment, (b) 205°C, (c) 315°C, (d) 425°C, (e) 540°C, (f) 650°C, (g) 800°C, (h) reference sample.....	158
Figure 5.4 - SEM images of Charpy coupons at 1000x magnification (a) no heat treatment, (b) 205°C, (c) 315°C, (d) 425°C, (e) 540°C, (f) 650°C, (g) 800°C, (h) reference sample	158
Figure 6.1 - Microstructure images showing melt pool layers (a) no heat treatment, (b) 205°C, (c) 315°C, (d) 425°C, (e) 540°C, (f) 650°C, (g) 800°C, (h) reference sample	164
Figure 6.2 - Microstructure images (a) no heat treatment, (b) 205°C, (c) 315°C, (d) 425°C, (e) 540°C, (f) 650°C, (g) 800°C, (h) reference sample	164

Figure 6.3 - Microstructure images with higher magnification (a) no heat treatment, (b) 205°C, (c) 315°C, (d) 425°C, (e) 540°C, (f) 650°C, (g) 800°C, (h) reference sample.....	165
Figure 6.4 - XRD results	165
Figure 6.5 – Effect of heat treatment causing formation of cementite (dark bands) and ferrite (bright regions)	167
Figure 6.6 – Effect of heat treatment causing spheroidisation.....	167
Figure 6.7 - Spheroidal carbides	168
Figure 6.8 – Effect of heat treatment ending up with recrystallisation.....	168
Figure 6.9 - Grain boundary strengthening	169
Figure 6.10 - Grain size determination of SLM produced sample with 800°C heat treatment.....	170
Figure 6.11 – Comparison of grain sizes of SLM processed sample with 800°C heat treatment (left), vs TMCP produced sample (right).....	171
Figure 7.1 - Photo of scaled complex joint processed by SLM	174
Figure 7.2 - Orientation of print of scaled complex joint	174
Figure 7.3 - Section of complex joint removed for examination (shaded in blue)	175
Figure 7.4 - Scaled model SEM imaging mapped to various printed faces.....	176
Figure 7.5 - Scaled model SEM imaging with larger magnification	177
Figure 7.6 - Graph of Vickers hardness numbers (scaled model).....	178
Figure 7.7 - Reference SEM images for comparison with scaled model (a) x-y plane, (b) z plane, (c) z plane	179

List of Tables

Table 1.1 – Typical fabrication steps for casting [14]	27
Table 1.2 - Reduced fabrication steps after considering AM	28
Table 2.1 - Tensile requirements for Ordinary-Strength and Higher-Strength Structural Steel in ASTM A131 [20]	34
Table 2.2 - Charpy V-notch impact requirements for Ordinary-Strength and Higher-Strength Structural Steel in ASTM A131 [20].....	35
Table 2.3 - Chemical requirements for Higher-Strength Structural Steel in ASTM A131 [20]	36
Table 2.4 - Major effects of alloying elements in high strength steel [21]	38
Table 2.5 - Other alloying elements in high strength steel [22, 24].....	39
Table 2.6 - Strategy alloying combinations to improve strength and toughness [23] ..	40
Table 2.7 - Carbon Equivalent for Higher-Strength Structural Steel Produced by TMCP from ASTM A131 [20]	41
Table 2.8 - Overview of TMCP stages, typical temperatures and features [21].....	48
Table 2.9 - Selection of grade of steel under ASTM A131	49
Table 2.10 - AM process categories	50
Table 2.11 - Differences between EBM and SLM [36].....	67
Table 2.12 - Selection of AM technology to process ASTM A131 EH36	72
Table 2.13 - Comparison of various DED and PBF build rates.....	75
Table 2.14 - Comparison of SLM and conventional processes in terms of Charpy V-notch toughness [54]	89
Table 2.15 - Ultimate tensile strength, 0.2% offset yield strength and elongation at failure from Riemer et al. [86]	90
Table 2.16 - Tensile properties of SLM processed metallic materials	92
Table 2.17 - Fatigue limits for stainless steel 316L from Riemer et al. [86]	93
Table 2.18 - Chemical requirements for ASTM A131 EH36 steel.....	108
Table 2.19 - Tensile requirements for ASTM A131 EH36	108
Table 2.20 - Charpy V-notch impact requirements for ASTM A131 EH36	109
Table 2.21 - Carbon Equivalent for ASTM A131 EH36	109
Table 3.1 - ASTM A131 Powder Tests [129].....	115
Table 3.2 - Elemental composition of ASTM A131 powder [129]	116
Table 3.3 - SLM process parameters (red values refer to laser scanning speed in mm/s) [129]	118

Table 3.4 - Results from density test (red values represent density in g/cm ³) [129] ..	120
Table 3.5 - XRD analysis conditions	122
Table 3.6 - Weldability based on Carbon Equivalent (CE) Content.....	126
Table 4.1 - Number of specimens for tensile and Charpy test.....	130
Table 4.2 - ASM International recommended temperatures for tempering of steel [140]	133
Table 4.3 - Heat furnace details	133
Table 4.4 - Table of tensile test results for SLM built samples	135
Table 4.5 - Table of elongation results for SLM built samples	141
Table 4.6 – Table of Charpy test results for SLM built samples	144
Table 4.7 – Table of Vickers hardness values for SLM built samples	149
Table 4.8 - Final test results for SLM built EH36 steel specimen (45° built specimens)	155
Table 5.1 - SEM details and parameters	156
Table 5.2 - Scanning velocity of density test in colour scale.....	160
Table 5.3 - Density values of density test in colour scale.....	161
Table 7.1 - Table of Vickers hardness values for SLM built scaled model.....	178

Abstract

Additive manufacturing (AM) technology can potentially disrupt offshore and marine industry by effectively reducing manufacturing processes and leadtime, and enabling new product designs. A review of existing literature has revealed limited knowledge in using AM to process shipbuilding materials, which can otherwise enhance existing shipbuilding manufacturing workflow. This has led to the research motivation to establish the technical feasibility of using selective laser melting (SLM) to process ASTM A131 EH36 shipbuilding steel.

SLM process is a widely understood AM technology that has been used extensively to process other type of steels, for example stainless steel 316L. EH36 belongs to a class of high tensile low alloy steel which has traditionally been processed through casting. However, knowledge on using lasers to process EH36 is largely unknown, especially in AM applications. Using SLM to process EH36 is novel and will solve the problem of lack of knowledge in this field. The study thus aims to further the understanding of the mechanical properties and microstructure of SLM processed EH36.

A preliminary investigation was first carried out to establish the technical feasibility of using SLM to process EH36. The process parameters obtained were then used to further the investigations. Heat treatment process was applied as a possible post processing technique. Mechanical testing was carried out to characterise its mechanical properties. The fracture surfaces and microstructures were then studied to characterise the material.

The results showed that EH36 can be processed using SLM without any visible cracks. The mechanical properties of as built SLM processed EH36 exhibit very high tensile strength, but low ductility. The ductility can be improved through tempering heat treatment process, but at the partial sacrifice of tensile strength. Fractography analysis also affirmed the lack of ductility in the SLM processed EH36 samples. Finally, the microstructure showed that fine grain size and martensitic microstructure were the primary drivers behind its high tensile strength. Tempered samples experience grain coarsening and phase transformation to a mainly ferritic structure, which led to recovery in its ductility but a decrease in the tensile strength. A scaled model was fabricated to validate the results from the microstructure studies, and the findings indicate similar

microstructures formed. This demonstrates the repeatability of the developed process parameters on fabrication of complex joints.

The study contributes to the scientific knowledge with regard to material and mechanical property characterisation of SLM processed EH36. The findings from the fractography and microstructural analysis will contribute towards building the knowledge and facilitate future work on AM of EH36.

Chapter One Introduction

1.1 Background

Additive manufacturing (AM), also commonly known as 3D Printing (3DP), is a manufacturing technique that differentiates itself from subtractive manufacturing (eg. milling) and formative manufacturing (eg. casting) in that components are formed by joining materials layer by layer. The American Society for Testing and Materials (ASTM) International Standards F2792-12a defines AM as a process of joining materials to make objects from 3D model data, usually layer upon layer [1]. The standard also provides a structure for grouping AM machine technologies by their process categories, namely binder jetting, directed energy deposition, material extrusion, material jetting, powder bed fusion, sheet lamination and vat photopolymerisation.

The concept of AM started as early as 1860, where layer by layer techniques were used to fabricate photosculpture and molds of topographical relief maps [2, 3]. Subsequently, features of modern day AM techniques could be identified from published work in the areas of stereolithography, direct deposition and powder laser sintering from 1951 to 1979, but none of these resulted in commercialisation [4]. In 1987, the first commercialised AM unit was introduced. It was based on stereolithography process, where thin layers of ultraviolet light sensitive liquid polymer are cured using a laser [5]. The technology then subsequently progressed rapidly within a span of 30 years, with developments in materials, speed, build size and applications.

Benefits of AM can be categorised into two main branches – technical and commercial. Under technical benefits, research work has shown that metal parts built with AM can achieve excellent mechanical properties, and in many cases better than parts built with conventional methods such as casting or forging. However, this does not

hold true for every metallic part built with AM. While AM produced metallic parts usually have better tensile and hardness properties compared to conventional methods, the impact toughness and ductility performance may be inferior. This is usually compensated for when the parts are put through post processing, such as heat treatment, after the AM process to recover the mechanical properties. Because of its ability to achieve superior mechanical properties, components conventionally built using casting or forging can now be re-designed to reduce the thickness and eventually the weight.

Another key technical benefit of AM is the enablement of complex design. Because AM uses a layer by layer manufacturing technique, it is able to fabricate components of complex structures that are conventionally impossible to manufacture in one process. This enables engineers to re-think the design and achieve other benefits such as weight saving, material reduction, topology optimisation and conformal cooling. Engineers can also now do part consolidation where assembly parts can be re-designed as a single component.

The industry has also realised the commercial value of AM technology. With regard to process automation, because of part consolidation, manufacturing process lines can now be re-designed to reduce the total number of processes and also to streamline processes. Hence, it reduces the factory footprint and potentially reduces manpower. With the concept of digital warehousing, the industry can also potentially reduce the need for inventories, thus freeing up precious space resource. Many companies have also acknowledged AM as an enabling technology that has the potential of quickly producing the prototype in the exact size and material as the end use part, thus providing a quick way to bring the product to market. In addition, because the technology is additive in nature, compared against subtractive technology, wastage of material is very much reduced, which eventually translate to cost savings for the companies.

With the above mentioned benefits, AM brings many advantages to the manufacturing industry. The aerospace industry has adopted it for titanium alloy components used in military, commercial and passenger aircrafts [6, 7]. The oil and gas industry used it in component re-design, with one excellent case study in the fabrication of nozzles [8-10]. The dental and medical industries have adopted it for the fabrication of dental crowns and implants [11, 12]. However, the potential for adoption of existing AM technologies in offshore and marine industry, while high, remains industrially limited within the short term [13].

In shipbuilding operations of the offshore and marine industry, structural components are usually fabricated through a series of production processes. Due to the relatively lower levels of technology used in the manufacturing processes, there exists an opportunity to explore advanced manufacturing technologies for shipbuilding.

The manufacturing technology in shipbuilding has evolved over the years. Conventionally, iron fasteners and fittings were used to join the planks of wooden vessels. When shipbuilding materials transitioned from wood to iron, rivets were used as fasteners. Present day shipbuilding uses carbon or high tensile steels for ship construction, utilising welding techniques to join the steels together.

Today, a shipbuilding process is made up of many stages. Raw metal materials are brought into a shipyard and cut according to the desired shapes and sizes. The cut parts are then welded to form sub components. Alternatively, these sub components may be manufactured through casting. The sub components are then welded together to form larger components. The larger components are then fitted and welded together to form modules. The modules are then transported to the assembly area and joined together.

The machinery is then installed. Further outfitting is done and the final vessel is completed.

During the earlier stages of shipbuilding, where materials are prepared to form large components, many intermediate processes are required. These include transportation, preparation of jigs and fixtures, alignment, surface preparations etc. If AM can be adopted for the fabrication of such sub components, then the potential to remove these processes may lead to the streamlining of shipyard production operations. Furthermore, the manpower associated with these processes may potentially be reduced and optimised, hence leading to improved manufacturing productivity. The facilities and space for the originally required equipment may also be reduced. In addition, the technology may enable engineers and naval architects the provision to re-think component and ship design to improve overall vessel performance.

The challenges faced during the fabrication stage can be summarised into one key point – long lead time due to the various processes and required resources involved. For example, in the fabrication of a joint node casting, the lead time required to produce the component may be reduced by up to 40% if AM is used in place of casting. The summary of steps required for fabrication using casting can be seen in Table 1.1.

Table 1.1 – Typical fabrication steps for casting [14]

Process	Time Required (Days)
Core and Mould Making	28
Casting	1
Cooling	21
Burning Off Riser and Feeder Head	7
Initial Heat Treatment	14
Fettling, NDT, Weld Repair	49
Machining	35
Final Heat Treatment	3
Final Inspection	7
Total	165

As many of the processes are related to casting, they may not need to be considered in AM. These include core and mould making, casting, cooling, burning off riser and feeder head, fettling, NDT and weld repair. This essentially removes a substantial amount of time from the manufacturing process. We can predict the total time taken if the same component is to be fabricated using AM technology. This is shown in Table 1.2.

Table 1.2 - Reduced fabrication steps after considering AM

Process	Time Required (Days)
Preparation and Fabrication	21
Removal of Part	1
Machining	35
Heat Treatment	3
Final Inspection	7
Total	67

It is assumed that the total time taken for fabrication of the component using AM would be 21 days, and the component produced would still require the final processes such as machining, heat treatment and final inspection. It should be highlighted that in both cases, design of the part has not been factored into the total time taken. While time taken for design may be significant for parts that are made only once, repeated components may re-use the same design. Hence, it would only be fair to assume that the time taken for design of part should not be factored into the comparison. With all these assumptions in place, the total time taken for AM to produce the component is very much reduced from 165 to 67 days. Furthermore, the advantages mentioned above, such as reduction in manpower, resources required, facilities, footprint and streamlining of the process, would provide good reasons to explore the technology.

Very recently, the technology has been identified to be used to produce metal fuel nozzles for gas turbines, a major step towards using the technology for mass-manufactured parts in the industry. [15, 16] However, there is still limited literature on AM's application in the fabrication of structural components in shipbuilding industry.

In order for the shipbuilding industry to adopt AM technology, there are many challenges to overcome. The materials used in shipbuilding are specially formulated and fabricated for the industry; hence there is a need to establish the availability of AM materials to be used in offshore and marine industry. Due to the different operating conditions of ships compared to other industries, there is a need to determine the mechanical performance of parts built using AM, especially on the tensile strength and impact toughness values.

In addition to limitations on materials, sizes of the sub components in shipbuilding are relatively larger than typical metal parts built using AM technology; hence there is also a need for size consideration. In [17] Wu et al. presented a review on additive manufacturing machines and their build sizes that are relevant to the offshore and marine industry. In the review, Wu et al. discussed about various build volumes of AM systems, from 300 x 350 x 300 mm (x,y,z) which may satisfy the size requirement for smaller components such as fittings and fasteners, to larger machines with build envelope up to 800 x 400 x 500 mm (x,y,z) [18], which may be applicable for larger components such as heat exchangers and manifolds. South African research institute the Council for Scientific and Industrial Research's (CSIR's) National Laser Centre (NLC) is also developing a large-area system, also known as the Aeroswift project, which is able to produce components with maximum dimensions of 2 × 0.6 × 0.6 mm (x,y,z) from metal powders [19].

Therefore, the project will identify a specific component to establish the technical feasibility of using AM to replace current manufacturing methods, and eventually complement the existing production process.

1.2 Research Motivation and Approach

The potential and technical feasibility of AM technology for offshore and marine industry is largely unknown and unexplored. Challenges include availability of AM materials, fabrication processes, mechanical properties of build parts, etc. It is thus imperative to study and investigate the processes and methodologies of AM technology suitable for offshore and marine metal parts. Based on the background provided in section 1.1, the following approach will be used:

- Literature review of materials used in shipbuilding, current commercial AM processes, properties of parts built using AM.
- Establish the need for research in AM of an identified shipbuilding material based on the literature review.
- Select an appropriate AM process for the identified material.
- Conduct preliminary investigations to ascertain the feasibility of using AM to process shipbuilding material.
- Optimise the AM process parameters.
- Characterise AM built part properties.
- Validate properties against industry requirements.

1.3 Research Objectives

The objectives of this study are to establish the technical feasibility of using selective laser melting (SLM) to process ASTM A131 shipbuilding marine grade steel and develop an understanding of the material characteristics of the SLM processed steel. The study will be focussed on the characterisation of the mechanical properties and microstructure of the SLM processed steel. This knowledge and development of shipbuilding materials for AM are important to enable for applications for AM of shipbuilding components.

1.4 Thesis Outline

- Chapter 1 introduces the background, motivation and objectives the research.
- Chapter 2 reviews the literature on ASTM A131 marine grade shipbuilding material, including the chemical composition, traditional processing and further justifies the selection of EH36 grade of material for the study. The chapter then further reviews the literature on various additive manufacturing technologies suitable for processing metallic components. The chapter finally reviews typical material properties processed by additive manufacturing.
- Chapter 3 describes the preliminary investigation conducted on using SLM to process EH36 and outlines the outcome.
- Chapter 4 describes the tensile and impact tests conducted to obtain mechanical properties of EH36. It also describes the heat treatment process applied onto the test samples.
- Chapter 5 describes and discusses the results from the fractography analysis on the tested samples.
- Chapter 6 describes and discusses the results from the microstructural analysis on the tested samples.
- Chapter 7 describes and compares the results from a fabricated scaled complex component, against the results from the mechanical test coupons.
- Chapter 8 outlines the conclusions based on the study and suggestions for future work.

Chapter Two Literature Review

Literature review will be conducted on existing metallic materials used in marine structures. The review will enable the research to streamline into an identified material to be studied on using AM technology. Since AM is an unexplored technology in the shipbuilding aspect of the offshore and marine industry, it is important to evaluate all available AM processes for fabrication of metal components. Each AM process has its strengths and limitations, hence there is no one AM process that suits all applications. In the research study, various AM processes will be evaluated to identify the most suitable process for fabrication of the identified shipbuilding material. One AM process will eventually be identified and in-depth literature review on this AM process will be carried out.

With the identified AM process, the research can then focus on developing an optimised set of parameters to fabricate repeatable components. The choice of component will be one that represents a huge variety of work performed in shipbuilding, thus providing a translation of the results to the fabrication of other shipbuilding components. Mechanical tests according to industry required standards will be performed to ascertain that the performance of the AM produced part meets the industry requirements.

The literature review will facilitate the technical feasibility of adopting additive manufacturing as a fabrication technology for marine structures used in shipbuilding, to achieve better design and improved performance. Outline of the literature review includes:

- 1) To study the metallic materials conventionally used in shipbuilding
- 2) To identify one material for the research work

- 3) To study the commercial AM processes and evaluate their feasibility in processing metallic materials
- 4) To identify a suitable AM process to process the identified material

2.1 Materials

2.1.1 ASTM A131 Shipbuilding Material

A131/A131M – 14: Standard Specification for Structural Steel for Ships covers structural steel plates, shapes, bars, and rivets intended primarily for use in ship construction [20]. Material under this specification is available as Ordinary Strength Steel (Grades A, B, D, and E with a specified minimum yield point of 34 ksi [235 MPa]), and Higher Strength Steel (Grades AH, DH, EH, and FH with a specified minimum yield point of 46 ksi [315 MPa], 51 ksi [355 MPa], or 57 ksi [390 MPa]). It is further categorised according to their tensile strength requirements by denoting the grade with numbers behind. The corresponding numbers for minimum yield point of 315 MPa, 355MPa, and 390MPa are 32, 36 and 40 respectively (see Table 2.1). While the alphabet “H” denotes higher strength steel, the other alphabets (A, D, E, F) denote the Charpy V-notch impact requirements at various test temperatures. Test temperatures at “A” (except ordinary strength steel, grade A is at 20 °C and B at 0 °C), “D”, “E”, and “F” are 0, -20, -40, -60 °C respectively (see Table 2.2).

**Table 2.1 - Tensile requirements for Ordinary-Strength and Higher-Strength Structural Steel in
ASTM A131 [20]**

Grade	Tensile Strength, ksi [MPa]	Yield Point, min, ksi [MPa]	Elongation in 8 in. [200mm], min, %	Elongation in 2 in. [50mm], min, %
Ordinary Strength:				
A, B, D, E	58 to 75 [400 to 520]	34 [235]	21	24
Higher Strength:				
AH32, DH32, EH32, FH32	64 to 85 [440 to 590]	46 [315]	19	22
AH36, DH36, EH36, FH36	71 to 90 [490 to 620]	51 [355]	19	22
AH40, DH40, EH40, FH40	74 to 94 [510 to 650]	57 [390]	19	22

Table 2.2 - Charpy V-notch impact requirements for Ordinary-Strength and Higher-Strength Structural Steel in ASTM A131 [20]

Grade	Test Temperature, °C	Average Absorbed Energy, min, J		
		t ≤ 50 mm	t > 50mm t ≤ 7 mm	t > 70mm t ≤ 100mm
A	20		34	41
B	0	27	34	41
AH32	0	31	38	46
AH36	0	34	41	50
AH40	0	39	46	55
D	-20	27	34	41
DH32	-20	31	38	46
DH36	-20	34	41	50
DH40	-20	39	46	55
E	-40	27	34	41
EH32	-40	31	38	46
EH36	-40	34	41	50
EH40	-40	39	46	55
FH32	-60	31	38	46
FH36	-60	34	41	50
FH40	-60	39	46	55

Table 2.3 - Chemical requirements for Higher-Strength Structural Steel in ASTM A131 [20]

Element	Chemical Composition, % max unless otherwise specified	
	Grades AH/DH/EH32, AH/DH/EH36, AH/DH/EH40	Grades FH32/36/40
Carbon, C	0.18	0.16
Manganese, Mn	0.90 – 1.60	0.90 – 1.60
Silicon, Si	0.10 – 0.50	0.10 – 0.50
Phosphorous, P	0.035	0.025
Sulphur, S	0.035	0.025
Aluminium (acid soluble), min, Al	0.015	0.015
Columbium, Cb/Niobium, Nb	0.02 – 0.05	0.02 – 0.05
Vanadium, V	0.05 – 0.10	0.05 – 0.10
Titanium, Ti	0.02	0.02
Copper, Cu	0.35	0.35
Chromium, Cr	0.20	0.20
Nickel, Ni	0.40	0.40
Molybdenum, Mo	0.08	0.08
Nitrogen, N	-	0.009

2.1.1.1 Chemical Composition

The requirements for chemical composition are given in Table 2.3. The chemical composition of higher strength steels may vary for different product thicknesses to meet particular mechanical property requirements. Usually, they have a manganese (Mn) content of up to 2.0 weight (wt)% in combination with very low carbon content (< 0.10 wt% C) and also minor additions of alloying elements such as niobium (Nb), vanadium (V), titanium (Ti), molybdenum (Mo) and boron (B). Rosado et al. [21] and Aung et al. [22] presented on the roles of alloying elements in high strength steel, shown in Table 2.4 and Table 2.5. The main function of the alloying additions is the strengthening of ferrite through the following mechanisms: grain refinement, solid solution and precipitation hardening. Solid solution hardening is closely related to the alloy element

content, whilst precipitation hardening and grain refinement depend on the interaction between chemical composition and Thermo-Mechanical Controlled Process (TMCP). Thus, each individual element coupled with the cooling rate will determine the type and volume fraction of phases that will form in a given steel processed under given conditions [21].

Williams et al. presented some aspects of the advances in alloy design and properties that have taken place for high strength steel [23]. In relation to the chemical composition, some strategic alloy combinations extracted from his work is summarised in Table 2.6.

Table 2.4 - Major effects of alloying elements in high strength steel [21]

Element (wt%)	Effect and reason of adding
C (0.03 - 0.10)	Matrix strengthening (by precipitation)
Mn (1.6 - 2.0)	Delays austenite decomposition during accelerated cooling process (increasing hardenability); Substitutional strengthening effect; Decreases ductile to brittle transition temperature; Indispensable to obtain a fine-grained lower bainite microstructure.
Si (up to 0.6)	Improvement in strength (solid solution).
Nb (0.03 - 0.06)	Reduces temperature range in which recrystallization is possible between rolling passes; Retard recrystallization and inhibit austenite grain growth (improves strength and toughness by grain refinement).
Ti (0.005 - 0.03)	Grain refinement by suppressing the coarsening of austenite grains (TiN formation); Strong ferrite strengthener; Fixes the free Ni (prevent detrimental effect of Ni on hardenability).
Ni (0.2 - 1.0)	Improves the properties of low-carbon steels without impairing field weldability and low temperature toughness; In contrast to Mg and Mo, Ni tends to form less hardened microstructural constituents detrimental to low temperature toughness in the plate (increases fracture toughness).
V (0.03 - 0.08)	Leads to precipitation strengthening during the tempering treatment; Strong ferrite strengthener.
Mo (0.2 - 0.6)	Improves hardenability and thereby promotes the formation of the desired lower bainite microstructure.

Table 2.5 - Other alloying elements in high strength steel [22, 24]

Element	Effect and reason of adding
Cu	Increases strength by ferrite strengthening.
Al	Control of grain size.
B	Improve hardenability of quenched and tempered grades.
Ca	Helps to control the shape of non-metallic inclusions, thereby improving toughness.
Cr	Wear resistance, corrosion resistance and improved hardenability.
N	Economically improves strength but is accompanied by drop in notch toughness (promotes brittle cleavage fracture), hence limited to 0.02%.

Table 2.6 - Strategy alloying combinations to improve strength and toughness [23]

Alloying combination	Purpose
V+Mo+Nb	To produce secondary hardening by forming carbides, nitrides and carbonitrides
Ni+Mo	Effective addition of microstructure refinement by suppressing austenite recrystallization during controlled rolling and steel strengthening by precipitation hardening and enhancement of hardenability
Ni+B	Synergistic improvement of hardenability
Nb+V	To increase strength properties. However, steels based on this combination may require relatively high carbon equivalent design, which can compromise the capability for preheat-free field welding
Mo+Nb+Ti	<p>Effective in achieving the strength requirements of high Mn steels</p> <p>A significantly finer ferrite grain size</p> <p>Low temperature transformation constituents such as bainite containing acicular carbide needles in leaner alloyed steels and martensite/austenite in highly alloyed steels;</p> <p>Enhances precipitation hardening. A synergistic benefit attributed to Ti addition.</p>

Equation (2.1) is known as the Carbon Equivalent (CE) formula. It calculates the CE content to determine properties of alloy when the material (usually ferrous) contains more than just Carbon. It is usually used in welding to determine the welding processes required to avoid defects. It is also used in heat treatment and casting applications of cast iron. The CE content stipulated under the ASTM A131 standards range from 0.36 to 0.42 [20]. For the whole list of CE content, please refer to Table 2.7.

$$C_{eq} = C + \frac{Mn}{6} + \frac{Cr + Mo + V}{5} + \frac{Ni + Cu}{15} (\%) \quad (2.1)$$

Table 2.7 - Carbon Equivalent for Higher-Strength Structural Steel Produced by TMCP from ASTM A131 [20]

Grade	Carbon Equivalent , max, %	
	Thickness (t) , mm	
	t ≤ 50 mm	t > 50 mm t ≤ 100 mm
AH32, DH32, EH32, FH32	0.36	0.38
AH36, DH36, EH36, FH36	0.38	0.40
AH40, DH40, EH40, FH40	0.40	0.42

2.1.1.2 Steel Transformation

An iron-carbon (Fe-C) phase diagram (see Figure 2.1) is often used for the basic understanding of the microstructures of the steel. It illustrates the effect of dissolved carbon in iron, and is critical for developing heat treatment regimes for large-scale production of cast irons and steel. It describes the primary formation of allotropes of iron, namely α -Fe (ferrite, bcc), γ -Fe (austenite, fcc) and δ -Fe (bcc), and also describes the intermediate phase Fe_3C (cementite) at the other end of the diagram.

Ae_1 , Ae_2 , Ae_3 and A_{cm} indicate the temperatures at which phase changes occur: they are arrest points for equilibria detected during thermal analysis. Slow cooling enables austenite with the composition 0.8% C to decompose eutectoidally at the temperature Ae_1 and form the microconstituent pearlite, a lamellar composite of soft, ductile ferrite (initially 0.025% C) and hard, brittle cementite (6.67% C). Slow cooling of austenite with hypo-eutectoid (<0.8% C) and hyper-eutectoid (>0.8% C) compositions results in a microstructure of pearlite embedded in ferrite and cementite, respectively. On the other hand, quenching of austenite from a temperature above Ae_3 forms a hard metastable phase known as martensite. [25]

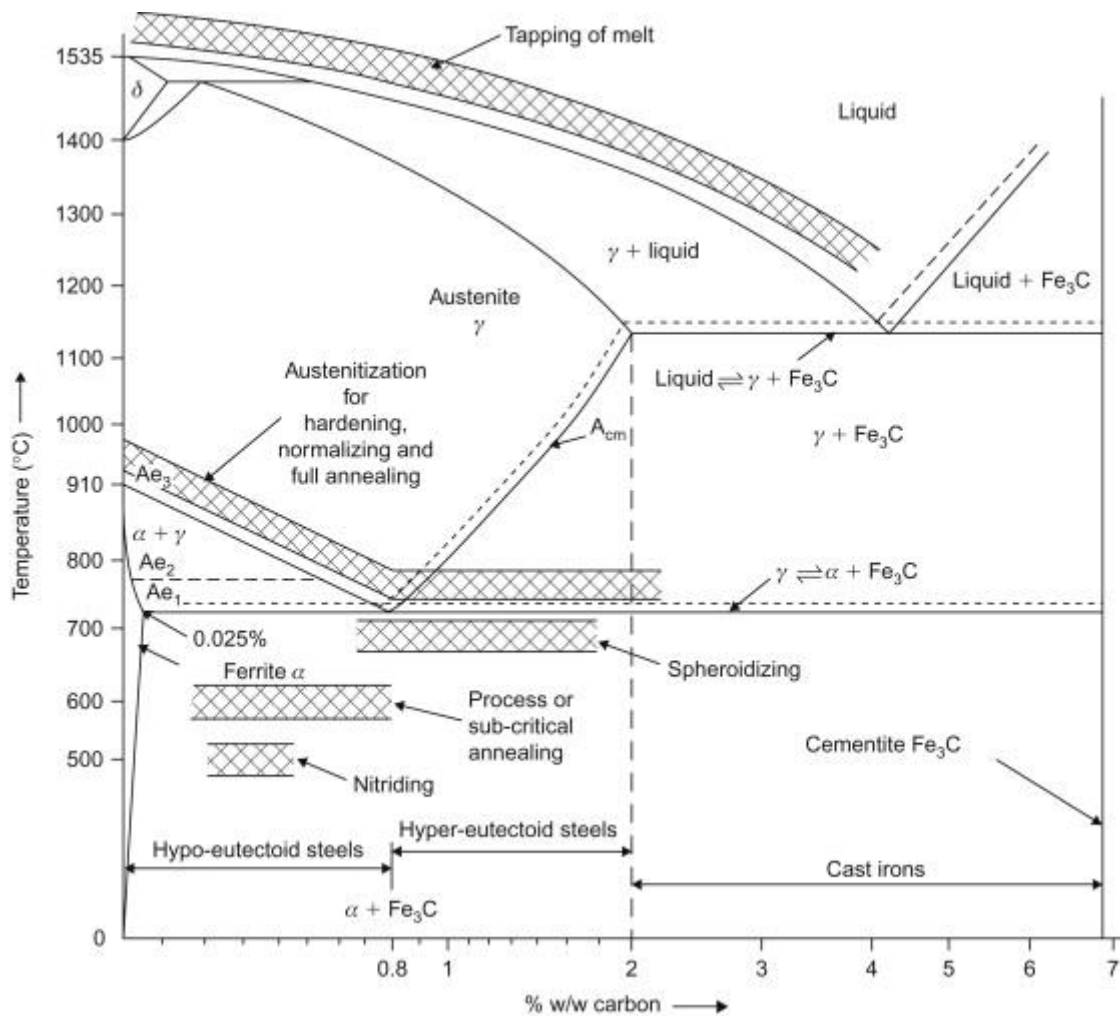


Figure 2.1 - Iron-carbon phase diagram [25]

Temperature and composition ‘windows’ for some important heat treatment operations have been superimposed upon the phase diagram in Figure 2.1. Heating may be carried out above or below the eutectic temperature for softening. Below the Ae_1 is a subcritical anneal which recrystallizes the ferrite but leaves the pearlite unaffected. This process anneal is usually applied to plastically deformed materials and is the most economical procedure. Heating above the eutectoid temperature recrystallizes the steel and results in a completely new γ -grain structure. Depending on time and temperature a refined grain structure can be produced with a corresponding improvement in yield strength and properties. The steel may also be air cooled (normalized) or furnace cooled (full annealing) to control the resultant grain size. A further heat treatment for medium- and high-carbon steels is a spheroidizing anneal during which with time the cementite

plates adopt a more spherical shape to reduce their surface energy. This improves the cold workability of the steel. [25]

In the iron–carbon system the γ -phase, austenite, which is a solid solution of carbon in fcc iron, decomposes on cooling to give a structure known as pearlite, composed of alternate lamellae of cementite (Fe_3C) and ferrite. However, on very rapid cooling conditions, a metastable phase called martensite, which is a supersaturated solid solution of carbon in ferrite, is produced. The microstructure of such a transformed steel is not homogeneous but consists of plate-like needles of martensite embedded in a matrix of the parent austenite. Apart from martensite, another structure known as bainite may also be formed if the formation of pearlite is avoided by cooling the austenite rapidly through the temperature range above 550°C , and then holding the steel at some temperature between 250°C and 550°C . A bainitic structure consists of plate-like grains of ferrite, somewhat like the plates of martensite, inside which carbide particles can be seen.

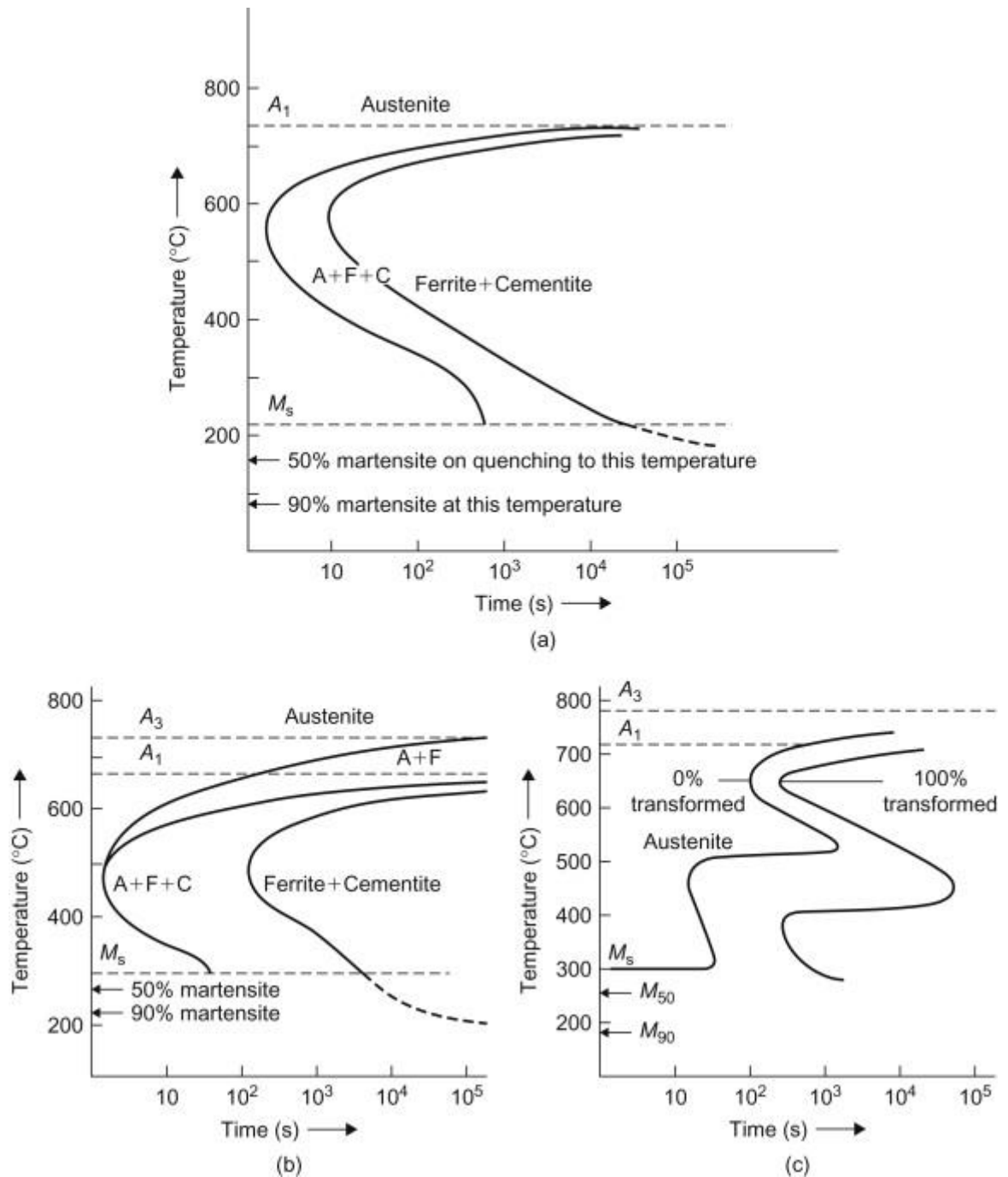


Figure 2.2 - Time-temperature transformation curves for (a) eutectoid, (b) hypo-eutectoid and (c) low-alloy (e.g. Ni/Cr/Mo) steels

A time-temperature transformation (TTT) curve as shown in Figure 2.2 plots the time necessary at a given temperature to transform austenite of eutectoid composition to one of the three structures, namely pearlite (when the steel will be soft and ductile), bainite or martensite (when the steel will be hard and brittle). From the TTT curve it can be seen that just below the critical temperature, A_1 , the rate of transformation is slow

even though the atomic mobility must be high in this temperature range. This is because any phase change involving nucleation and growth (e.g. the pearlite transformation) is faced with nucleation difficulties, which arise from the necessary surface and strain energy contributions to the nucleus. Of course, as the transformation temperature approaches the temperature corresponding to the knee of the curve, the transformation rate increases. The slowness of the transformation below the knee of the TTT curve, when bainite is formed, is also readily understood, since atomic migration is slow at these lower temperatures and the bainite transformation depends on diffusion. The lower part of the TTT curve below about 250–300°C indicates, however, that the transformation speeds up again and takes place exceedingly fast, even though atomic mobility in this temperature range must be very low. For this reason, it is concluded that the martensite transformation does not depend on the speed of migration of carbon atoms and, consequently, it is often referred to as a diffusionless transformation. The austenite only starts transforming to martensite when the temperature falls below a critical temperature, usually denoted by M_s . Below M_s the percentage of austenite transformed to martensite is indicated on the diagram by a series of horizontal lines.

Martensite, the hardening constituent in quenched steels, is formed at temperatures below about 200°C. The regions of the austenite which have transformed to martensite are lenticular in shape and may easily be recognized by etching or from the distortion they produce on the polished surface of the alloy. The lenticular shape of a martensite needle is a direct consequence of the stresses produced in the surrounding matrix by the shear mechanism of the transformation and is exactly analogous to the similar effect found in mechanical twinning. The strain energy associated with martensite is tolerated because the growth of such sheared regions does not depend on diffusion, and since the regions are coherent with the matrix they are able to spread at great speed through the crystal. The large free energy change associated with the rapid formation of the new phase outweighs the strain energy, so that there is a net lowering of free energy. [26]

2.1.1.3 Steel Processing

ASTM A131 higher strength steels are conventionally fabricated through the Thermo-Mechanical Controlled Process (TMCP). It was developed to meet the demand

for strength and toughness in high strength steel, through grain refinement as the most effective metallurgical mechanism. After the steel is processed through rolling, a cooling process, known as accelerated cooling process (AcC), is performed to meet the higher requirements for strain based design, with respect to strain hardenability, toughness as well as high strength [27]. Alternatively, the steel plate may first be hot rolled and soaked (held at a temperature until the desired microstructural changes take place) and then submitted to an inline quenching and tempering (QT) process. Such QT treatment is performed to produce a bainite-martensite microstructure without applying AcC process. By tempering it is possible to reduce the brittleness of martensite and improve ductility and toughness [28].

Shinmiya et al. [29] described an improved conceptual TMCP with the addition of an extra process known as the Online Heat-treatment Process (HOP). It was developed in order to obtain not only high strength by transformation strengthening but also high toughness by refinement of transformed microstructure, resulting in a combination of high strength/high toughness steel with reduced alloying elements. The microstructure consists of a bainitic matrix and finely dispersed martensite-austenite constituent (MA) as second phase with a volume fraction above 7%. The process consists of an advanced accelerated cooling device, with the purpose of reaching highest cooling rates and an induction heating equipment for HOP, with high heating capacity to heat thick plates up to 40 mm. This combination enabled the new ‘unconventional’ TMCP to reach a novel metallurgical controlling process that cannot be achieved by the ‘conventional’ TMCP.

Figure 2.3 illustrates a schematic TMCP diagram for ‘conventional’ and ‘unconventional’ production processes and some morphological changes in the microstructure. In the ‘conventional’ TMCP process, the steel plate is controlled rolled, accelerated cooled and then air-cooled. On the other hand, in the ‘unconventional’ TMCP process, the plate is rapidly reheated by the induction coils immediately after accelerated cooling and followed by air cooling. Rosado presented an overview of the relevant parameters of the TMCP [21], shown in Table 2.8. Figure 2.3(b) shows a schematic explanation of the microstructural changes promoted during HOP process.

Both TMCP processes are typically performed at strictly controlled and relatively low temperatures (i.e. between T_{nr} and $T_{A_{r3}}$) in order to produce very fine

grains. More clearly, the last hot rolling steps are performed below the non-recrystallization temperature (T_{nr}). As a result, the severely deformed ('pancaked') austenite grains do not completely recrystallize, which provides a large number of nucleation sites for the transformation of austenite to ferrite or bainite. Investigation of AcC conditions reports that lowering both, starting and stopping temperatures promote formation of ferrite and martensite/austenite constituents respectively [28, 29].

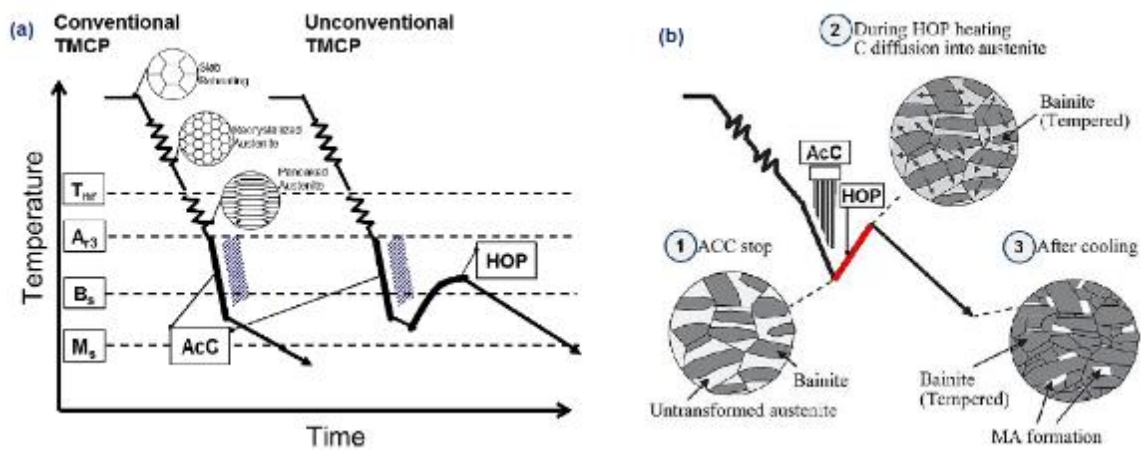


Figure 2.3 - (a) TMCP diagram for 'conventional' vs 'unconventional' processing; (b) microstructural changes promoted by HOP [29]

Table 2.8 - Overview of TMCP stages, typical temperatures and features [21]

Processing Parameters		Range	Features
Rolling	Reheat Temp. ($^{\circ}\text{C}$)	1140 – 1180	Dissolution of precipitates; Produce a fine, polygonal austenitic grain; Maintain within the range of the T_{nr} ;
	Reduction ratio (%)	40 – 75	
	Finishing Temp. ($^{\circ}\text{C}$)	760 – 800	
AcC	Start Temp. ($^{\circ}\text{C}$)	730 – 760	Enhances grain refinement of ferrite; Prevents formation of pearlite during cooling;
Tempering	Cooling rate ($^{\circ}\text{C}/\text{s}$)	20 – 50	
	Stop Temp. ($^{\circ}\text{C}$)	150 – 400	Reduce excess hardness and residual stresses.
	Heat Temp. ($^{\circ}\text{C}$)	600	

2.1.1.4 Selection of Grade of ASTM A131 Steel

The ASTM A131 group of steels is specifically designed with TMCP as the manufacturing process. The steel properties, process parameters and guidelines are thus unique to those typically processed by TMCP. For a selection of the grade of steel under ASTM A131 to be processed by AM, it is understood that this existing ASTM standard is not suitable, and a different set of material properties and parameters should be referenced. However, there is insufficient literature on AM processed ASTM A131 steels available that can be referenced for this study. Hence, a practical approach would be to use the existing standard as-is, as a starting point to develop preliminary results and findings, and to lay the foundation for future work, which may then include developing an optimised set of properties and parameters for using AM to process the steels.


There are several grades of steel under the ASTM A131 standard. When selecting the specific grade of material for this research, it is important to consider the scalability of the research outcome. The research findings must be easily translated to

other grades of materials in order to facilitate the research of the rest of the materials under the ASTM A131 standard. In order to identify the grade of material to conduct the research work, it is hence proposed to study the ways to categorise the various grades. Table 2.1 shows the tensile requirements for ordinary strength and higher strength grades of steels under the ASTM A131 standards. Since higher strength grades of steels have higher tensile values, it is more often selected for the ship hull structural steels [30]. According to Table 2.3, the types of steels can also be categorised by their chemical composition into two main groups, with the AH, DH and EH grades in one category, and the FH grades in the other category. This can also be cross referenced with Table 2.2, where lower temperature tests equate to better performing impact toughness values. However, steels with FH grades are specifically used for operating regions where temperatures are extremely low, for example in the Northern and Arctic regions, where the materials are subjected to severe climatic conditions [31, 32]. FH grades are not often chosen during the materials selection process because these operating regions constitute only a minority of the global footprint [33]. Out of the remaining AH, DH and EH, it is thus imperative to select the more stringent one, which will be the EH grade of steel. The selection argument can thus be summarised and shown in Table 2.9.

Table 2.9 - Selection of grade of steel under ASTM A131

		Minimum Yield Requirements (MPa)			
		Ordinary-Strength Steel	Higher-Strength Steel		
		235	315	355	390
Charpy V-notch Impact Requirements (Average absorbed energy, $t \leq 50$ mm, J)	20	A (NA)			
	0	B (27)	AH32 (31)	AH36 (34)	AH40 (39)
	-20	D (27)	DH32 (31)	DH36 (34)	DH40 (39)
	-40	E (27)	EH32 (31)	EH36 (34)	EH40 (39)
	-60		FH32 (31)	FH36 (34)	FH40 (39)

Legend:  Not Applicable

 Eliminated based on discussion

Grades A, B, D, E, AH, DH and FH are eliminated based on the discussion above. The final selection from the remaining grades EH32, EH36 and EH40 is then determined by the highest strength, which then narrows it down to EH40. However, with reference to the use of high tensile strength steel for shipbuilding, EH32 and EH36 are more commonly used than EH40 [34]. Hence, the mechanical requirements of EH36 was eventually identified as the benchmark properties to be referenced for this research.

2.2 Additive Manufacturing Technologies

Under the ASTM F2792 – 12a Standard Terminology for Additive Manufacturing Technologies, the technology can be categorised by their processes into seven main groups. Table 2.10 below shows the process categories.

Table 2.10 - AM process categories

Process	Description
Binder Jetting	An additive manufacturing process in which a liquid bonding agent is selectively deposited to join powder materials.
Directed Energy Deposition (DED)	An additive manufacturing process in which focused thermal energy (an energy source (e.g., laser, electron beam, or plasma arc) that is focused to melt the materials being deposited) is used to fuse materials by melting as they are being deposited.
Material Extrusion	An additive manufacturing process in which material is selectively dispensed through a nozzle or orifice.
Material Jetting	An additive manufacturing process in which droplets of build material are selectively deposited.
Powder Bed Fusion	An additive manufacturing process in which thermal energy selectively fuses regions of a powder bed.

Sheet Lamination	An additive manufacturing process in which sheets of material are bonded to form an object.
Vat Photopolymerisation	An additive manufacturing process in which liquid photopolymer in a vat is selectively cured by light-activated polymerisation.

Based on commercially available data, Louis Davis, AM consultant and director of marketing at Stone Interactive Group, has created two diagrams setting out the various machines and processes now available in AM [35]. The diagrams show industrial grade metal additive manufacturing processes (Figure 2.4) and machines (Figure 2.5). Louis categories metal additive manufacturing into four main branches, namely Powder Bed Fusion, Directed Energy Deposition, Binder Jetting and Sheet Lamination.

Industrial-Grade Metal Additive Manufacturing Processes

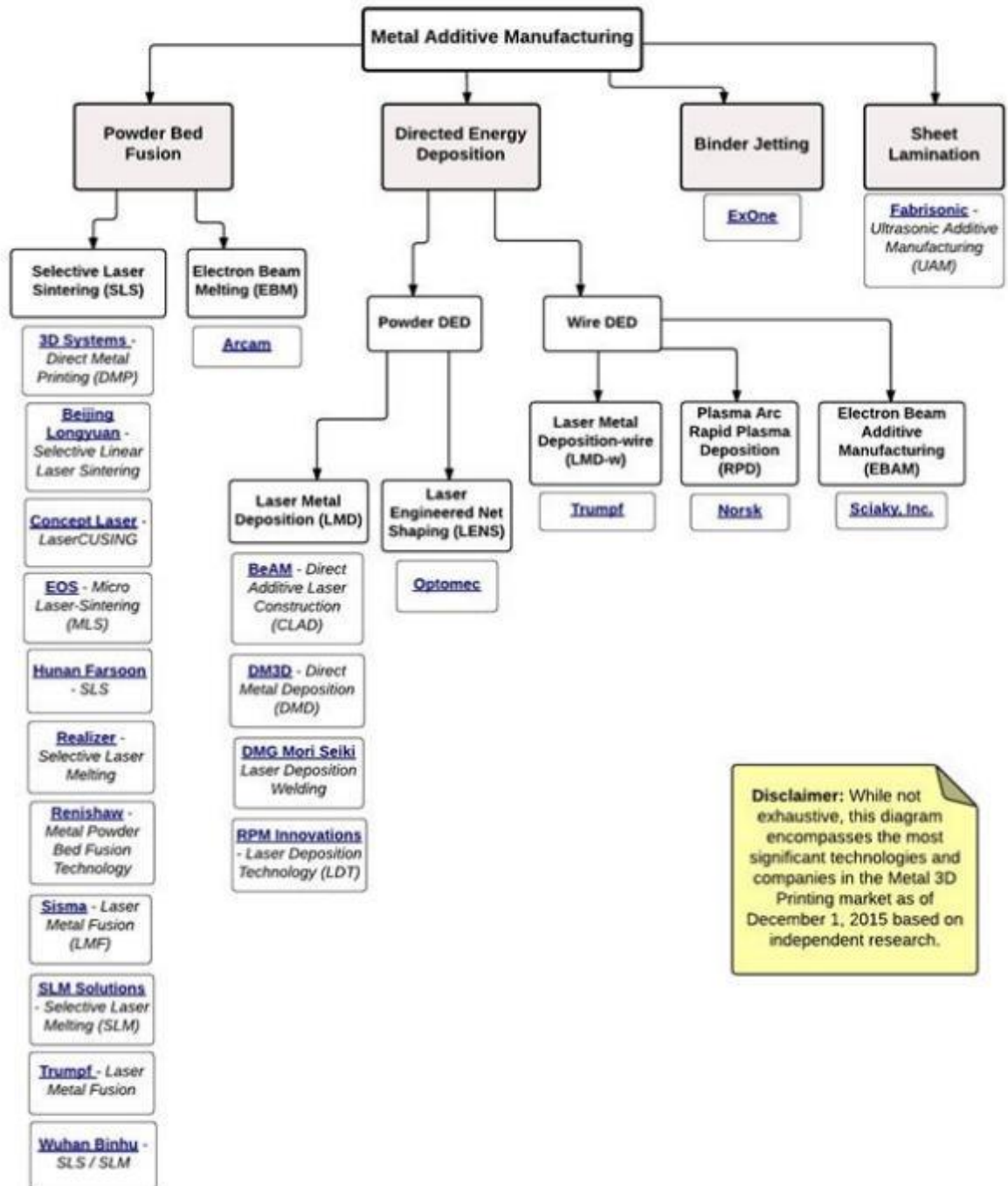
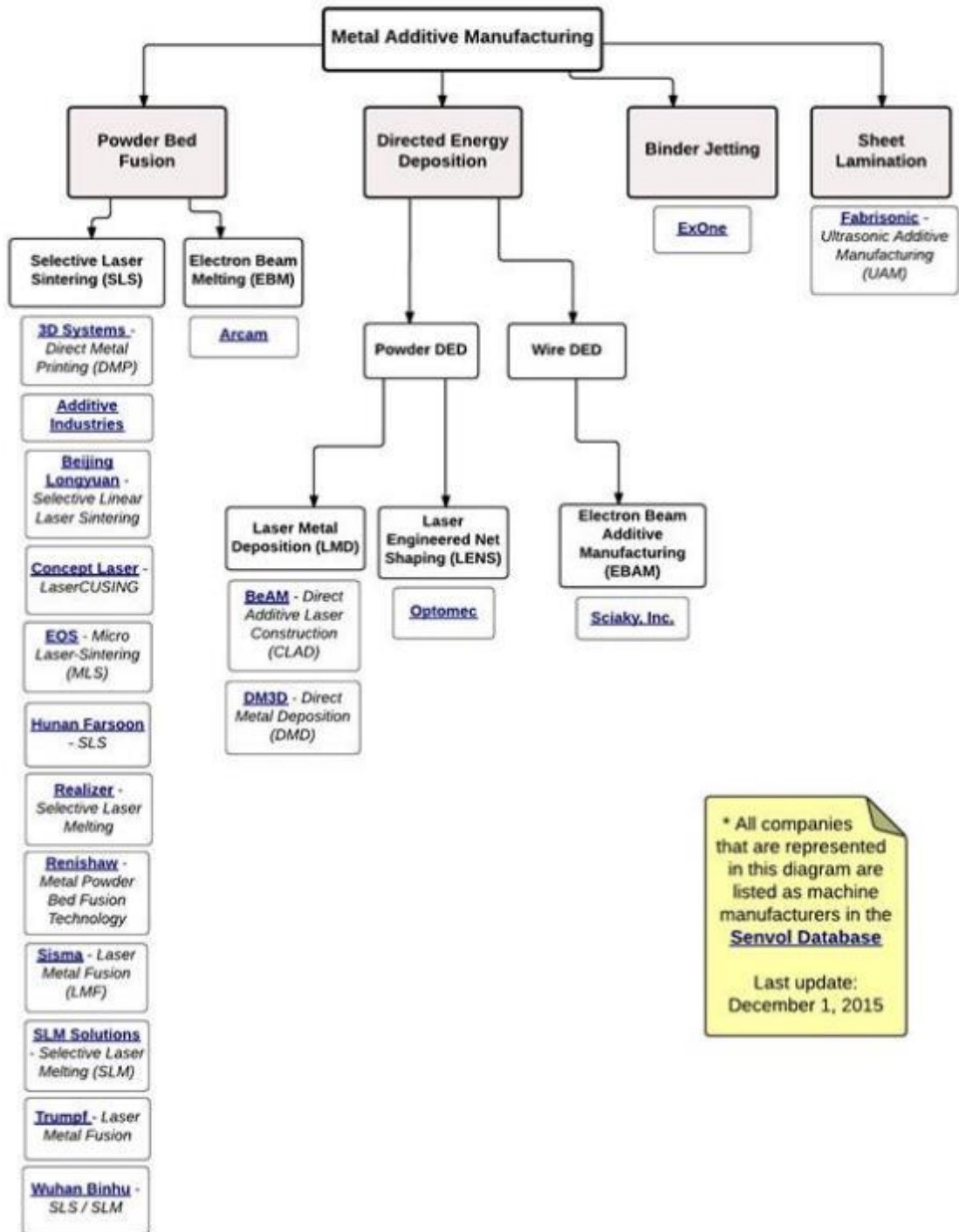


Figure 2.4 - Industrial-Grade Metal Additive Manufacturing Processes [35]

Industrial-Grade Metal Additive Manufacturing Machines - Available for Purchase* -



* All companies that are represented in this diagram are listed as machine manufacturers in the [Senvol Database](#)

Last update:
December 1, 2015

Figure 2.5 - Industrial-Grade Metal Additive Manufacturing Machines [35]

Each of the technologies has their own strengths and limitations, and there is no single technology that can suit all applications. As discussed in Chapter **Error! Reference source not found.**, the scope of the research project will be limited to ASTM

A131 EH36 high tensile strength steel. A preliminary literature review will first be conducted to identify the suitable AM processes for EH36 material.

Regardless of which AM process, the concept of AM are similar throughout and may be summarised as follows. The process starts with a 3D CAD model, either by scanning a physical object or through creating a 3D model using a CAD software. The 3D CAD model is then sent to the AM machine where it will be mathematically sliced into layers. The AM machine will then begin creating the predetermined shape layer by layer according to the sliced data. The layers will build up to form the 3D shape required, and at the end of the process, the object will be formed. In the following sections, brief descriptions of each category will be discussed with relevance to producing metal components.

2.2.1 Binder Jetting

In binder jetting, powder is selectively bonded together through deposited binding agent, layer by layer (see Figure 2.6). The print head strategically drops binder into the powder. The job box lowers and another layer of powder is then spread and binder is added. The end result will be a cube of powder with the solid bonded component inside. The part will then be removed from the cube of powder and post-processed with an air compressor to remove any residual powder. The end product will form a net shape 3D component, which is useful for prototyping purposes. One of the commonly known binder jetting technology is Three-Dimensional Printing (3DP), which was invented at MIT and has been licensed to more than five companies for commercialization [36]. The advantages of 3DP process includes – parts are self-supporting in the powder bed so that support structures are not needed; parts can be arrayed in one layer and stacked in the powder bed to greatly increase the number of parts that can be built at one time; assemblies of parts and kinematic joints can be fabricated since loose powder can be removed between the parts.

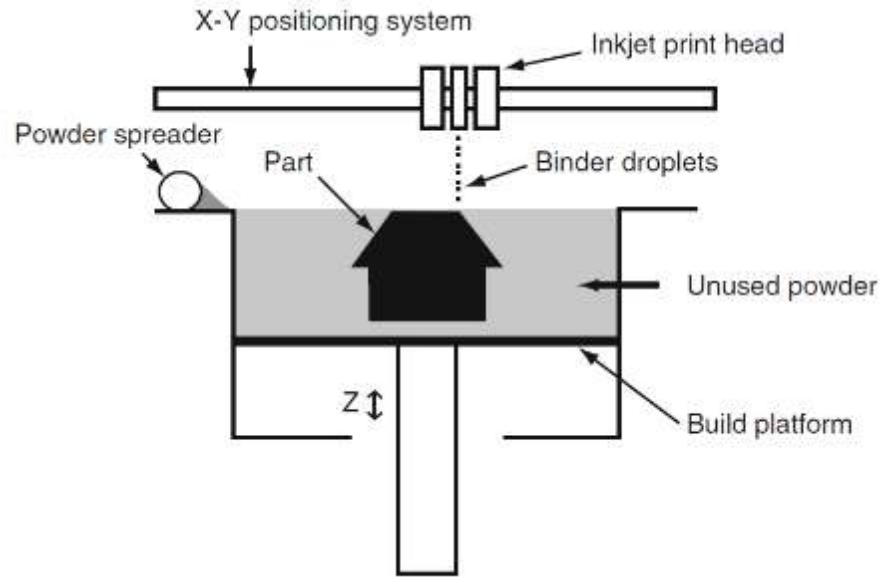


Figure 2.6 - Schematic of binder jetting process [36]

In order to use binder jetting technology to produce metal parts, the completed component may then be infiltrated with an appropriate material and sintered as an additional post process. Hot isotropic pressing is sometimes applied to achieve the desired mechanical properties. One example of such machine is the Ex One 3D printer. Applications of this machine include prototypes of metal parts and some low-volume manufacturing, as well as tooling. In the tooling area, Ex One is usually used to produce conformal cooling in injection moulds. In conformal cooling, cooling channels are routed close to the surfaces of the part cavity, particularly where hot spots are predicted. Using conventional machining processes, cooling channels are drilled as straight holes. With AM processes, however, cooling channels of virtually any shape and configuration can be designed into tools.

However, the relative density of built parts using this method is generally poorer. Bai et al. demonstrated using a binder jetting AM process (ExOne R2) to fabricate green parts made of high purity copper powder [37]. Once printed, the green part was sintered under a reducing atmosphere to create copper parts in pure metal form. The resulting sintered part had a relative density of 85%. The author attributed this to the relatively coarse powder and loose packing of the powder bed.

The overall cost of building metal components using this technology as compared to other AM technologies is also relatively lower, attributed to four main reasons – lower process energy, lower cost of material, lack of need for support material

and recycling of unused powder. Components produced by binder jetting generally have finer resolution in the z-direction. However, the surface finish may be generally poorer [38], and will usually require post processing to achieve better mechanical properties. The process is typically accurate to ± 0.125 mm.

2.2.2 Direct Energy Deposition

In DED AM process, a focussed thermal energy is used to fuse materials together by melting. It is normally used to process metallic materials. The thermal energy may be based on laser, electron beam or plasma arc. The materials may come in the form of powder or wire. Wire, as compared to powder, has less accuracy but is more material efficient. The method of material melting varies between a laser, an electron beam or plasma arc, all within a controlled environment that has reduced oxygen levels. In the case of electron beam, the environment will be a vacuumed one.

As shown in Figure 2.7, in a typical DED process, material is deposited via a nozzle. Thermal energy melts the deposited material with the substrate material to form a melt pool. The material is deposited according to the sliced CAD data and the trail of melt pool quickly solidifies to form the desired geometry. This technology may be commonly used to add materials to existing parts, making it very useful for adding features to components built by conventional methods (eg casting), but it can also be used to build up parts to form net shape components. Recent hybrid approaches have seen DED combined with CNC milling to achieve an accurate end use part that promises more extensive adoption of this technology in the future.

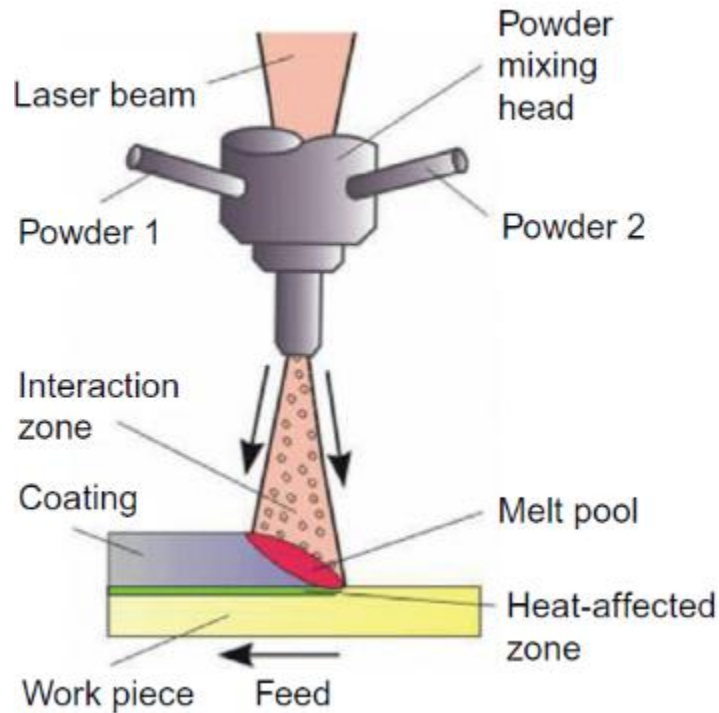


Figure 2.7 - Schematic of powdered based direct energy deposition process [39]

The kinetic energy of powder particles being fed into the melt pool is greater than the effect of gravity on these powders during flight. As a result, nonvertical deposition is just as effective as vertical deposition. Multi-axis deposition head motion is therefore possible and, indeed quite useful. In particular, if the substrate is very large and/or heavy, it is easier to accurately control the motion of the deposition head than the substrate. Conversely, if the substrate is a simple flat plate, it is easier to move the substrate than the deposition head. Whilst in most cases, it is the arm that moves and the object remains in a fixed position, this can be reversed and a platform could be moved instead and the arm remain in a fixed position. The choice will depend on the exact application and object being printed. Thus, depending on the geometries desired and whether new parts will be fabricated onto flat plates or new geometry will be added to existing parts, the optimum design will change.

Material cooling times are very fast, typically between 10^3 to 10^8 K/s [40, 41]. Depending upon the material or alloy being deposited, these high cooling rates can produce unique solidification grain structures and/or non-equilibrium grain structures which are not possible using traditional processing. The cooling time will in turn affect the final grain structure of the deposited material, although the overlapping of material must also be considered, where the grain structure is changed as the overlapping can

cause re-melting to occur, resulting in a uniform but alternating micro-structure. At lower cooling rates (when using higher beam powers or lower traverse speeds), the grain features grow and look more like cast grain structures [36].

Based on a literature study by Gu et al. [42], metallic parts processed by DED generally have excellent tensile and yield properties, and in most cases comparable to that produced by other AM processes. However, the porosity in most cases are about generally higher than powder bed processes.

2.2.3 Material Extrusion

In material extrusion, material is drawn through a nozzle, where it is heated and is then deposited layer by layer (Figure 2.8). The nozzle can move horizontally and a platform moves up and down vertically after each new layer is deposited. Advantages of the material extrusion process include use of readily available ABS plastic, which can produce models with good structural properties, close to a final production model. In low volume cases, this can be a more economical method than using injection moulding. However, the process requires many factors to control in order to achieve a high quality finish. The nozzle which deposits material will always have a radius, as it is not possible to make a perfectly square nozzle and this will affect the final quality of the printed object. Accuracy and speed are low when compared to other processes and the quality of the final model is limited to material nozzle thickness. By far the most common extrusion-based AM technology is Fused Deposition Modeling (FDM), produced and developed by Stratasys, USA.

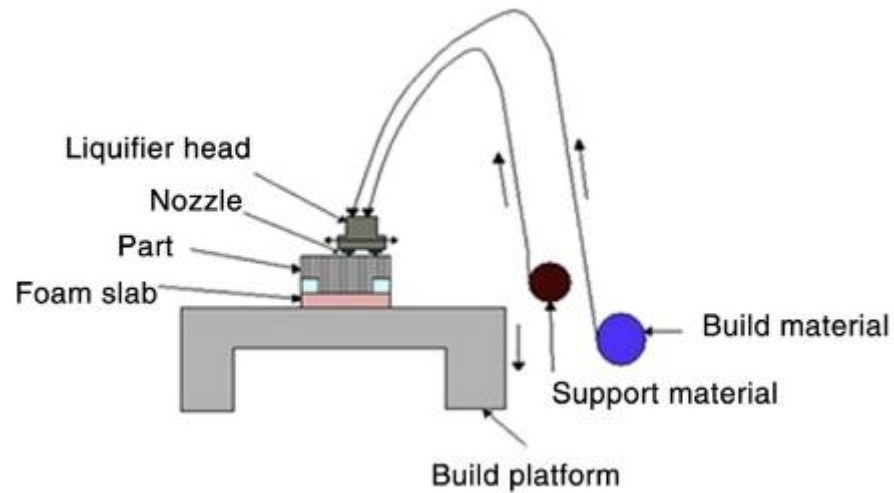


Figure 2.8 - Schematic of material extrusion additive manufacturing (Fused Deposition Modelling) [43]

One of the limitations of this technology is speed. The speed of an FDM system is reliant on the feed rate and the plotting speed. Feed rate is also dependent on the ability to supply the material and the rate at which the liquefier can melt the material and feed it through the nozzle. If the liquefier were modified to increase the material flow rate, most likely it would result in an increase in mass. This in turn would make it more difficult to move the extrusion head faster. For precise movement, the plotting system is normally constructed using a lead-screw arrangement. Lower cost systems can use belt drives, but flexing in the belts make it less accurate and there is also a lower torque reduction to the drive motor [36].

The FDM technology has established a prominent position in AM since its inception about two decades ago. The technology has attained the market leadership in terms of the largest number of units installed in plastics-based AM [43]. The main strength of FDM technology is the wide range of high strength engineering plastics it can use to create parts not only for design verification, but also for functional testing and end-use applications in tooling and casting. The simplicity and reliability of the technology has also prompted development of several others non-filament-type extrusion-based FDM systems, and it has also lead to the proliferation of several low-cost FDM-type 3D printers for domestic and hobbyist consumers. The FDM process has been extensively used by research and development community at universities and research organizations to further enhance the process and part quality, and to develop new materials for a variety of new engineering applications. The technology offers a

distinct advantage in creating biomedical implants and TE scaffolds of desired characteristics and this has also led to the development and testing of several biomaterials for the FDM technology.

It is expected that future research in FDM process will be directed to increasing the build speed of this process, improving surface texture and development of new materials, plastics, composites, and biomaterials in filament form for specific commercial applications. In speeding up the process, research could involve the incorporation of multiple extrusion nozzles, or incorporating intelligent build strategies where the interior of the part can be filled faster by thicker extruded rods and outer surfaces by thinner rods. Research in new FDM materials will be dictated by the intended applications and the success in rapid and cost-effective production of durable filaments suitable for FDM processing conditions.

When considering this AM process for metal fabrication, the greatest limitation is in the material that can be processed. Since material extrusion works by melting the feedstock before depositing onto the substrate, the heating element must be able to melt metals of more than 1000 degree Celsius melting temperature. This method has been demonstrated on metals with very low melting temperature, such as Gallium with a melting temperature of 86 degree Celsius [44]. Alternatively, special preparations of the feedstock may also allow for the use of this process for metal fabrication. In the work by Wu et al. [45], commercially available stainless steel 17-4PH powder and special in-house developed binder were used. After coating the powder with stearic acid, by ball milling, the powder was mixed with the binder from the mixer to create the compounding mixture. Parts produced by this method however may have inferior properties compared to the actual steel.

Another type of material extrusion based metal AM uses special profiles (rods) made up of metal or ceramic powder with a thermoplastic binder system. This method is used by two companies based in the USA, Desktop Metal Inc. and Markforged Inc. The profiles are fit into cartridges and are then fed into a plasticizing unit where the highly-filled thermoplastic composite is soft enough for extrusion. The soft material accumulates in a reservoir and finally a mechanical drive system (e.g., plunger) pushes the soft material and deposits it onto the building platform in a layer-by-layer manner. In general, they meant to be used for shaping parts that eventually will be made out of

only metal or ceramic, thus the rods have a large amount of powder and the printed parts will require to be sintered to obtain a dense part [46]. This method has shown to be successful in various metallic materials, including stainless steel, high-performance steel, copper and tool steel,

2.2.4 Material Jetting

In material jetting, build material and support material are selectively deposited onto the x-y plane using print heads (similar to a document inkjet printer). When the layer is complete, the build platform moves in the z direction by a pre-determine layer thickness, and the process repeats until the part is completed. Droplets are formed and positioned into the build surface, in order to build the object being printed, with further droplets added in new layers until the entire object has been made. The nature of using droplets, limits the number of materials available to use. Polymers and waxes are often used and are suitable due to their viscous nature and ability to form drops. The polyjet technology from Objet Geometries is one such system that utilises this technology (see Figure 2.9 Figure 2.9 - Schematic of material jetting process (Polyjet from Objet Geometries) [36]).

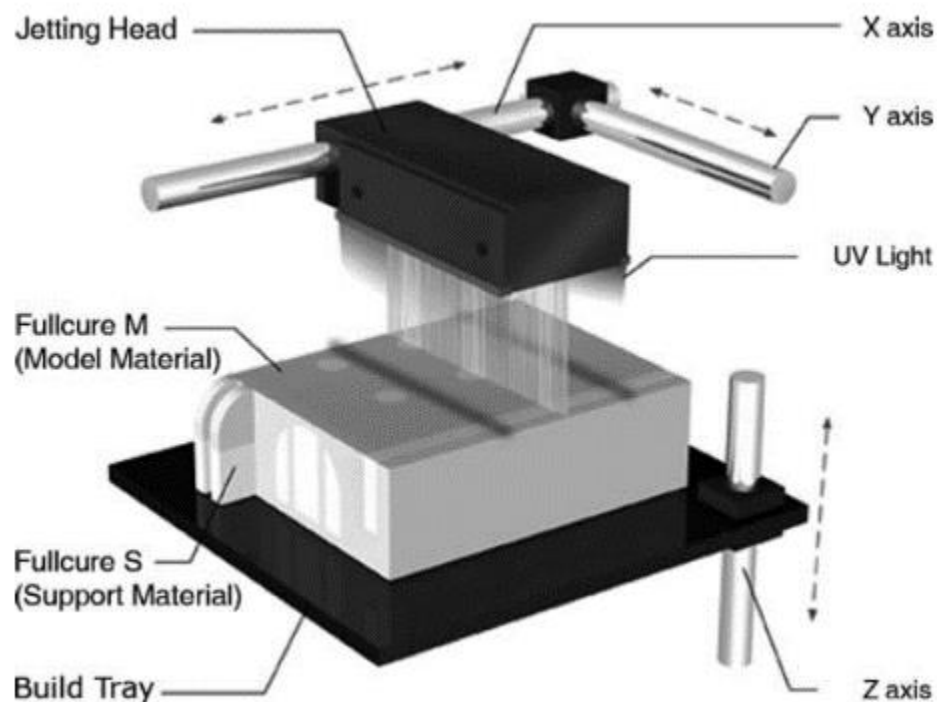


Figure 2.9 - Schematic of material jetting process (Polyjet from Objet Geometries) [36]

The most common material used in material jetting is a liquid photopolymer. This material will remain a liquid until exposed to Ultra Violet (UV) light, upon which it hardens into a solid. UV lights are typically attached to either side of the print head, so that the material will solidify the instant it is laid down. There is recent development work conducted on using material jetting technology to manufacture metal components. Similar to resin based material jetting, the technology forms parts from liquid metals, rather than the powder metals that are used by current AM technologies [47, 48].

Literature on using this method to fabricate metal components is largely limited, especially in the context of commercial applications. Zambelli et al. [49] provided a good review of development work using material jetting technology for micro scale metallic material deposition, but concluded that the techniques cannot be applied without expert knowledge, and the majority of the research is still focussed on the understanding and optimisation of the single processes. Perhaps XJet's NanoParticle Jetting technology is the closest to realising metallic material deposition using material jetting, but it is usually used for small component fabrication, and will still require debinding and sintering [50].

2.2.5 Powder Bed Fusion

Powder bed fusion (PBF) is perhaps one of the most common methods for building metal components that can be commercially used. The process involves the selective fusing of materials in a powder bed. The technique fuses parts of a layer, then the working platform moves downwards, and another layer of powder is added. The process is repeated until the component has been built up. PBF uses either a laser, electron beam or a thermal print head to melt and fuse material powder together. In the process, the powder can either be sintered or fully melted. A number of proprietary processes have been developed using various combinations of energy source and sintering or melting mechanism. These are described below.

2.2.5.1 Selective Laser Sintering

Selective laser sintering (SLS) machines are made up of three components – a heat source to fuse the material, a method to control this heat source and a mechanism to add new layers of material over the previous. SLS fuses thin layers of powder (typically ~0.1 mm thick) which have been spread across the build area using a counter-rotating powder levelling roller. The part building process takes place inside an enclosed chamber filled with nitrogen gas to minimize oxidation and degradation of the powdered material. The powder in the build platform is maintained at an elevated temperature just below the melting point and/or glass transition temperature of the powdered material [36]. Infrared heaters are placed above the build platform to maintain an elevated temperature around the part being formed; as well as above the feed cartridges to pre-heat the powder prior to spreading over the build area. In some cases, the build platform is also heated using resistive heaters around the build platform. This pre-heating of powder and maintenance of an elevated, uniform temperature within the build platform is necessary to minimize the laser power requirements of the process (when pre-heating, less laser energy is required for fusion) and to prevent warping of the part during the build due to non-uniform thermal expansion and contraction (curling).

The process begins by applying a layer of powder and then preheating it. Once the appropriate powder layer has been formed and preheated, a focused CO₂ laser beam is directed onto the powder bed and is moved using galvanometers in such a way that it thermally fuses the material to form the slice cross-section. Surrounding powder remains loose and serves as support for subsequent layers, thus eliminating the need for the secondary supports which are necessary for many other AM processes. After completing a layer, the build platform is lowered by one layer thickness and a new layer of powder is laid and levelled using the counter-rotating roller. The beam scans the subsequent slice cross-section. This process repeats until the complete part is built. A cool-down period is typically required to allow the parts to uniformly come to a low-enough temperature that they can be handled and exposed to ambient temperature and atmosphere. If the parts and/or powder bed are prematurely exposed to ambient temperature and atmosphere, the powders may degrade in the presence of oxygen and parts may warp due to uneven thermal contraction. Finally, the parts are removed from the powder bed, loose powder is cleaned off the parts, and further finishing operations, if necessary, are performed. Please refer to Figure 2.10 for the schematics.

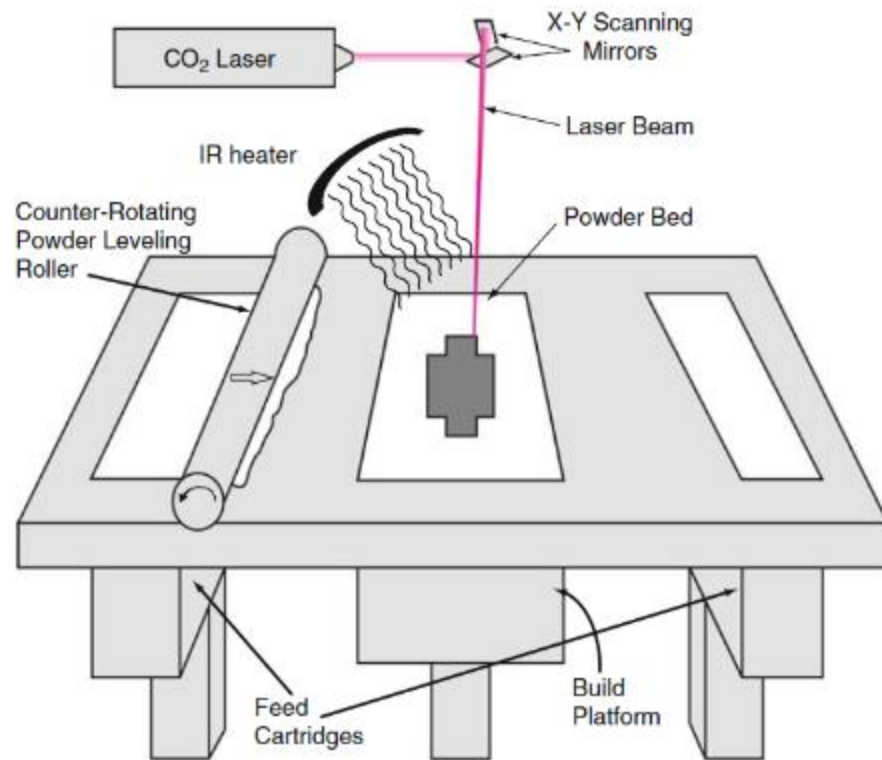


Figure 2.10 - Schematic of Selective Laser Sintering process [36]

2.2.5.2 Selective Laser Melting

Selective Laser Melting (SLM) is similar to SLS, except it is commonly used to achieve metal components with high relative density [51]. However, as compared to SLS, SLM is often faster, but requires the use of an inert gas, has higher energy costs and typically has a poor energy efficiency of 10 to 20 % [36]. The process uses either a roller or a blade to spread new layers of powder over previous layers. A hopper or a reservoir below or aside the bed provides a fresh material supply. SLM research in the late 1980s and early 1990s by various research groups was mostly unsuccessful. Compared to polymers, the high thermal conductivity, propensity to oxidize, high surface tension, and low absorptivity of metal powders make them significantly more difficult to process than polymers. Today, the use of lasers with wavelengths better tuned to the absorptivity of metal powders was one key for enabling SLM of metals. The other key enablers for SLM, compared to SLS, are different laser scan patterns, the

use of f-theta lenses to minimize beam distortion during scanning, and low oxygen, inert atmosphere control.

Kruth et al. described SLM as a technology that has been developed to produce near full dense objects, with mechanical properties comparable to those of bulk materials [52]. In SLM, the metallic powders are fully melted. Kruth et al. also presented literature on using SLM to process single material powder, alloy powder, and powder mixture, and concluded that almost 100% relative part density can be achieved, with mechanical properties comparable to bulk material except ductility, which is strongly reduced.

2.2.5.3 Selective Heat Sintering

Selective Heat Sintering (SHS) uses a heated thermal printhead to fuse powder material together. As before, layers are added with a roller in-between fusion of layers. The process is used in creating concept prototypes and less so structural components. The use of a thermal print head and not a laser benefits the process by reducing significantly the heat and power levels required. Baumers et al. presented SHS as a low cost alternative to SLS for the additive deposition of polymer objects [53]. Thermoplastic powders are used and act as support material. Hence, this process is not suitable to process metallic components.

2.2.5.4 Electron Beam Melting

In Electron Beam Melting (EBM), layers are fused using an electron beam to melt metal powders (see Figure 2.11). Due to the use of electron beam, the chamber usually requires a vacuum environment. EBM provides models with very good strength properties due to an even temperature distribution of during fusion. Similar to SLM, in the EBM process, a focused electron beam scans across a thin layer of pre-laid powder, causing localized melting and resolidification as per the slice cross-section. However, there are a number of differences between how SLM and EBM are typically practiced, which are summarized in Table 2.11.

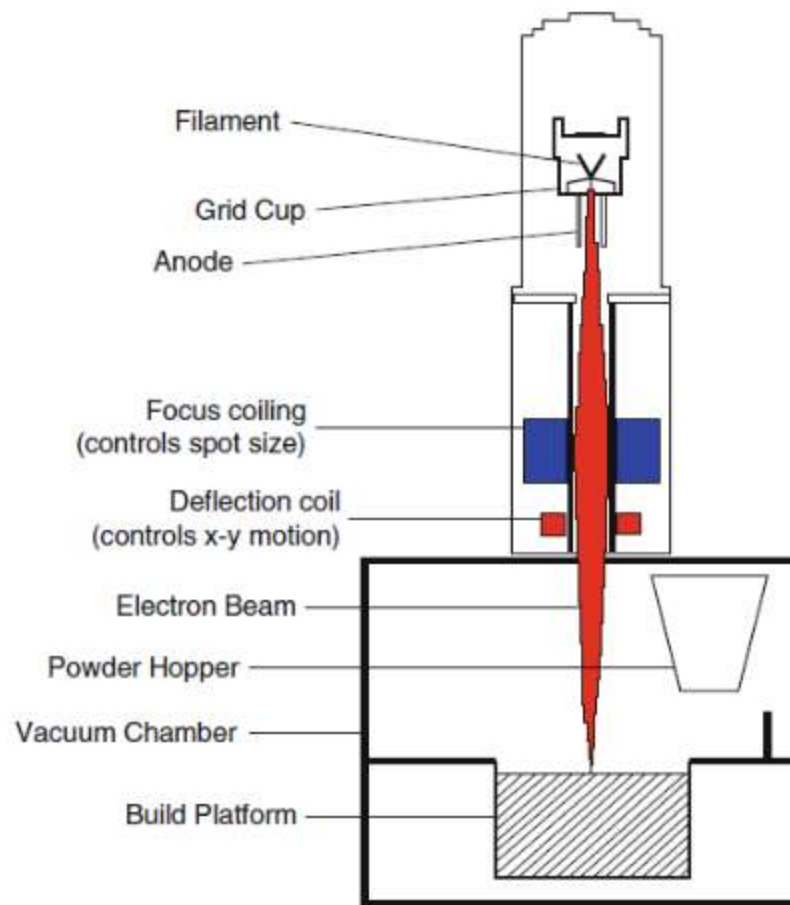


Figure 2.11 - Schematic of Electron Beam Melting [36]

Table 2.11 - Differences between EBM and SLM [36]

Characteristic	Electron beam melting	Selective laser melting
Thermal source	Electron beam	Laser
Atmosphere	Vacuum	Inert gas
Scanning	Deflection coils	Galvanometers
Energy absorption	Conductivity-limited	Absorptivity-limited
Powder pre-heating	Use electron beam	Use infrared heaters
Scan speeds	Very fast, magnetically-driven	Limited by galvanometer inertia
Energy costs	Moderate	High
Surface finish	Moderate to poor	Excellent to moderate
Feature resolution	Moderate	Excellent
Materials	Metals (conductors)	Polymers, metals and ceramics

Electron beams are inherently different from laser beams, as electron beams are made up of a stream of electrons moving near the speed of light, whereas, laser beams are made up of photons moving at the speed of light. When an electron beam is passed through a gas at atmospheric pressure, for instance, the electrons interact with the atoms in the gas and are deflected. In contrast, a laser beam can pass through a gas unaffected as long as the gas is transparent at the laser wavelength. Thus, EBM is practiced in a low-partial-pressure vacuum environment (a small amount of inert gas is swept through to remove gaseous by-products and oxygen), whereas SLM is practiced in an inert gas atmosphere at atmospheric pressure. Electrons have a negative charge and are focused and deflected magnetically, whereas photons are optically focused and deflected using mirrors attached to motors. As a result, since magnetic coils have an almost instantaneous response to changing input conditions, an electron beam can be scanned slowly or very rapidly. In essence an electron beam can be moved instantaneously from one location to another without needing to traverse the area in-between. In contrast,

galvanometers are mirrors attached to motors. For a laser beam focal spot to move from point A to point B, the galvanometer motors have to move the mirrors accordingly. Thus, virtually instantaneous motion is not possible and the scan speed is determined by the mass of the mirrors, the characteristics of the motors, and the distance from the mirrors to the powder bed.

Laser beams heat the powder when photons are absorbed by powder particles. Electron beams, however, heat powder by transfer of kinetic energy from incoming electrons into powder particles. As powder particles absorb electrons they gain an increasingly negative charge. This has two potentially detrimental effects: (1) if the repulsive force of neighbouring negatively charged particles overcomes the gravitational and frictional forces holding them in place, there will be a rapid expulsion of powder particles from the powder bed, creating a powder cloud; and (2) increasing negative charges in the powder particles will tend to repel the incoming negatively charged electrons, thus creating a more diffuse beam. There are no such complimentary phenomena with photons. As a result, the conductivity of the powder bed in EBM must be high enough that powder particles do not become highly negatively charged, and scan strategies must be used to avoid build-up of regions of negatively charged particles. In practice, electron beam energy is more diffuse; in part, so as not to build up too great a negative charge in any one location. As a result, the effective melt pool size increases, creating a larger heat-affected zone. Consequently, the minimum feature size, resolution and surface finish of an EBM process is typically larger than an SLM process. As mentioned above, in EBM the powder bed must be conductive. Thus, EBM can only be used to process conductive materials (e.g., metals) whereas, lasers can be used with any material that absorbs energy at the laser wavelength (e.g., metals, polymers and ceramics).

Electron beam generation is typically a much more efficient process than laser beam generation. When a voltage difference is applied to the heated filament in an electron beam system, most of the electrical energy is converted into the electron beam, and higher beam energies (above 1 kW) are available at a moderate cost. By contrast, it is common for only 10–20% of the total electrical energy input for laser systems to be converted into beam energy, with the remaining energy lost in the form of heat [36]. In addition, lasers with beam energies above 1 kW are typically much more expensive than comparable electron beams with similar energies. Thus, electron beams are a less costly

high energy source than laser beams. Newer fibre lasers, however, are more simple in their design, more reliable to maintain, and more efficient to use (with conversion efficiencies reported of 70–80% for some fibre lasers) and thus, this energy cost advantage for electron beams may not be a major advantage in the future.

EBM powder beds are maintained at a higher temperature than SLM powder beds. There are several reasons for this. First, the higher energy input of the beam used in the EBM system naturally heats the surrounding loose powder to a higher temperature than the lower energy laser beams. In order to maintain a steady-state uniform temperature throughout the build (rather than having the build become hotter as the build height increases) the EBM process uses the electron beam to heat the metal substrate at the bottom of the build platform before laying a powder bed. By defocusing the electron beam and scanning it very rapidly over the entire surface of the substrate or the powder bed, the bed can be preheated rapidly and uniformly to any pre-set temperature. As a result, the radiative and resistive heaters present in most SLM systems for powder bed heating are not typically used in EBM. By maintaining the powder bed at an elevated temperature, however, the resulting microstructure of a typical EBM part is significantly different from a typical SLM part. In particular, in SLM the individual laser scan lines are typically easily distinguishable, whereas individual scan lines are often indistinguishable in EBM microstructures. Rapid cooling in SLM creates smaller grain sizes [54] and subsequent layer deposits only partially re-melt the previously deposited layer. The powder bed is held at a low enough temperature that elevated temperature grain growth does not erase the layering effects. In EBM, the higher temperature of the powder bed, and the larger and more diffuse heat input result in a contiguous grain pattern that is more representative of a cast microstructure [55], with less porosity than an SLM microstructure.

Post processing requirements include removing excess powder and further cleaning and CNC work. One advantage and common aim of post processing is to increase the density and therefore the structural strength of a part. Liquid phase sintering is a method of melting the metal powder or powder combination in order to achieve homogenisation and a more continuous microstructure throughout the material. However, shrinking during the process must be accounted for. Hot isotactic pressing is another method to increase density; a vacuum sealed chamber is used to exert high

pressures and temperatures of the material. Although this is an effective technique to improve strength, the trade-off is a longer and more expensive build time.

2.2.6 Sheet Lamination

Sheet lamination processes use sheets of materials joined together to form solid objects. Commonly known processes include laminated object manufacturing (LOM) and ultrasonic additive manufacturing (UAM). Laminated object manufacturing (LOM) uses paper (or plastic sheets) as material and adhesive to join the paper together. The material is first positioned in place on the cutting bed. The material is then bonded in place, over the previous layer, using adhesive. The required shape is then cut from the layer, by laser or knife. The process uses a cross hatching method at the unused areas during this cutting process to allow for easy removal post build. The process then repeats until the part is complete.

Sheet lamination process has also been used for metal component fabrication and is very well known for its applications in joining dissimilar metals. Known as UAM, it uses ultrasonic metal welding to sequentially bond metal sheets together, and integrates machining to remove material to achieve the desired geometry. This happens at every layer and is repeated layer by layer until the component is formed (see Figure 2.12).

During UAM, a rotating sonotrode travels along the length of a thin metal foil (typically 100–150 mm thick) [36]. The foil is held closely in contact with the base plate or previous layer by applying a normal force via the rotating sonotrode, as shown schematically in Figure 2.12. The sonotrode oscillates transversely to the direction of motion, at a constant 20 kHz frequency and user-set oscillation amplitude. After depositing a foil, another foil is deposited adjacent to it. This procedure is repeated until a complete layer is placed. The next layer is bonded to the previously deposited layer using the same procedure. Typically four layers of deposited metal foils are termed one level in UAM. After deposition of one level, the CNC milling head shapes the deposited foils/layers to their slice contour (the contour does not need to be vertical, but can be a curved or angled surface, based on the local part geometry). This additive-subtractive process continues until the final geometry of the part is achieved.

UAM uses metals and includes aluminium, copper, stainless steel and titanium. The process is low temperature and allows for internal geometries to be created. The process can bond different materials and requires relatively little energy, as the metal is not melted. However, Schick et al. [56] showed that metals parts built by UAM had voids or unbonded areas, which reduce the load-bearing cross section and create a stress intensity factor. In the same research work, tensile testing revealed that the weld interface strength was 15% of the bulk foil; shear tests of the weld interfaces was 50% of the bulk shear strength of the material; and optical microscopy of the fracture surfaces from the tensile tests revealed that 34% of the interface area was unbonded.

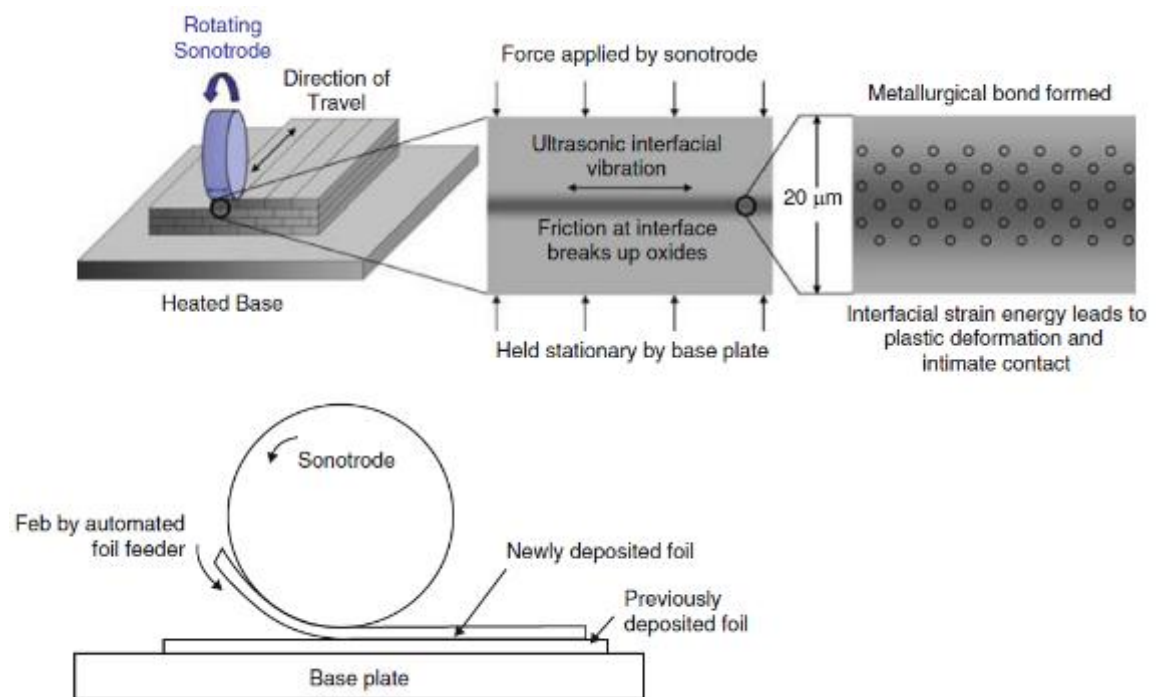


Figure 2.12 - Schematic of ultrasonic additive manufacturing [36]

2.2.7 Vat Photopolymerisation

Vat photopolymerisation uses a vat of liquid photopolymer resin to build parts layer by layer. An ultraviolet (UV) light is used to cure or harden the resin where required, whilst a platform moves the object being made downwards after each new layer is cured. As the process uses liquid to form objects, there is no structural support from the material during the build phase. In this case, support structures will often need to be added. Resins are cured using a process of photo polymerisation or UV light, where

the light is directed across the surface of the resin with the use of motor controlled mirrors. Where the resin comes in contact with the light, it cures or hardens. However, there is no known literature on using this AM technology to fabricate metallic components.

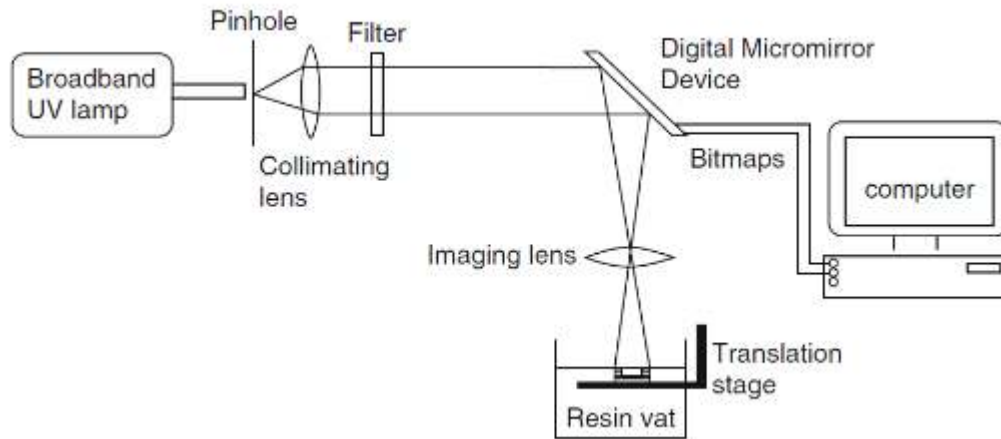


Figure 2.13 - Schematic of vat photopolymerisation [36]

2.2.8 Selection of Additive Manufacturing Technology

Based on the above literature review of the AM processes categorised by ASTM F2972, it can be concluded that ASTM A131 EH36 can be directly processed by processes stated in Table 2.12.

Table 2.12 - Selection of AM technology to process ASTM A131 EH36

Process	Metal Fabrication Summary	Main Limitations for Metal Fabrication
Binder Jetting	Binder jetting, infiltration, sintering.	Multiple processes required in the fabrication of metals.
Directed Energy Deposition (DED)	Thermal energy to fuse materials together.	Surface finish, complexity of parts (eg conformal channels).

Material Extrusion	Melting feedstock before depositing onto substrate	Only works on metals with low melting point, or require debinding and sintering.
Material Jetting	Jetting liquid metals to form components.	Existing literature is largely based on development work on micro scale metal parts.
Powder Bed Fusion (PBF)	Direct a thermal energy onto a powder bed, thermally fusing the material.	Requires environmentally controlled chamber.
Sheet Lamination	Uses ultrasonic metal welding to sequentially bond metal sheets together.	Requires subtractive manufacturing.
Vat Photopolymerisation	Light-activated polymerisation.	No known literature to fabricate metals.

While most of the AM processes can be used to fabricate metallic components, each of them has their own limitations. Listed in Table 2.12 are also the main limitations that would eventually determine which technology is more suitable to process EH36. Binder jetting technology can not directly produce reliable end use metallic components due to the nature of porosity caused by the binding method, and requires additional infiltration and sintering procedures. Material extrusion methods have a limitation on the temperature of the materials that can be processed. Material jetting and vat photopolymerisation both have very limited literature to process metallic components. Sheet lamination seems viable but it requires subtractive manufacturing as part of its process to create geometries and features. That narrows the selection down to directed energy deposition and powder bed fusion.

Both directed energy deposition and powder bed fusion have shown excellent processing capabilities for metallic components. Gu et al. [42] did a review of the current status of research and development of end-use metallic components. From bulk of the data from literature, parts built by powder bed fusion generally is capable of achieving higher bulk density than those built using directed energy deposition. As discussed in

Chapter 2.2.5, there are four sub-processes under powder bed fusion, namely selective laser sintering, selective laser melting, selective heat sintering and electron beam melting. In the same literature review by Gu et al. [42], metallic parts built using selective laser sintering showed generally higher porosity. Selective heat sintering, as discussed in Chapter 2.2.5.3, only works on thermoplastic powders and hence cannot process metallic materials. Selective laser melting and electron beam melting processes produce parts with high mechanical performance and both have been widely researched and used, but electron beam requires a vacuum chamber to operate. While this may not be an issue for small parts, it may be a technical constraint as the need to build larger components arises.

Another important factor to consider would be the build rate of the AM processes, especially because the intention is for the application of the AM technology for large structural steels. Directed energy deposition usually has two types of feedstock, namely powder or wire, and both are vastly different in their process parameters and deposition rates. For powder bed fusion, techniques and advancements in both machine and method designs have greatly influenced its build rates. Khorasani discussed about the various industrially practised techniques in [57]:

- Interchangeable cylinders as well as automatic powder management systems to reduce setup times and increase productivity through machine utilization rate.
- Closed-loop control powder handling and removable cylinders to increase the speed of productions.
- Circular platforms to prevent dispersion of powder and remove need for any powder filling or unloading throughout the building cycle, even when printing at full capability.
- Single automatic powder handling system are used for several machines in a production line improve machine efficiency.
- Automated powder sieving and recirculation are used to reduce the production time.

Multi-layer concurrent printing is the latest technology used to reduce the time of printing and to increase the speed of printing by around 100 times faster than the

existing systems. This process spreads multiple layers of powder on the build surface at the same time allowing a laser to scan multiple spots simultaneously [57].

Table 2.13 shows a curated list of build rates of existing and new AM processes, and their associated manufacturers. From the list, it can be observed that while PBF processes generally have lower build rates than DED processes, manufacturers have made innovation breakthroughs in their process designs to increase the build rates, especially true for Aeroswift and Aurora Labs. Regardless, it is still true that the build rates are designed for specific applications, with lower build rates for smaller high precision parts and high build rates for larger parts which are generally near net shape and require post machining.

Table 2.13 - Comparison of various DED and PBF build rates

AM Process	Manufacturer	Build Rate (cm³/hr)	Ref
Selective laser melting	EOS	5-20	[58]
	SLM Solution	20-70	[58]
	Concept Laser	120	[59]
	Renishaw	5-20	[58]
	Aeroswift	50-1200	[60] ¹
	Aurora Labs	3300	[61] ^{1,2}
	G.E. A.T.L.A.S.	180	[57]
Electron beam melting	ARCAM	80	[58]
Directed energy deposition	WAAM	160-1300	[62, 63]
	Norsk Titanium	1100-2200	[64]
	Optomec LENS	50-65	[62]
	Aeromet Lasform	1000	[65]

¹ Marketed figures with limited literature available in peer-reviewed journal articles

Hence, selective laser melting was eventually selected as the AM process for EH36 steel due to the following reasons:

- Competence to directly fabricate complex shaped metallic components
- Good source of literature and understanding of process
- Higher bulk density for processing metallic components
- High mechanical performance
- Potential to build large parts [19]

2.3 Part and Material Properties in SLM of Metals

After the material and AM process selections are completed, further investigations will then be carried out using SLM to process ASTM A131 EH36 material. Literature search showed that there is a substantial amount of research done on SLM, and its maturity as compared to other AM techniques that can process metallic materials gave confidence to the AM process selection results. Kruth et al. [54] discussed the key characteristics of processing metals using SLM, which includes density, surface quality, mechanical properties and microstructure. SLM can be characterised by high temperature gradients, causing no equilibrium to be maintained at the solid and liquid interface. This leads to the formation of non-equilibrium phases and subsequently changes in the general microstructural features. At higher cooling rates, finer structures can be observed in the microstructure as compared to conventionally manufactured metal parts. Grain structure is also influenced by previously solidified layer grain structure and the SLM processing parameters. Since microstructural features affect material properties, parts produced by SLM will have mechanical properties different from bulk materials fabricated by conventional manufacturing techniques.

2.3.1 Density

Density determines a part's mechanical properties, which in turn determines the part performance. Parts built by conventional manufacturing, such as moulding process, usually obtain high density due to mechanical pressure. Since the SLM process is characterised by temperature effects, gravity and capillary forces, it is difficult to achieve 100% dense parts. In addition, gas bubbles may become entrapped in the material during the SLM process, thus leading to increase in porosity of the part built.

Porosities formed during the SLM process may be attributed to several factors. Porosities may be formed due to a decrease in the solubility of the dissolved elements in the melt pool during cooling and solidification and evaporation of elements with a high vapor pressure [66]. High surface roughness can also cause low density – high-roughness peaks and valleys that are formed after each layer can prevent the coater from depositing a new homogenous powder layer. Moreover, the laser energy may be not enough to melt the new layer completely since the thickness of the powder in some regions will be higher because of the high-surface roughness. Morgan et al. has investigated and provided findings that show that a rough surface may cause the entrapment of gas upon deposition of a new powder layer [67]. When the new layer is being scanned, the gas is superheated and expands rapidly removing the liquid metal above it, thus creating a pore.

Environmental conditions and process parameters influence the attainable density. Zhang et al. studied the effect of environment variables on density of AISI 316L stainless steel parts built using SLM. The work focussed on investigating the effect of protective gases and preheating on the density of the part produced. The study showed that oxidation reaction between the stainless steel powders and oxygen would be limited when the oxygen content in the working chamber is key to below 0.5%. Four protective gases, namely Argon (Ar), Nitrogen (N₂), Helium (He) and Hydrogen (H₂) were used in various mixtures, and it was shown that samples fabricated using Ar and N₂ exhibited near full densities with values above 99%. Figure 2.14 shows the density of sample fabricated. When Ar and N₂ are mixed with H₂, the densities of the samples built do not change. Hence it was concluded that influence of H₂ as a deoxidiser is relatively weak due to low oxygen content and low density (H₂ rises and stays at the top of the working chamber because its density is lower than Ar and N₂).

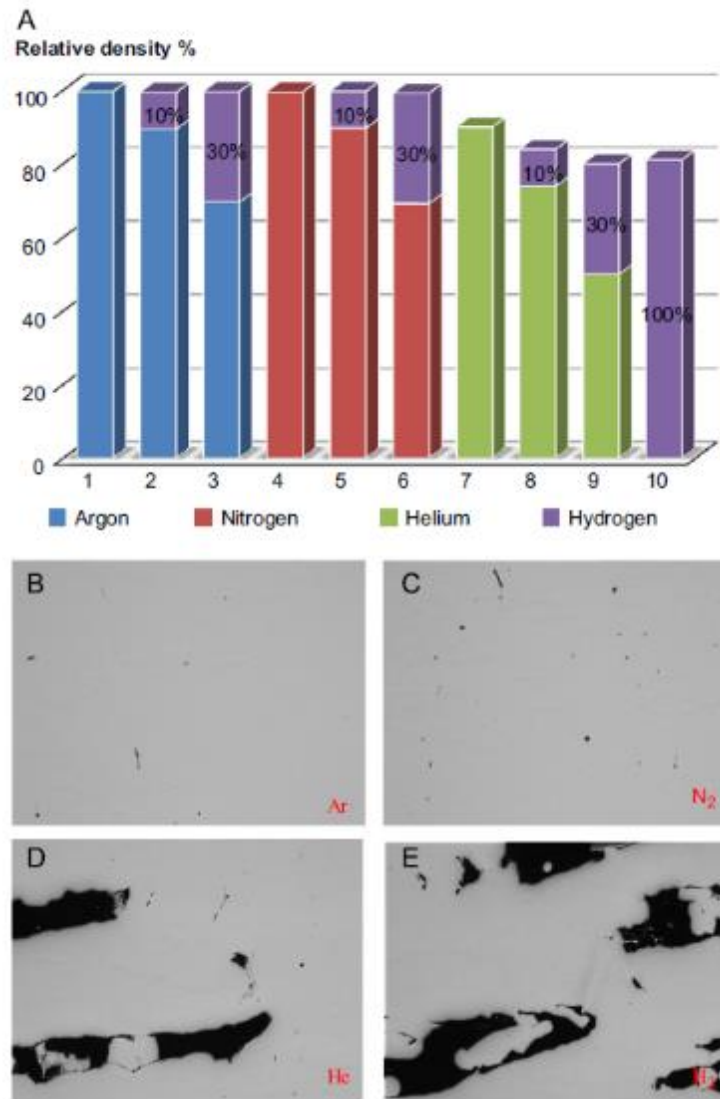


Figure 2.14 - Relative density (a) and optical image (b) of SLM processed SS316L powder

The study also presented findings that preheating will improve densities of samples fabricated under Ar environment. Furthermore, preheating can reduce part deformation and increase dimensional accuracy. Figure 2.15 shows the findings from the study.

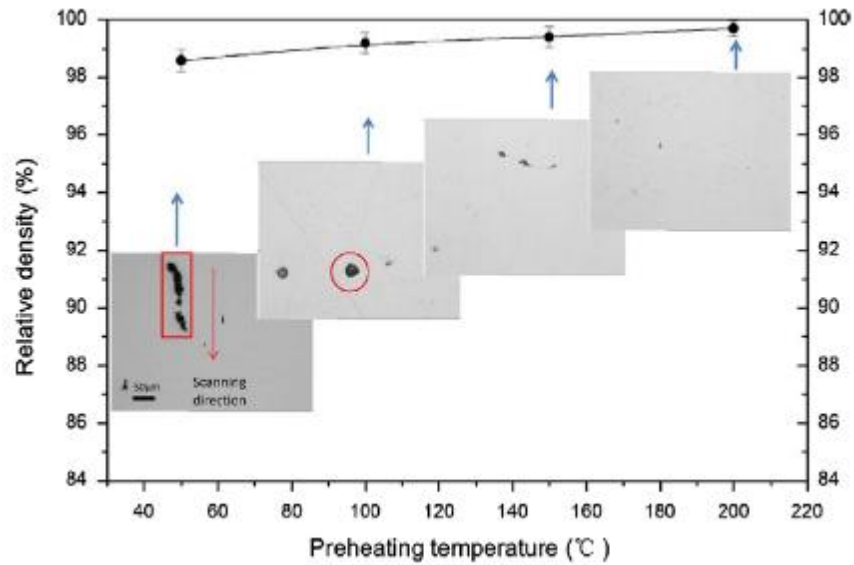


Figure 2.15 - Material density versus preheating temperature of powder bed

Badrossamay et al. presented how scanning speed has an effect on the relative density at three different layers thicknesses for AISI 316L stainless steel [68]. At sufficiently low scan speeds, the relative density is almost independent of the layer thickness for the selected range of the layer thickness, and a maximum of 99% relative density is achievable. At higher scan speed values, a higher layer thickness results in less density. However, the layer thickness can be increased if the scan speed is sufficiently lowered to achieve the same density values.

Study has also shown that scanning strategy also has an effect on the relative density of parts produced using SLM. Kruth et al. discussed on the comparison of three types of scanning patterns – uni-directional, bi-directional and alternating bi-directional [54]. In alternating bi-directional, the scan lines are rotated 90 degrees in each layer (see Figure 2.16 below). The study has found that alternating bi-directional provides the highest relative density. Jhabvala et al. investigated four scanning strategies and concluded that the best scanning strategy is chessboard (island) scanning (see Figure 2.17 below) [69]. Lu et al. expanded the investigation on island scan strategy by focusing on the effect of differing island sizes [70]. The results indicate that the relative density is increased with the enlargement of island size. Figure 2.18 shows that 2 x 2 mm² (22) islands achieved much lower relative density values than 5 x 5 mm² (55) and 7 x 7 mm² (77) islands.

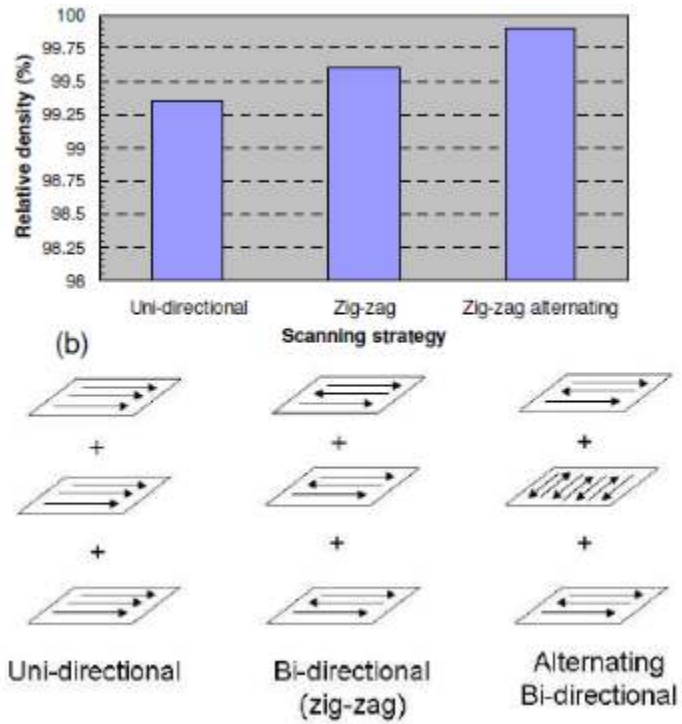


Figure 2.16- (a) Effect of scanning strategy; (b) Different scanning strategies by Kruth et al. [54]

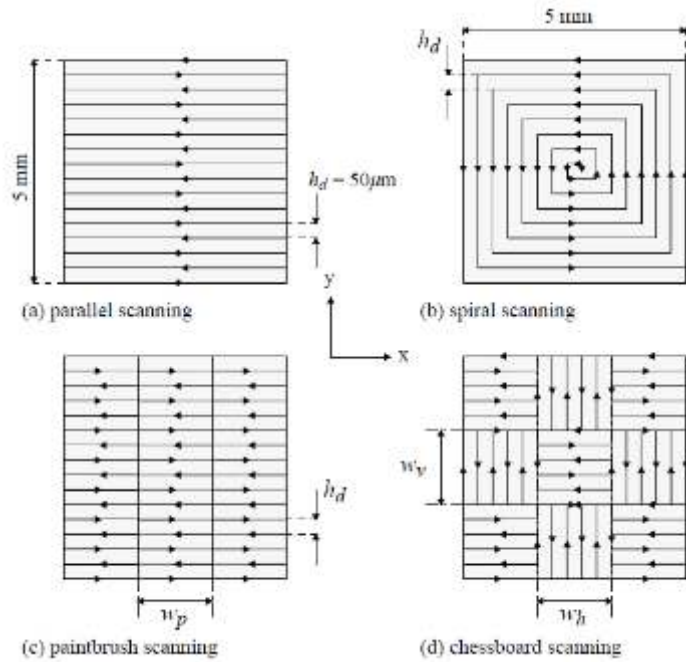


Figure 2.17 - Four scanning strategies investigated by Jhabvala et al. [69]

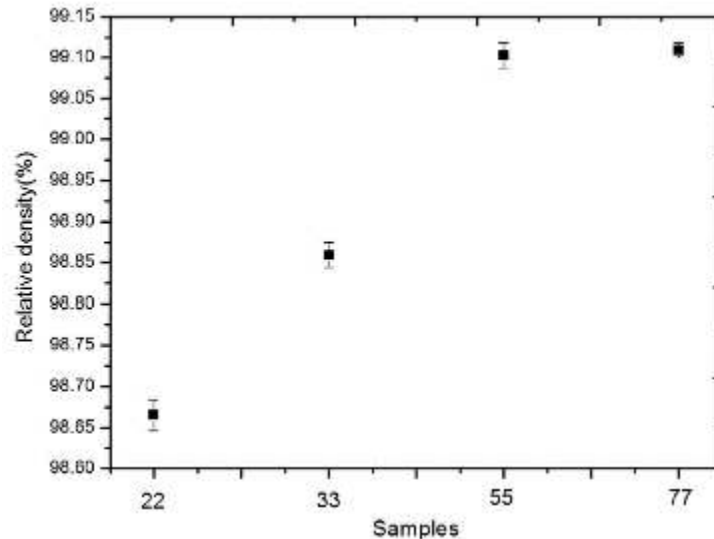


Figure 2.18 - Relative density values formed at differing island sizes in island scanning strategy [70]

Even though parts produced by a properly optimised SLM process often exhibit relative density values of 97% to 99%, small residual porosities may still decrease the mechanical performance of the part, especially in the areas fatigue and ductility performance. Laser re-melting is often used to solve this problem and to increase the density. In SLM process, the term “laser re-melting” is used to refer to a second pass of the laser beam over the same 2D layer for different purposes such as further material densification, surface quality and microstructural enhancement of SLM fabricated parts. Kruth et al. and Yasa et al. has shown that laser re-melting can reduce porosity by three to five times, thus significantly improving density [54, 66]. In their investigations, optical microscopy images of cross sections of a SLM produced part without re-melting were obtained (see Figure 2.19). Similar micrographs were subsequently obtained for SLM produced part with re-melting (see Figure 2.20). The results show that applying laser re-melting technique will definitely yield an improvement in the density of the SLM produced part, but the number of re-melting may not be directly related to the amount of density improvement.

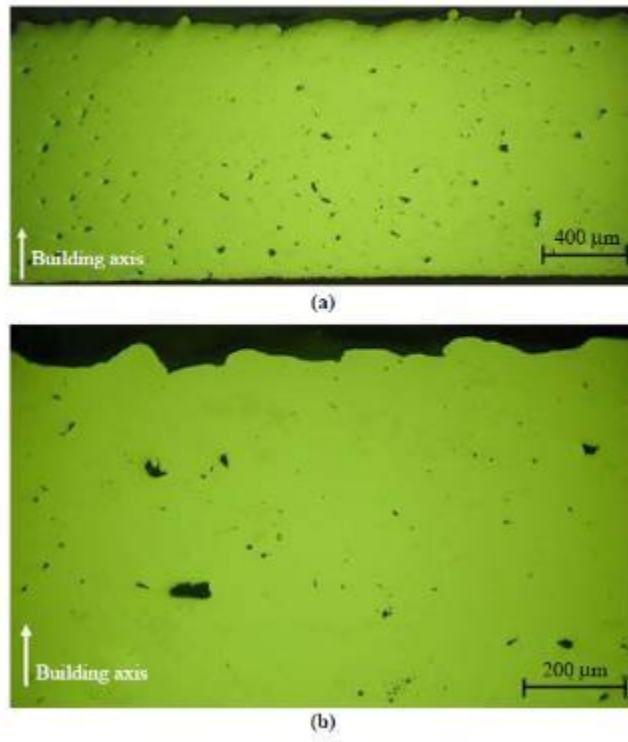


Figure 2.19 - Optical microscopy images of SLM produced part without re-melting [54, 66]

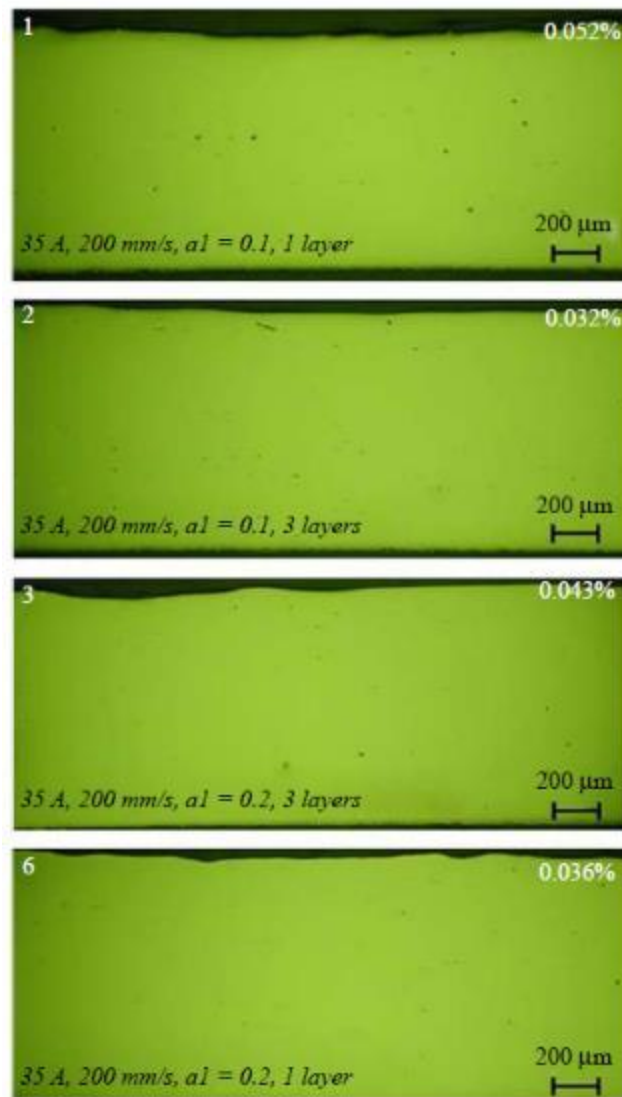


Figure 2.20 - Optical microscopy images of SLM produced part with re-melting [54, 66]

2.3.2 Surface Quality

Surface quality has always been a key issue in SLM processed metal parts. High surface roughness can lead to unacceptable tolerances, increased friction and potentially becoming a source of fatigue crack initiation [71]. Marimuthu et al. explained that the surface quality may be caused by 2 phenomena – surface deformation produced by vaporisation; and surface tension gradient, which influences the direction of melt pool movement [72].

The top surface roughness of a melt pool can be affected by a rippling effect that occurs due to surface tension forces exerting a shear force on the liquid surface. This is

primarily due to a surface temperature difference between the laser beam and the solidifying zone caused by the motion of the laser beam. As the thermal gradients reduce, gravity and melt pool surface curvature counter this external shear force, eventually restoring the surface height of the melt pool to the free level [73]. However, viscous forces delay this relaxation process, quick melt pool solidification time often ensures that complete relaxation is not fully achieved.

Investigations using pulsed lasers have reported that top surface roughness can be reduced using a low scan speed and high repetition rate due to melt pool stabilization and reduced surface profile variation on top of the solidified melt pool [74, 75]. However, low scan speeds and high repetition rates can significantly increase the volume of melt pool produced and promote a phenomenon known as balling. Balling is the breakup of the melt pool into small spheres. It occurs when molten material does not wet well to the underlying substrate or material due to high surface tension differences generated as a result of variations in thermal properties within the melt pool [51, 76, 77]. These thermal gradients cause a thermocapillary flow of a fluid within the melt pool from regions with low surface tension to regions with high surface tension, known as Marangoni convection [78]. The breaking up of the melt pool into smaller entities reduces the variation in melt pool surface tension. Balling can increase with the generation of excessive molten material or if too low viscosity exists within a melt pool [79]. Kruth et al. stated that when the total surface of a molten pool becomes larger than that of a sphere with the same volume, the balling effect takes place [51]. Balling is a severe impediment on interlayer connection, it decreases part density and increases top surface roughness and side roughness. However, the balling effect more dominantly affects the side roughness of parts due to the direction of balling scattering to either side of the melt pool rather than settling on the top surface.

Mumtaz et al. investigated the SLM of Inconel 625 using an Nd:YAG pulsed laser to produce thin wall parts with an emphasis on attaining parts with minimum top surface and side surface roughness [71]. His findings showed that the surface finishes in the z direction and the x-y planes are inversely related. As top average surface roughness improves, the side average surface roughness worsens. Similarly, as side average surface roughness improves, the top average surface roughness worsens. This is primarily due to surface tension forces that arise as a result of thermal variation within the melt pool. Low top average surface roughness is generally achieved using a high

laser spot overlap (above 90 per cent) due to reduced variation in the peaks and troughs generated by individual overlapping spheres. Low processing scan speeds improve the top average surface roughness as melt pool is given more time to flatten before melt pool solidification. The melt pool is flattened by gravity and surface curvature forces that counteract the external shear forces generated by temperature difference caused by the moving laser. However, both a high laser spot overlap and low scan speed will increase the volume of liquid produced within the melt pool. This has a tendency to widen the melt pool causing a larger variation in thermal properties across the melt pool. This subsequently generates a greater variation in surface tension and causes the melt pool to break off into smaller entities (balling) as the melt pool attempts to reduce surface tension differences. The entities solidify at the edge of the melt pool subsequently increasing top average surface roughness. The balling effect limits the SLM process resolution because it causes the formation of discontinuous tracks [71], therefore limiting the formation of very sharp geometries. It is also responsible for a non-uniform deposition of material on the previous layers, thus inducing a possible porosity and delamination between layers that is detrimental to the functional performance of parts. Side average surface roughness can be reduced using high scan speeds and low laser spot overlap (below 85 per cent). This encourages quicker melt pool solidification and minimizes the volume of liquid within the melt pool. This produces relatively thin melt pools with less variation in the thermal properties across the melt pool than that of a larger melt pool. The melt pool is more stable and is less likely to suffer from balling. However, the fast melt pool solidification and low laser spot overlap will have a detrimental effect on top average surface roughness.

Mamtaz et al. also concluded that the common factor that reduces both top and side average surface roughness is pulse energy. However it is believed that the increased peak power generated with the use of a higher pulse energy at a fixed pulse duration is the main reason for this to occur. High peak powers generate large recoil pressures. Work has shown that higher peak powers flatten out the melt pool [77] improving interlayer connection and increasing the wettability of the melt [80]. Improved wettability reduces a melt pool's tendency to undergo balling by relieving surface tension variations [51, 79]. Kruth et al. believes that high peak powers reduce the tendency for a melt pool to undergo balling due to a higher attained temperature within the melt [51]. Mamtaz et al. also provided another possible explanation for the decrease

in balling with the use of higher peak powers, which is, relation to the increase in recoil pressure causing any balling formation to completely detach from solidifying melt pool (and disperse onto the powder bed). However, if peak powers become too high large amounts of material vaporization can occur with recoil pressures that disrupt the melt pool surface and increase top average surface roughness. In conclusion, Mamtaz et al. identified that the parameters that promote a reduction in top average surface roughness (increased overlap, increased repetition and reduced scan speed) tend to increase the balling effect and increase side average surface roughness. Parameters that reduce side average surface roughness (reduced overlap, reduced repetition rate and increased scan speed) increase the top average surface roughness of parts. However, a parameter that aids a reduction in both top and side average surface roughness is the use of a higher peak power due to the flattening/smoothing of the melt pool surface and an improved wettability of the melt pool reducing its tendency to undergo the balling mechanism.

Kruth et al. used laser re-melting to improve the surface quality. As illustrated in Figure 2.21 below, the surface quality of parts manufactured by SLM and then exposed to laser re-melting demonstrated a significant improvement [54]. By applying appropriate process parameters, Kruth et al. was able to show that a SLM built component with laser re-melting technique can be produced with no edge-effect (see Figure 2.22) [54]. However, Strano et al. investigated the surface roughness at various sloping angles (see Figure 2.23) and concluded that on inclined surfaces, unlike on horizontal ones, laser re-melting is not possible with SLM technology, since material can only be sintered horizontally [81].

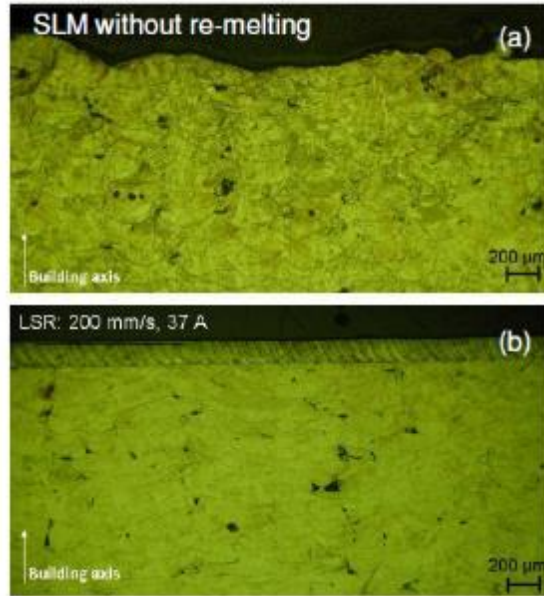


Figure 2.21 - Surface quality enhancement with laser re-melting: (a) SLM without re-melting (b) Laser re-molten part [54]

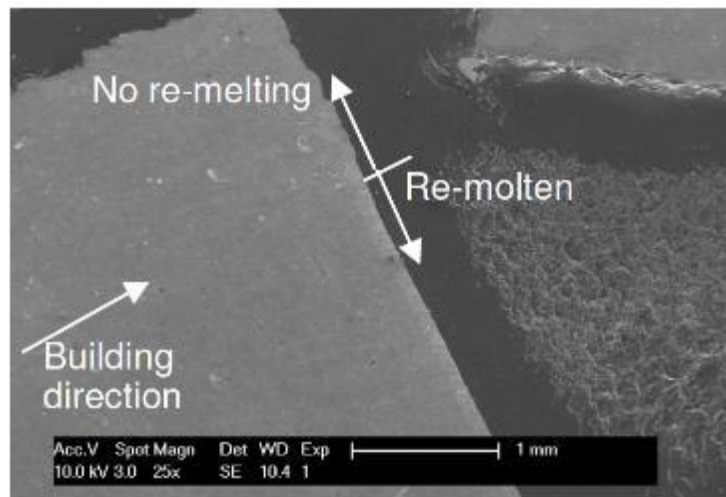


Figure 2.22 - SEM image of a SLM laser re-molten surface with no obvious edge-effect [54]

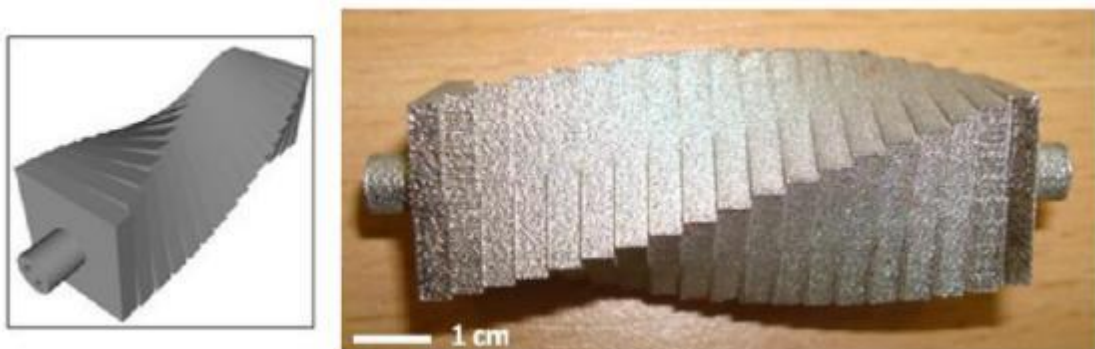


Figure 2.23 - SLM manufactured "truncheon" test part [81]

2.3.3 Mechanical Properties

2.3.3.1 Toughness

The mechanical properties obtained with SLM for metal materials have been widely studied by many research groups in the world. Kruth et al. described the mechanical properties of SLM parts as comparable to those of bulk materials, apart from the ductility, which is lower in SLM fabricated parts. Kruth et al. [54] studied the impact toughness of three materials – AISI 316L stainless steel, Ti6Al4V and maraging steel 300. The Charpy impact test was used to determine the impact toughness values, both with notch and without notch. From the study, Figure 2.24 shows that specimens with notch have less resistance to breakage, which means that the high roughness of the SLM process does not behave like stress-concentrating notches. The study also concluded that in the case of a good connection between successive layers without any pores, the building axis does not play a significant role in the toughness results. Hence, the way of producing the notch does not affect the toughness results. It was also observed that scatter in impact toughness for the notched samples is significantly lesser than the samples without notch. The reason for this observation was not stated in Kruth's discussions, and an analysis would require a good understanding of the experiment setup, which was not described in [54].

The results were then compared with that of conventional manufacturing. From the study, Table 2.14 shows that the toughness of bulk materials is higher than that of SLM parts. The reason of having lower toughness with SLM can be attributed to the presence of defects like pores, pick-up of impurities like oxygen and nitrogen (especially for titanium alloys) and the presence of more brittle non-equilibrium phases. The findings imply that aging reduces the impact energy but increases the strength and hardness.

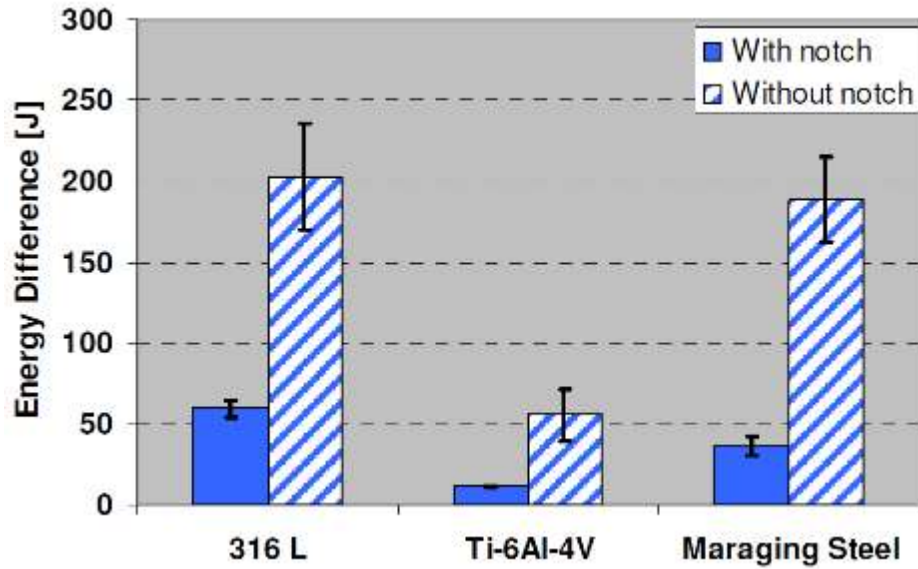


Figure 2.24 - Charpy test results for SLM produced parts [54]

Table 2.14 - Comparison of SLM and conventional processes in terms of Charpy V-notch toughness [54]

Material	SLM	Conventional
Ti6Al4V	11.5 ± 0.5 (as built)	15 J
	10.1 ± 0.5 J (annealed)	Investment casting
Maraging Steel 300	36.3 ± 4.8 J (as built)	18 J
	10.1 ± 1.4 J (after aging)	After aging
Stainless Steel 316L	59.2 ± 3.9 (as built)	160 J
		cast CF-3M

2.3.3.2 Ductility

In the SLM of steel, many research works have reported low ductility in the SLM built samples, usually with strong anisotropy associated with building direction. Song et al. [82] compared the elongation values of SLM built samples with traditionally built samples. In the comparison, Song et al. presented wrought AISI 316L stainless steel samples with elongation values of 40% in X, Y, Z axes, and SLM as-built samples with elongation values of 13-16% in the X and Y axes, but up to 50% in the Z axis. Yadroitsev

et al. also reported similar findings. Yadroitsev et al. [83] investigated the mechanical properties of SLM built AISI 316L stainless steel samples. The findings showed that the elongation values for the SLM built samples are between 6-13.5%, while wrought stainless steel elongation value is 40%.

However, some studies have shown that SLM is capable of producing components with ductility performance close to that of conventional manufacturing. Spierings et al. [84] investigated the effect of varying stainless steel 316L powder granulations on the resulting part mechanical properties. The investigation achieved elongation values of typically 30% (see Figure 2.25), with peak values reaching 50%. This meets the stated elongation values for wrought stainless steel 316L of 40% obtained from American Society for Metals (ASM) handbook [85]. Riemer et al. also achieved similar results [86], with elongation values of 53.7% in his SLM as-built stainless steel 316L tensile test coupons (see Table 2.15). The study concluded that the high elongation values may be attributed to fine substructures present in the as-built microstructure.

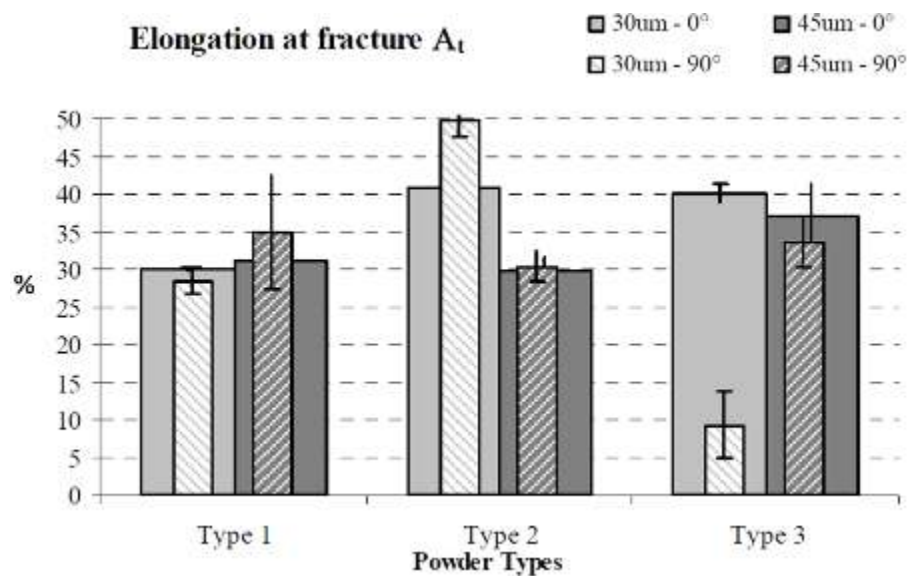


Figure 2.25 - Elongation values for SLM built SS316L from Spierings et al. [84]

Table 2.15 - Ultimate tensile strength, 0.2% offset yield strength and elongation at failure from Riemer et al. [86]

Condition	UTS (MPa)	YS (MPa)	Elongation (%)
As-built/SLM surface	565	462	53.7
650°C/Turned surface	595	443	48.6

Kanagarajah et al. presented an explanation to the conflicting results for ductility of metallic materials produced by SLM process [87]. Kakagarajah et al. presented findings on high ductility in SLM as-built nickel based alloy (Inconel 939). The paper attributed this to the presence of substructures, e.g. low-angle grain boundaries, eventually acting as barriers for dislocation motion. Vilaro et al, on the other hand, reported low ductility for nickel based alloy (Nimonic 263) [88]. Kanagarajah et al. then attributed this difference to the defects between layers found in Vilaro's study, which was not observed in Kanagarajah's study. Kanagarajah et al. concludes that smaller grain sizes led to the higher ductility due to a more homogeneous deformation.

2.3.3.3 Tensile Strength

Tensile yield strength and ultimate tensile strength of SLM built metallic samples are generally excellent, and in many cases exceed that of wrought samples [89]. Table 2.16 shows some of the tensile properties of SLM processed metallic materials, which when compared to traditional processing, are more superior if not the same. Song et al. attributed this characteristic to the grain refinement in SLM produced parts [82]. The fine grain characteristics of SLM produced parts are due to high cooling rates associated with the process. Song et al. [90] investigated the microstructure and tensile properties of iron parts fabricated by selective laser melting and proposed multiple self-strengthening mechanisms to explain the high mechanical strength, based on grain size, dislocation density and precipitated second phase effect on the yield strength. The most significant strengthening mechanism is proposed to be grain refinement. Abd-Elghany reported relatively high ultimate tensile strength in the investigation of 304L stainless steel fabricated by SLM and similarly attributed this to the rapid melting and cooling characteristic of SLM process [91].

Table 2.16 - Tensile properties of SLM processed metallic materials

Material	Process	Ultimate Tensile Strength (MPa)	Yield Strength (MPa)	Reference
SS316L	Wrought	450-620	170-310	ASM Handbook [85]
	SLM	369-555	312-465	Yadroitsev et al. [83]
	SLM	649.8-667	628-649.3	Tolosa et al. [92]
SS304	Casting	520	205	Guan et al. [93]
	Wrought	515-620	205-310	ASM Handbook [85]
	SLM	714-717	566-570	Guan et al. [93]
17-4PH	Wrought	795-1310	515-1170	ASM Handbook [85]
	SLM	947-1305	435-537	Luecke [94]
Ni718	Wrought	1340	1100	Zhao et al. [95]
	SLM	889-907	1137-1148	Wang et al. [96]
Ti6Al-4V	Wrought	828	897	Frazier et al. [97]
	SLM	1166-1206	962-1137	Vilaro et al. [98]

2.3.3.4 Fatigue

Studies have shown that the fatigue behaviour of SLM produced specimens is very sensitive to pores, and it is critical for the amount of porosity to be reduced to obtain high performance in fatigue [99]. Riemer et al. [86] investigated the effect of post-processing on the fatigue properties of SLM processed 316L. Four conditions were tested – namely, as built, as-built with machined surface, post-process heat treatment with machined surface, and hot isostatically pressed with machined surface. The results are shown in Table 2.17. The results show that the performance of SLM-processed 316L under cyclic loading can be increased by a suitable post-treatment. Riemer attributed this to the reduction of residual stresses achieved by the 650°C annealing, resulting in a

small increase in the fatigue limit of about 30 MPa. Riemer then compared the results with Strizak et al.'s fatigue investigation of conventionally process 316L stainless steel [100], and concluded that stainless steels processed by SLM can meet or even outperform the fatigue performance of the conventionally processed ones.

Table 2.17 - Fatigue limits for stainless steel 316L from Riemer et al. [86]

Condition	Fatigue limit (MPa)
As-built/SLM surface	108
As-built/Turned surface	267
650°C/Turned surface	294
HIP/Turned surface	317
Traditionally processed [100, 101]	240-381

Stoffregen et al. [102] reviewed existing work on fatigue analysis of SLM parts and subsequently investigated the fatigue performance of 17-4PH stainless steel. The study observed a strong divergence between the fatigue behaviour of as-built and machined SLM 17-4PH stainless steel specimens in the high cycle fatigue regime. For the machined specimens, the fatigue strength at $N = 10^7$ cycles is 492 MPa and accounts for 51% of the measured ultimate tensile strength (UTS = 961 MPa). Compared to the results on conventionally manufactured 17-4PH stainless steel [103], this results show fatigue strength values in the same magnitude. This indicates that the fatigue behaviour of machined SLM generated specimens is comparable to conventional manufactured ones. For the as-built specimens, the fatigue strength at $N = 10^7$ cycles is 219 MPa, which is significantly below the value of machined specimens. The fatigue strength accounts for only 23% of the ultimate tensile strength. Stroffregen et al. attributed this to the high surface roughness of as-built specimens and the associated notch effect [104].

However, in another study by Spierings et al. [105], the fatigue performances (see Figure 2.26) of SLM processed parts are significantly lower (77%) than those of the standard values for wrought alloy. Song et al. has attributed this to the porosity of

parts being the key contributor to the decrease in fatigue life [82]. This conclusion is consistent with that of Riemeret al.

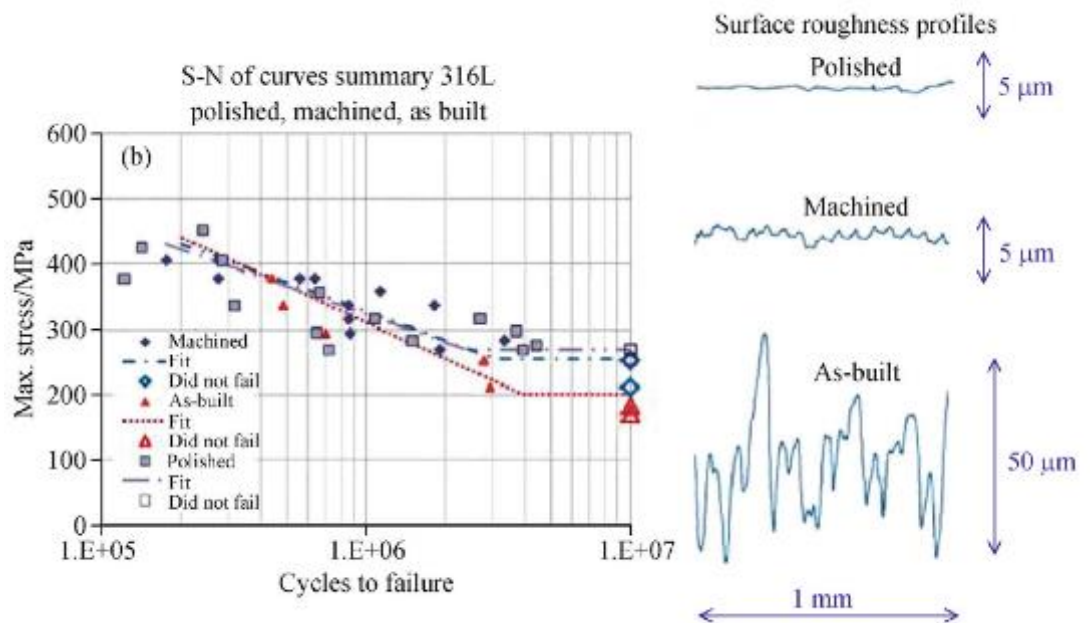


Figure 2.26 - Fatigue results of SLM process stainless steel 316L [105]

Hence, it can be concluded that fatigue properties of SLM produced metallic materials can meet that of conventionally produced samples if the two critical conditions are met:

- Surface roughness should be reduced through post-processing such as machining, to avoid notch effect;
- Porosity should be reduced as much as possible, increase fatigue life.

One of the possible techniques that can be employed to ensure that the two conditions mentioned above can be met will be laser re-melting. Yasa et al. [106] employed laser re-melting on the SLM of stainless steel 316L and the results showed that the relative density of the part obtained is close to 100% (and hence reduced porosity), and the surface roughness improved by 90%.

2.3.3.5 Hardness and Wear

Hardness property of SLM produced metallic materials are usually excellent, and is often superior to conventional processing methods (eg. casting and forging) [107-

109]. For a relatively fully dense part without the formation of cracks, the remaining of a reasonable level of residual stresses in laser processed components favours the enhancement of hardness [110]. Associated with hardness property, recent researches start to study the wear and tribology performance of AM processed components. Kruth et al. [111] have investigated the wear behaviour of prealloyed tool steel produced by SLM, showing that AM technique is capable to offer excellent surface wear properties. The densification level of AM processed parts has a fundamental influence on wear performance. Better wear resistance is obtained for fully dense components. Gu et al. [112] investigated the SLM of commercially pure Ti and presented findings to show that superior hardness property compared to conventional powder metallurgy (PM) processed Ti was obtained. He also agreed that residual stress in SLM-processed parts favours the enhancement of hardness, and added that the significant grain refinement effect (Figure 2.27) due to laser rapid solidification favours a further increase in the obtainable hardness.

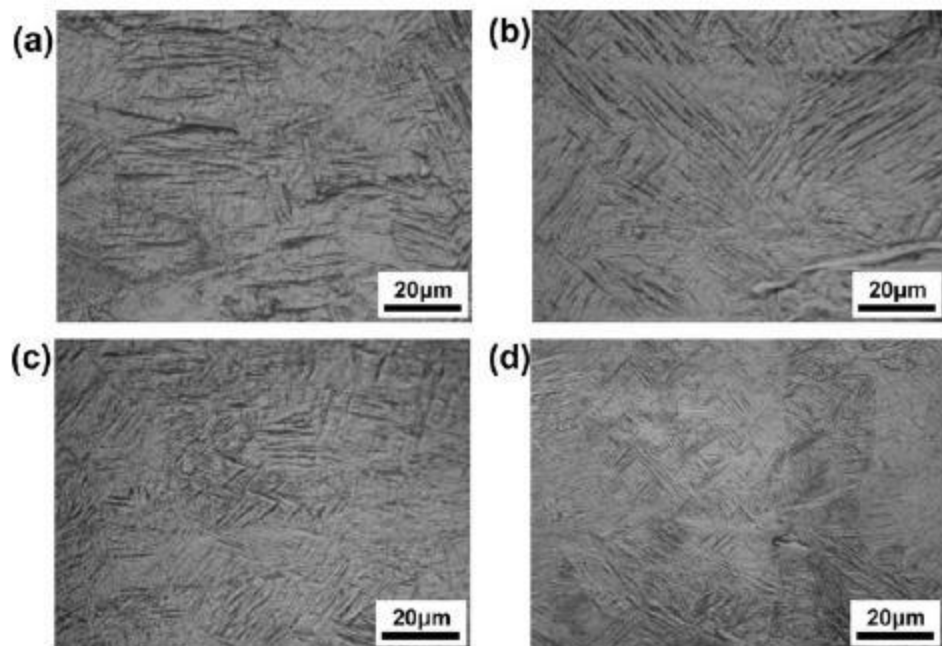


Figure 2.27 - Optical microscopy images showing characteristic microstructures of SLM-processed Ti parts at different processing parameters [112]

Yasa et al. [113] investigated on the effect of process parameters on hardness performance of Maraging Steel 300. The findings showed that hardness is significantly affected by density, where, as the scan speed is increased, the hardness values are significantly reduced due to increased porosity (see Figure 2.28). Yasa et al. also

commented that the high cooling rate and rapid solidification unique to SLM prevents formation of a lath martensite. SEM images (Figure 2.29) showing intercellular spacing of less than 1 μm contributes to the excellent hardness properties. Yasa et al. also applied laser re-melting strategy and the findings showed that the hardness values improved by 4.5% with re-melting, and are generally higher than those of maraging steel parts produced with conventional production techniques. This is consistent with another of Yasa et al.'s work, where higher hardness encountered in the laser re-melted zone is attributed to finer microstructure [66]. In that work, it is also observed that the cellular/dendritic microstructure is more homogenous and has a smaller cell size in the laser re-melted zone than the regions which is built by SLM with no laser re-melting.

In the same literature, Yasa et al. also investigated on the effect of heat treatment on hardness [113]. Aging is performed to form a uniform distribution of fine nickel-rich intermetallic precipitates during the aging of the martensite. These precipitates serve to strengthen the martensitic matrix. Secondly, it is aimed to minimize or eliminate the reversion of metastable martensite into austenite and ferrite [114]. In the literature, the hardening of maraging steels during aging has been attributed to two mechanisms, namely the short-range ordering in the cobalt-bearing solid solution and precipitation of nickel-rich intermetallic compounds in the lath martensitic structure [114]. The study concluded that aging improves hardness by up to 64% when aging for 5 hours at 480°C. However, at prolonged durations, the hardness starts to drop slightly. This is an indication of overaging, meaning that the re-heating starts reversion of metastable martensite into austenite, which is an equilibrium phase. Additionally, when a maraging steel is overaged, the coarsening of the intermetallic precipitates takes place. Yasa et al. concluded that these two phenomena together decrease the hardness as the part is kept at elevated temperatures for a prolonged time.

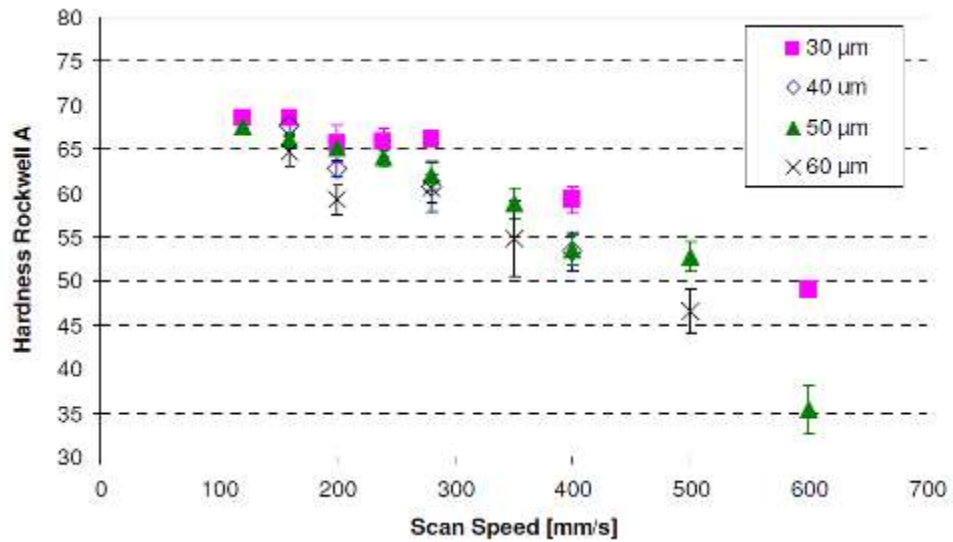


Figure 2.28 - Average macro hardness measured on cross-sections versus scan speed for different layer thicknesses with 95% confidence intervals [113]

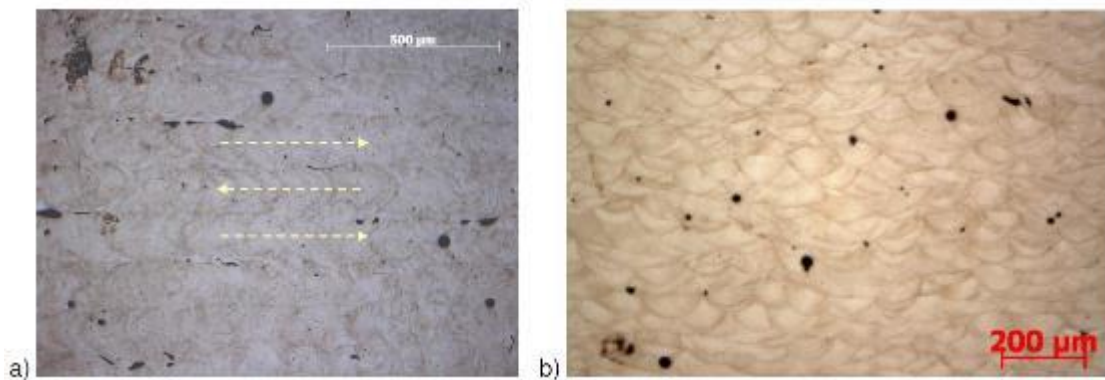


Figure 2.29 - Micrographs after etching of cross-sections of Maraging Steel 300 from Yasa et al. [113]

2.3.4 Microstructure

SLM is an additive manufacturing process that can be characterised by a high cooling rate of 10^3 to 10^8 K/s [40, 41]. Rapid cooling results in a non-equilibrium solidification process and enhances the limitation of solid solubility, refinement of grains, and possible formation of new metastable, even amorphous phases [82]. Due to large temperature gradients and complex heat transfer formed in a molten pool, preferential grain growth and heterogeneous structure may be formed in SLM built parts [115]. Song et al. [82] reviewed relevant studies on metal material fabrication through SLM, and presented results on microstructure, properties, dimensional accuracy and

application of SLM. In the review, Song et al. presented results on typical microstructure and characteristic of SLM built parts.

Song et al. reviewed the works by Wen et al. [116] and Gu et al. [117] and reported overlaps between molten pool boundaries (MPBs) observed in stainless steel 316L fabricated by SLM. In the review, Song et al. studied the SEM images of MPBs on a cross section of the SLM samples. MPB as a typical microstructure has been observed in 316L stainless steel, 304 stainless steel [93], and Ni625 fabricated by SLM. The cross sectional molten pool of a single track presented an arc-shape configuration (Figure 2.30), which can be attributed to Gaussian energy distribution of the laser beam. Multi-line and multi-layer single tracks accumulate to form a 3D object different from traditional processing. Similar grain orientations on both sides of MPB layers can be observed (Figure 2.31), where dotted lines indicate grain orientations, displaying an obvious inheritance. Fine cellular and dendritic structures with a grain size of less than $1\ \mu\text{m}$ is also observed (Figure 2.32). According to Hall-Petch formula [118], finer grain size leads to better mechanical properties. In the SLM process, large amount of non-metallic elements including C, O and Si often concentrate around the MPBs to form non-metallic inclusions. The unstable state of the non-metallic inclusions near the MPBs greatly affects the mechanical properties of the SLM parts. Figure 2.33 shows that cracks always originate from MPBs under vertical and horizontal loading direction conditions [116].



Figure 2.30 - MPBs on the cross section parallel to the laser scanning direction [82]

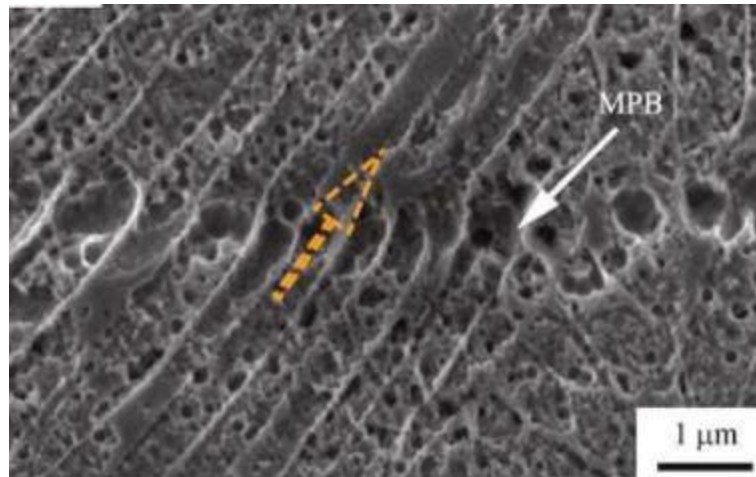


Figure 2.31 - Morphology of the cross section perpendicular to the scanning direction [82]

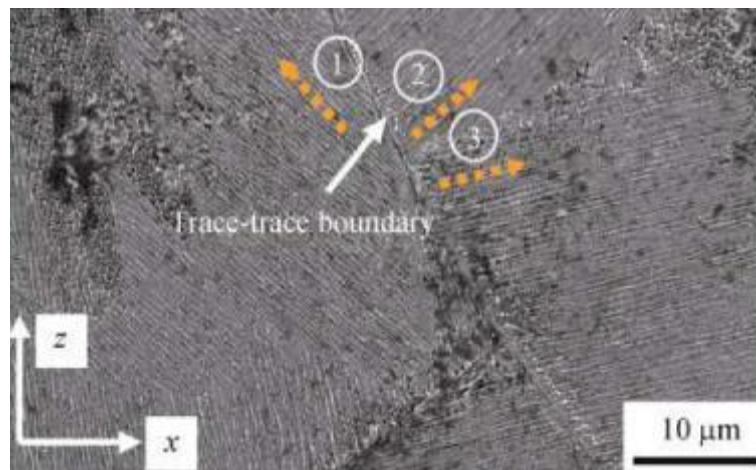


Figure 2.32 - MPB boundary

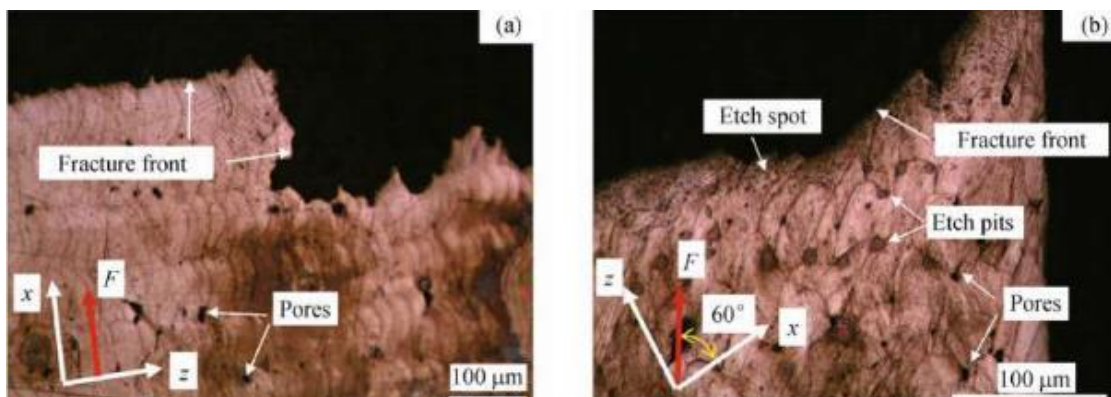


Figure 2.33 - Tensile fracture morphologies of the sample fabricated along the direction (a) perpendicular to the laser scanning direction and (b) with an angle of 60° between the tensile loading direction and x-y plane [116]

The microstructure of SLM built parts can be controlled by adjusting the following main parameters: Laser power (P), scanning velocity (V), hatch spacing (d),

powder layer thickness (h), and scanning strategy, among others. Higher laser energy density $P/(Vdh)$ and slower scanning speed will contribute to grain size growth and change the grain morphology [90, 119, 120]. Song et al. [90] presented results of smaller grain size with increasing laser scanning speed. Song et al. attributed this to lower cooling rate with increasing laser scanning speed. As cooling rate in the solidification process decreases, nucleation rate increases and hence small grains will be formed. Refinement of the grain size contributes to the observed strengthening of the material compared with ordinary iron. Figure 2.34 shows the metallographic observation of the SLM built iron cubes from [90]. It can be found that the grain morphology from the side views were different from that of the microstructure from the top views. Grains are larger and more irregular. During the SLM process, the powder particles are irradiated and heat is transferred from the top to the bottom of pre-laid powder layers, so that the elongated grains formed during the solidification process due to temperature gradient that is created between the powder layers along the building direction, as reported in the papers [93, 121-124]. But in the SLM-fabricated iron parts, those elongated grains usually were not very obvious. It can be explained that due to the presence of phase change during the process of melting and solidification of iron powder, the temperature gradient has been weakened. Elongated grains could not be obviously observed, although there were some non-equiaxed grains.

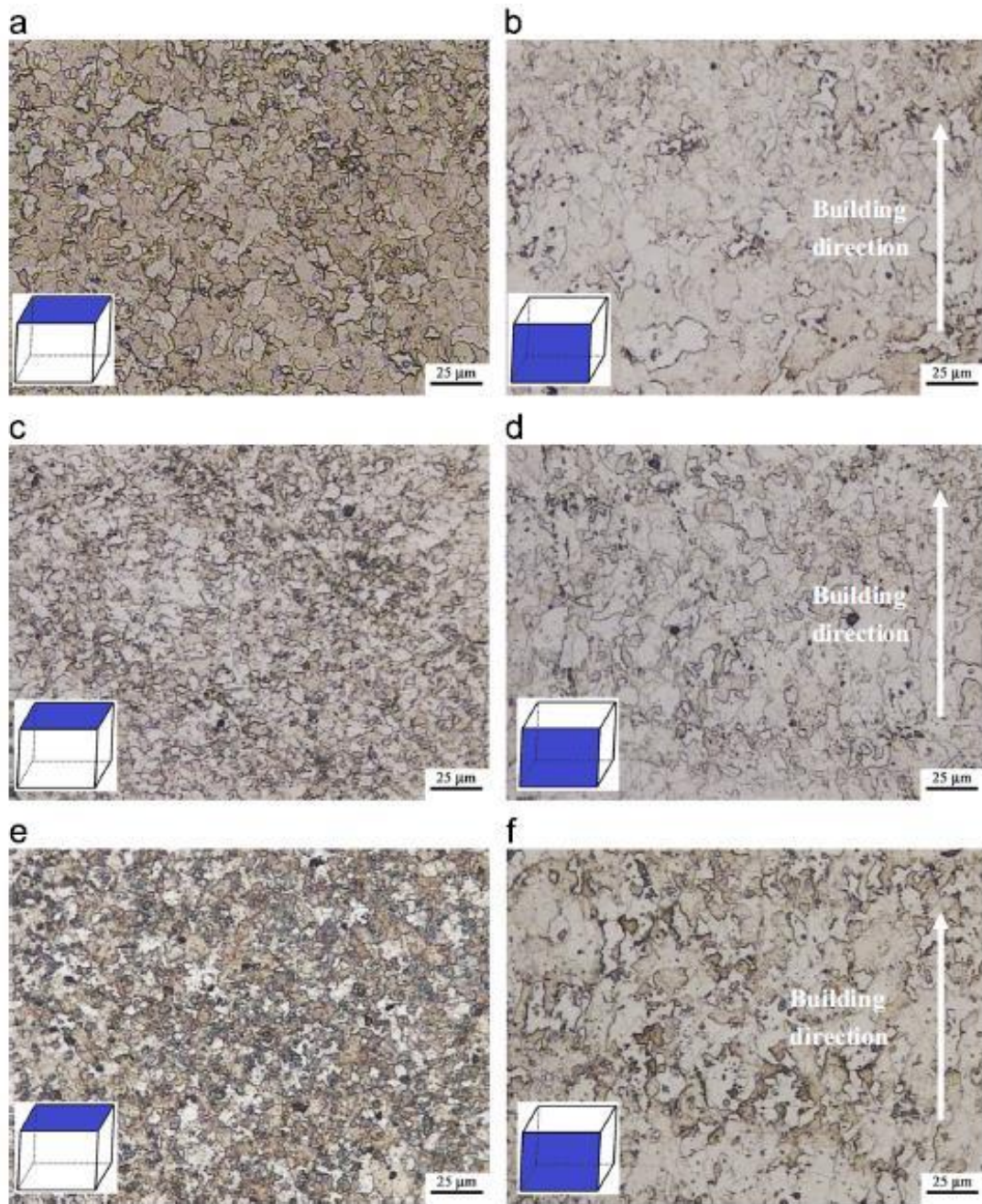


Figure 2.34 - Metallographic observation from the top view and from the side view of SLM-fabricated iron cubes at the laser power of 100W using different laser scanning speeds of: (a)–(b) 0.27m/s,(c)–(d) 0.33m/s and (e)–(f) 0.4m/s, respectively [90]

Kruth et al. [54] investigated the microstructure of metallic components after SLM. Based on his findings, high temperature gradients during SLM process leads to fine acicular martensite. In the investigation, he suggested that heat transfer direction will play a large role in the determination of the orientation of grains. Elongated grains appear along the building directions (Figure 2.35), with heights longer than the layer thickness. He concluded that the elongated grains are a result of epitaxial solidification.

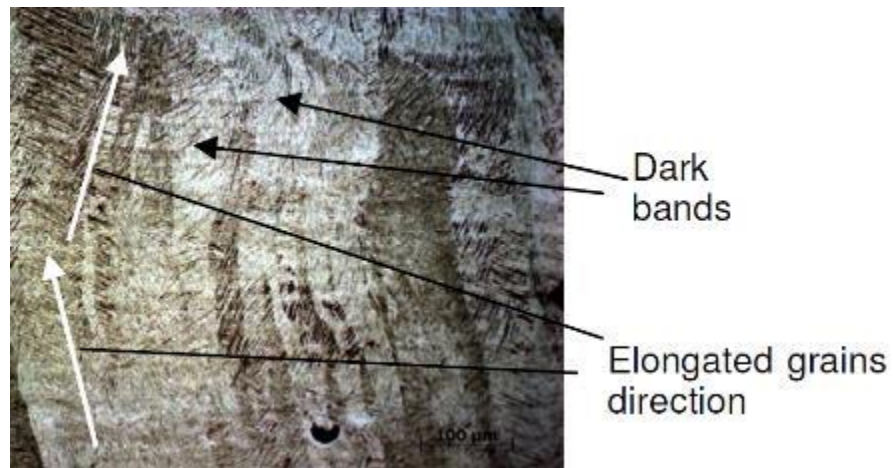


Figure 2.35 - Micrographs of SLM sample showing elongated grains along build direction [54]

Kruth et al. also investigated the microstructure of SLM built AISI 316L stainless steel [54]. He suggested that during SLM, a fully molten pool forms a depth of approximately 100 μm, significantly higher than the layer thickness of 30 μm (Figure 2.36). SEM pictures of the cross-section of the AISI 316L parts reveals a fine cellular-dendritic structure (Figure 2.37). This microstructure is formed as a result of rapid solidification due to very high cooling rates encountered in SLM.

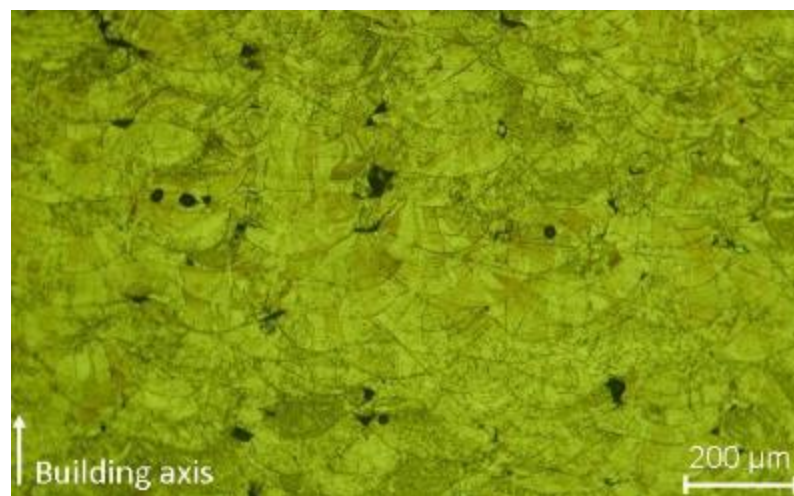


Figure 2.36 - Frontal section of a SLM part from AISI 316L stainless steel [54]

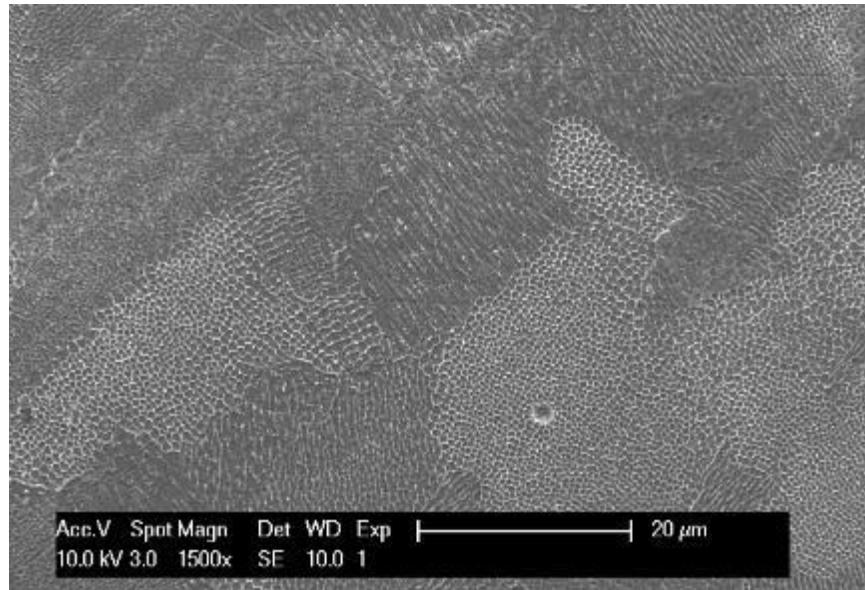


Figure 2.37 - SEM image of the cross-section of SLM built AISI 316L part [54]

Since temperature gradient and the local heat transfer conditions determine the grain growth of a SLM part, Kruth et al. investigated how changing the process parameters as well as the scanning strategy may affect the resulting microstructure.

Figure 2.38 shows side and front views of a Ti6Al4V part produced with lowered scan speed of 50mm/s. The micrographs indicate that decreasing scanning speed results in coarser grains size. Lowering the scanning speed has also resulted in an elongated and more irregular melt pool, thereby deteriorating part quality by formation of large pores. A lower scanning speed also results in grains that are better aligned with the building direction (see Figure 2.38(b)).

Due to the higher energy input at lower scan speed, the dark zones that indicate the melt pool boundaries in the side and front views (Figure 2.38) are more intense. Kruth et al. used the bands to estimate the actual layer thickness, based on the vertical separation of the bands in the front views. Kruth et al. suggested that these bands become visible due to the preferential etching of the intermetallic Ti₃Al phase. As a result of fast solidification during the SLM process, segregation of Al occurs and zones rich in Al are formed. When a higher amount of heat is applied to the material, e.g. lowering scan speed, the material will reach higher temperatures and more material will remain longer at higher temperatures, thereby increasing the volume of precipitates.

Kruth et al. also concluded that formation of aligned pores within the SLM-fabricated parts may likely be a consequence of choosing inappropriate scan spacing.

Insufficient overlap between neighbouring scan tracks, caused by increased scan spacing, results in almost vertically aligned pores in the front section of a SLM part as shown in Figure 2.39(a). In this case the scan spacing was increased to 100 μm while the other optimised parameters were kept unchanged. Decreasing the scan spacing below the optimised setting, may also create diagonally aligned pores in the front section. It is suggested that the angle of slope of pore alignment is affected by the scan spacing: the higher the spacing, the higher the slope angle [125]. When the hatch spacing equals the melt pool width, as shown in Figure 2.39, the angle is 90° and the pores are aligned vertically.

Figure 2.39(b) shows the side view of a Ti6Al4V part that is produced at optimised process parameters using unidirectional scanning strategy. The layers are scanned from right to the left, thereby remaining identical thermal profiles when each layer is being scanned. Since the grains solidify in the direction perpendicular to the isotherms, the grains are tilted from the building direction as observed in the figure. Therefore the orientation of the grains is highly dependent on the scanning speed and scanning strategy, but also on the local part geometry. Consequently, the scanning strategy may be a powerful tool to control the grain orientation, and hence the microstructural texture.

Kruth et al. also performed laser re-melting (LSR) and investigated the microstructure formed. The LSR parameters are scan speed of 200mm/s, laser power of 100W, spot size of 200 μm , and a scan spacing factor of 0.1. From the investigation, the cellular/dendritic structure of the LSR zone is more apparent than that of the layers that are not re-melted (see Figure 2.40). In addition, the cell size is finer in the LSR microstructures, being equiaxed and homogeneously visible throughout the re-melted zone.

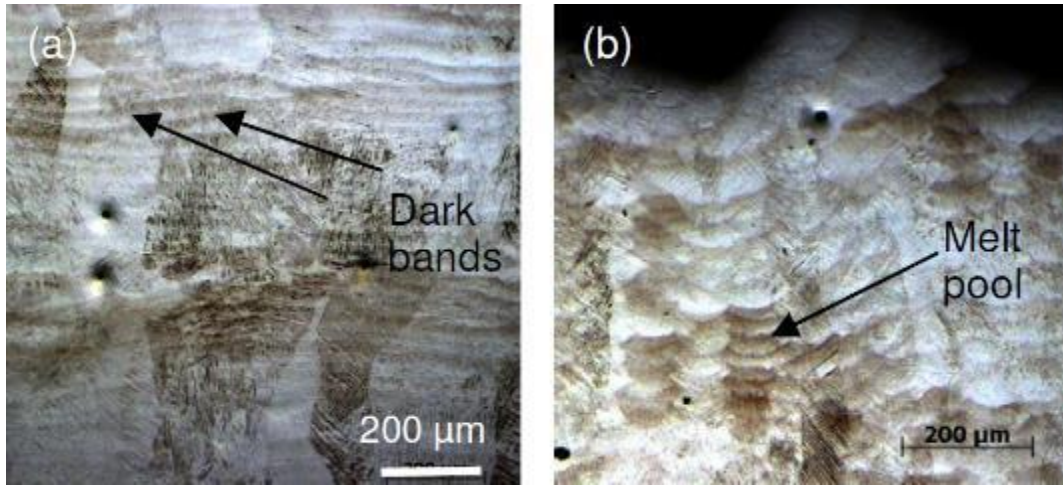


Figure 2.38 - Influence of scanning speed on microstructure of SLM built parts, (a) side view, (b) front view [54]

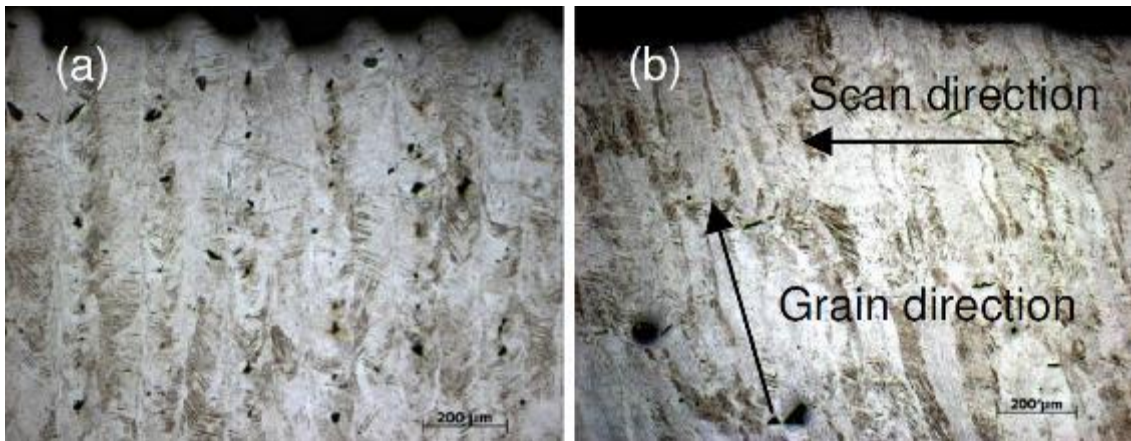


Figure 2.39 - Micrographs of SLM built parts: (a) front view of an increased scan spacing, (b) influence of scan strategy on grain direction [54]

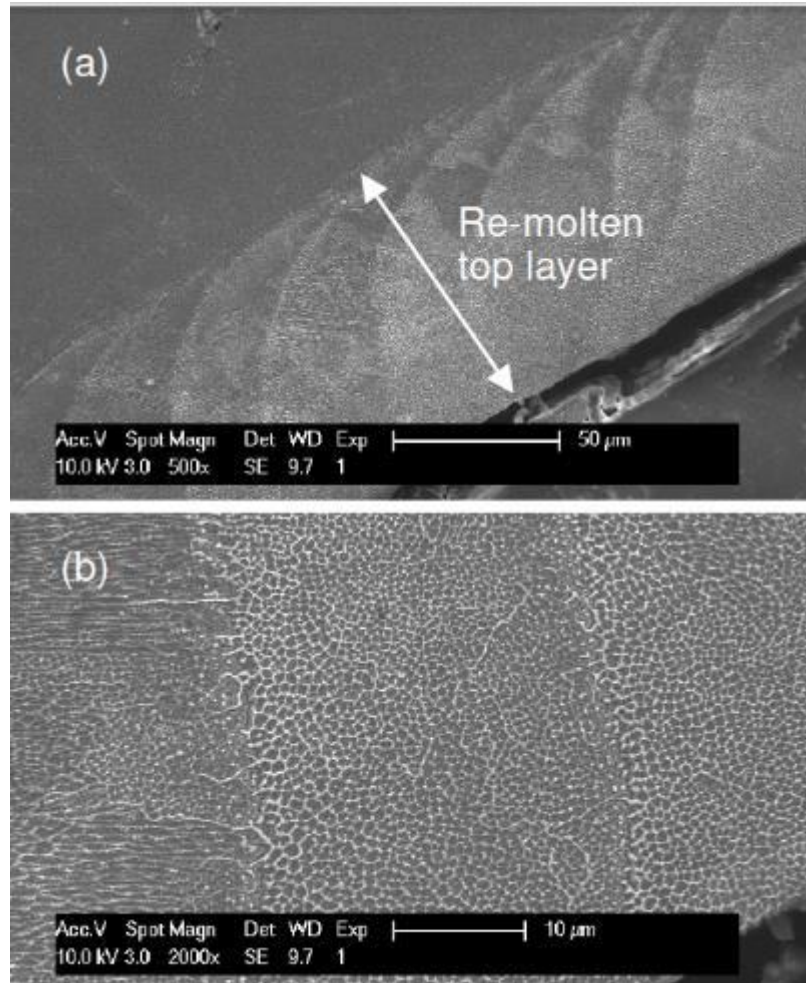


Figure 2.40 - SEM pictures of AISI 316L stainless steel part when last layer was re-melted 10 times, (a) low magnification, (b) high magnification [54]

Gu et al.[89] reviewed the grain size and structure of AM processed metallic components. High energy laser interaction gives rise to superfast heating and melting of materials, which is inevitably followed by a rapid solidification on cooling. Laser based AM processes normally offer high heating/cooling rates at the solid/liquid interface in a small sized molten pool. In addition, the rates of quenching that occurs by conduction of heat through the substrate are sufficiently fast to produce a rapid solidification microstructure. Hence, Gu et al. concludes, as a characteristic of AM processed materials, grain refinement is generally expected, due to an insufficient time for grain development/growth.

Gu et al. also discussed about the anisotropic characteristics of AM processed metallic materials. The conventional dendritic solidification features of Fe based materials are not well developed after AM, but showing a directional cellular microstructure, due to the insufficient growth of secondary dendrite arms. On the other

hand, either chemical concentration or temperature gradients in molten pool may generate surface tension gradient and resultant Marangoni convection [126, 127] making the solidification a non-steady state process. Meanwhile, rapid solidification has the kinetic limitation of crystal growth that normally follows the direction of maximum heat flow. The simultaneous but competitive action of the above two mechanisms, i.e. a non-equilibrium solidification nature versus a localised directional growth tendency, may result in a variety of crystal orientations with a localised regularity [128]. Therefore, AM processed metallic materials may have the inherent, more or less, anisotropic characteristics.

Gu et al. described another important feature that is intrinsic to AM processed components as the microstructural difference, both in grain size and its structure, between the bottom and top of a part along laser deposition direction. As the conduction, convection, and radiation conditions change, the different thermal histories of different layers of the part lead to the variation of microstructures along the height direction. Hence, Gu et al. concluded that the occurrence of grain coarsening is due to: (i) considerable remelting of the top of previous layer; (ii) long term thermal accumulation.

2.4 Literature Review Summary

Based on the literature review, under the ASTM A131 standard specification for structural steel for ships, EH36 grade has been chosen for this research. The material is a high tensile strength steel commonly used in structural components for shipbuilding. Its chemical composition, tensile requirements and impact requirements are stated in Table 2.18, Table 2.19 and Table 2.20 respectively. Literature search on the roles of alloying elements have also been conducted and it will contribute towards the understanding of the microstructure and mechanical properties of AM processed EH36 material.

Table 2.18 - Chemical requirements for ASTM A131 EH36 steel

Element	Chemical Composition, % max unless otherwise specified
	Grades EH36
Carbon, C	0.18
Manganese, Mn	0.90 – 1.60
Silicon, Si	0.10 – 0.50
Phosphorous, P	0.035
Sulphur, S	0.035
Aluminium (acid soluble), min, Al	0.015
Columbium, Cb/Niobium, Nb	0.02 – 0.05
Vanadium, V	0.05 – 0.10
Titanium, Ti	0.02
Copper, Cu	0.35
Chromium, Cr	0.20
Nickel, Ni	0.40
Molybdenum, Mo	0.08
Nitrogen, N	-

Table 2.19 - Tensile requirements for ASTM A131 EH36

Grade	Tensile Strength, ksi [MPa]	Yield Point, min, ksi [MPa]	Elongation in 8 in. [200mm], min, %	Elongation in 2 in. [50mm], min, %
	EH36	71 to 90 [490 to 620]	51 [355]	19

Table 2.20 - Charpy V-notch impact requirements for ASTM A131 EH36

Grade	Test Temperature, °C	Average Absorbed Energy, min, J		
		t ≤ 50 mm	t > 50 mm	t > 70 mm
			t ≤ 70 mm	t ≤ 100 mm
EH36	-40	34	41	50

Even though the chemical composition may be optimised for conventional steel processing, it is important to consider the carbon equivalent (CE). CE is calculated based on the alloying elements, and is used to determine properties of alloy when the material (usually ferrous) contains more than just Carbon. CE is especially used in welding to determine the welding processes required to avoid defects. This would be the main consideration factor because the parts produced will eventually be joined or welded to other parts. CE is also used in the development of heat treatment methodology. The CE for EH36 is shown in Table 2.21.

Table 2.21 - Carbon Equivalent for ASTM A131 EH36

Grade	Carbon Equivalent , max, %	
	Thickness (t), mm	
	t ≤ 50 mm	t > 50 mm
		t ≤ 100 mm
EH36	0.38	0.40

A literature review on the various AM processes under the ASTM F2792 – 12a Standard Terminology for Additive Manufacturing Technologies standard has also been conducted. The review focussed on the technologies that can process metallic material. Selective laser melting (SLM) was eventually selected for this research. Based on the literature review, parts produced by SLM could achieve very high relative density of more than 99%. As compared to the same material processed by conventional manufacturing, SLM produced metallic components have superior tensile and hardness properties, but lacks in toughness and fatigue performance. These properties are usually recovered using post processing (eg. heat treatment). Surface quality is usually poor, and is especially important when considering fatigue crack initiation. Literature showed

that the microstructure of SLM built metallic parts are usually characterised by fine grains with elongation due to temperature gradient in the building direction. SLM built steels are usually anisotropic and exhibit acicular martensitic structure. The microstructure can be controlled by varying the process parameters, such as laser power, scan velocity, hatch spacing, layer thickness and scanning strategy.

A literature search based on using SLM to process EH36 steel was conducted but no results were found. There is no known literature to use SLM to process EH36 steel. Hence, based on the literature, it has been concluded that the research will characterise EH36 steel processed by SLM.

2.5 Research Objective and Scope

The overarching objective of the research work is to determine the technical feasibility of adopting additive manufacturing as a fabrication technology for marine structures used in shipbuilding, to achieve better design and improved performance. The objective can be further divided into four main sections:

- 1) To study the metallic materials conventionally used in shipbuilding and identify one material for the research work.
- 2) To study the commercial AM processes and identify a suitable AM process.
- 3) To develop a repeatable and optimised set of processing parameters for the fabrication of parts using identified AM process.
- 4) To establish the mechanical performance of parts produced using the identified AM process and validate it against industry requirements.

Based on the derived objectives, a set of intended scope is developed. Main points of the scope can be summarised as follows:

- 1) To review marine grade shipbuilding steel and provide justifications into the selection of ASTM A131 EH36 grade
- 2) To review existing AM technologies and provide justifications into the selection of SLM process

- 3) To conduct preliminary investigations into using SLM to process ASTM A131 EH36 steel.
- 4) To develop a set of SLM process parameters to process ASTM A131 EH36 steel for achieving high relative density.
- 5) To characterise ASTM A131 EH36 samples built using developed SLM process parameters.
- 6) To evaluate and determine the mechanical properties according to ASTM standards.
- 7) To investigate using heat treatment to enhance the mechanical properties.
- 8) To analyse and characterise microstructure.
- 9) To print a scaled 3D complex joint and validate against microstructure results.

ASTM A131 EH36 grade is an unknown material in the AM materials development area. Although primarily a low carbon steel, its applications in high strength and low temperatures areas may put the material under a separate category from the common low carbon steel materials. Hence, it is important to understand the melting and forming mechanism of EH36 material using AM technology. This can be achieved by building samples and observing the microstructure using techniques such as light optical microscopy (LOM) and scanning electron microscopy (SEM). Further analysis to complement the investigation could be performed on fracture surfaces.

The process parameters are predicted to have an effect on the final microstructure of the test sample. Hence, the research project will also investigate how different process parameters may have an effect on the microstructure and final mechanical properties. This allows for the material properties to be correlated to the in-process behaviour and can thus be used to predict the performance of future research projects.

Mechanical tests will be carried out according to ASTM standards and marine Classification standards. Coupons will be printed to undergo tests such as tensile and Charpy v-notch impact toughness tests at specified temperatures. The test results may be used to correlate the microstructure analysis results and the mechanical properties. An actual component will then be fabricated and subsequently have its microstructure observed, and the results will be validated against that obtained from the test coupons.

2.6 Proposed Research Roadmap

The proposed research activities to cover the above scope will be outline here.

Literature Review

- Marine grade shipbuilding steel and EH36 Steel
- AM and SLM technologies
- Properties of metal produced by SLM



Preliminary Investigations

- Derive preliminary SLM process parameters
- Fabrication of density cubes
- Testing of density cubes
- Microstructure analysis using LOM and SEM



Optimisation of Process Parameters

- Modify SLM process parameters
- Fabrication of density cubes
- Testing of density cubes
- Microstructure analysis using LOM and SEM



Mechanical Properties Characterisation

- Tensile tests
- Impact tests
- Analysis of tests specimens (eg fracture surfaces)



Post Processing Investigations

- Heat treatment methodology
- Microstructure analysis using LOM and SEM

Chapter Three Preliminary Investigations

A preliminary investigation of ASTM A131 EH36 high tensile strength steel used in shipbuilding applications was conducted by Wu et al. [129]. In the study, critical SLM process parameters such as hatch spacing and scanning speed were investigated to produce benchmark parts with high density and tensile and impact toughness properties comparable to conventionally produced EH36 parts. Microstructural analysis was also carried out to investigate the effects of varying process parameters. The results will facilitate future studies on SLM of shipbuilding steel.

3.1 Material

The ASTM A131 EH36 high tensile strength steel powder used in the investigation was supplied by Sandvik Osprey Limited (UK) produced by gas atomisation process using Nitrogen as the atomisation gas. According to the data sheet provided by Sandvik Osprey, 95.8% of the particle ranges between particle sizes of 20 μm to 53 μm , while 2.2% is less than 20 μm . Powder tests were carried out and the results are shown in Table 3.1. The particle size distribution was carried out by an independent test body and the results show that the median diameter of particle was 44 μm , with less than 10% smaller than 28 μm and 90% with diameter up to 49 μm . The results also indicated that the mean diameter of particles was 47 μm .

Table 3.2 shows the composition of the EH36 powder in weight percentage provided by Osprey (based on results from the independent test body) compared with the elemental composition specified in ASTM A131 standard. Except for Chromium (Cr) and Vanadium (V), the rest of the elements are within the range stipulated by the standard. V exceeded the range by 10%, but is relatively less significant compared to Cr, which exceeded the range by 80%. As discussed in Chapter 2.1.1.1, Cr has a positive effect on hardenability for high strength steel, and hence the higher percentage of the element in the EH36 powder is not expected to have detrimental effect. Nonetheless, since EH36 is an unknown material processed by SLM, this set of elemental composition was still used in the preliminary studies and will be used as a reference for future works. Using the elemental composition of EH36 powder provided by Osprey, the CE obtained is 0.45%.

Figure 3.1 shows a scanning electron microscopy (SEM) image of the particles provided by Osprey. From the image, it can be observed that the particles are mostly spherical in shape, except for a small percentage of irregularities which did not cause any deposition issues in the study.

Table 3.1 - ASTM A131 Powder Tests [129]

Powder Tests

Tap Density	5.1 g/cc	Particle Size Distribution	
Hall Flow	27.6 sec/50g	D10	28 μm
		D50	44 μm
		D90	49 μm

Table 3.2 - Elemental composition of ASTM A131 powder [129]

<u>Element</u>	<u>Osprey</u>	<u>ASTM A131</u>
	%	%
Manganese, Mn	1.14	0.9-1.6
Chromium, Cr	0.36	0.2 (max)
Silicon, Si	0.24	0.1-0.5
Nickel, Ni	0.11	0.4 (max)
Carbon, C	0.15	0.18 (max)
Vanadium, V	0.11	0.05-0.1
Niobium, Nb	0.03	0.02-0.05
Molybdenum, Mo	0.02	0.08 (max)
Aluminum, Al	0.02	0.015 (min)
Copper, Cu	0.05	0.35 (max)
Phosphorous, P	0.06	0.035 (max)
Titanium, Ti	<0.01	0.02 (max)
Sulphur, S	0.007	0.035 (max)
Calcium, Ca	0.003	0.005 (max)
Iron, Fe	Balance	Balance

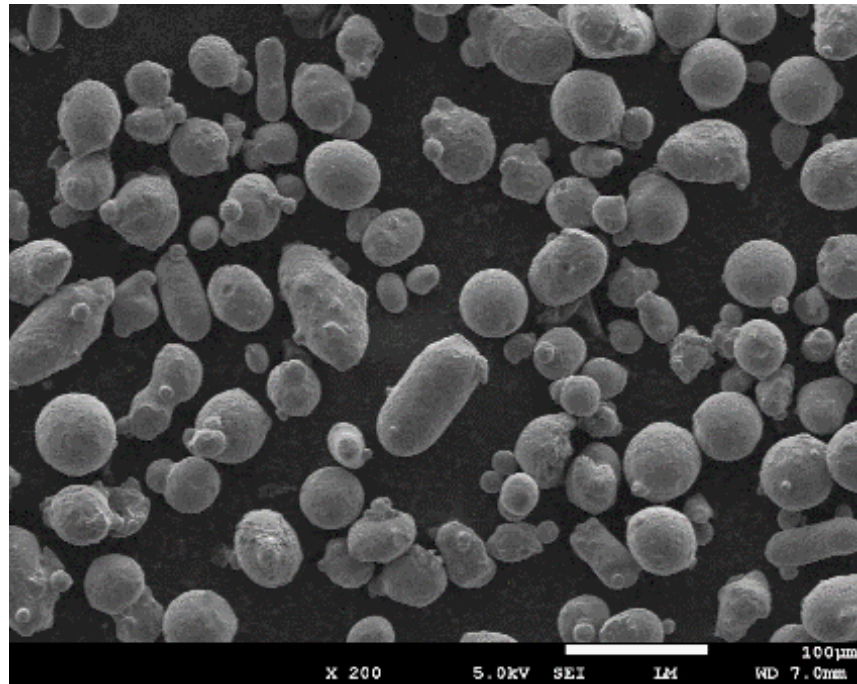


Figure 3.1 - SEM image of ASTM A131 powder particles [129]

3.2 SLM Machine and Process Parameters

In the investigation work, a SLM™ Solutions 250 HL selective laser melting (SLM) machine was used. A 400 W Yb:YAG laser (operating at 175W) in continuous wave mode was used to produce EH36 test specimens. The laser beam profile follows the Gaussian distribution and has a wavelength of 1.064 μm , with a focal diameter of 81 μm . The powder layer thickness was set at 50 μm . The stainless steel substrate plate was preheated to 100 °C to reduce the thermal gradients and thermal stresses experienced by the specimens during the SLM process. Energy density, which was investigated to directly impact the properties of steel parts, is a key factor in the SLM process [130]. The critical range of process parameters are selected based on literature [131-137], and hence does not follow any design of experiment methodologies. The scanning speeds were varied from 260 mm/s to 880 mm/s, and hatch spacing were varied from 0.08 mm to 0.12 mm, to obtain the various energy densities. The volume based energy density E (J/mm^3) is defined in Equation 3.1, where P is laser power (W), v is scan speed (mm/s), h is hatch spacing (mm) and t is layer thickness (mm).

$$E = \frac{P}{v \times h \times t} \quad (3.1)$$

Based on Equation (3.1), a set of parameters were obtained for energy densities ranging from 50 J/mm³ to 111 J/mm³. The parameters are detailed in Table 3.3, where the values in the table refer to laser scanning speed values in mm/s.

Table 3.3 - SLM process parameters (red values refer to laser scanning speed in mm/s) [129]

Power: 175W	Layer Thickness: 50 μm				
Energy (J/mm³)	Hatch Spacing (mm)				
	0.08	0.09	0.1	0.11	0.12
111	390	350	310	290	260
105	422	376	336	312	280
99	454	402	362	334	300
92	486	428	388	356	320
86	518	454	414	378	340
81	550	480	440	400	360
75	616	540	492	448	404
69	682	600	544	496	448
62	748	660	596	544	492
56	814	720	648	592	536
50	880	780	700	640	580

3.3 Results

Two sets of specimens were built for preliminary investigations. The first set investigated feasibility of printing of designs with thin wall, curved and straight vertical

surfaces, and slopes with 45 degrees. They were visually observed to have no visible cracks, distortion or surface porosities as illustrated in Figure 3.2. The second batch of specimens made of up 5mm x 5mm x 5mm cubes are printed for density tests as shown in Figure 3.3. They were then put through several other analyses to determine the integrity of the specimens – x-ray diffraction, light optical microscopy and scanning electron microscopy.

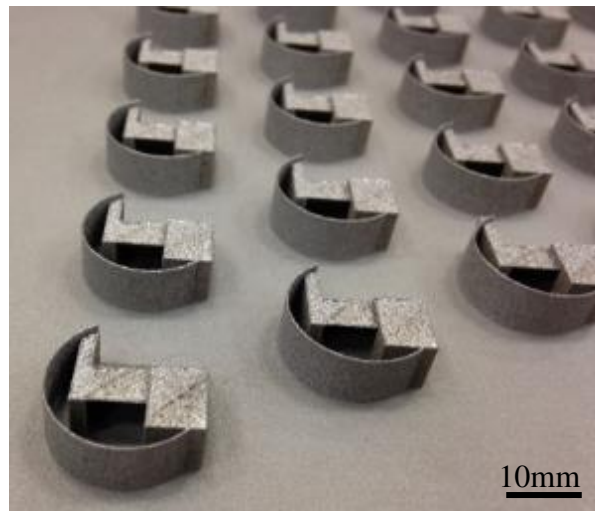


Figure 3.2 - SLM built test specimens [129]

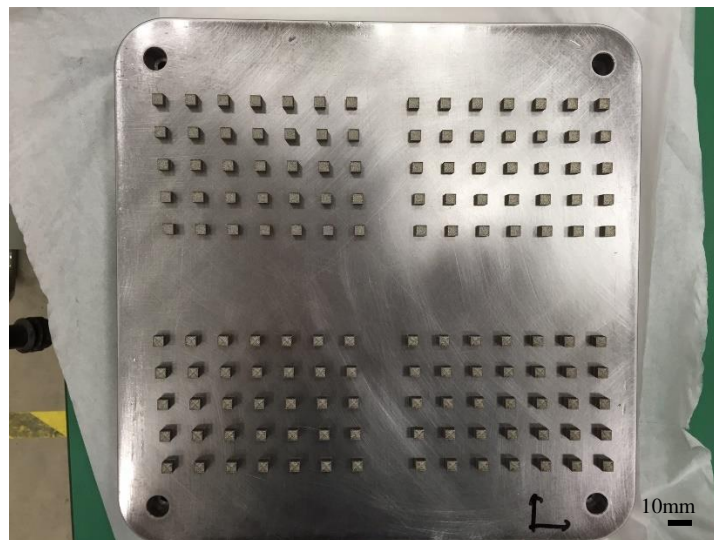


Figure 3.3 - SLM built density cubes

3.3.1 Density Test

Density tests were carried out as the optimisation variable during the process parameter selection because it is a significant factor affecting mechanical properties [138]. As discussed in Chapter 2.3.1, density determines a part’s mechanical properties, which in turn determines the part performance, and during process parameter optimisation, the goal is to achieve as high a density as possible. The tests are performed in accordance to ASTM B962 – 13: Standard Test Methods for Density of Compacted or Sintered Powder Metallurgy (PM) Products Using Archimedes’ Principle. Masses of each specimen in air (m_a) and water (m_w) were measured independently on an electronic balance with ± 1 mg accuracy. The measured values were then inserted into Equation (3.2) to obtain specimen density ρ_s , where ρ_w is the density of water (1 g/cm^3).

$$\rho_s = \frac{m_a}{m_a - m_w} \times \rho_w \quad (3.2)$$

The results of the tests are shown in Table 3.4, where table values represent density values in g/cm^3 . The highest density value of 7.64 g/cm^3 was obtained at an energy density of 92 J/mm^3 using parameters of 0.12 mm hatch spacing, powder at 175W , $50 \text{ }\mu\text{m}$ layer thickness and 320 mm/s laser scanning speed. Compared to the relative density of the compacted supplied powder (7.83 g/cm^3), or the material’s bulk density of 7.85 g/cm^3 , the results translated to 97.57% fully dense part. Graph of SLM built part density vs energy density (Figure 3.4) was plotted with a polynomial fit based on the results to identify the effects of the parameters on part density. It was observed that increasing energy density generally improves part density, but the two peaks represented 2 separate optimal energy density values of approximately 60 J/mm^3 and 100 J/mm^3 . At the points with higher density, it was observed that hatch spacings were generally higher and scan speeds were generally lower.

Table 3.4 - Results from density test (red values represent density in g/cm^3) [129]

Power: 175W	Layer Thickness: 50 μm				
	Hatch Spacing (mm)				
Energy (J/mm^3)	0.08	0.09	0.1	0.11	0.12

111	7.178	7.519	7.433	7.489	7.535
105	7.374	7.512	7.528	7.46	7.594
99	7.489	7.483	7.526	7.56	7.573
92	7.476	7.477	7.466	7.528	7.64
86	7.419	7.486	7.494	7.48	7.525
81	7.385	7.465	7.469	7.43	7.401
75	7.503	7.419	7.456	7.434	7.42
69	7.523	7.516	7.482	7.473	7.47
62	7.511	7.537	7.378	7.332	7.361
56	7.47	7.468	7.278	7.391	7.365
50	7.471	7.273	7.014	7.075	6.982

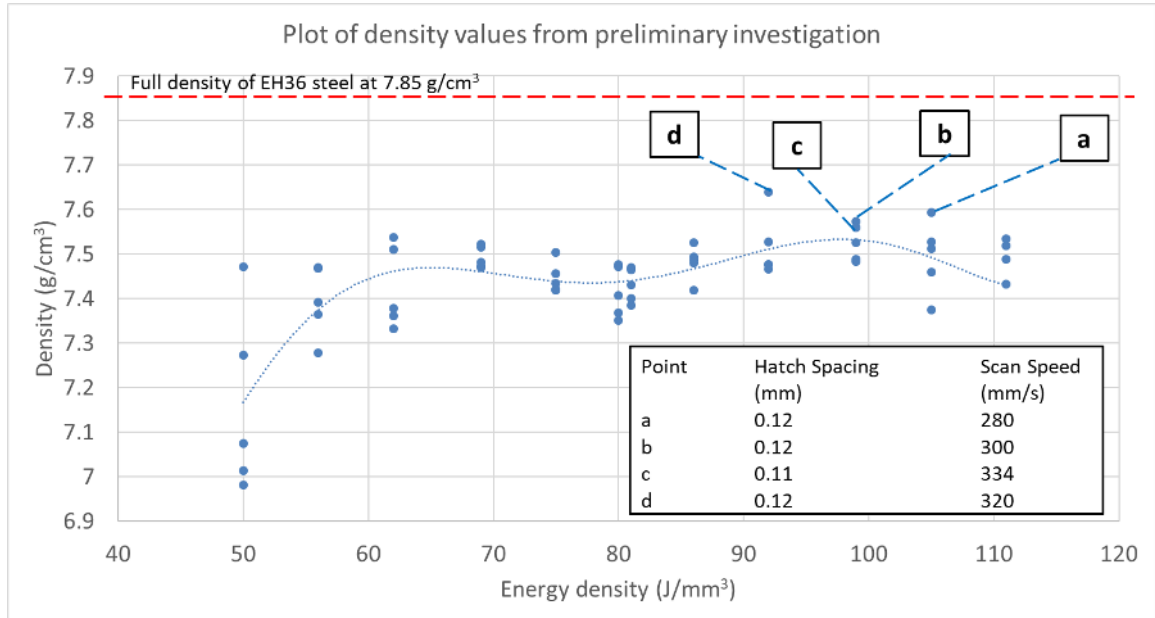


Figure 3.4 - Graph of SLM built part density vs energy density [129]

3.3.2 X-Ray Diffraction

X-ray diffraction (XRD) analysis was conducted on the sample powder and SLM built specimen using Philips X'pert instrument. The raw data was collected and analyzed using X'pert Highscore software Version 1.0d. The data analysis library was from JCPDS – International Centre for Diffraction Data. The analysis conditions are listed in Table 3.5. The XRD analysis is capable of identifying compounds in concentrations greater than 1.0 wt%. The XRD results shown in Figure 3.5 indicated Fe α -phases in both the sample powder and SLM built specimen. (A complete set of XRD results for the subsequent part of the research can be found in Chapter 6.3. Please refer to Figure 6.4.)

Table 3.5 - XRD analysis conditions

Target	Voltage	Current	2 θ scan range	Step size and time
Cu with Ni filter	40 kV	35 mA	10° – 90°	0.01° and 0.25s

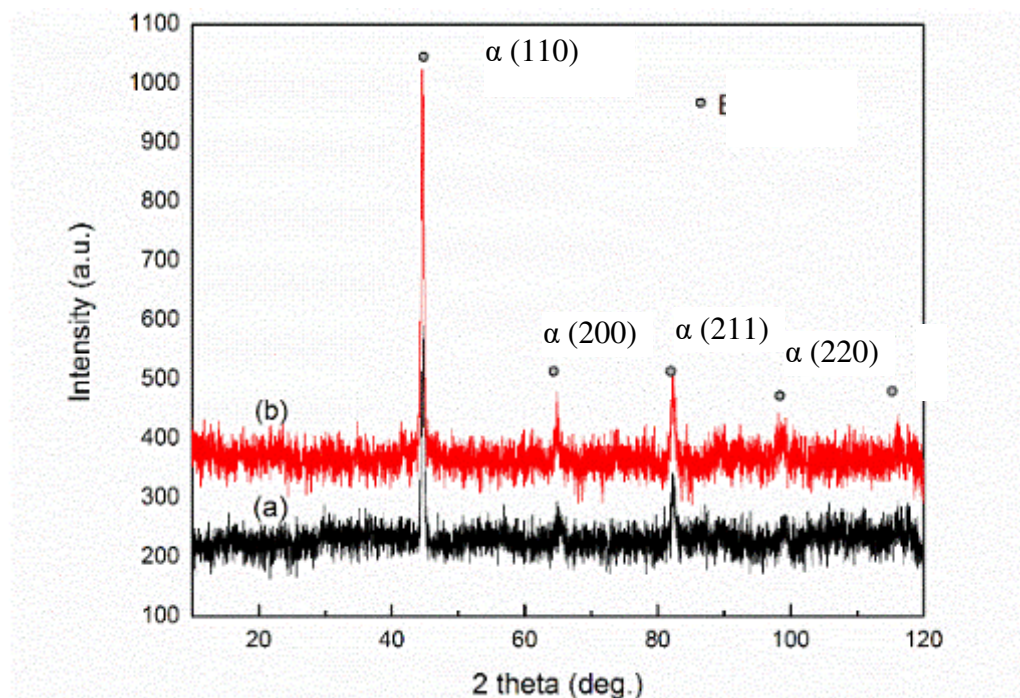


Figure 3.5 - XRD of EH36 (a) powder sample, (b) SLM built specimen [129]

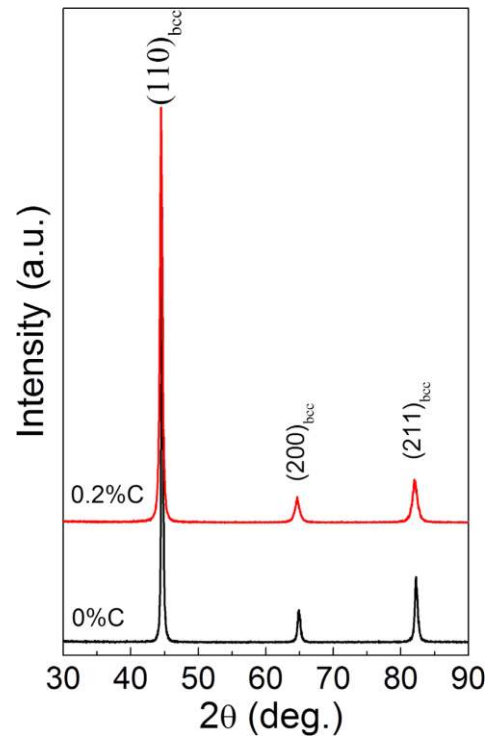


Figure 3.6 - XRD of quenched commercial low carbon steel [139]

3.3.3 Light Optical Microscopy

Figure 3.7 shows the micrographs of the SLM built specimen taken with light optical microscopy (LOM). Slight porosities could be observed, which were consistent to the density test results discussed earlier. No surface cracks were observed through LOM. The specimen was then etched using 3% nital and observed under LOM. The micrographs revealed distinct dark and light bands, as shown using the red dotted lines, indicating possible areas of different microstructural evolution.

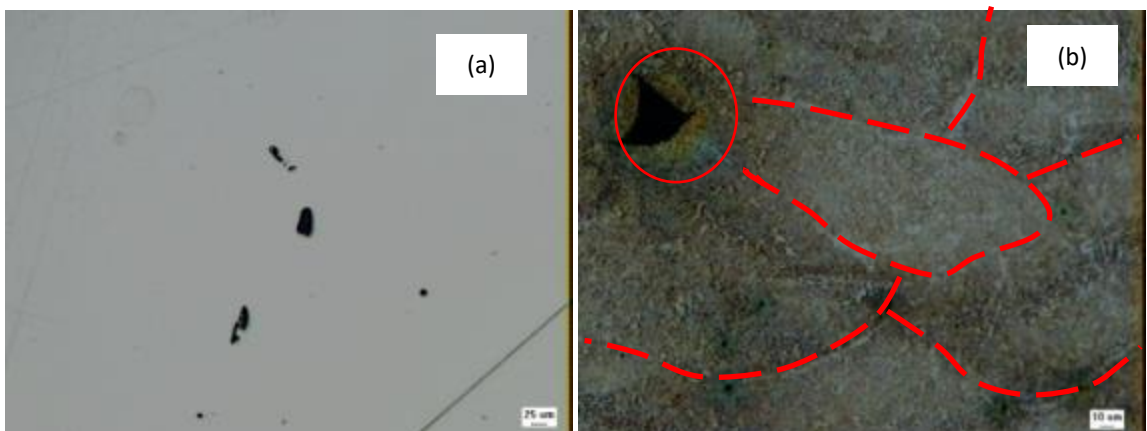


Figure 3.7 - (a) Image of unetched SLM built specimen showing slight porosities, (b) etched sample showing microstructure and porosity indicating incomplete melting of powder particle [129]

3.3.4 Scanning Electron Microscopy

The SLM built specimen was then observed under scanning electron microscopy (SEM). Figure 3.8 shows the micrographs obtained. In (a), 2 distinct zones were observed, where Zone A shows finer grains and Zone B shows coarser grains. This indicated a possible laser melt track along Zone A, where the higher energy intensity in the middle of the melt produced finer grain structure. This is a typical phenomena of SLM processed metals due to the overlapping effect of the laser scanning melt track [140]. (b) shows possible acicular martensitic structure in the SLM built specimen consistent with previous works conducted on SLM of steel [141]. A high magnification SEM image of such possible acicular martensitic microstructure is shown in Figure 3.9.

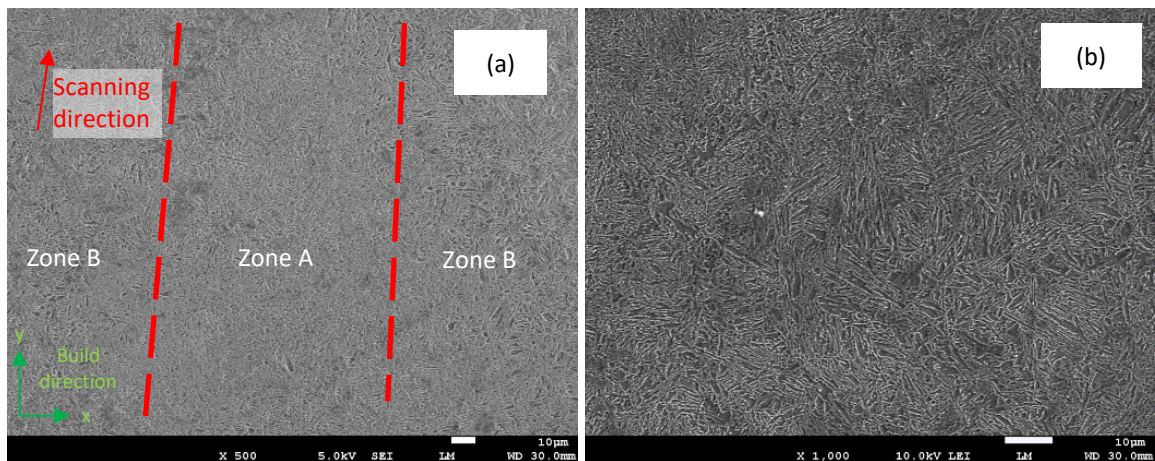


Figure 3.8 - SEM images of SLM built specimen showing (a) fine grains (Zone A) vs coarse grains (Zone B), (b) acicular martensitic structure [129]

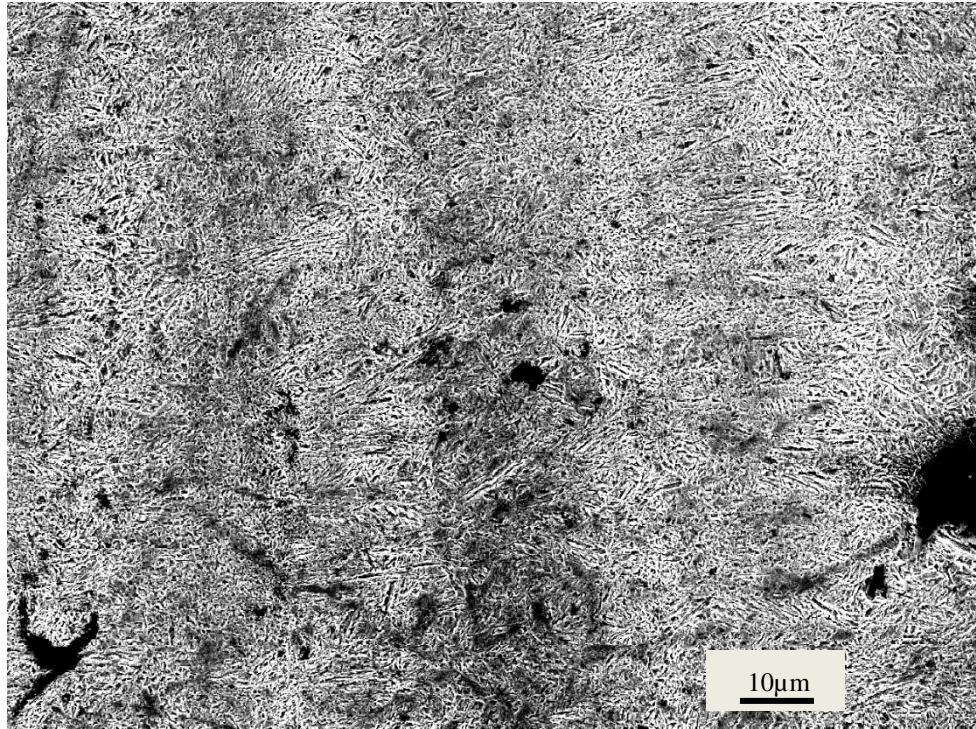


Figure 3.9 - High magnification SEM image of SLM built specimen showing acicular martensitic structure

3.4 Discussion

In the preliminary investigation of SLM of EH36 high tensile strength steel, parts were successfully produced with SLM without any cracks. The calculated CE content is 0.45%, which is more than the recommend 0.4% for welding applications without cracks (see Table 3.6). During common welding practices in shipbuilding, weldability of steels with CE contents of more than 0.4% is improved by performing heat passes before the weld, and during interim weld passes. In this preliminary investigation work, the parts were successfully produced with SLM without any cracks even though the CE content of 0.45% was more than the recommended 0.4%. This could be attributed to the preheating of the steel substrate plate to 100 °C to reduce the thermal gradients and thermal stresses experienced by the built specimens during the SLM process. It is also known that thermal gradients exist between the substrate plate and the top layer of the powder during SLM processes [142], hence, one of the reasons why the parts were successfully produced without cracks may also be due to the small number of layers of 100 (total height of 5mm at a layer thickness of 50µm) used in fabricating the specimens.

Table 3.6 - Weldability based on Carbon Equivalent (CE) Content

<u>Carbon equivalent (CE)</u>	<u>Weldability</u>
Up to 0.35	Excellent
0.36–0.40	Very good
0.41–0.45	Good
0.46–0.50	Fair
Over 0.50	Poor

The density results obtained in this investigation showed that parts with more than 97% of relative density could be fabricated. It has been shown in many studies that the higher the density of fabricated parts, the better the tensile and impact toughness properties [143, 144]. The relative density of 97% would mean that components fabricated using additive manufacturing may possess relatively good mechanical properties. However, more experiments to obtain actual values of mechanical properties

of EH36 components produced using additive manufacturing are required to ascertain this assumption.

From the XRD results, the peak positions for both sample powder and SLM built specimen are similar, indicating no change in phases after the SLM process, which suggests that the powder may be martensitic to begin with. This is true for gas atomised steel powder as demonstrated in the work by Gulsoy et al. in [145]. It can also be observed that there was no traces of austenite or carbide detected in the diffraction patterns, indicating a possible full martensitic microstructure formed during the SLM inherent rapid cooling process similar to that of quenching. This is consistent with the work done by Zhang et al. in [139], where XRD was used to inspect quenched commercial low carbon steel with 0.2%C and lath martensite was observed.

The micrographs also showed the possible formation of acicular martensitic structure in the SLM built parts, concurring with the results and observation from the XRD analysis. This is consistent with other reported works for steels built using SLM process [146, 147]. This means that the parts produced may exhibit properties similar to martensitic steel, which means high strength and hardness, but relatively low on the toughness values. Hence, heat treatment processes need to be developed to recover these mechanical properties.

3.5 Conclusion

- (1) The preliminary investigation suggested that SLM is capable of producing EH36 high tensile strength steel parts with a relative density of more than 97%, without visual and surface cracks. This was achieved at an energy density of 92 J/mm³ using parameters of 0.12 mm hatch spacing, power at 175W, 50 µm layer thickness and 320 mm/s laser scanning speed. The stainless steel substrate plate was preheated to 100 °C to reduce the thermal gradients and thermal stresses experienced by the specimens during the SLM process.
- (2) In the SLM fabrication of specimen pieces, slight irregularities in powder shape did not affect the SLM process and deposition.
- (3) The study also indicated the possibility of producing higher density EH36 parts as the energy density could be increased further.

- (4) Since the microstructure formed is preliminarily determined to be primarily martensitic in nature, it was thus suggested for more work to be performed to confirm, and thereafter develop a suitable heat treatment method to recover the mechanical properties.
- (5) It was also suggested to conduct more work to determine the mechanical properties of parts produced using SLM for EH36 high tensile strength steel.
- (6) This lays the foundation for future work of additive manufacturing of EH36, which will be important in establishing the technical feasibility of fabricating high tensile strength steel components for the shipbuilding industry.

Chapter Four Mechanical Tests

The preliminary investigation suggested that SLM is capable of producing EH36 parts with a relative density of more than 97%, without visual and surface cracks. Hence, the mechanical performance of SLM produced EH36 parts are next studied, namely tensile, impact toughness and hardness. In this mechanical performance study, the identified critical SLM process parameters from the preliminary investigation, including hatch spacing, laser power, layer thickness and scanning speed, were used to produce tensile and impact toughness test specimens. The hardness values are then obtained from the tensile test specimens. The results will facilitate future studies on SLM of shipbuilding steel.

4.1 Experimental

The material used in this study is from the same batch as the preliminary investigations. Hence, the powder characteristics are exactly similar. The machine used in this study is a SLM™ Solutions 280 HL SLM machine. Based on the results from the preliminary investigation, the Yb:YAG laser will be operating at 175W in continuous wave mode to produce the test specimens. The laser beam profile follows the Gaussian distribution and has a wavelength of 1.064 nm, with a focal diameter of 81 μm. The powder layer thickness was set at 50 μm. The stainless steel substrate plate was preheated to 100 °C to reduce the thermal gradients and thermal stresses experienced by the specimens during the SLM process. The scanning speed will be set to 320 mm/s and the hatch spacing will be set at 0.12 mm.

A total of 210 specimens were fabricated according to the configuration shown in Table 4.1. The dimensions of the test coupons are shown in Figure 4.1. The tensile test coupons were fabricated in 3 different positions, namely horizontal (XY plane), vertical (Z direction) and 45 degrees to the vertical (45°). The dimensions and test methods are in accordance to E8/E8M – 13a: Standard Test Methods for Tension Testing of Metallic Materials. For the horizontal specimens, two sets of tensile test coupons will be tested – the as built test coupons and the machined test coupons – to investigate the effect of machining on the tensile properties. The machined test coupons are printed with an additional layer of material all round with thickness 1.5mm.

The Charpy V-notched test coupons were fabricated in 3 positions, namely the notch facing upwards (Notch Up), sideways (Notch Side) or 45 degrees to the vertical (Notch 45°). The dimensions and test methods are in accordance to E23 – 12c: Standard Test Methods for Notched Bar Impact Testing of Metallic Materials. The notches are printed together with the specimens, instead of machined in afterwards. The Charpy tests will be conducted at both 0°C and -40°C. The various build orientations are illustrated in Figure 4.2. Three specimens are produced for each configuration and the average values from the tests will be taken.

The hardness test coupons are prepared from the tensile test coupons. The test methods are in accordance to E92 – 17: Standard Test Methods for Vickers Hardness and Knoop Hardness of Metallic Materials. The Vickers hardness values are measured.

Table 4.1 - Number of specimens for tensile and Charpy test

Test Coupons	Heat Treatment (°C)						
	Nil	205	315	425	540	650	800
Tensile Test Coupons (XY plane, Machined)	3	3	3	3	3	3	3
Tensile Test Coupons (XY plane, As-Built)	3	3	3	3	3	3	3
Tensile Test Coupons (Z direction)	3	3	3	3	3	3	3
Tensile Test Coupons (45°)	3	3	3	3	3	3	3
Charpy Test Coupons (Notch Up), 0 °C	3	3	3	3	3	3	3
Charpy Test Coupons (Notch Side), 0 °C	3	3	3	3	3	3	3
Charpy Test Coupons (Notch 45°), 0 °C	3	3	3	3	3	3	3
Charpy Test Coupons (Notch Up), -40 °C	3	3	3	3	3	3	3
Charpy Test Coupons (Notch Side), -40 °C	3	3	3	3	3	3	3
Charpy Test Coupons (Notch 45°), -40 °C	3	3	3	3	3	3	3

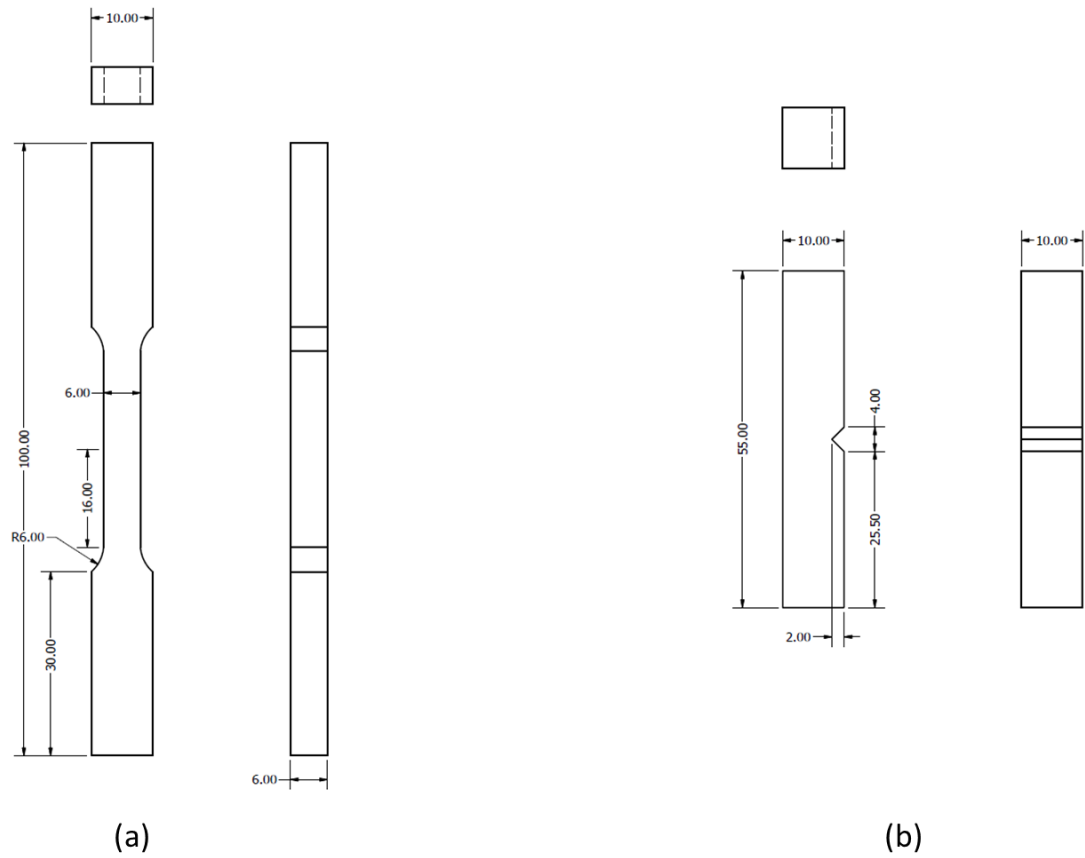


Figure 4.1 - Dimensions of SLM built test coupons (a) tensile test coupons, (b) Charpy test coupons

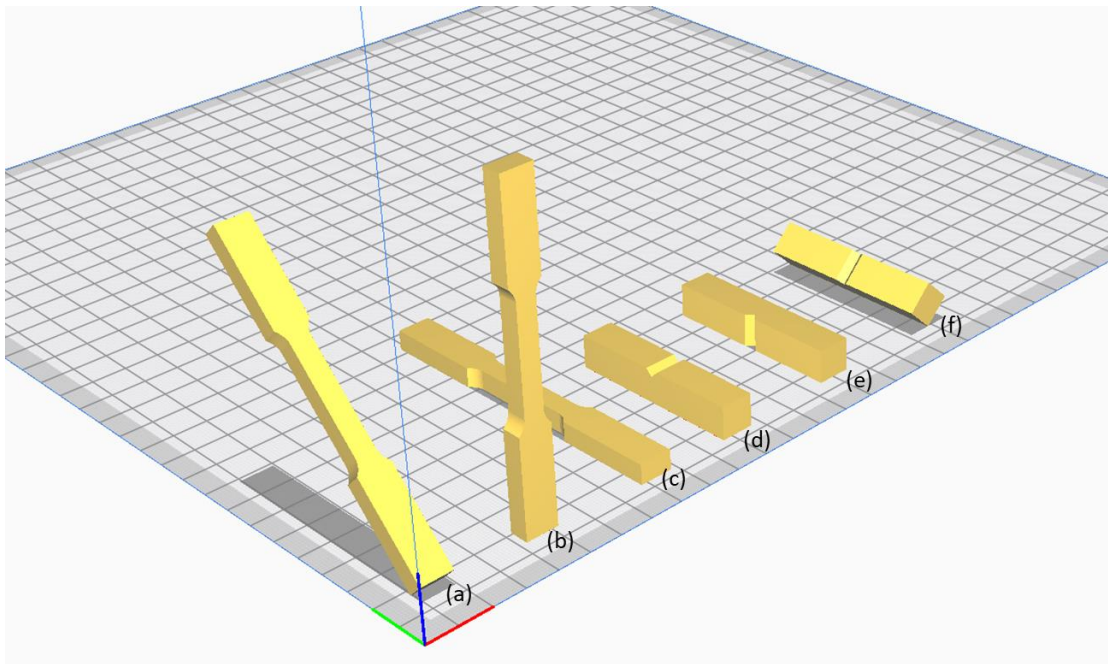


Figure 4.2 - SLM test coupon orientations (a) tensile test coupon, 45°; (b) tensile test coupon, vertical; (c) tensile test coupon, horizontal; (d) Charpy test coupon, notch facing up; (e) Charpy test coupon, notch facing side; (f) Charpy test coupon, notch facing 45°

4.2 Heat Treatment

As discussed in Chapter 2.3.4, SLM of steel produces martensitic microstructure, and this is also shown in the preliminary investigations in Chapter 3.3.3. Although the martensite structure is thermodynamically unstable (see discussion in Chapter 2.1.1.2), the steel will remain in this condition more or less indefinitely at room temperature because for a change to take place bulk diffusion of carbon, with an activation energy Q of approximately 83 kJ mol^{-1} atom, is necessary [25]. The presence of martensite in a quenched steel, while greatly increasing its hardness and tensile strength, causes the material to be brittle. The hardness and strength of martensite increase sharply with increase in C content. Contributions to the strength arise from the carbon in solution, carbides precipitated during the quench, dislocations introduced during the transformation and the grain size. Thus, by a carefully controlled tempering treatment, the quenching stresses can be relieved and some of the carbon can precipitate from the supersaturated solid solution to form a finely dispersed carbide phase. In this way, the toughness of the steel can be vastly improved with very little detriment to its hardness and tensile properties.

A tempering heat treatment process is applied to obtain a preliminary understanding of the behaviour of EH36 steel after post process heat treatment. For each of the configuration of the test coupons, six temperatures of heat treatment are applied, with the seventh specimen receiving no heat treatment, which is it will be tested as-built. The samples received heat treatment in a non-inert gas atmosphere heat furnace (see Table 4.3). The target temperatures selected for this heat treatment investigation (see Table 4.2) are based on industry guidelines from ASM International for tempering of steels [148]. The maximum target temperature was purposely kept below the material's eutectoid temperature to prevent recrystallisation. With reference to the Fe-C phase diagram shown in Figure 2.1, it is expected that spheroidisation will be observed in specimens which underwent heat treatment of $650 \text{ }^{\circ}\text{C}$ and above.

The heat treatment process is as follows:

1. Heat to target temperature at rate of 100⁰C/Hr
2. Hold for 2 hours
3. Chamber cool to room temperature

Table 4.2 - ASM International recommended temperatures for tempering of steel [148]

Fahrenheit (°F)	Degrees Celsius (°C)
400	205
600	315
800	425
1000	540
1200	650
1470	800

Table 4.3 - Heat furnace details

Model	ThermConcept KL 15/13
Operating Parameters:	
Max Temperature	1340 °C
Protective Gas Connection	Nil
Dimensions (mm) Width x Depth x Height	250 x 340 x 170

4.3 Results

The SLM fabricated test coupons were observed to have no visible cracks, but this is expected because the process parameters and powder used are exactly the same as in the preliminary investigation, where the results showed that SLM is capable of producing EH36 parts with a relative density of more than 97%, without visible surface

cracks. Figure 4.3 shows the SLM built test coupons. The parts are built on the build plate, shown in (a), and removed via wire-cut electrical discharge machining (EDM) and put through heat treatment. The tensile test coupons in (b) and Charpy test coupons in (c) both showed discolouration after heat treatment.

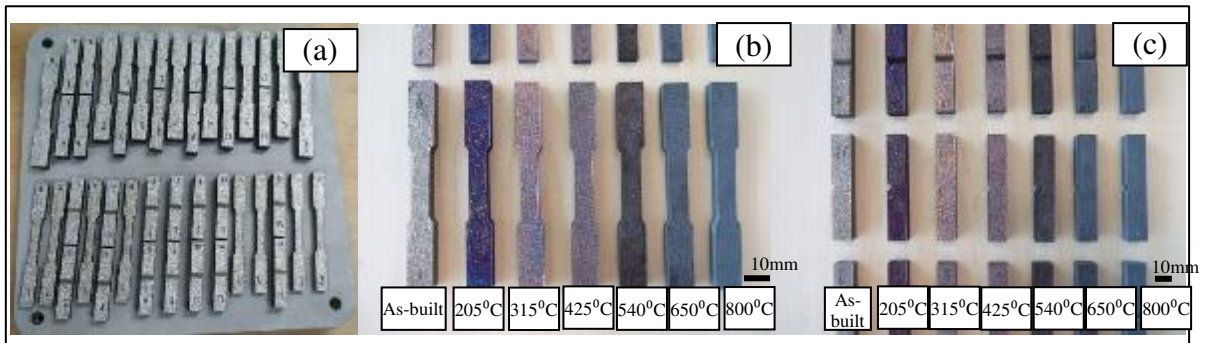


Figure 4.3 - SLM built test coupons. (a) As-built on build plate; (b) Tensile test coupons following heat treatment; (c) Charpy test coupons following heat treatment

4.3.1 Tensile Strength

The tensile test methods are in accordance to E8/E8M – 13a: Standard Test Methods for Tension Testing of Metallic Materials, on a Universal Testing Machine, Instron Model 8801. The yield strength (0.2% offset) and ultimate tensile strength are obtained, as well as the elongation which will be shown in Chapter 4.3.2. The results of the tensile tests are shown in Table 4.4, Figure 4.4 and Figure 4.5. Figure 4.6 to Figure 4.13 show the individual tensile results with error bars, which show the precision of the measured tensile properties. A traditionally manufactured coupon is also inserted as reference data. The highest tensile yield strength of 1030 MPa is obtained at the machined condition fabricated along the XY plane. The highest ultimate tensile strength of 1057 MPa is obtained at the machined condition with post-processing heat treatment of 205°C, fabricated along the XY plane. This far exceeded the requirements stipulated in the ASTM A131 standards, where the yield strength required is 355 MPa and the ultimate tensile strength is 490 MPa.

Z direction built coupons generally have poorer tensile properties while coupons built in the XY plane and the 45° directions exhibit generally similar tensile properties. Machined coupons generally perform slightly better in terms of the tensile properties.

For the yield strength, as built 45°, XY plane and machined coupons perform 32%, 26% and 34% respectively better than the z direction built coupons. For the ultimate tensile strength, as built 45°, XY plane and machined coupons perform 36%, 35% and 36% respectively better than the z direction built coupons. As the temperature for the heat treatment increases, it can be observed that both the yield strength and ultimate tensile strength decreases slightly, by up to 20% (or 170MPa) from 205°C to 540°C, but especially drastically after 540°C, with a reduction of 20% to 40% (or 385MPa) for the 650°C coupons and 50% to 65% (or 648MPa) for the 800°C coupons. Compared against the ASTM A131 standards, results from all temperatures of heat treatment meet the requirements, except at 800°C, where the yield strength and ultimate tensile strength do not meet the standards.

Table 4.4 - Table of tensile test results for SLM built samples

Test Coupons		Heat Treatment (°C)						
		Nil	205	315	425	540	650	800
Yield Strength (MPa)	Tensile Test Coupons (XY, Machined)	1030	996	960	980	967	645	382
	Tensile Test Coupons (XY, As-Built)	966	972	901	952	934	670	341
	Tensile Test Coupons (Z)	767	618	599	654	733	629	311
	Tensile Test Coupons (45°)	1011	1027	1037	923	1007	759	393
	ASTM A131 Standards	355						
Ultimate Tensile Strength (MPa)	Tensile Test Coupons (XY, Machined)	1054	1057	1008	988	988	734	522
	Tensile Test Coupons (XY, As-Built)	1045	1026	895	993	977	736	448
	Tensile Test Coupons (Z)	775	708	614	745	748	681	334
	Tensile Test Coupons (45°)	1054	984	981	927	1049	835	499
	ASTM A131 Standards	490 - 690						

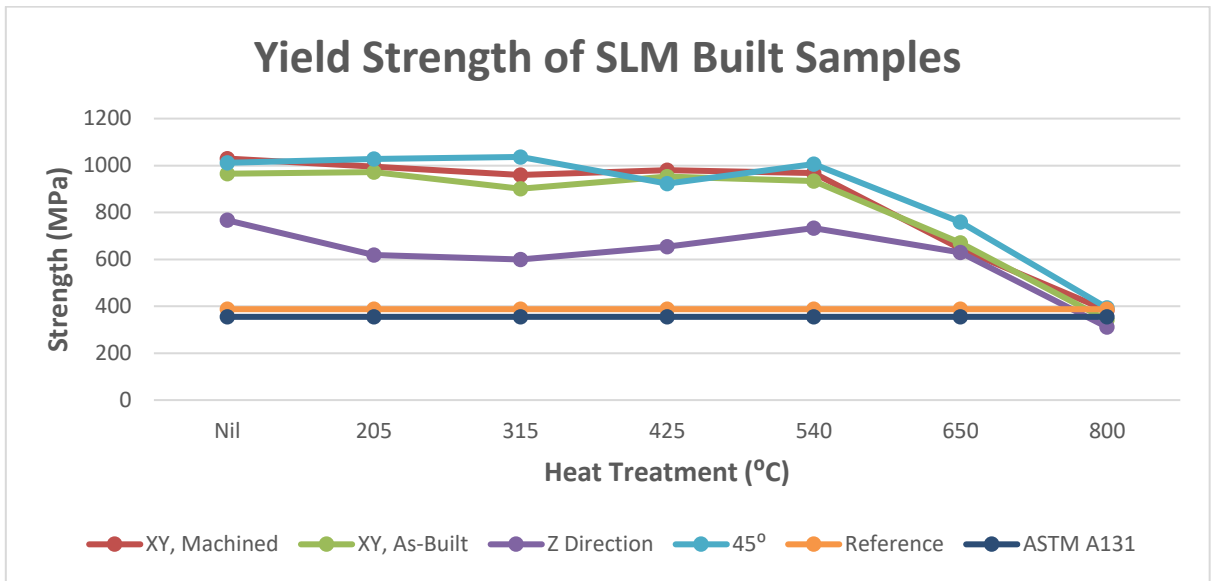


Figure 4.4 - Graph of tensile test results (Yield Strength) for SLM built samples

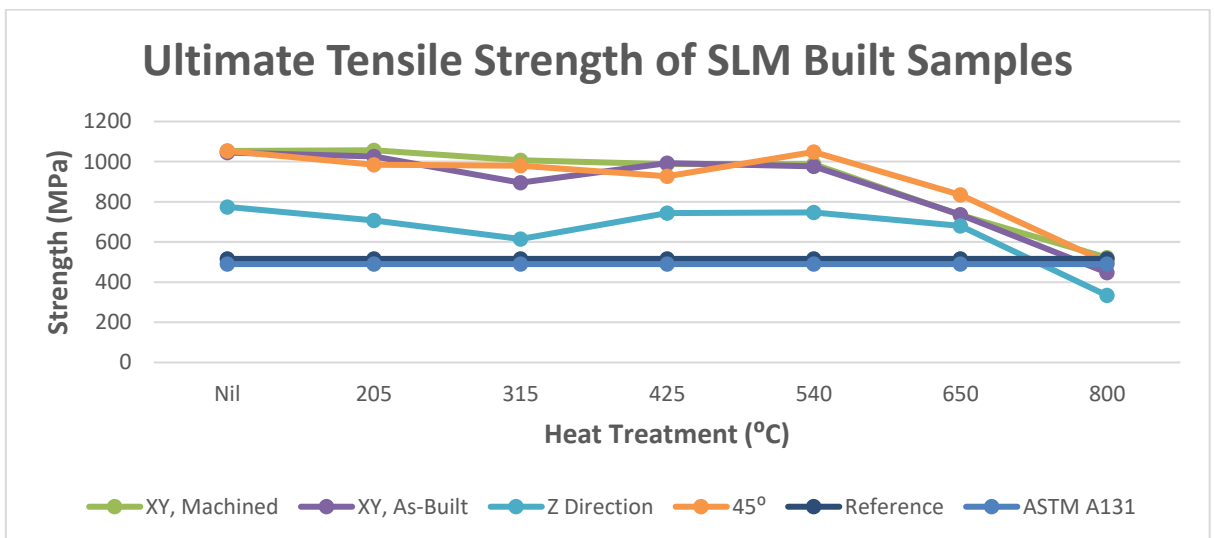


Figure 4.5 - Graph of tensile test results (Ultimate Tensile Strength) for SLM built samples

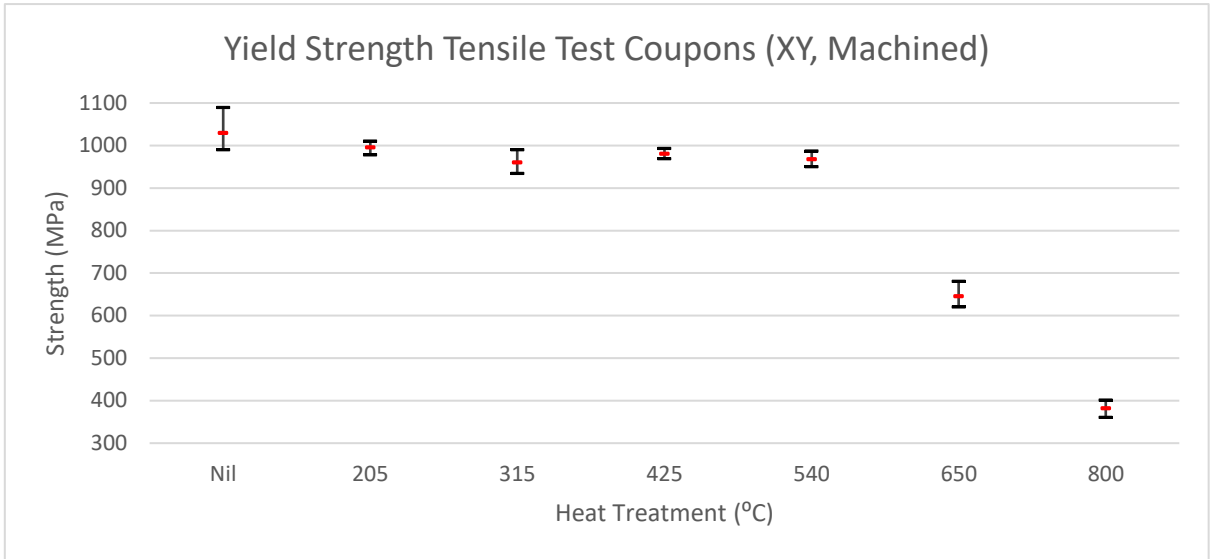


Figure 4.6 - Graph of Yield Strength (XY, Machined) with error bar

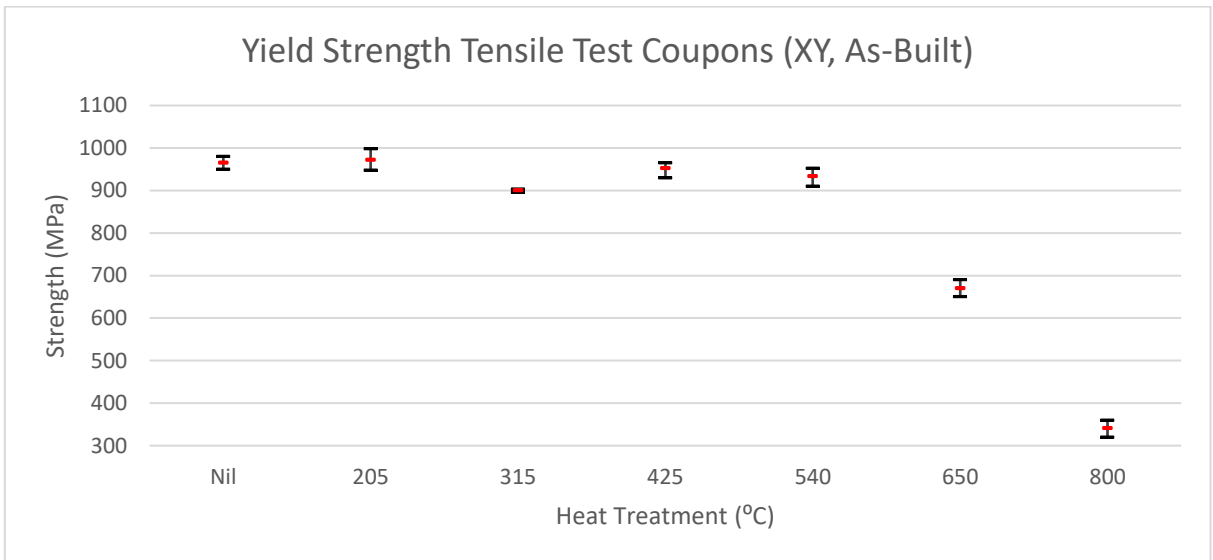


Figure 4.7 - Graph of Yield Strength (XY, As-built) with error bar

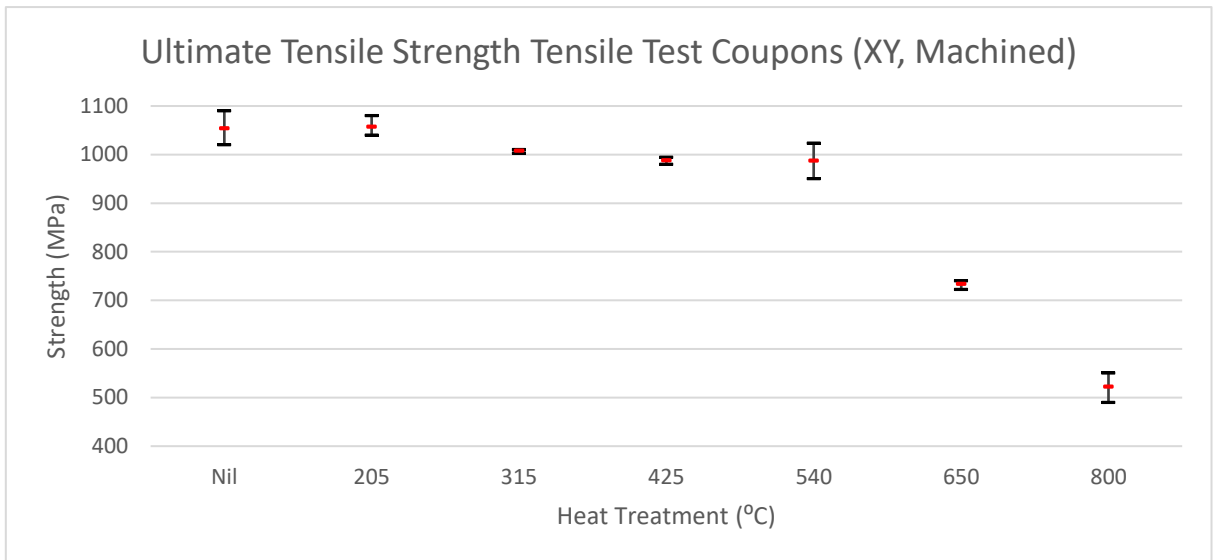


Figure 4.8 - Graph of Ultimate Tensile Strength (XY, Machined) with error bar

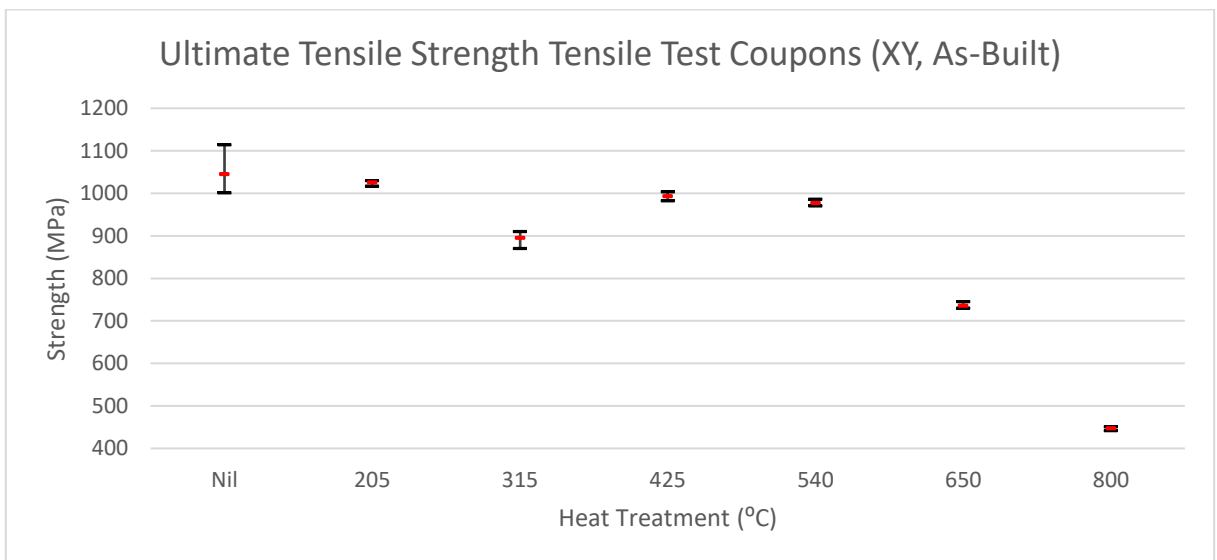


Figure 4.9 - Graph of Ultimate Tensile Strength (XY, As-built) with error bar

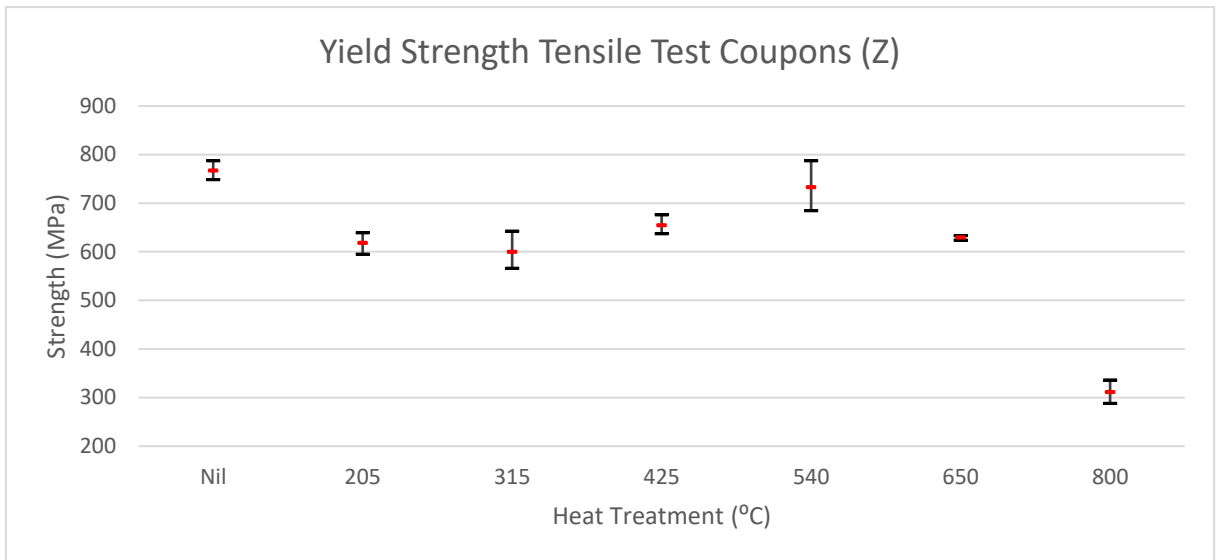


Figure 4.10- Graph of Yield Strength (Z) with error bar

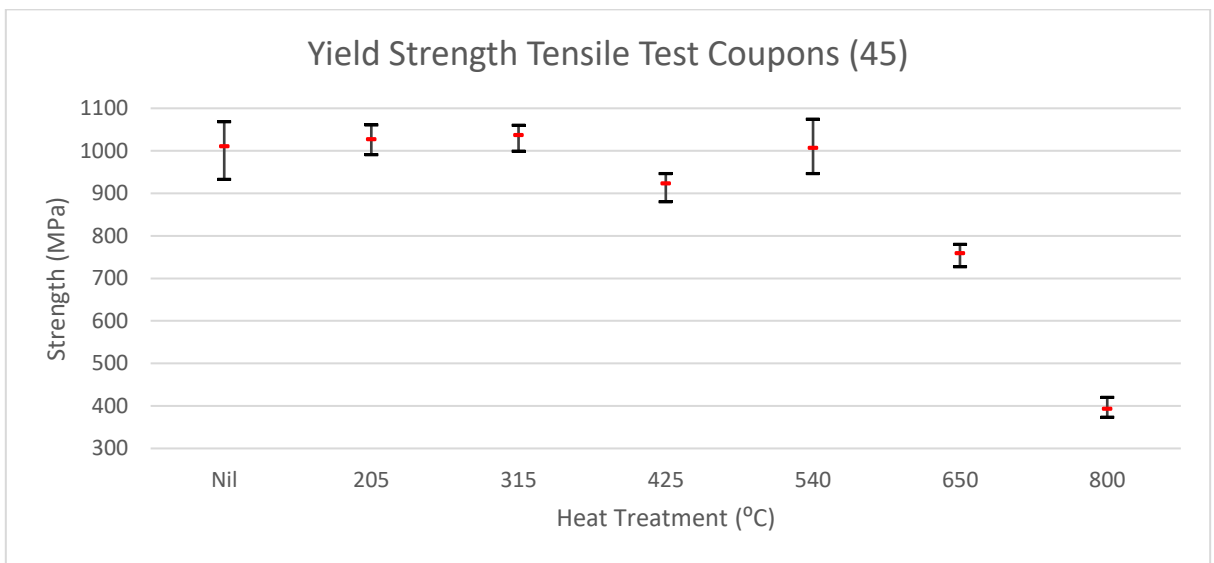


Figure 4.11 - Graph of Yield Strength (45°) with error bar

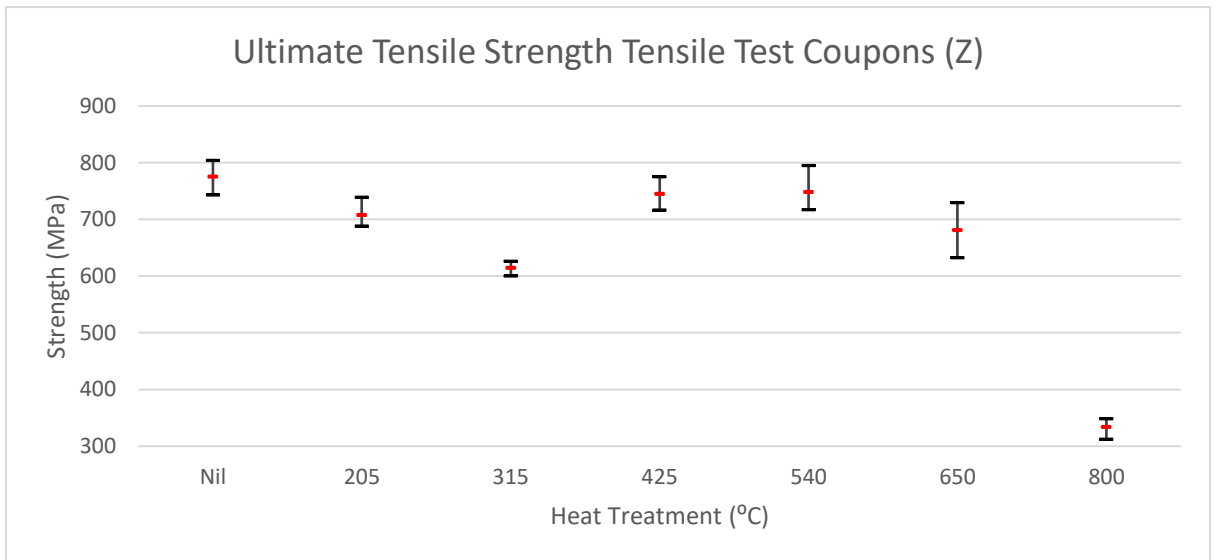


Figure 4.12- Graph of Ultimate Tensile Strength (Z) with error bar

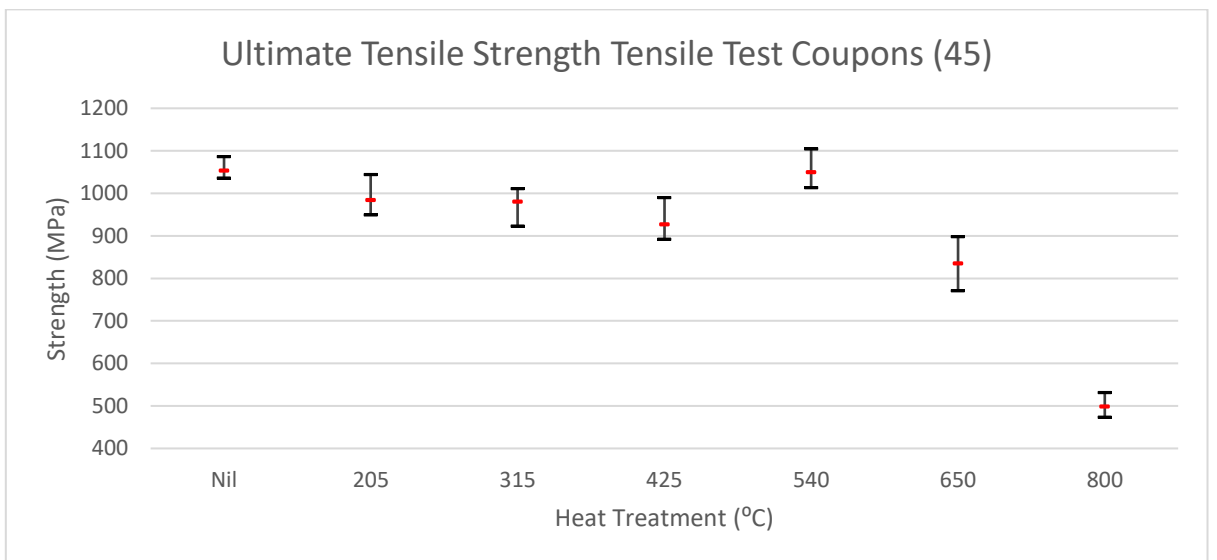


Figure 4.13 - Graph of Ultimate Yield Strength (45°) with error bar

4.3.2 Elongation

The results of the elongation values are shown in Table 4.5 and Figure 4.14. Figure 4.15 to Figure 4.18 show the individual elongation results with error bars. Except for the coupons built in the 45° direction, the rest of the as-built coupons without post-process heat treatment have low elongation values of less than 6%. Heat treatment with

temperatures up to 540⁰C show little or no significant improvement to the elongation values. At 650⁰C, elongation values for all coupons show significant improvement to as high as 23.3% in the 45⁰ coupons. At 800⁰C, the elongation values improved even more significantly to 25.3% for XY machined coupons, 29% for XY as-built coupons, and 37.3% in the 45⁰ coupons. The coupons built in the Z direction performed relatively poorly regardless of heat treatment. Compared to the ASTM A131 standards of elongation value at 22%, the 45⁰ coupons meet the requirements at 650⁰C heat treatment, while the XY machined and the XY as-built coupons will require a heat treatment of up to 800⁰C.

Table 4.5 - Table of elongation results for SLM built samples

Test Coupons		Heat Treatment (°C)						
		Nil	205	315	425	540	650	800
Elongation, L ₀ = 4d (%)	Tensile Test Coupons (XY, Machined)	3.3	5.8	4.3	6.2	5.2	12.3	25.3
	Tensile Test Coupons (XY, As-Built)	4.4	3.6	2.8	4.4	5.7	10.1	29.0
	Tensile Test Coupons (Z)	5.1	4.9	2.1	6.2	4.7	5.1	8.0
	Tensile Test Coupons (45 ⁰)	13.2	12.3	14.8	12.1	16.2	23.3	37.3
	ASTM A131 Standards	22						

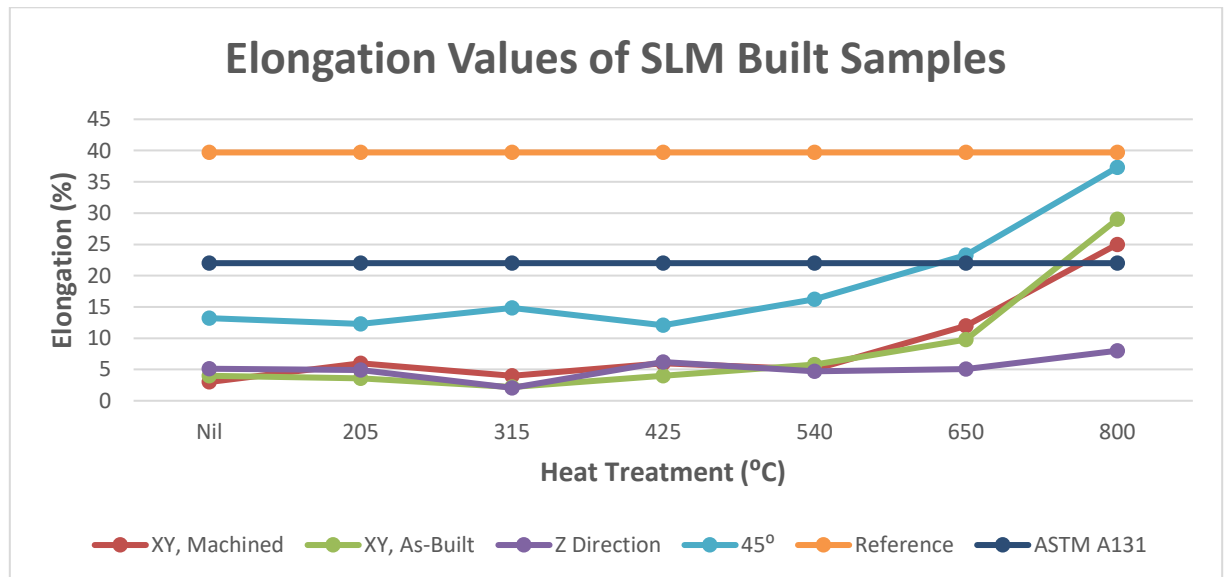


Figure 4.14 - Graph of elongation results for SLM built samples

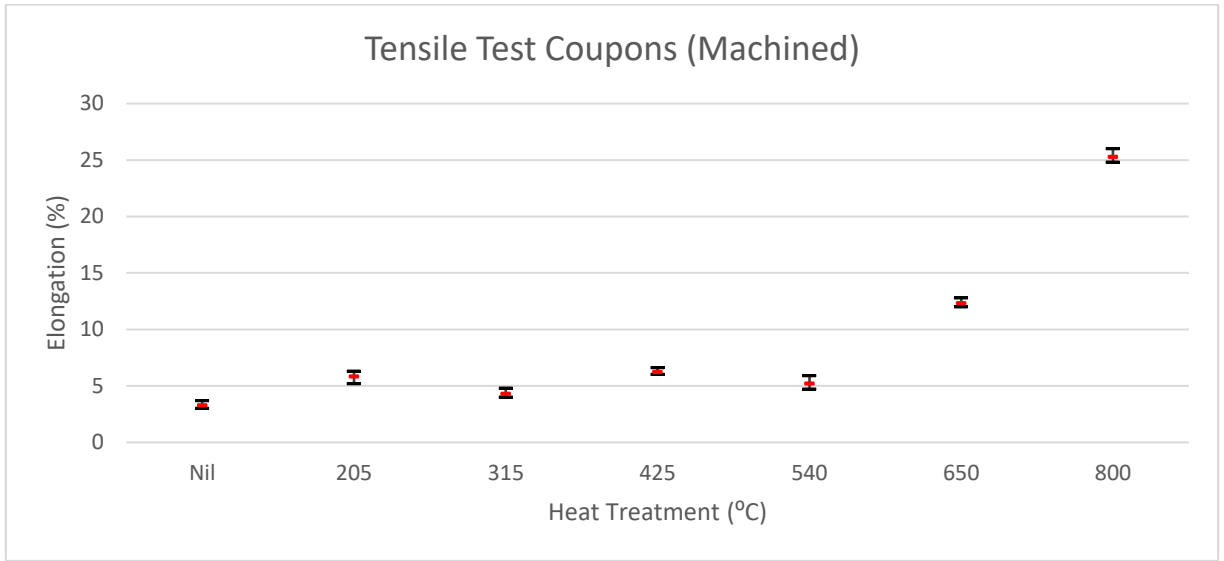


Figure 4.15 - Graph of elongation results (XY, machined) with error bar

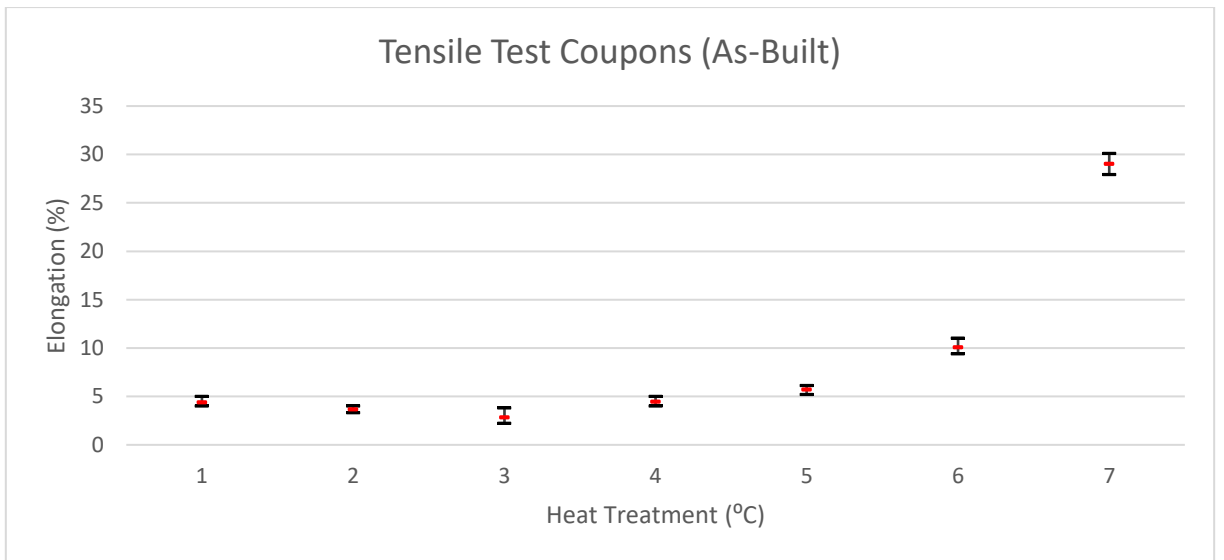


Figure 4.16 - Graph of elongation results (XY, As-Built) with error bar

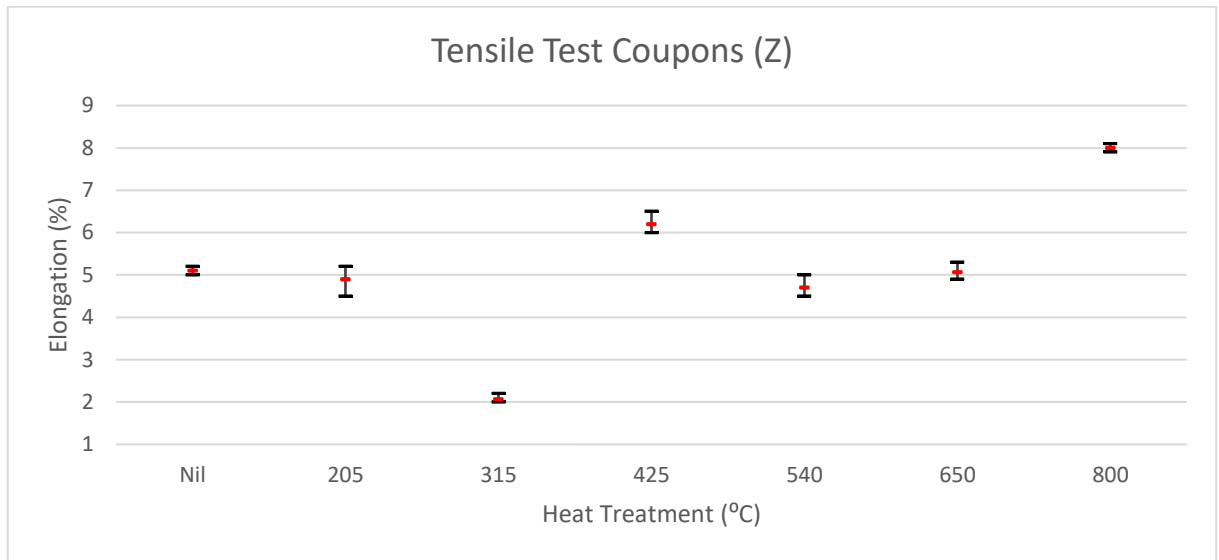


Figure 4.17 - Graph of elongation results (Z) with error bar

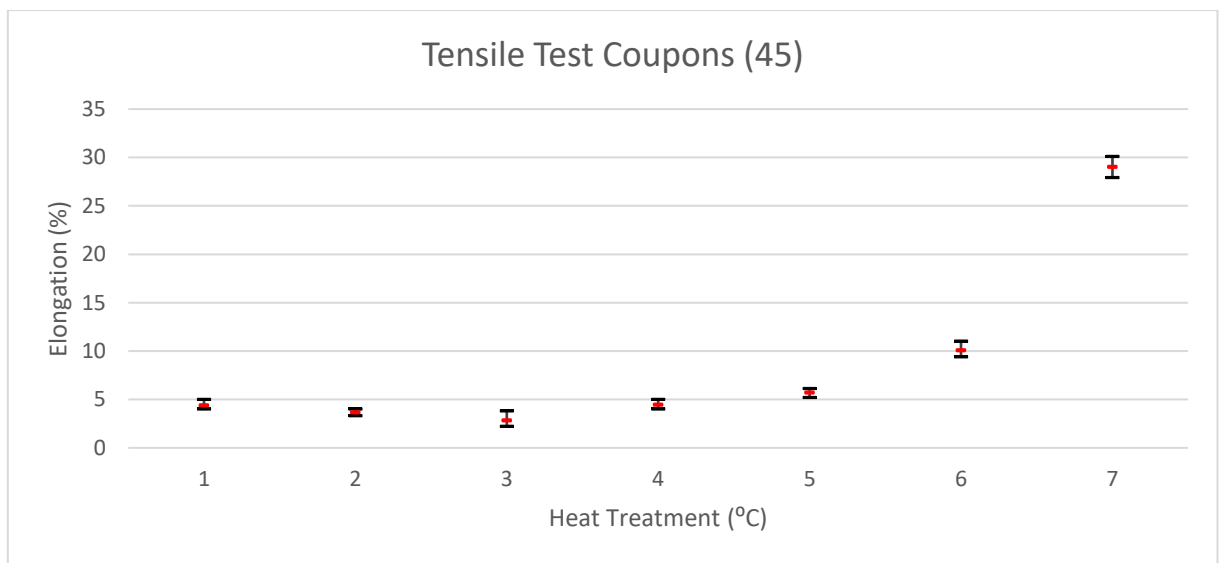


Figure 4.18 - Graph of elongation results (45°) with error bar

4.3.3 Charpy V-Notched Impact Toughness

The test methods are in accordance to E23 – 12c: Standard Test Methods for Notched Bar Impact Testing of Metallic Materials, on a Zwick Impact Machine. The results of the Charpy V-notched impact toughness tests are shown in Table 4.6 and Figure 4.19 and Figure 4.20. Figure 4.21 to Figure 4.26 show the individual Charpy

results with error bars. For the non-heat treated test coupons, the Charpy values built with notches facing up and to the side are relatively lower at 28J and 25J for Charpy tests conducted at 0°C and -40°C respectively, and the Charpy values built with notches facing 45° are relatively higher at 46J and 44J for Charpy tests conducted at 0°C and -40°C respectively. The Charpy values for all types of coupons remain about their respective ranges as the temperatures for heat treatment increases, until about 540°C. The Charpy values increase significantly after 540°C. At 650°C heat treatment temperature, the Charpy values for both the test coupons built with the notches facing the sides and facing 45° have values beyond the required 34J at both 0°C and -40°C testing temperatures, ranging from 32J to 89J. In general, the Charpy values of coupons built with notches facing 45° are almost twice as high as those built with the notch facing up or to the side. The maximum results of approximately 89J for Charpy coupons built with notches facing 45° occurs at a heat treatment temperature of 800°C.

Concluding the results from Charpy tests, compared against the ASTM A131 standards which has a requirement of 34J at both 0°C and -40°C, test coupons built with the notches facing the sides met the requirements with heat treatment at 650°C and 800°C, while for test coupons built with notches facing the top, only the results with heat treatment at 800°C meets the requirements. For test coupons with notches facing 45°, all the results from non-heat treated to all heat treated coupons met the requirements.

Table 4.6 – Table of Charpy test results for SLM built samples

Test Coupons		Heat Treatment (°C)						
		Nil	205	315	425	540	650	800
Energy (J)	Charpy Test Coupons (Notch Up), 0 °C	28.3	27.3	27.7	28.7	35.7	32.7	56.3
	Charpy Test Coupons (Notch Side), 0 °C	28.3	30.3	27.0	28.3	25.3	38.7	83.3
	Charpy Test Coupons (Notch 45°), 0 °C	46.3	48.7	47.7	48.0	48.0	64.0	89.0
	ASTM A131 Standards, 0 °C	34						
	Charpy Test Coupons (Notch Up), -40 °C	24.7	26.3	24.7	21.7	27.7	33.3	48.3
	Charpy Test Coupons (Notch Side), -40 °C	25.0	28.0	29.3	24.0	28.0	35.7	49.0
	Charpy Test Coupons (Notch 45°), -40 °C	44.7	46.0	51.7	47.8	46.3	62.5	89.2
	ASTM A131 Standards, -40 °C	34						

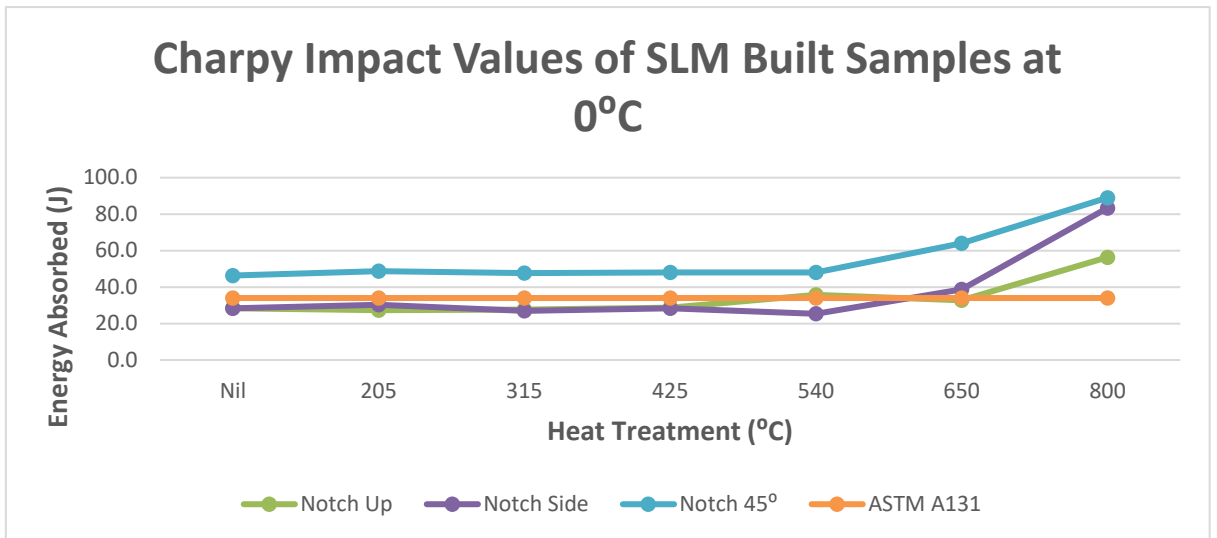


Figure 4.19 – Graph of Charpy test results for SLM built samples at 0°C

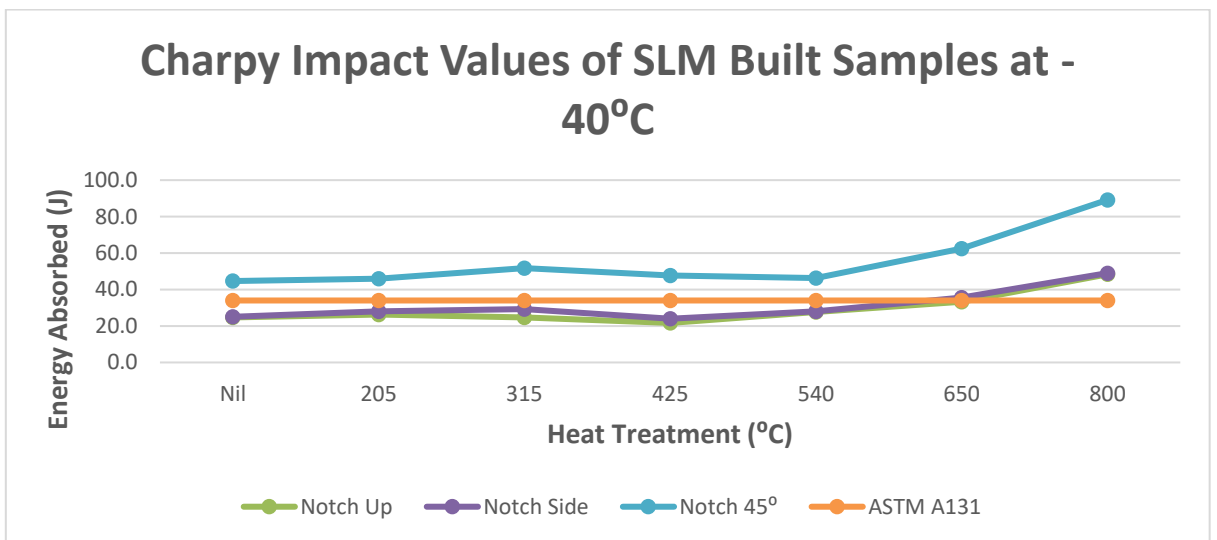


Figure 4.20 – Graph of Charpy test results for SLM built samples at -40°C

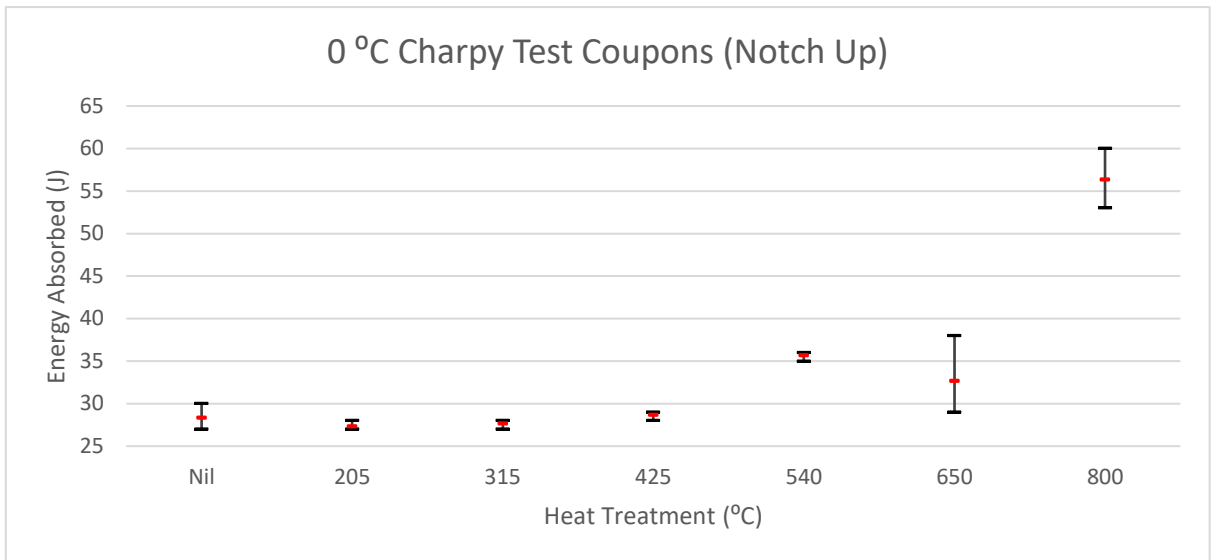


Figure 4.21 – Graph of Charpy test results (Notch Up) at 0°C with error bar

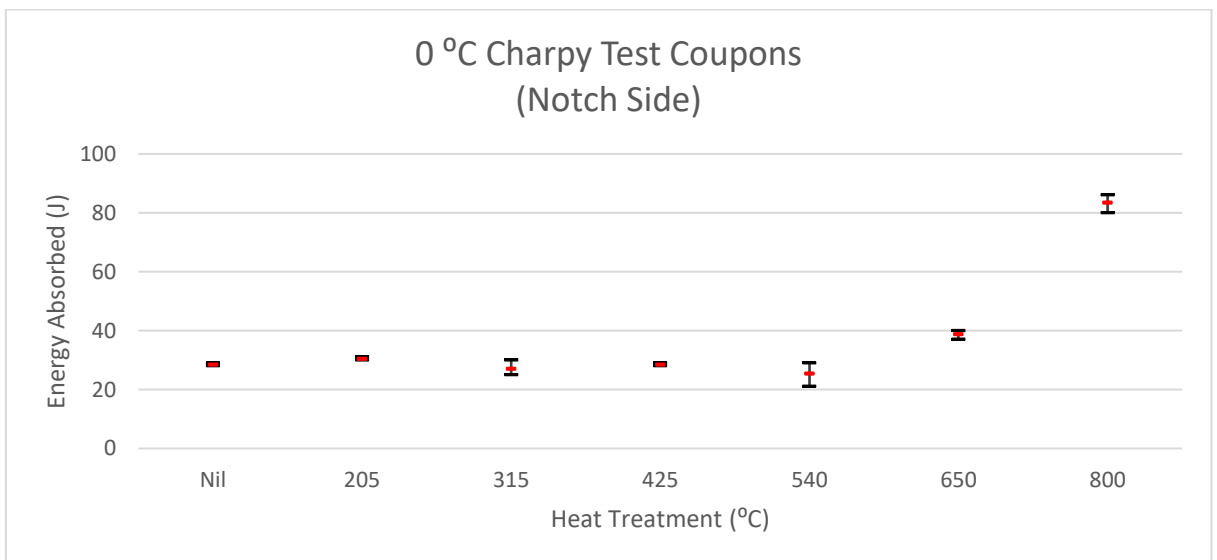


Figure 4.22 – Graph of Charpy test results (Notch Side) at 0°C with error bar

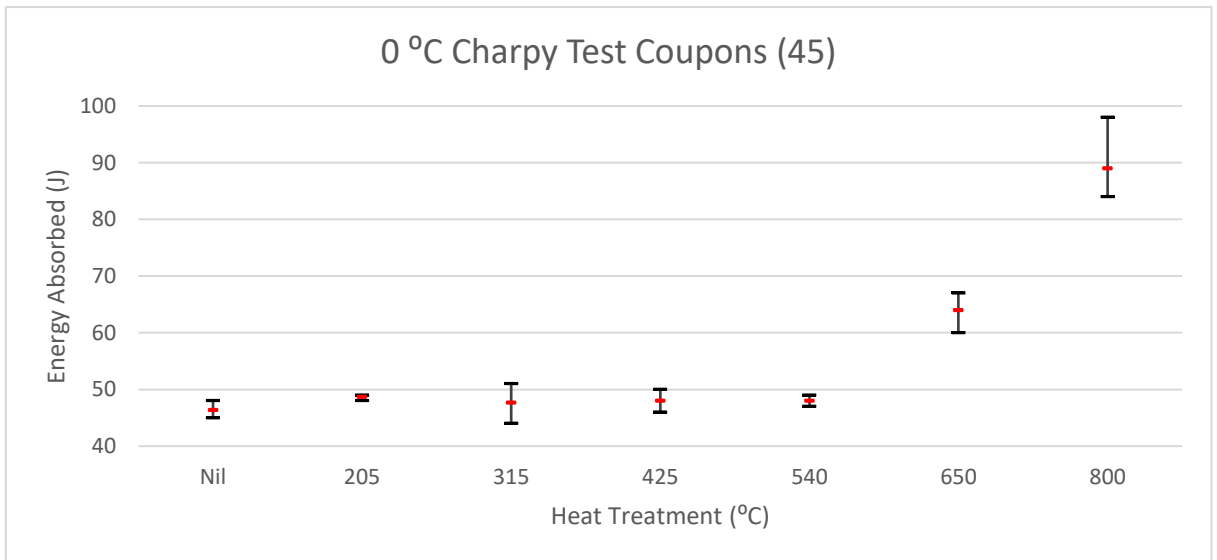


Figure 4.23 – Graph of Charpy test results (Notch 45°) at 0°C with error bar

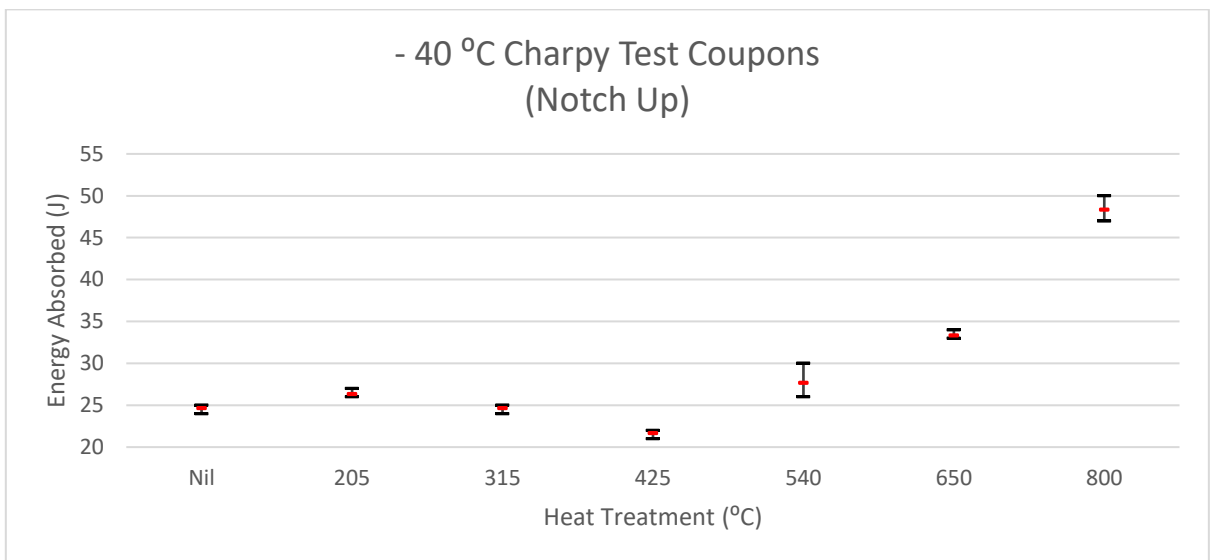


Figure 4.24 – Graph of Charpy test results (Notch Up) at -40°C with error bar

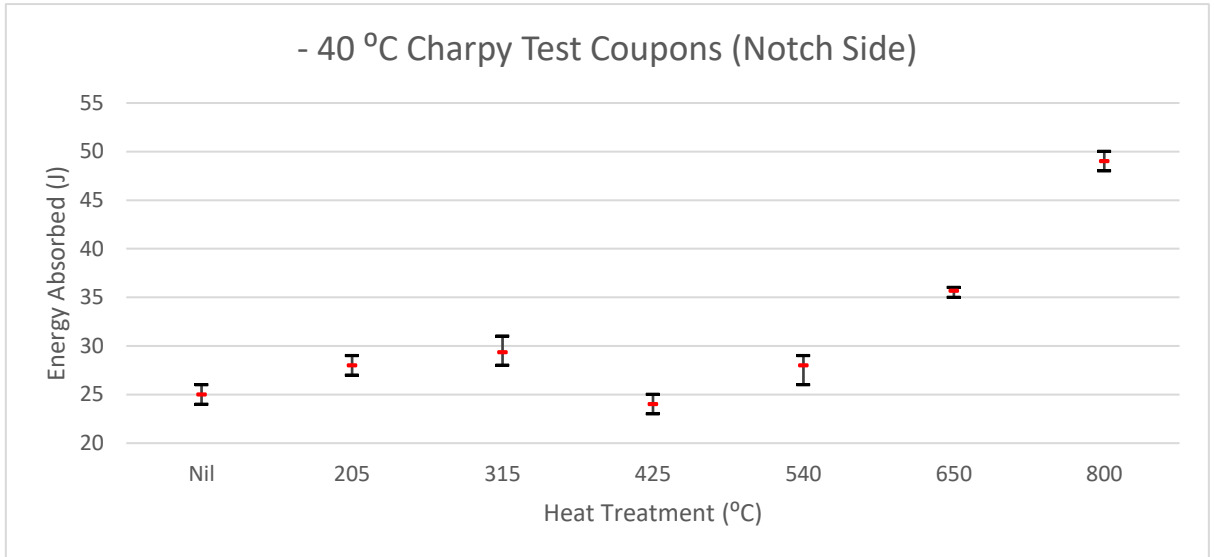


Figure 4.25 – Graph of Charpy test results (Notch Side) at -40°C with error bar

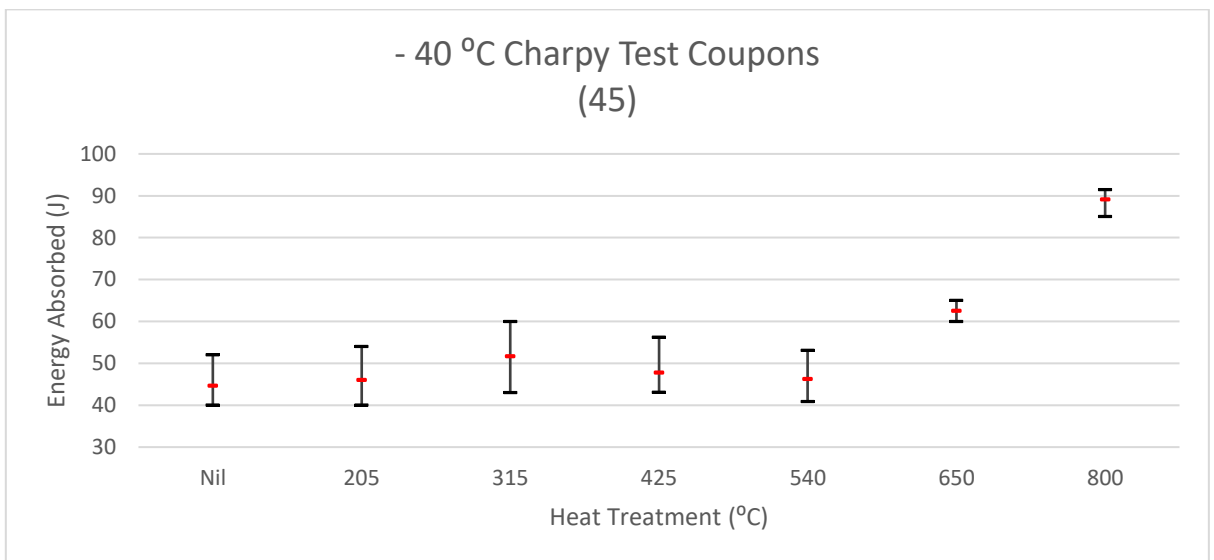


Figure 4.26 – Graph of Charpy test results (Notch 45°) at -40°C with error bar

4.3.4 Vickers Hardness

The test methods are in accordance to E92 – 17: Standard Test Methods for Vickers Hardness and Knoop Hardness of Metallic Materials, on a Future-Tech Microhardness Tester FM-300e. Vickers hardness measurements were made with a low-load hardness tester at load level of 300g and at a constant indenter dwell time of 15s.

All indentation tests were carried under ambient laboratory conditions. After indentation, the length of each of the two diagonals of the square-shaped Vickers indentation was immediately measured by optical microscopy with a magnification of 500 and an error of measurement of $\pm 0.01 \mu\text{m}$. The Vickers hardness numbers, H_v , for the specimens are listed in Table 4.7. Each of the data points represents an average of measurements from at least five tests.

The Vickers hardness numbers are generally high at about 350 to 370 for the as-built and samples with heat treatment of up to 540 °C. The value decreases from 650 °C, and decrease further at 800 °C. Vickers hardness values are not a requirement in the ASTM A131 standards for EH36, but it will be used to ascertain martensitic microstructure in the discussions.

Table 4.7 – Table of Vickers hardness values for SLM built samples

Test Coupons	Heat Treatment (°C)						
	Nil	205	315	425	540	650	800
H_v	352	372	353	355	369	252	200

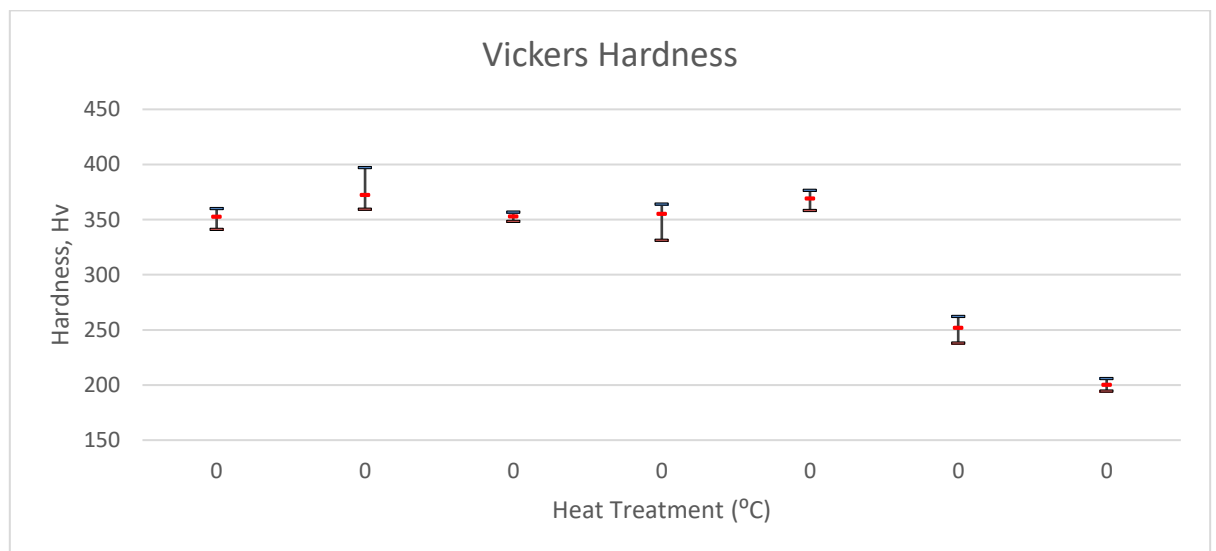


Figure 4.27 – Graph of Vickers hardness numbers (test coupons)

4.4 Discussion

The SLM built test coupons were fabricated using the process parameters from the previous preliminary investigation, hence they were successfully built without visible surface cracks. The as-built tensile values obtained are relatively higher than the requirements stated in ASTM A131 (based on casting), with the test coupons built in the 45°, XY as-built and XY machined having about 25%-36% higher tensile values than the coupons built in the z-direction. These equate to an approximately 200-280 increase in MPa. Maximum yield strength is at 1030 MPa and maximum ultimate tensile strength is at 1054 MPa. Elongation values are lower than requirements stated in ASTM A131, measuring between 3.3% to 5.1% for the XY machined, XY as-built and z-direction coupons, and 13.2% for the 45° coupons. Even at 13.2% elongation, this is only about 60% of the ASTM A131 requirements of 22%. The as-built Charpy values are generally lower than the requirements of 34J as stated in ASTM A131, at about 24J to 28J, except for those built with the notch facing 45° which measures about 44J to 46J.

This characteristics of SLM built steels having high tensile strength and low ductility performance is consistent with the results obtained from other studies [54, 83]. Based on the preliminary investigation, the microstructure of the SLM built specimens exhibit martensitic-like characteristics, which explains the high strength and low ductility performance [149]. This is consistent with previous discussions in Chapter 2.1.1.2, as the SLM process creates a very rapid cooling of the EH36 built specimens by staying on the left of the TTT curve (see Figure 2.2). This is also further evidenced in the high Vickers hardness numbers consistent with that of low carbon steel with as-quenched martensitic microstructure [150], where Vickers hardness values are in the range of 300 to 400 for low carbon steel (see Figure 4.28).

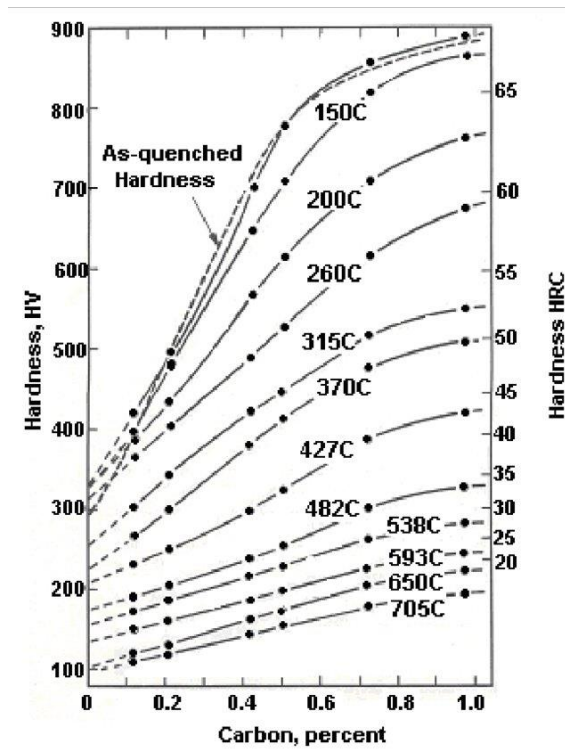


Figure 4.28 - Hardness of tempered martensite in iron-carbon (Fe-C) steel [150]

However, Zhao et al. has shown that an optimised heat treatment process may improve impact toughness performance by up to 50% [151]. In the work, a novel heat-treatment process was performed on two low-C high-Si/Al steels, and effectively reduces the size and volume fraction of blocky martensite/austenite phases, giving rise to much enhanced impact toughness and improved tensile properties. The preliminary tempering heat treatment process developed in this study showed results consistent with that of the study conducted by Zhao et al., where the Charpy values in this study significantly improved at heat treatment temperatures of more than 540⁰C.

The structural changes which occur on tempering may be considered to take place in three stages. In the primary stage, fine particles of iron carbides precipitates, with the corresponding formation of low-carbon martensite. This low-carbon martensite grows at the expense of the high-carbon martensite, and causes a loss of tetragonality in martensite. This usually occurs between room temperature and 250⁰C. During the second stage any retained austenite in the steel begins to decompose, usually in the temperature range of 230-300⁰C. However, the direct observation of retained austenite in the microstructure has always been rather difficult, particularly if it is present in low

concentrations. The little available evidence suggests that in the range 230-300°C, retained austenite decomposes to bainite, ferrite and cementite, but there is almost no literature on detailed comparison between this phase and lower bainite. The third stage is marked by the formation of cementite platelets. During tempering, transition carbides and low-temperature martensite are replaced by cementite and ferrite. The degree to which these three stages overlap will be affected by the temperature and the carbon content. [25]

At temperatures beyond the third stage, the cementite particles undergo a coarsening process and essentially lose their crystallographic morphology, becoming spheroidized. The coarsening commences between 300 and 400°C, while spheroidization takes place increasingly up to 700°C. At the higher end of this range of temperature the martensite lath boundaries are replaced by more equiaxed ferrite grain boundaries by a process which is best described as recrystallization. The final result is an equiaxed array of ferrite grains with coarse spheroidized particles of Fe₃C partly, but not exclusively, in the grain boundaries. In consequence, the final structure produced will be governed by the initial choice of steel and the properties, and hence thermal treatment, required.

It was also observed that the Charpy values for different build orientations are different. This was also reported in the works by Kruth et al. [54], which presented results of SLM built maraging steel toughness test coupons, and the test coupon built with the notch facing up had the lowest toughness values.

In general, coupons built in the Z direction have the poorest mechanical performance results. This is consistent with literature of typical SLM built parts, which attributes this to weak regions between the melting layers, a characteristic of layer by layer fabrication techniques [152]. The results presented in the studies from the reference literature may not be representative of those in this study. Zhang et al. investigated the effect of the orientation of the build on the mechanical properties of stainless steel 316L, and the results show that the specimens built in the z-direction have the lowest mechanical properties. Zhang et al. attributed the poorer properties to a poorer bonding strength between two adjacent slices/layers, than two adjacent meltings (track or tool path).

However, in certain works, vertically SLM built samples were reported to have better mechanical performance than horizontally built sample [153]. Wen et al. explained the mechanics behind this observation by examining the molten pool boundaries (MPB) in [116]. In his work, Wen et al. investigated 2 types of MPBs (see Figure 4.29) formed by the SLM process, namely the “layer-layer” MPB and the “track-track” MPB”. The MPBs generated from the layer-by-layer overlapping along the Z-axis are called as “layer-layer” MPBs (Figure 4.29 (b)), and those generated through track-by-track overlapping in the X–Y plane are referred to as “track-track” MPBs (Figure 4.29 (c)). For the horizontal specimen, the crack begins at “track–track” MPBs (see Figure 4.30 (a)) when the tensile loading reaches a certain value, and then extends quickly along “track–track” MPBs slipping surfaces with the continuous increase of the tensile loading until the occurrence of fracture and the formation of cleavage surfaces. For the vertical specimen, the tensile direction is along the “track–track” MPBs (see Figure 4.30 (b)) slipping surfaces. Cracks initiate first at the “track–track” MPBs when the tensile loading increases to a certain extent, and then form cleavage steps along the loading direction. Subsequently, the cracks extend along the “layer–layer” MPBs, resulting in the fine dimples. Compared with the horizontal specimen, the vertical specimen has less quantity of “track–track” MPBs on the same cross-sectional area, which means a lower probability of cracking and better tensile performance for the vertical samples. In addition, the bonding force of “layer–layer” MPBs is stronger than that of track–track MPBs, and “layer–layer” MPBs will slip when exerted with a tensile loading.

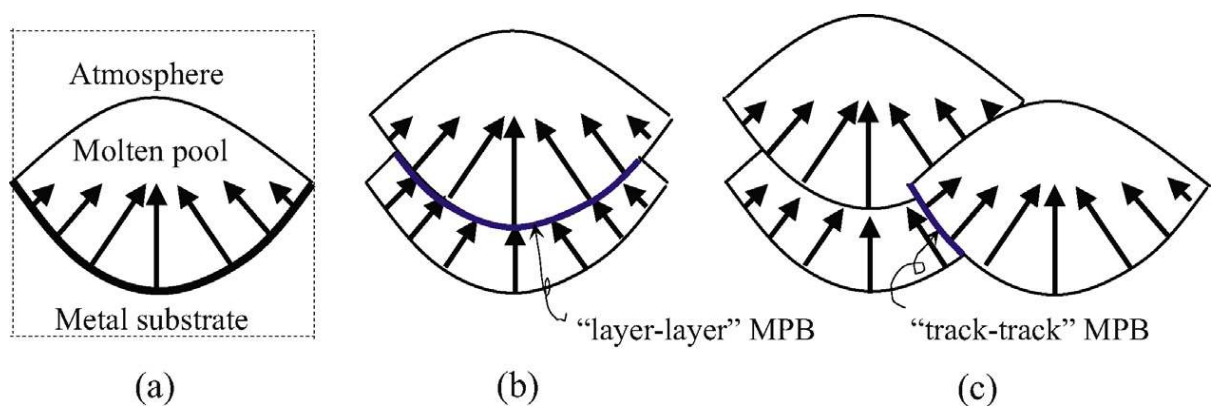


Figure 4.29 - Schematic diagram of molten pools during SLM process: (a) single molten pool; (b) “layer–layer” MPBs; (c) “track–track” MPBs. The arrows represent the grain orientations. [116]

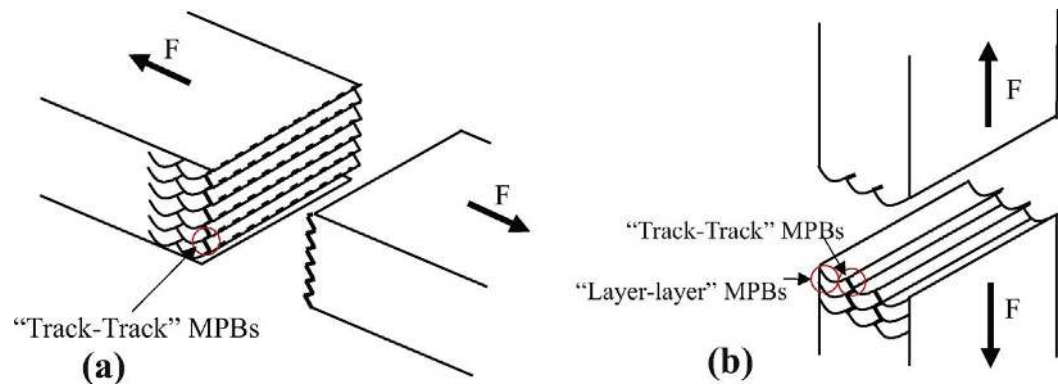


Figure 4.30 - Schematic diagrams of MPBs on the stress cross sections of (a) the horizontal and (b) vertical specimens. [116]

Regardless, in all the literature on using SLM to process steel based components, parts built in the 45° direction (from the bed substrate) usually improves the mechanical properties as compared parts built in the horizontal and vertical directions. In the work conducted by Wang et al. [154], where crystallographic orientation was used to determine the relation to mechanical properties, the Schmid factor was lowest in specimens built in the 45° direction, which then gives the highest tensile strength (recall that tensile strength can be determined by dividing the critical resolved shear stress value by the maximum Schmid factor). In the work conducted by Wen et al. [116], where MPBs was used to determine the relation to mechanical properties, the properties were highest in the 45° built direction. When the loading direction is parallel to the X–Y plane (i.e. the horizontal specimens), the slipping occurs preferentially along the “track–track” MPBs surfaces. When the loading direction is along Z-axis (i.e. the vertical specimens), the slipping will occur primarily along the “layer–layer” MPBs, but also slightly affected by the “track–track” MPBs surfaces. As the angle of the built transits to 45° to the horizontal, slipping at both “track–track” and “layer–layer” MPBs surfaces decreases for both the horizontal and vertical specimens respectively, hence minimising slipping for both built directions.

In the work conducted in this study, specimens built in the vertical direction generally have the poorest mechanical properties, and specimens built in the 45° direction have the best mechanical properties. Based on the analysis above, the poor mechanical properties found in the vertically built specimens may be speculated to be due to the poor bonding between layers as presented in literature studies. In addition, the presence of porosities (recall that the density achieved is 97.57%) may have also contributed to the increase in defects and crack initiations. By printing the specimens in

the 45° direction, the mechanical properties can be improved by minimising slipping occurring in both horizontal and vertical specimens, which usually have high slipping along “layer-layer” and “track-track” MPBs surfaces at vertical and horizontal specimens respectively.

4.5 Conclusion

- (1) Tensile test coupons and impact toughness test coupons were successfully built and tested (in accordance to ASTM E8 and E23) with process parameters and powder identical to that of the preliminary investigation. Preliminary post process heat treatment was conducted.
- (2) Mechanical properties are generally poorer in the vertical built direction and best in the 45° built direction.
- (3) Tensile, Elongation and Charpy results showed that building in the 45° direction to horizontal and with heat treatment, the properties meet ASTM A131 requirements. Final selection of the test results as shown in Table 4.8.

Table 4.8 - Final test results for SLM built EH36 steel specimen (45° built specimens)

Properties	Standards (ASTM A131)	SLM As-Built	SLM Built with Heat Treatment @ 650 °C
Yield Strength (MPa)	355	1011±69.9	759±28.2
Ultimate Tensile Strength (MPa)	490 – 620	1054±28.0	835±63.5
Elongation (%)	22	13.2±0.17	23.3±1.03
Charpy at -40 °C (J)	34	44.7±6.43	62.5±14.57

Chapter Five Fracture Surface Morphology

Studying the morphology of fracture surfaces allows for the analysis of causes of material failures. Through examination of the origin of cracking, the cause of crack initiation may be determined, which includes common features such as inclusions, voids, contamination, and stress concentrations. Many studies have been conducted to characterise fracture surface morphology to correlate the results and their corresponding mechanical properties[155]. From Chapter Four, the tensile and impact properties of EH36 can thus be validated and characterised by studying the fracture surface morphologies.

5.1. Procedure

The tensile and impact Charpy samples from Chapter Four were then prepared for examination using a scanning electron microscope (SEM, please refer to Table 5.1 for details). Fractography images of the samples were obtained at 50 times and 1000 times magnification.

Table 5.1 - SEM details and parameters

Model	Zeiss EVO MA 15 (Tungsten filament)
Operating Parameters:	
Vacuum Mode	High Vacuum
Imaging Detector	Backscattered electron detector (BSD)
Excitation Voltage	20kV
Working distance	10 mm

5.2. Results

The images from SEM show clearly the fracture morphologies, indicating the fracture modes whether they were brittle or ductile failures. Figure 5.1 and Figure 5.2 show SEM images of tensile coupons at 50x and 1000x magnification respectively,

while Figure 5.3 and Figure 5.4 show that of the Charpy coupons. Regions showing unmelted particles and voids at the failure zone were purposely selected for discussion.

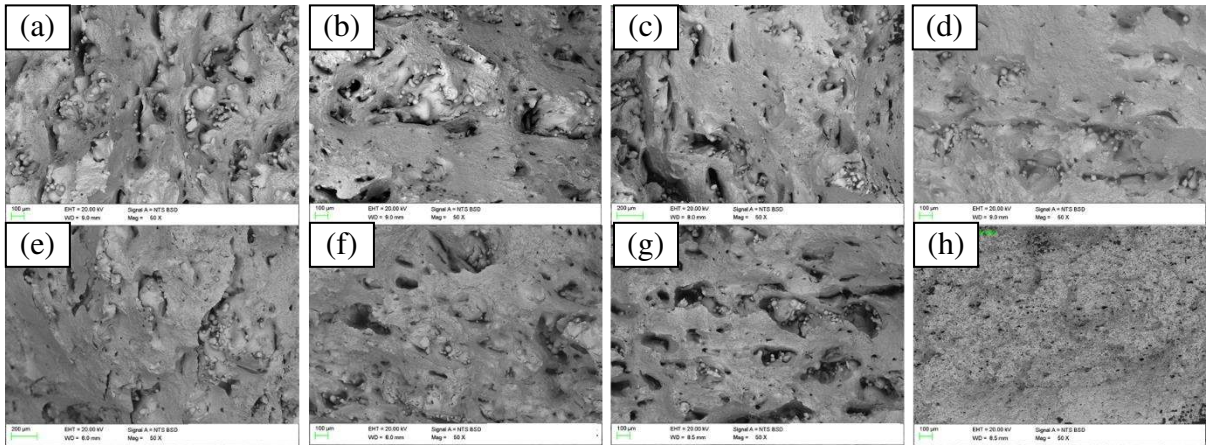


Figure 5.1 - SEM images of tensile coupons at 50x magnification (a) no heat treatment, (b) 205°C, (c) 315°C, (d) 425°C, (e) 540°C, (f) 650°C, (g) 800°C, (h) reference sample

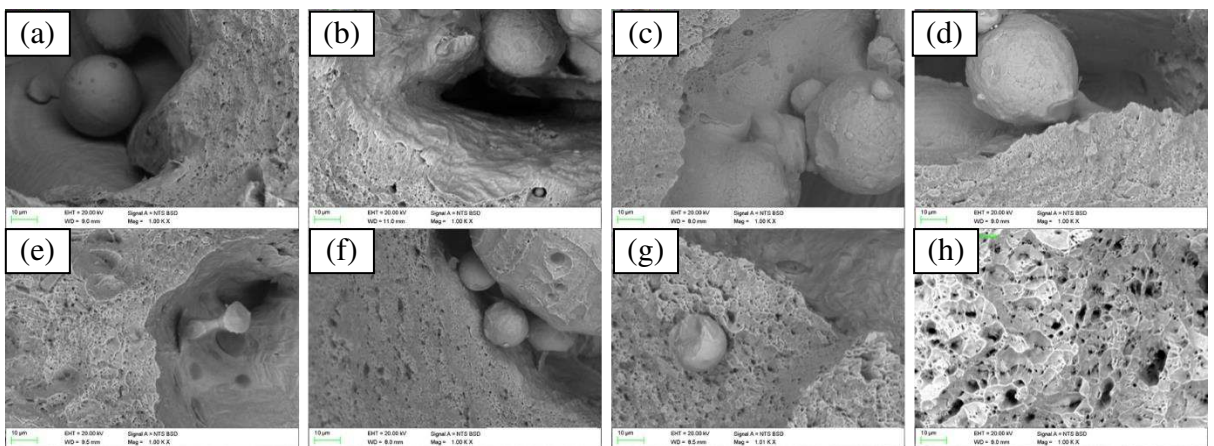


Figure 5.2 - SEM images of tensile coupons at 1000x magnification (a) no heat treatment, (b) 205°C, (c) 315°C, (d) 425°C, (e) 540°C, (f) 650°C, (g) 800°C, (h) reference sample

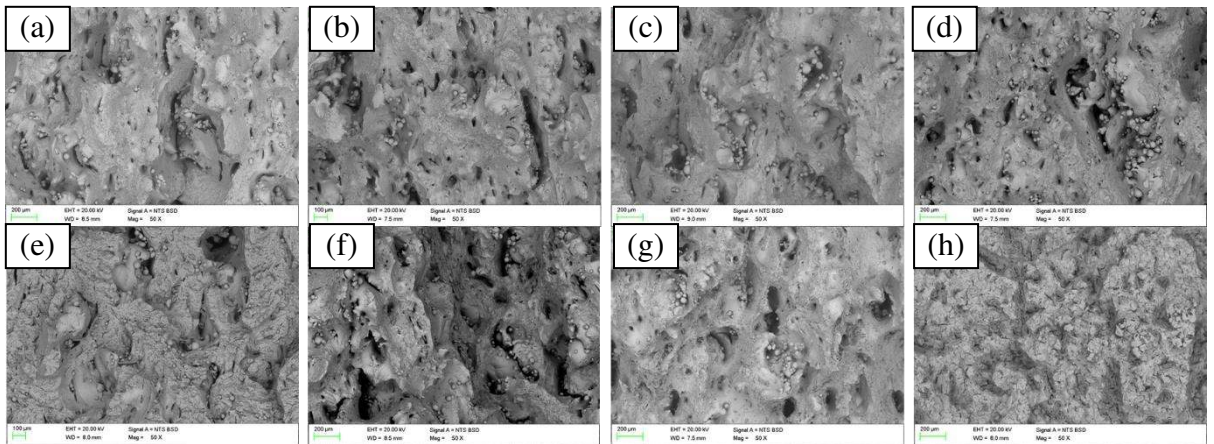


Figure 5.3 - SEM images of Charpy coupons at 50x magnification (a) no heat treatment, (b) 205°C, (c) 315°C, (d) 425°C, (e) 540°C, (f) 650°C, (g) 800°C, (h) reference sample

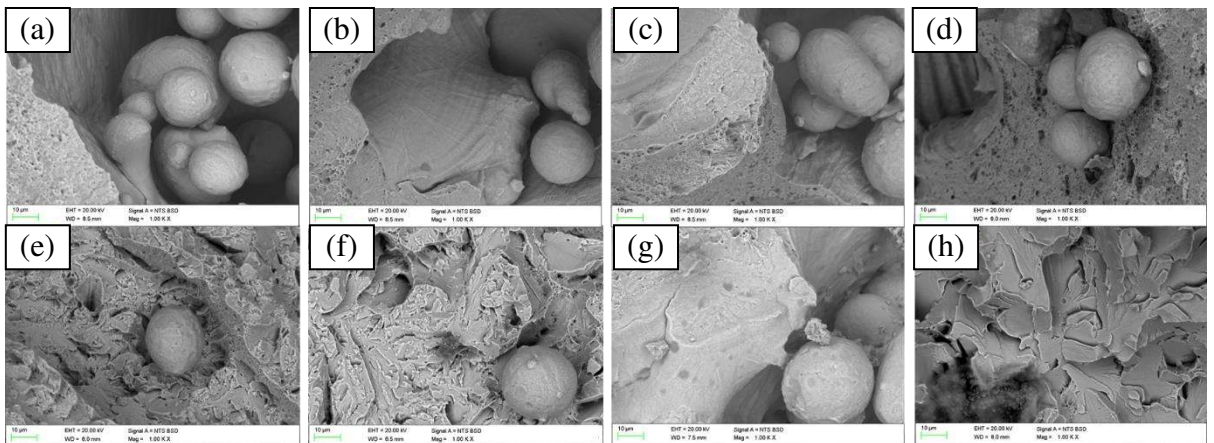


Figure 5.4 - SEM images of Charpy coupons at 1000x magnification (a) no heat treatment, (b) 205°C, (c) 315°C, (d) 425°C, (e) 540°C, (f) 650°C, (g) 800°C, (h) reference sample

5.3. Discussion

5.3.1 Ductility

The fractography images of the SLM produced test samples (see images (a) to (g) of Figure 5.1 to Figure 5.4) show a general trend of higher proportion of fine faceted cleavage structures. It is observed that the reference sample (see images (h)), which is produced by TMCP (see Chapter 2.1.1.3), shows larger, river-like cleavage structure (Figure 5.4 (h)). In general, during fracture, the crack propagates until it is impeded, for example at precipitates or grain boundaries. Because the grains are generally at different orientations to one another, the crack usually divides into terrace-like steps when

crossing a grain boundary. The newly created different crack planes join together during further crack propagation producing a characteristic river-like pattern.

Both types of samples show dimple like structures as secondary structure, with the TMCP produced ones having more significant dimple secondary structure. In a ductile failure, cavities arisen from inclusions or coarser precipitates are enlarged and during further yielding the material between them is necked and sheared. It was also observed that the dimple like structures are more apparent as the temperature of heat treatment increases. The depth of these dimples can be used as a first approximation to the level of ductility. The SLM produced samples also had smaller dimples (approximately 1-5 microns wide) compared to the TMCP produced one which had larger dimples (approximately 8-10 microns wide). A study [156] was conducted to correlate the size of dimples to its mechanical properties, and have concluded that larger dimple sizes correlate with higher ductility values. Comparing these, the SLM produced samples can thus be considered less ductile.

In addition to the observed fracture structure, powder particles of up to 50 microns were also seen in the micrographs. These spherical powder particles are clear evidence of incomplete melting during the SLM process. The presence of these un-melted powder may have contributed to the initiation of the fracture, which had also been discussed in works by Gong et al. [157], where he correlated regions of brittle fracture to lack of fusion defects. Interconnected porosity is more conducive to crack propagation because the crack grows through the path of least resistance[144], and in this case seems especially likely since several of the un-melted particles are seen in the same region. As a result, these fractures may have been prematurely accelerated due to the presence of such defects.

5.3.2 Density and Defects

The SEM images also show a large scatter of unmelted particles, giving rise to several pockets of void across the samples. The amount of voids also slightly decreased with the increase in temperature of heat treatment. This is consistent with the density tests results obtained in Chapter 3.3.1, where the density obtained for SLM as-built part was approximately 97.57%. It is well documented in prior studies that a fully dense

SLM produced part will achieve excellent mechanical properties, and many techniques have been used to achieve 100% dense parts [54], while defects generally decrease mechanical properties performance, mainly due to increase in crack initiations [157, 158], This may indicate a generally lower than achievable mechanical properties for example poorer fatigue properties [159], lower tensile and toughness values [160].

In SLM process, unmelted particles and voids are usually co-related to the process parameters, namely laser power, laser scanning speed, hatch spacing, layer thickness and other parameters such as containments, oxygen content etc [161]. While this is true, some of the process parameters have greater influence over the others, and hence may be considered as the optimisation focus for defect reduction. For example, Kasperovich et al. [162] described the scanning velocity (of the laser) as the most dominant influence on the porosity fractions, followed by laser power. Hatch distance was found to be the least sensitive. Referencing this knowledge with the density results from Chapter 3.3.1, we can compare the scanning velocity versus the results of the density. The density results are colour coded and compared as shown in Table 5.2 and Table 5.3 – red shows higher scanning velocity and lower density values while green shows lower scanning velocity and higher density, or it can be also represented by red showing the higher possibility of defects and voids and green showing the lower possibility, according to the observation described by Kasperovich et al. [162]. It can be clearly observed that the higher density values are obtained in the regions of lower velocities. Kasperovich et al. attributed the formation of defects to lack of fusion as the number one reason. It can thus be concluded that higher velocities lead to insufficient time for complete fusion of the metal particles. However, it should also be highlighted that although scanning velocity may be the top contributing factor to porosity formation, it is the combination of all the process parameters that eventually lead to a fully dense component. As described in Chapter 3.3.1, the energy density obtained played the most important part in the material density of SLM built parts.

Table 5.2 - Scanning velocity of density test in colour scale

Energy (J/mm³)	Hatch Spacing (mm)				
	0.08	0.09	0.1	0.11	0.12
111	390	350	310	290	260
105	422	376	336	312	280
99	454	402	362	334	300
92	486	428	388	356	320

86	518	454	414	378	340
81	550	480	440	400	360
75	616	540	492	448	404
69	682	600	544	496	448
62	748	660	596	544	492
56	814	720	648	592	536
50	880	780	700	640	580

Table 5.3 - Density values of density test in colour scale

Energy (J/mm ³)	Hatch Spacing (mm)				
	0.08	0.09	0.1	0.11	0.12
111	7.178	7.519	7.433	7.489	7.535
105	7.374	7.512	7.528	7.46	7.594
99	7.489	7.483	7.526	7.56	7.573
92	7.476	7.477	7.466	7.528	7.64
86	7.419	7.486	7.494	7.48	7.525
81	7.385	7.465	7.469	7.43	7.401
75	7.503	7.419	7.456	7.434	7.42
69	7.523	7.516	7.482	7.473	7.47
62	7.511	7.537	7.378	7.332	7.361
56	7.47	7.468	7.278	7.391	7.365
50	7.471	7.273	7.014	7.075	6.982

5.4. Conclusion

The above observations generally agree with the mechanical properties results obtained in Chapter Four. The mechanical test results show that SLM as-built EH36 samples generally exhibit high strength, but low elongation and Charpy values. From a density and defects perspective, the tensile strength increases with increasing density and decreasing porosity, while ductility decreases with increasing porosity[144]. The above fractography observations indicate brittle fracture, absence of ductility and the voids observed may also contribute to undesired failure. Heat treatment generally decreases the presence of voids and shows a more dimple-like structure, suggesting that tensile properties decrease as heat treatment temperature increases, and ductility is recovered as heat treatment temperature increases (see Figure 4.4, Figure 4.5, Figure 4.14, Figure 4.19 and Figure 4.20). These results are consistent with other works on

SLM processing of steel based materials [83, 90, 113]. The following conclusions can be made.

- (1) Tensile and impact samples were examined under scanning electron microscope to characterise the fracture surface morphology.
- (2) SLM produced samples are less ductile as compared to TMCP produced samples.
- (3) Tensile strength increases with increasing density and decreasing porosity, while ductility decreases with increasing porosity.

Chapter Six Microstructure Characterisation

Studying the microstructure of the samples allows a good understanding of the properties of the materials being processed. Different microstructures determine the different properties of the material, and hence is one of the important factors to be studied. In this study, the microstructure will also be correlated to the mechanical properties obtained from Chapter Four.

6.1. Iron-Carbon Binary Phase Diagram

The material in this study (EH36) is considered a low alloy low carbon steel. Its microstructural development may be referenced to the iron-carbon binary phase diagram (see Figure 2.1), which is a comprehensive illustration of microstructural development in iron-carbon alloys. It shows the development of microstructure in iron-carbon alloys depending on the carbon content composition and heat treatment, which will give a good understanding of the microstructure of steels [163].

In the case of the EH36 material used in this study, its carbon content is 0.15%, which puts it at the far left of the phase diagram. The maximum target temperature of 800°C was purposely kept below the material's eutectoid temperature to prevent recrystallisation. With reference to the Fe-C phase diagram, it is expected that spheroidisation will be observed in specimens which underwent heat treatment of 650°C and above.

6.2. Experimental

Samples were grinded and polish with reference to ASTM E3 - 11(2017): Standard Guide for Preparation of Metallographic Specimens. Samples were chemically etched with 5% nital acid (95% methanol – 5% nitric acid) to expose the grain boundaries and microstructure images were then taken by using an optical microscope (Model: Zeiss M2M) at 100 times and 1000 times magnification. The samples are also put through X-Ray Diffraction (XRD) to validate the phase transformations, if any.

6.3. Results

Figure 6.1 and Figure 6.2 show microstructure image at 100x magnification, and Figure 6.3 show that of 1000x magnification. The images show distinctly the layer by layer formation unique to additive manufacturing, grain growth through the various heat treatment temperatures and type of microstructure formed. These will be discussed further in Chapter 6.4.

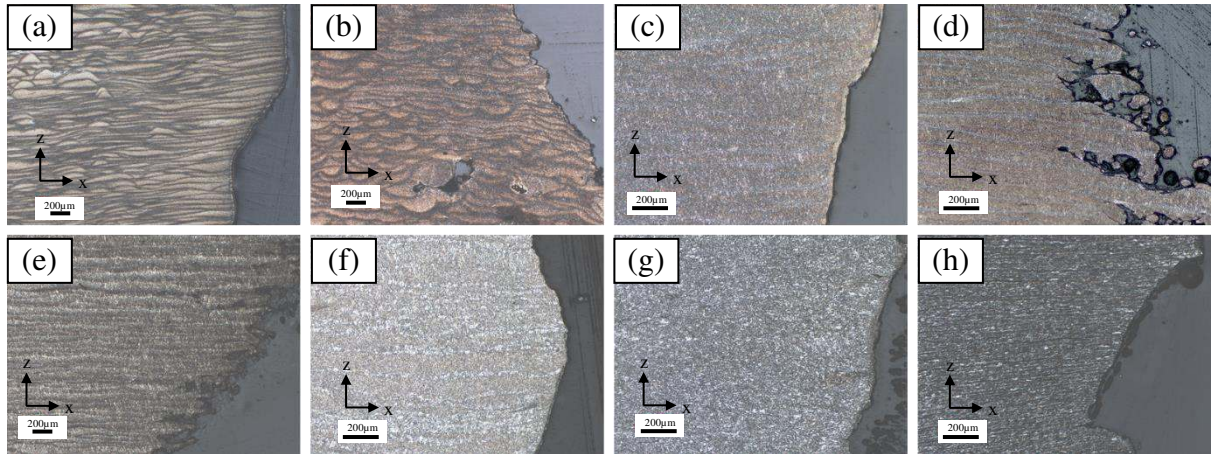


Figure 6.1 - Microstructure images showing melt pool layers (a) no heat treatment, (b) 205°C, (c) 315°C, (d) 425°C, (e) 540°C, (f) 650°C, (g) 800°C, (h) reference sample

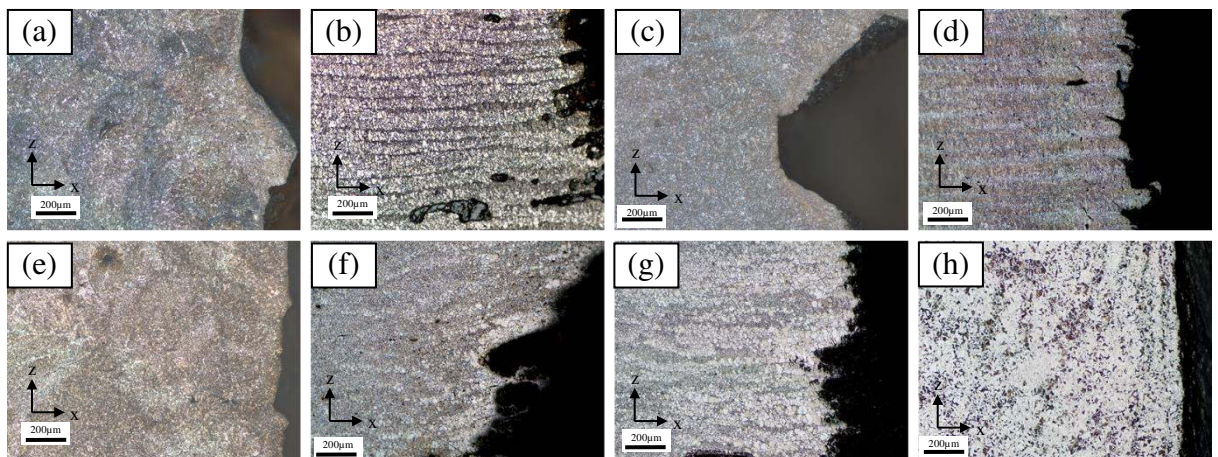


Figure 6.2 - Microstructure images (a) no heat treatment, (b) 205°C, (c) 315°C, (d) 425°C, (e) 540°C, (f) 650°C, (g) 800°C, (h) reference sample

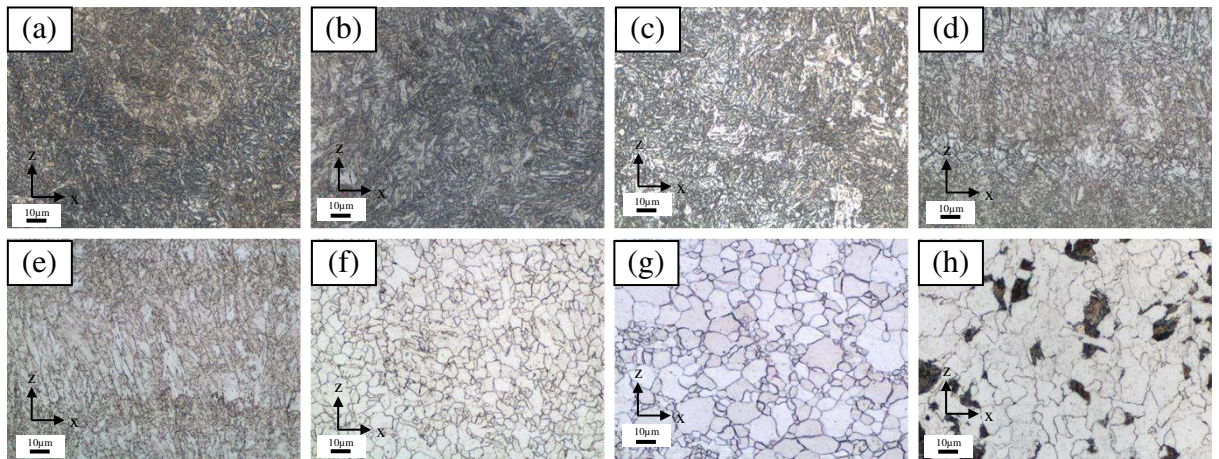


Figure 6.3 - Microstructure images with higher magnification (a) no heat treatment, (b) 205°C, (c) 315°C, (d) 425°C, (e) 540°C, (f) 650°C, (g) 800°C, (h) reference sample

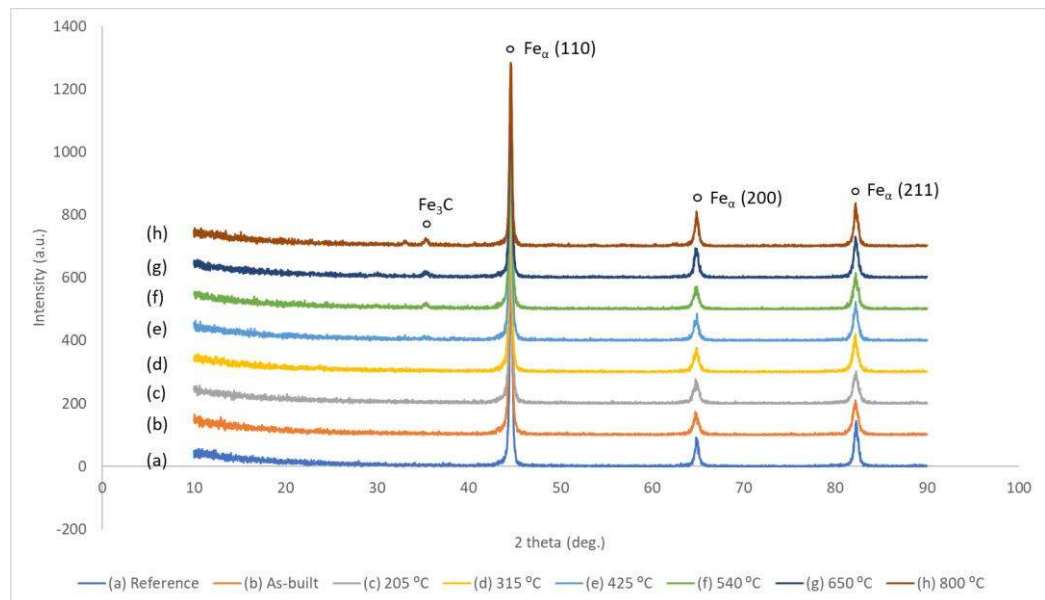


Figure 6.4 - XRD results

6.4. Discussion

As discussed in Chapter 2.3.4, literature has shown that SLM produced specimens can generally be characterised by a very fine microstructure due to its rapid cooling process. The results from the preliminary investigation shown in Chapter 3.3.4 agreed with the literature, with SLM as-built EH36 samples exhibiting very fine acicular martensitic-like microstructure. This was also verified from the hardness values in

Chapter 4.3.4. Further work is then performed to study the change in the microstructure with relation to heat treatment temperatures.

The microstructure images shown in Figure 6.1 show very distinct layer by layer deposition paths of the SLM process. This observation decreases as the heat treatment temperature increases. In image (g), the layering effect can be observed to be totally absent. From Figure 6.2 and Figure 6.3, several characteristics can be observed. The grain size has coarsened with the increase in heat treatment temperature, from approximately 1-3 micron in the as-built sample to 5-20 microns in the sample heat treated with a temperature of 800°C. It has also changed from a martensitic-like microstructure to a ferrite-like dominant microstructure. This transition of microstructure is also supported by the results of Vickers hardness tests in Chapter 4.3.4, where the Vickers hardness values for the as-built and samples with heat treatment of up to 540 °C coincide with that of a martensitic microstructure, and later decreases at 650 °C and 800 °C. This is consistent with existing past works discussed in Chapter 2.3.4, where high temperature gradients during SLM process leads to fine acicular martensite [54].

In image (a), the fine grains are generally elongated but without a pre-determined direction. From literature (see Chapter 2.3.4), during the SLM process, the powder particles are irradiated and heat is transferred from the top to the bottom of pre-laid powder layers, so that the elongated grains formed during the solidification process due to temperature gradient that is created between the powder layers along the building direction, a result of epitaxial solidification [54]. However, in SLM-fabricated iron parts, these elongated grains usually were not very obvious. This can be explained by the weakened temperature gradient due to the presence of phase change during the process of melting and solidification of iron powder. Nonetheless, there exists elongated grain shape which changes to more equiaxed as heat treatment temperature increases.

6.4.1 Effect of Heat Treatment

The heat treatment process has a big effect on the microstructure changes in this study. During the tempering process, the sample is allowed to cool slowly, rather than cool rapidly, which will result in the martensitic microstructure. The maximum heat

treatment temperature of 800°C was selected such that the sample can be heated to a temperature below the lower critical temperature and allowed to cool at a slower rate.

Referencing Figure 6.1, it can be observed that EH36, being a steel with 0.15% Carbon, will undergo phase transformation during tempering in the following manner. In images (a), (b) and (c) from Figure 6.3, from temperatures as low as 100°C to 300°C, any transition carbides and martensite starts to be replaced by cementite and ferrite (see Figure 6.5). Past 300°C to 400°C, images (d) to (e) shows coarsening of cementite commences to form spheroids, a process known as spheroidisation. This results in a microstructure of fine spherical cementite particles in a soft ferritic matrix (see Figure 6.6). At this stage, it can be observed that the microstructure is generally ferritic with small amounts of spheroidised particles of cementite at the grain boundaries (Figure 6.7). This is also validated through the conduct of XRD (see Figure 6.4), where presence of cementite is significant enough to be picked up starting from 425°C. This will continue until about 700°C, where at the higher range of the temperatures, recrystallisation occurs to form equiaxed ferrites (see Figure 6.8).

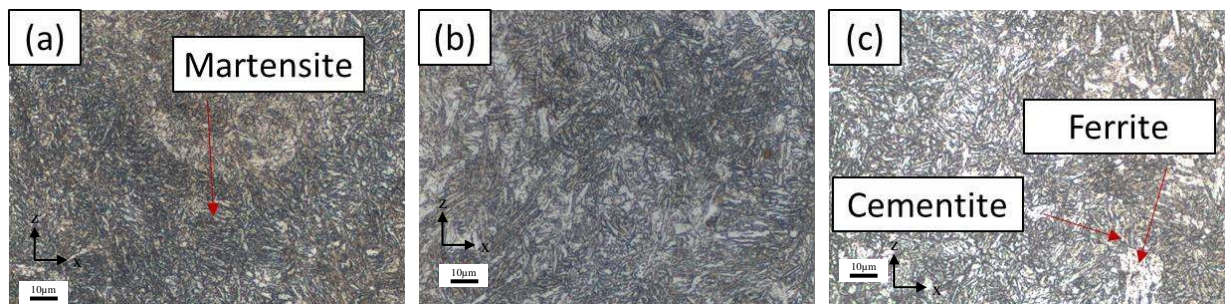


Figure 6.5 – Effect of heat treatment causing formation of cementite (dark bands) and ferrite (bright regions)

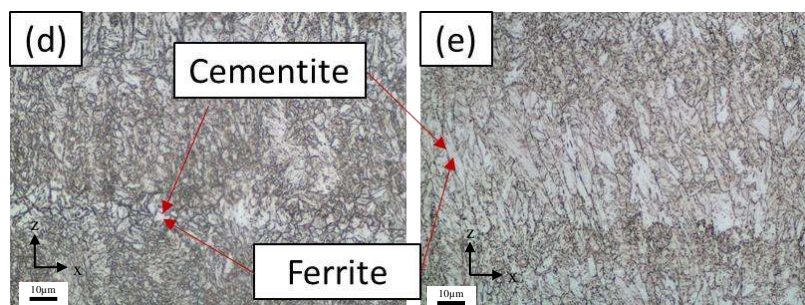


Figure 6.6 – Effect of heat treatment causing spheroidisation

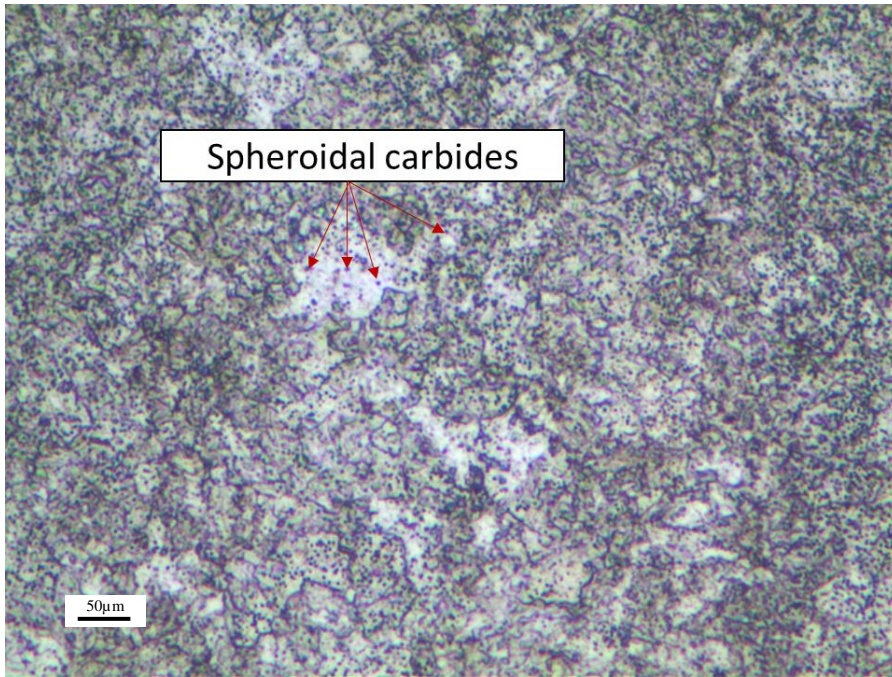


Figure 6.7 - Spheroidal carbides

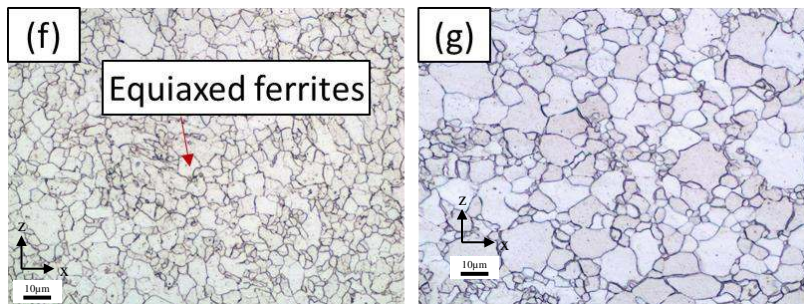


Figure 6.8 – Effect of heat treatment ending up with recrystallisation

The coarsening of the grains leading to grain growth combined with the recrystallisation process to form ferrites is particularly important to the explanation of the mechanical properties. Chapters 6.4.2 and 6.4.3 below will explain these phenomena and correlate them back to the mechanical properties obtained in Chapter Four.

6.4.2 Grain Boundary Strengthening

The above observations agree very well with the results from the mechanical testing from Chapter Four. At lower tempering temperatures, the samples produced had very high strength due to their very fine grained martensitic microstructure. As the grain size is reduced, strength increases through Hall-Petch equation, or grain boundary strengthening. In grain boundary strengthening, the grain boundaries act as pinning points to prevent further dislocation propagation. As shown in Figure 6.9, both slips planes in Grains A and B are inhibited by the grain boundary shown in green. Since the grains differs in orientation, more energy is required for a dislocation to change directions. Since dislocation movement leads to plasticity, this lack of motivation to dislocate increases the strength. As strength increases, usually ductility decreases since dislocations have a higher number of boundaries to pile up into and the volume available for their movement is greatly reduced.

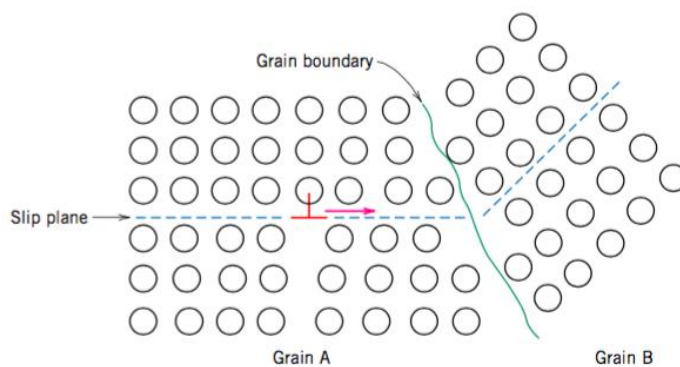


Figure 6.9 - Grain boundary strengthening

This grain boundary strengthening phenomenon unique to SLM due to its process related rapid cooling rate is also observed and discussed in various other works [87, 164-166]. The smaller grain sizes, which then increases dislocations at grain boundaries and creates higher resistance of the dislocations to slip transfer, is reported in these other works to also affect other materials such as Aluminium, Inconel and Titanium. It can hence be concluded that the grain boundary strengthening effect is not unique to only steel. Coupled with the high strength properties of martensitic microstructures in steel [167], the SLM built samples exhibited high strength at lower tempering temperatures. However, it is also the same reason that resulted in the low ductility of the samples.

6.4.3 Transformation of Microstructure

Grain size analysis has been performed according to E112-13: Standard Test Methods for Determining Average Grain Size, and the intercept method is used to determine the grain sizes. An example of the grain size determination is shown in Figure 6.10.

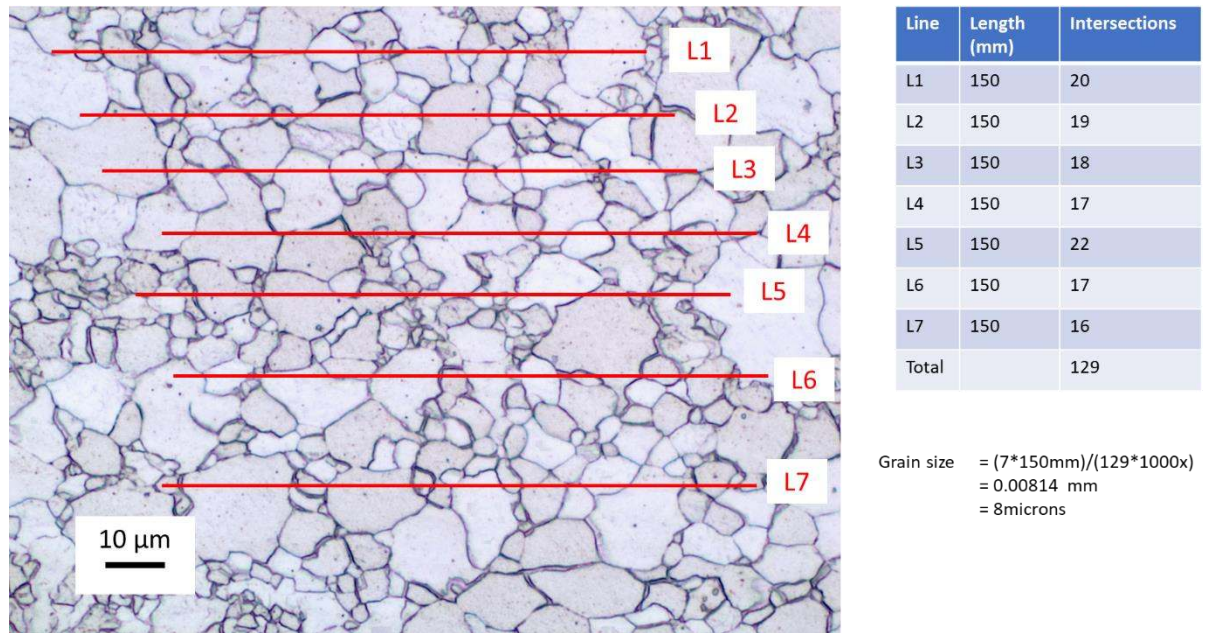


Figure 6.10 - Grain size determination of SLM produced sample with 800°C heat treatment

The as-built samples exhibited a generally fine martensitic-like microstructure (see Chapter 3.3.3) of less than 1 microns grain size, which gives the material its high strength but low ductility properties. However, martensite is an unstable phase, and as the tempering temperature increases, as discussed above, spheroidisation occurs and the martensitic structure starts to transform into a primarily ferritic microstructure with small amounts of cementite. This transformation will result in a loss in high strength but will recover its ductility. As shown at the 650°C sample (see image (f) of Figure 6.3), the microstructure has started to transform into ferrite, and the grains have coarsened significantly to 5 microns. This, as shown in the results from the mechanical testing, has resulted in an improvement in its Charpy value, but a decrease in the tensile strength. As the tempering temperature continues to increase to 800°C, the grain size would have increased to 8 microns, which is close to the TMCP produced sample of 11 microns (see

Figure 6.11), but is still smaller and finer, and the ductility would be very much recovered, but at the sacrifice of tensile strength.

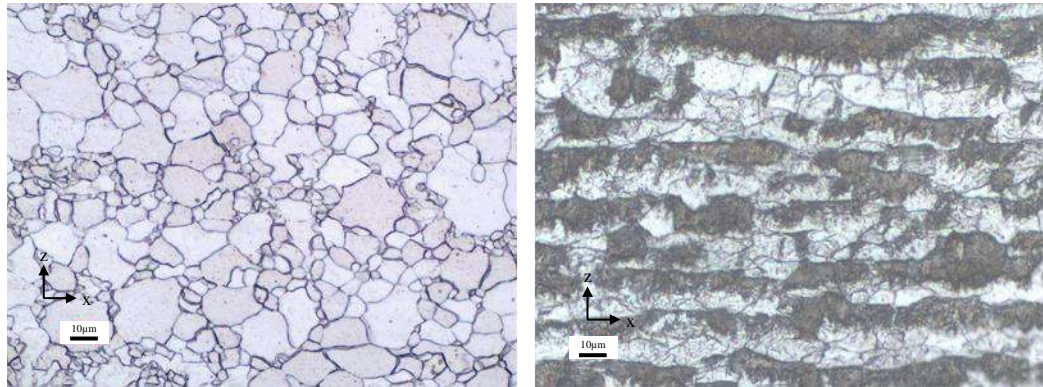


Figure 6.11 – Comparison of grain sizes of SLM processed sample with 800°C heat treatment (left), vs TMCP produced sample (right)

Based on images (e) to (g) of Figure 6.3 showing the transformation of the microstructure from tempering temperatures of 540°C to 650°C and 800°C, it seems a fine grained ferritic microstructure may be the optimal requirement for the appropriate strength versus ductility combination. At 540°C, the microstructure is only starting to transform to ferrites, but the presence of the martensite with its fine grain sizes provides the required high tensile strength. With reference to the Fe-C phase diagram in Figure 2.1, heating the samples to 800°C and then allowing it to cool slowly enables the decomposition of austenite to form pearlite embedded in ferrite. Furnace cooling to room temperature also allows the control of the grain sizes, and also allows the cementite plates to adopt a more spherical shape. At 800°C, the grain sizes would have grown too large for achieving the required strength, although the primarily ferritic microstructure is desired for its toughness. Between these temperatures, further work needs to be carried out to optimise and obtain the best combination of microstructure versus the grain sizes.

6.5. Conclusion

- (1) The SLM built and TMCP built samples are prepared and observed under 100x and 1000x magnifications to characterise the microstructures.
- (2) The microstructures obtained were speculated to be primarily fine acicular martensite in the SLM as-built samples, transforming to fine spherical cementite

particles in a soft ferritic matrix as heat treatment temperatures increase, and eventually forms equiaxed ferrites with grain sizes smaller than the TMCP produced samples. While there is indirect evidence of the presence of such phases, the occurrence is speculated based on existing literature studies.

- (3) The smaller grain sizes help to provide higher tensile properties due to grain boundary strengthening.
- (4) Performing heat treatment on the SLM built samples can improve the impact properties but at a sacrifice of the tensile properties, due to transformation of microstructure from martensite to cementite and ferrite.

Chapter Seven Complex Joint Fabrication and Examination

As discussed in Chapter One, the marine and offshore industry can be characterised by the multiple processes required to fabricate complex design components. The objective of this work is to validate AM technology as a complementary manufacturing technology to eliminate long leadtime associated with such multiple processes. In this chapter, a scaled version of the typical complex joint component will be fabricated using the developed process parameters and validated against the results using microstructural analysis. While a scaled complex joint model may not accurately represent the process conditions and the results, it provides a foundation for future work to scale the fabrication of the part to its actual size. For example, in the processing of a large component using SLM, it is expected that the thermal conditions within the build chamber will be significantly different from the scaled model, leading to different microstructural results in the final product, and a different microstructural transformation in its subsequent heat treatment regime. Nonetheless, the results from a scaled model will be able to validate the process parameters developed from the preliminary work and establish a foundation for future endeavours to achieve large scale fabrication by SLM.

7.1 Overview of Complex Joint

The complex joint used in this study is based on a node of a structural body, typically used to join 6 trusses or more. A scaled version was fabricated using SLM process (see Figure 7.1) based on the process parameters obtained in Chapter Three, with its print orientation as shown in Figure 7.2. Only one print direction was chosen as the microstructure analysis will be performed in all 3 planes (ie x, y and z), which will represent similar analysis in other directions of print. In this case, the scaled model was printed vertically to enable the observation of the microstructure formed at the region furthest from the build bed. In order to analyse the microstructure at this furthest region, a section of the complex joint was then removed and examined as shown in Figure 7.3.

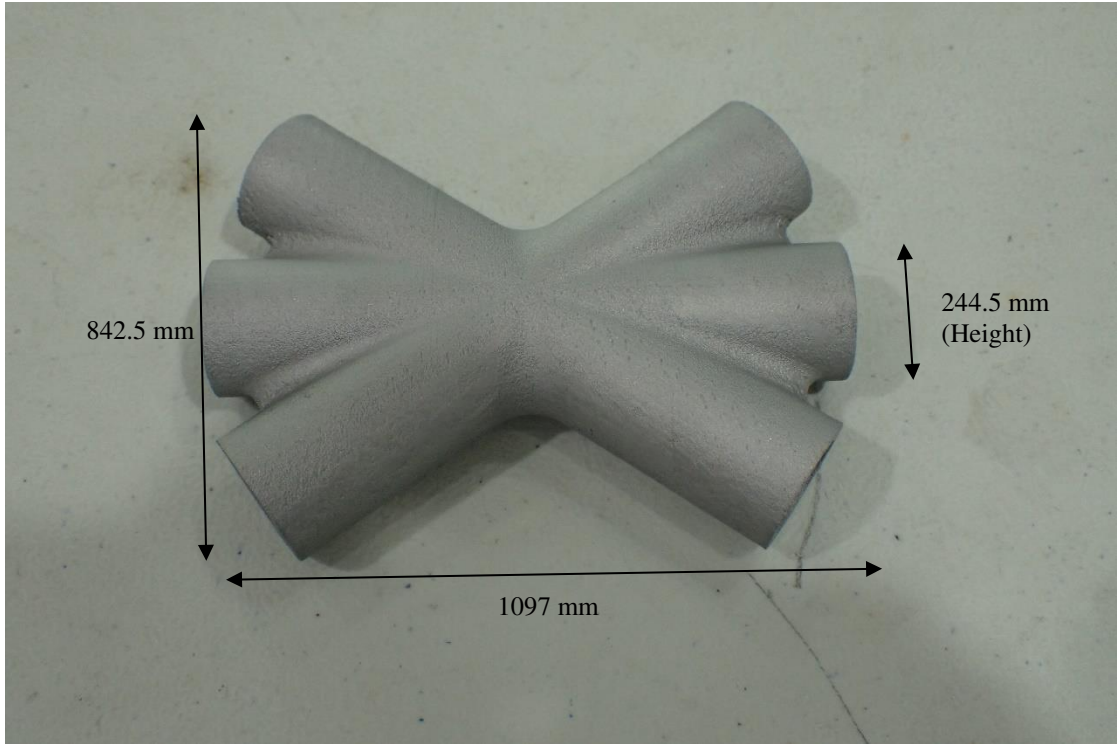


Figure 7.1 - Photo of scaled complex joint processed by SLM

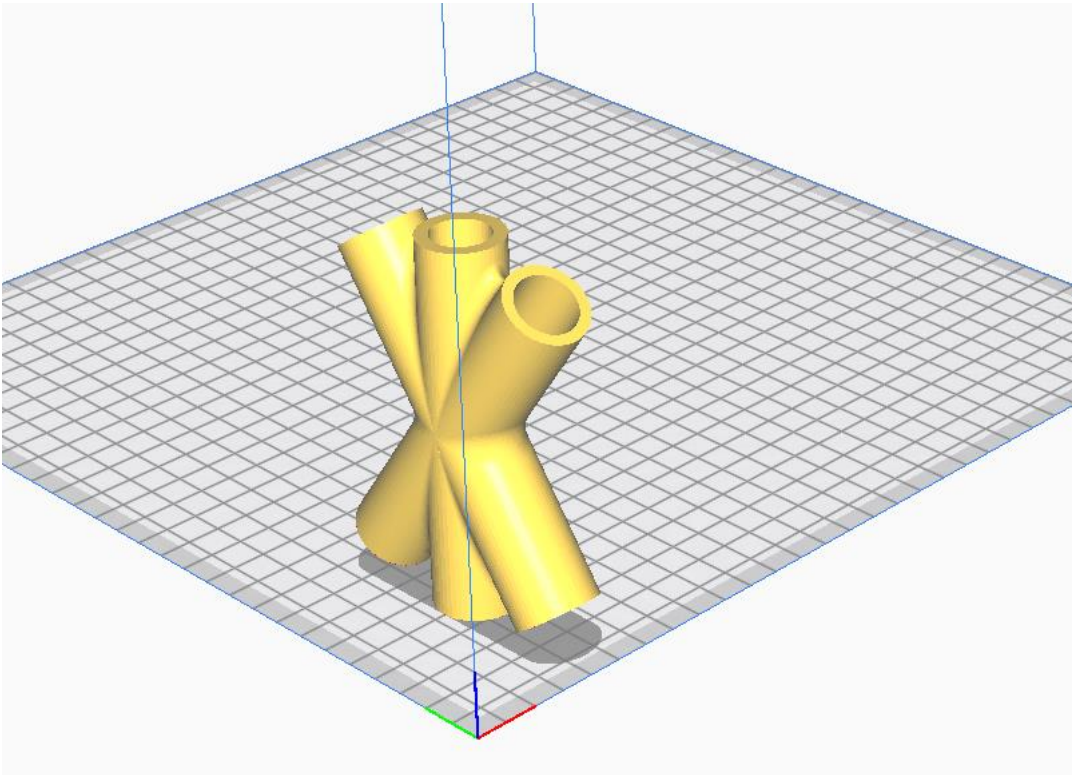


Figure 7.2 - Orientation of print of scaled complex joint

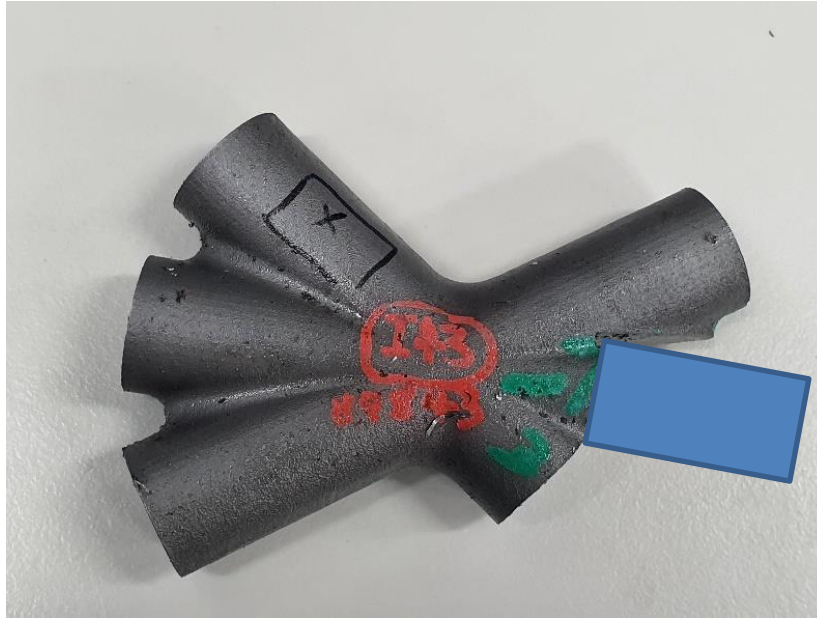


Figure 7.3 - Section of complex joint removed for examination (shaded in blue)

7.2 Microstructure Examination and SEM-Imaging

In order to validate SLM process for the fabrication of complex joints, microstructure examination was performed and compared against those obtained from the test coupons. The examination was performed using scanning electron microscopy (SEM) on the scaled model as-built without heat treatment.

Figure 7.4 shows 50 times magnification of the cut-out section of the scaled model, with Face 1 as the x-y plane to the printing process, and Face 2 and Face 3 as the z plane to the printing process. Doing a 50 times magnification allows understanding of the SLM process and the types of defects formed. The images show distinct layer by layer deposition, which is a characteristic of the SLM process. There is also evidence of porosities between the layers.

Figure 7.5 shows 500 times magnification with the same orientation. A larger magnification allows for examination of the microstructure formed. The results show very fine grain structure with an evenly distributed acicular martensitic-like microstructure.

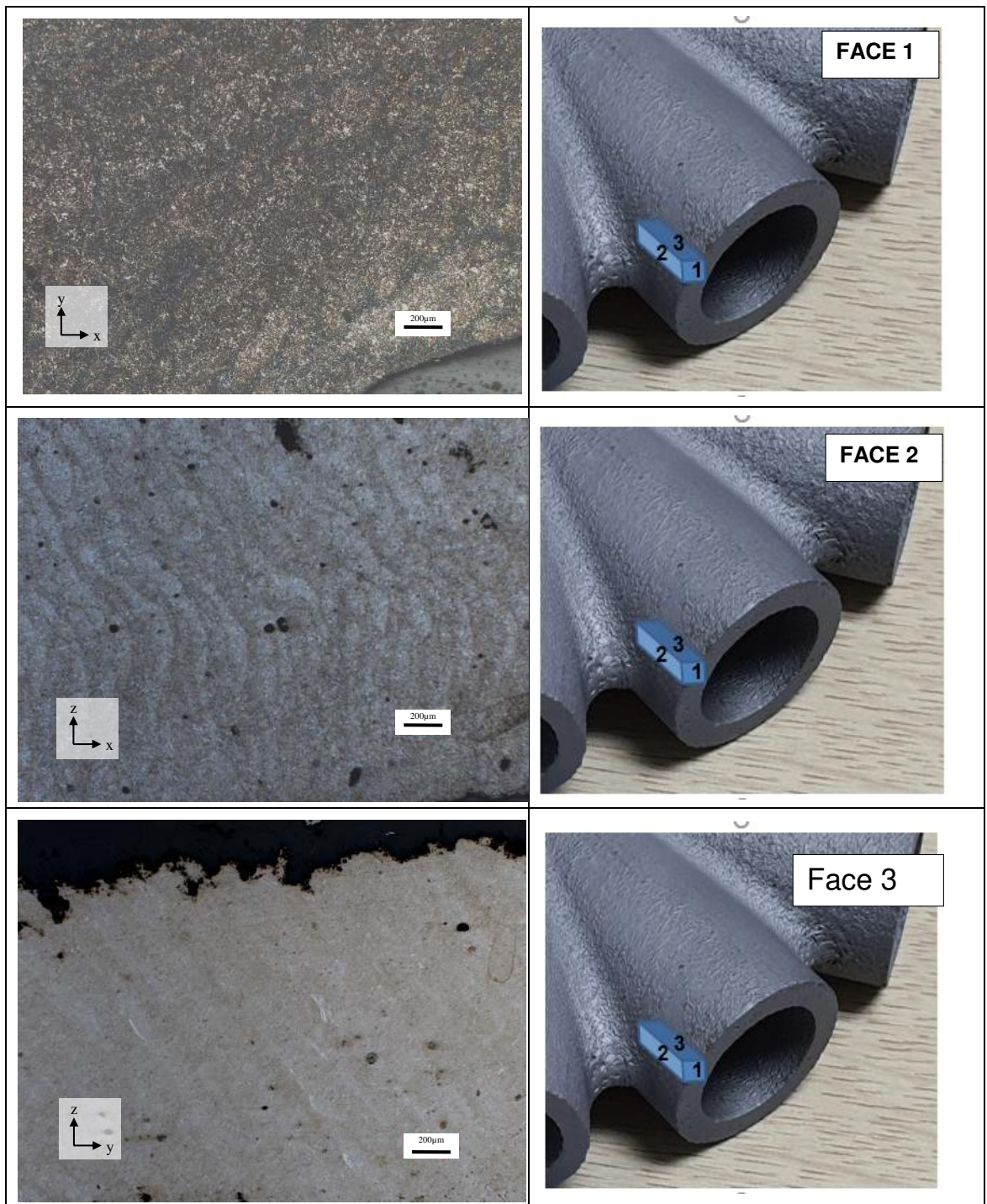


Figure 7.4 - Scaled model SEM imaging mapped to various printed faces

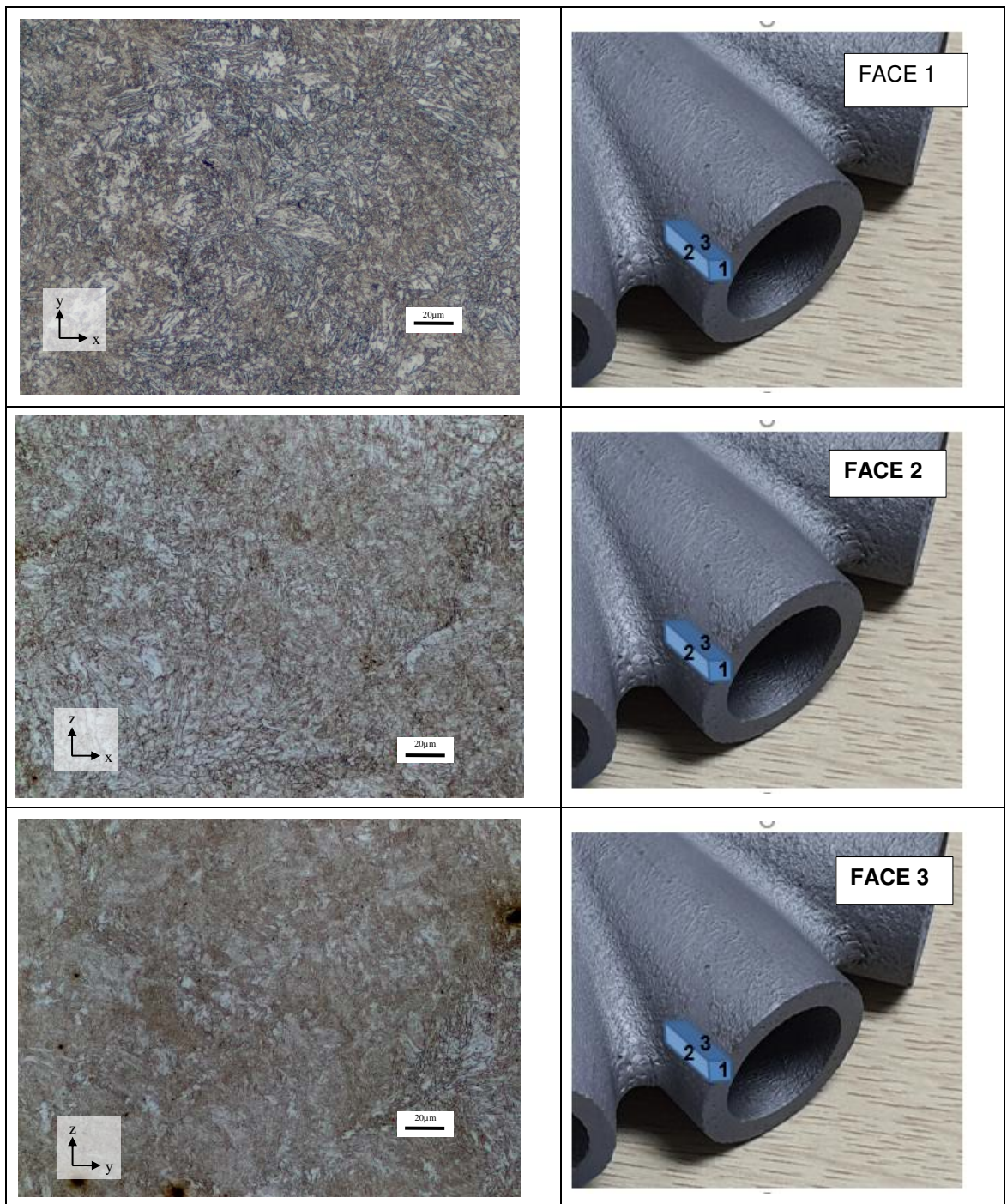


Figure 7.5 - Scaled model SEM imaging with larger magnification

7.3 Vickers Hardness

Vickers hardness measurements were made to be able to perform a comparison with the analysis in Chapter 4.4. All tests parameters are similar to the hardness measurements conducted in Chapter 4.3.4. The Vickers hardness numbers, H_v , for the

specimens are listed in Table 7.1. Each of the data points represents an average of measurements from at least five tests, and the results are plotted in Figure 7.6.

The Vickers hardness numbers are generally high at 323 to 398, with an average of 349 to 358, for the as-built scaled model. Vickers hardness values are not a requirement in the ASTM A131 standards for EH36, but it will be used to ascertain the martensitic-like microstructure in the discussions.

Table 7.1 - Table of Vickers hardness values for SLM built scaled model

Vickers Hardness	Sample locations on node	
	1	2
H _v	349	358

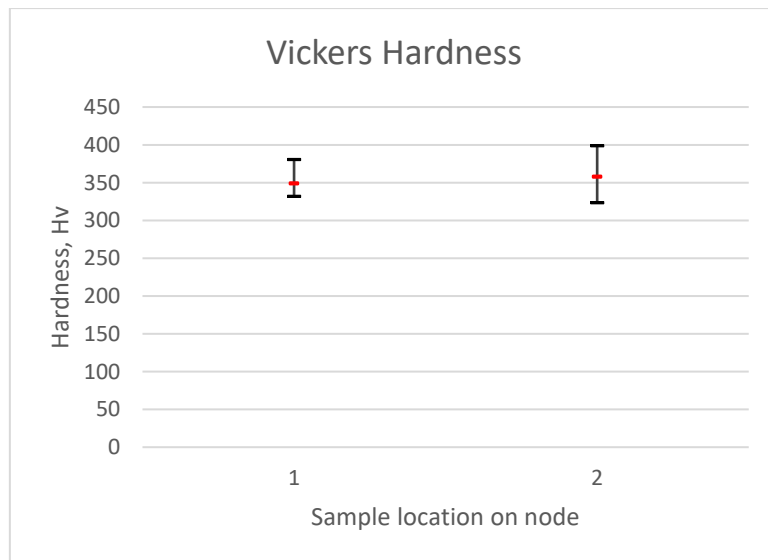


Figure 7.6 - Graph of Vickers hardness numbers (scaled model)

7.4 Discussion

The microstructure obtained from the SEM examination of the scaled model was used to compare against that obtained from the test coupons. A sample test coupon was put under SEM with a 500 times magnification and matched with the corresponding faces of the scale model as shown in Figure 7.7, where (a) shows x-y plane to the printing process, and (b) and (c) as the z plane to the printing process.

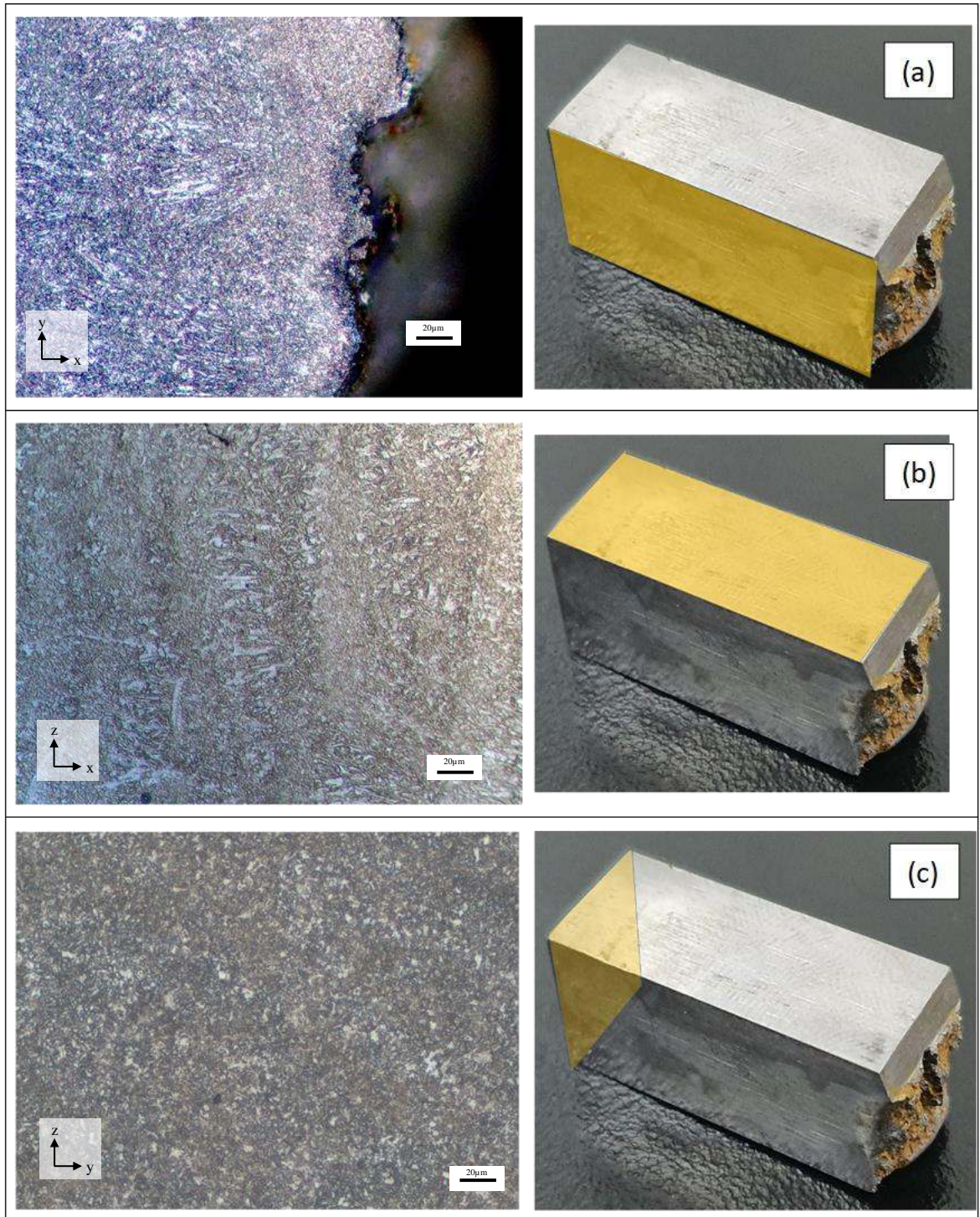


Figure 7.7 - Reference SEM images for comparison with scaled model (a) x-y plane, (b) z plane, (c) z plane

Based on the micrographs obtained from the scaled model, a large number of martensite-like phase was observed, consistent with that of the micrographs from the test coupon. The presence of a martensitic-like microstructure is also validated by the

hardness measurements of approximately 350 H_v, which is consistent with the hardness values of as-built test coupons of 352 H_v shown in Chapter 4.3.4. The microstructure is made up of fine grains, at less than 1 micron, which gives the specimen its mechanical properties, as discussed in Chapter Six. This observation is also consistent with other work, for example from Song et al. [168], where the work identified as-built samples consisting of cellular and columnar microstructures due to the fast cooling and solidification rates during SLM. Similar observation was also made by Larimian et al. [169], which identified as-built samples with refined microstructure and attributed it to the higher cooling rate obtained in SLM process.

However, in Figure 7.7 (b), the micrograph of the test coupon showed distinct layers of coarser and finer grains, which signifies the layer by layer deposition of SLM process. In the corresponding micrograph in Figure 7.5 Face 2, this layer by layer observation is absent. This observation is critical in comparing and identifying the effect of building a component versus building test coupons. It thus explains why the study chose to analyse the microstructure at the region furthest from the build bed. Based on literature, the microstructure formed should be similar no matter the thickness of the built specimen, as demonstrated in the work by Dzugan et al. [170]. This lack of distinct layers of coarser and finer grains in the built scaled model can be explained as follows. During the SLM process, the heat flux is the highest at the solid-liquid interface. The heat is transferred to the substrate through the previously built layers along the direction opposite to the building direction during solidification. This repeated thermal gradient provides epitaxial columnar grain growth in the SLM produced alloys [171]. This grain growth is not present in the scaled model and could be attributed to the inherent annealing effect during the SLM process. During the laser scanning, the heat affected zone from the next scan path may cause partial heat transfer to the previously scanned layer, creating an annealing effect [172]. This inherent annealing effect may cancel the effect of the epitaxial columnar grain growth, hence the difference in the micrographs. Based on this explanation, we can also predict that in the larger actual sized z-oriented print, the start of the build should look similar to the end of the build.

7.5 Conclusion

- (1) A scaled typical complex joint component was fabricated using the developed process parameters and validated against the results using microstructural

analysis. The microstructure obtained from the SEM examination of the scaled model was used to compare against that obtained from the test coupons.

- (2) The microstructure formed in both coupons and scaled model are largely similar, showing fine acicular martensitic-like microstructure, which will give the material its high strength but low ductility properties. While there is indirect evidence of the presence of such phases, the occurrence is speculated based on existing literature studies.
- (3) The consistency between both test coupon and scaled model microstructures demonstrate repeatability of the developed process parameters and hence validates the fabrication of complex joints.
- (4) The mechanical properties of the as-built samples can hence be improved (elongation and impact toughness) through the application of heat treatment regime as discussed in Chapter Four.

Chapter Eight Conclusion & Future Work

In this study, selective laser melting (SLM) has been used to process ASTM A131 EH36 shipbuilding steel, which would have traditionally been processed using thermomechanical controlled process (TMCP). The approach into the study can be summarised into two main portions – preliminary investigation into feasibility of using SLM to process EH36; characterisation of EH36 through mechanical properties and microstructure analysis.

The research outcome can be summarised as follows.

- 1) Conducted in-depth literature review on using selective laser melting to fabricate EH36 material, including density, mechanical properties and microstructure.
- 2) The preliminary investigation suggested that selective laser melting is capable of producing EH36 high tensile strength steel parts with a relative density of more than 97%, without visible cracks. This was achieved at an energy density of 92 J/mm³ using parameters of 0.12 mm hatch spacing, power at 175W, 50 μ m layer thickness and 320 mm/s laser scanning speed. The stainless steel substrate plate was preheated to 100 °C to reduce the thermal gradients and thermal stresses experienced by the specimens during the SLM process.
- 3) Conducted tensile and impact toughness tests to obtain mechanical performance of EH36 steel processed by selective laser melting. The results obtained indicated that with heat treatment (tempering) at 650⁰C, yield strength obtained is at 759 MPa, ultimate tensile strength obtained is 835 MPa, elongation obtained is 23.3% and Charpy V-notched impact toughness value obtained is 62.5J. All of these met the requirements stated in ASTM A131 standards.
- 4) Fractography studies were conducted and concluded that SLM produced samples are less ductile as compared to TMCP produced samples.
- 5) Generally fine martensitic-like microstructure is observed at the as-built and low tempering temperatures samples, as validated by the XRD results and hardness measurements. The samples undergo spheroidisation and the microstructure transforms to ferritic microstructure as the tempering temperature increases. At 800 °C, the microstructure is primarily ferritic with small amounts of cementite at its boundaries. This gives rise to its mechanical properties. While there is

indirect evidence of the presence of such phases, the occurrence is speculated based on existing literature studies.

- 6) A scaled model was fabricated and the microstructure analysed using SEM techniques. The as-built microstructure formed was validated to be similar to that of the test coupons, ie generally fine acicular martensitic-like microstructure. Hence it can be concluded that the process parameter developed can be used to fabricate complex joints.
- 7) The work has contributed to the understanding of characteristics of EH36 material when processing using SLM, which is a novel technique as compared to traditional TMCP.
- 8) In conclusion, it can be generalised that EH36 is technically feasible to be processed using SLM and the resulting properties from this research have been characterised for future studies.

However, the investigation of using SLM to process EH36 is not entirely complete and further work can be conducted to complement the findings from this study. The following are the suggested work to be conducted to further facilitate the research progress.

- 1) Heat treatment optimisation – in this research, a tempering process was used. However, more work can be performed to vary the process parameters in the tempering process to investigate different effects. In addition, different heat treatment processes can also be investigated.
- 2) Tempering temperature optimisation – specific tempering temperatures were selected for this research but they are not conclusive on the best temperature for recovering the mechanical properties of SLM processed EH36.
- 3) Large scale fabrication by SLM – in this study, the developed process parameters are validated to fabricate the scaled complex joint. However, if a complex joint is to be fabricated in its actual scale, the results presented in this work may not be directly applicable and will require further work to investigate the changes required to the process parameters. Consequently, the investigative work should include an in-depth study of its associated mechanical properties and microstructural transformation, so that the process parameters and heat treatment

regime developed in study can be co-related to the actual fabrication and post-processing requirements of the large scale component.

- 4) SLM was used to process EH36 in this study, but it may not be the best additive manufacturing (AM) process. Other processes, for example directed energy deposition, leverages different technology and will yield different results. The process parameters will also differ. It is hence encouraged to also investigate varying AM processes.

References

1. ASTM, *F2792-12a, Standard Terminology for Additive Manufacturing Technologies*. 2012, ASTM International: West Conshohocken, PA,.
2. Baese, C., *Photographic Process for the Reproduction of Plastic Objects*. 1904: US Patent #774,549.
3. Blather, J.E., *Manufacture of Contour Relief Maps*. 1892: US Patent #473,901.
4. Bourell, D., et al., *A brief history of additive manufacturing and the 2009 roadmap for additive manufacturing: looking back and looking ahead*. Proceedings of RapidTech, 2009: p. 24-25.
5. Wohlers, T. and T. Gornet, *History of additive manufacturing*. Wohlers Report 2011, 2011. **24**.
6. Hiemenz, J., *Additive manufacturing trends in aerospace*. White Paper, Stratasys, USA, 2014: p. 1-11.
7. Joshi, S.C. and A.A. Sheikh, *3D printing in aerospace and its long-term sustainability*. Virtual and Physical Prototyping, 2015. **10**(4): p. 175-185.
8. Burns, M. and C. Wangenheim. *Metal 3D printing applications in the oil & gas industry*. in *SPE Middle East Oil and Gas Show and Conference*. 2019. Society of Petroleum Engineers.
9. Omiyale, B.O. and P.K. Farayibi, *Additive manufacturing in the oil and gas industries-A review*. *Analecta Technica Szegedinensia*, 2020. **14**(1): p. 9-18.
10. Sireesha, M., et al., *A review on additive manufacturing and its way into the oil and gas industry*. RSC advances, 2018. **8**(40): p. 22460-22468.
11. Tahayeri, A., et al., *3D printed versus conventionally cured provisional crown and bridge dental materials*. *Dental Materials*, 2018. **34**(2): p. 192-200.
12. Dawood, A., et al., *3D printing in dentistry*. *British dental journal*, 2015. **219**(11): p. 521-529.
13. Strickland, J.D., *Applications of Additive Manufacturing in the marine industry*. Proceedings of PRADS2016, 2016. **4**: p. 8th.
14. *Taking nodes to a new level*. 11 March 2014 12 November 2018]; Available from: <https://www.oedigital.com/news/456517-taking-nodes-to-a-new-level>.
15. Burke, P. *3D Printing In The Oil And Gas Industry*. 2014 [cited 2014 April]; Available from: <http://3dprintingchannel.com/3d-printing-in-the-oil-and-gas-industry/>.
16. EISENHAMMER, S. *Oil industry joins world of 3D printing*. 2014 [cited 2014 April]; Available from: <http://www.reuters.com/article/2014/01/23/ge-3dprinting-idUSL5N0KW2OA20140123>.
17. Wu, W., et al., *Study of Additive Manufacturing in Offshore & Marine*, in *RAPID 2014*. 2014: Detroit, US.
18. Laser, C. *X line 2000R @ Technical Data*. 2016 11 February 2016]; Available from: http://www.concept-laser.de/fileadmin/branchenbilder/PDFs/1509_X%20line%202000R_DE.pdf.

19. Scott, C., *South Africa's giant aeroswift 3D printer gearing up for commercial production*. 2017.
20. ASTM, *A131/A131M - 14, Standard Specification for Structural Steel for Ships*. 2014, ASTM International: West Conshohocken, PA.
21. Rosado, D.B., et al., *Latest developments in mechanical properties and metallurgical features of high strength line pipe steels*. International Journal Sustainable Construction & Design, 2013. **4**(1).
22. Aung, H., *An analysis of the study of mechanical properties and microstructural relationship of HSLA steels used in ship hulls*. 2007.
23. Williams, J. *Advances in steels for high strength ERW linepipe application in Australia*. in *Materials forum*. 2007.
24. Regina, J., J. Dupont, and A. Marder, *The effect of chromium on the weldability and microstructure of Fe-Cr-Al weld cladding*. WELDING JOURNAL-NEW YORK-, 2007. **86**(6): p. 170.
25. Smallman, R.E. and A.H.W. Ngan, *Chapter 12 - Steel Transformations*, in *Modern Physical Metallurgy (Eighth Edition)*, R.E. Smallman and A.H.W. Ngan, Editors. 2014, Butterworth-Heinemann: Oxford. p. 473-498.
26. Davenport, E. and E. Bain, *General Relations Between Grain Size and Hardenability and the Normality of Steels*. Trans. Amer. Soc. Metals, 1934. **22**: p. 879-921.
27. Grimpe, F., et al. *Improvement of Mechanical Properties of Heavy Plates for High Strength Pipeline Application ie in Arctic Regions*. in *Proceedings of 2nd International Conference on Super-High Strength Steels*. 2010.
28. Koo, J.Y., et al., *Metallurgical design of ultra high-strength steels for gas pipelines*. International Journal of Offshore and Polar Engineering, 2004. **14**(1): p. 2-10.
29. Shinmiya, T., et al., *Development of High Deformability Linepipe with Resistance to Strain-aged Hardening by Heat Treatment On-line Process*. International Journal of Offshore and Polar Engineering, 2008. **18**(4): p. 308-313.
30. Okumoto, Y., et al., *Design of ship hull structures: a practical guide for engineers*. 2009: Springer Science & Business Media.
31. Gao, X.H., et al. *The Development of High Strength Hull Steel Plate FH40*. in *Applied Mechanics and Materials*. 2011. Trans Tech Publ.
32. Goli-Oglu, E.A., *Improving the Cold Resistance of 70–100-mm-Thick Heavy Plates FH40 for Marine Structures Built for Arctic Service*. Metallurgist, 2015. **59**(5): p. 498-504.
33. contributors, W. *List of oil fields*. 6 June 2016]; Available from: [https://en.wikipedia.org/w/index.php?title=List of oil fields&oldid=720244042](https://en.wikipedia.org/w/index.php?title=List_of_oil_fields&oldid=720244042).
34. Cronin, D., *Guidance Notes on High Tensile Steel*, in *2013 Shipbuilders meeting*. 2013, Tanker Structure Cooperative Forum: Shanghai China.
35. Davis, L. *Diagrams cover AM machines and processes*. 2016 11 January 2016]; Available from: <http://www.materialstoday.com/additive-manufacturing/news/diagrams-cover-am-machines-and-processes/>.
36. Gibson, I., D.W. Rosen, and B. Stucker, *Additive manufacturing technologies*. 2010: Springer.
37. Bai, Y. and C.B. Williams, *An exploration of binder jetting of copper*. Rapid Prototyping Journal, 2015. **21**(2): p. 177-185.

38. Chen, H., et al., *Process parameters optimization for improving surface quality and manufacturing accuracy of binder jetting additive manufacturing process*. Rapid Prototyping Journal, 2016. **22**(3): p. 527-538.
39. Brückner, F., S. Nowotny, and C. Leyens. *Innovations in laser cladding and direct metal deposition*. in *SPIE LASE*. 2012. International Society for Optics and Photonics.
40. Loh, L.-E., et al., *Numerical investigation and an effective modelling on the Selective Laser Melting (SLM) process with aluminium alloy 6061*. International Journal of Heat and Mass Transfer, 2015. **80**: p. 288-300.
41. Das, M., et al., *Laser processing of SiC-particle-reinforced coating on titanium*. Scripta Materialia, 2010. **63**(4): p. 438-441.
42. Gu, D., et al., *Laser additive manufacturing of metallic components: materials, processes and mechanisms*. International materials reviews, 2012. **57**(3): p. 133-164.
43. Masood, S.H., *10.04 - Advances in Fused Deposition Modeling*, in *Comprehensive Materials Processing*, S.H.F.B.J.V.T. Yilbas, Editor. 2014, Elsevier: Oxford. p. 69-91.
44. Ladd, C., et al., *3D Printing of Free Standing Liquid Metal Microstructures*. Advanced Materials, 2013. **25**(36): p. 5081-5085.
45. Wu, G.H., et al., *Solid freeform fabrication of metal components using fused deposition of metals*. Materials & Design, 2002. **23**(1): p. 97-105.
46. Gonzalez-Gutierrez, J., et al., *Additive manufacturing of metallic and ceramic components by the material extrusion of highly-filled polymers: A review and future perspectives*. Materials, 2018. **11**(5): p. 840.
47. Kritchman, E., R. Mimon, and H. Gothait, *Printing system with self-purge, sediment prevention and fumes removal arrangements*. 2014, Google Patents.
48. Benichou, A. and L. LAUFER, *Tungsten-carbide/cobalt ink composition for 3d inkjet printing*. 2015, Google Patents.
49. Zambelli, T., et al., *Additive Manufacturing of Metal Structures at the Micrometer Scale*. Advanced Materials, 2017. **29**(17): p. 1604211.
50. Strauss, J.T. and T. Pelletiers, *Metal Additive Manufacturing and Powder Metallurgy*.
51. Kruth, J.P., et al., *Selective laser melting of iron-based powder*. Journal of Materials Processing Technology, 2004. **149**(1-3): p. 616-622.
52. Kruth, J.-P., et al., *Binding mechanisms in selective laser sintering and selective laser melting*. Rapid prototyping journal, 2005. **11**(1): p. 26-36.
53. Baumers, M., C. Tuck, and R. Hague, *SELECTIVE HEAT SINTERING VERSUS LASER SINTERING: COMPARISON OF DEPOSITION RATE, PROCESS ENERGY CONSUMPTION AND COST PERFORMANCE*.
54. Kruth, J.-P., et al. *Part and material properties in selective laser melting of metals*. in *Proceedings of the 16th international symposium on electromachining*. 2010.
55. Cormier, D., O. Harrysson, and H. West, *Characterization of H13 steel produced via electron beam melting*. Rapid Prototyping Journal, 2004. **10**(1): p. 35-41.
56. Schick, D., et al., *Microstructural Characterization of Bonding Interfaces in Aluminum 3003 Blocks Fabricated by Ultrasonic Additive Manufacturing-Methods were examined to link microstructure and linear*

- weld density to the mechanical properties of ultrasonic additive manufacturing. *Welding Journal*, 2010. **89**(5): p. 105S.
57. Khorasani, A., et al., *A review of technological improvements in laser-based powder bed fusion of metal printers*. *International Journal of Advanced Manufacturing Technology*, 2020.
 58. Bhavar, V., et al. *A review on powder bed fusion technology of metal additive manufacturing*. in *4th International conference and exhibition on Additive Manufacturing Technologies-AM-2014*. 2014.
 59. Fey, M. and P. HSFK, *3D Printing and International Security*. Peace Research Institute Frankfurt (PRIF), 2017.
 60. *PROJECT AEROSWIFT HELPS UNLOCK THE GROWTH POTENTIAL OF ADDITIVE MANUFACTURING IN SOUTH AFRICA*. 2020 12 November 2020]; Available from: <https://www.csir.co.za/project-aeroswift>.
 61. *AURORA LABS INCREASES RMP1 METAL 3D PRINTING SPEED BY "2000%"*. 26th September 2019 20 October 2019]; Available from: <https://3dprintingindustry.com/news/aurora-labs-increases-rmp1-metal-3d-printing-speed-by-2000-162272/>.
 62. Ruan, J., et al. *A review of layer based manufacturing processes for metals*. in *2006 International Solid Freeform Fabrication Symposium*. 2006.
 63. Peleshenko, S., et al., *Analysis of the current state of additive welding technologies for manufacturing volume metallic products*. *Восточно-Европейский журнал передовых технологий*, 2017(3 (1)): p. 42-52.
 64. *MERKE IV: THE MACHINE BEHIND RAPID PLASMA DEPOSITION*. 2018 5 May 2020]; Available from: <https://www.norsktitanium.com/technology>.
 65. Sears, J.W., *Direct laser powder deposition-'State of the Art'*. 1999, Knolls Atomic Power Lab., Niskayuna, NY (US).
 66. Yasa, E., J. Deckers, and J.P. Kruth, *The investigation of the influence of laser re-melting on density, surface quality and microstructure of selective laser melting parts*. *Rapid Prototyping Journal*, 2011. **17**(5): p. 312-327.
 67. Morgan, R.H., et al., *High density net shape components by direct laser re-melting of single-phase powders*. *Journal of Materials Science*, 2002. **37**(15): p. 3093-3100.
 68. Badrossamay, M., et al., *Improving productivity rate in SLM of commercial steel powders*. status: published, 2009.
 69. Jhabvala, J., et al., *On the effect of scanning strategies in the selective laser melting process*. *Virtual and physical prototyping*, 2010. **5**(2): p. 99-109.
 70. Lu, Y.J., et al., *Study on the microstructure, mechanical property and residual stress of SLM Inconel-718 alloy manufactured by differing island scanning strategy*. *Optics and Laser Technology*, 2015. **75**: p. 197-206.
 71. Mumtaz, K. and N. Hopkinson, *Top surface and side roughness of Inconel 625 parts processed using selective laser melting*. *Rapid Prototyping Journal*, 2009. **15**(2): p. 96-103.
 72. Marimuthu, S., et al., *Laser polishing of selective laser melted components*. *International Journal of Machine Tools & Manufacture*, 2015. **95**: p. 97-104.

73. Ramos, J.A. and D.L. Bourell, *Modeling of surface roughness enhancement of indirect-SLS metal parts by laser surface polishing*. Rapid Prototyping of Materials, Proceedings, ed. F.D.S. Marquis and D.L. Bourell. 2002, Warrendale: Minerals, Metals & Materials Soc. 191-202.
74. Fischer, P., et al., *Sintering of commercially pure titanium powder with a Nd : YAG laser source*. Acta Materialia, 2003. **51**(6): p. 1651-1662.
75. Niu, H.J. and I.T.H. Chang, *Liquid phase sintering of M3/2 high speed steel by selective laser sintering*. Scripta Materialia, 1998. **39**(1): p. 67-72.
76. Fuh, J., et al., *Improvement of the UV curing process for the laser lithography technique*. Materials & Design, 1995. **16**(1): p. 23-32.
77. Morgan, R., C.J. Sutcliffe, and W. O'Neill, *Density analysis of direct metal laser re-melted 316L stainless steel cubic primitives*. Journal of Materials Science, 2004. **39**(4): p. 1195-1205.
78. Rombouts, M., et al., *Fundamentals of selective laser melting of alloyed steel powders*. Cirp Annals-Manufacturing Technology, 2006. **55**(1): p. 187-192.
79. Agarwala, M., et al., *Direct selective laser sintering of metals*. Rapid Prototyping Journal, 1995. **1**(1): p. 26-36.
80. Mumtaz, K.A. and N. Hopkinson, *Laser melting functionally graded composition of Waspaloy((R)) and Zirconia powders*. Journal of Materials Science, 2007. **42**(18): p. 7647-7656.
81. Strano, G., et al., *Surface roughness analysis, modelling and prediction in selective laser melting*. Journal of Materials Processing Technology, 2013. **213**(4): p. 589-597.
82. Song, B., et al., *Differences in microstructure and properties between selective laser melting and traditional manufacturing for fabrication of metal parts: A review*. Frontiers of Mechanical Engineering, 2015. **10**(2): p. 111-125.
83. Yadroitsev, I., et al., *Mechanical properties of samples fabricated by selective laser melting*. 14èmes Assises Européennes du Prototypages & Fabrication Rapide, Paris, 2009.
84. Spierings, A., N. Herres, and G. Levy, *Influence of the particle size distribution on surface quality and mechanical properties in AM steel parts*. Rapid Prototyping Journal, 2011. **17**(3): p. 195-202.
85. Aggen, S.D.W.a.G., *ASM Handbook: Wrought Stainless Steels, Properties and Selection: Irons, Steels, and High-Performance Alloys Vol. 1*. 1990: ASM International.
86. Riemer, A., et al., *On the fatigue crack growth behavior in 316L stainless steel manufactured by selective laser melting*. Engineering Fracture Mechanics, 2014. **120**: p. 15-25.
87. Kanagarajah, P., et al., *Inconel 939 processed by selective laser melting: Effect of microstructure and temperature on the mechanical properties under static and cyclic loading*. Materials Science and Engineering: A, 2013. **588**: p. 188-195.
88. Vilaro, T., et al., *Microstructural and mechanical approaches of the selective laser melting process applied to a nickel-base superalloy*. Materials Science and Engineering a-Structural Materials Properties Microstructure and Processing, 2012. **534**: p. 446-451.

89. Gu, D.D., et al., *Laser additive manufacturing of metallic components: materials, processes and mechanisms*. International Materials Reviews, 2012. **57**(3): p. 133-164.
90. Song, B., et al., *Microstructure and tensile properties of iron parts fabricated by selective laser melting*. Optics and Laser Technology, 2014. **56**: p. 451-460.
91. Abd-Elghany, K. and D. Bourell, *Property evaluation of 304L stainless steel fabricated by selective laser melting*. Rapid Prototyping Journal, 2012. **18**(5): p. 420-428.
92. Tolosa, I., et al., *Study of mechanical properties of AISI 316 stainless steel processed by "selective laser melting", following different manufacturing strategies*. The International Journal of Advanced Manufacturing Technology, 2010. **51**(5-8): p. 639-647.
93. Guan, K., et al., *Effects of processing parameters on tensile properties of selective laser melted 304 stainless steel*. Materials & Design, 2013. **50**: p. 581-586.
94. Luecke, W.E. and J.A. Slotwinski, *Mechanical properties of austenitic stainless steel made by additive manufacturing*. Journal of research of the National Institute of Standards and Technology, 2014. **119**: p. 398.
95. Zhao, X., et al., *Study on microstructure and mechanical properties of laser rapid forming Inconel 718*. Materials Science and Engineering: A, 2008. **478**(1): p. 119-124.
96. Wang, Z., et al., *The microstructure and mechanical properties of deposited-IN718 by selective laser melting*. Journal of Alloys and Compounds, 2012. **513**: p. 518-523.
97. Frazier, W.E., *Metal additive manufacturing: A review*. Journal of Materials Engineering and Performance, 2014. **23**(6): p. 1917-1928.
98. Vilaro, T., C. Colin, and J.D. Bartout, *As-Fabricated and Heat-Treated Microstructures of the Ti-6Al-4V Alloy Processed by Selective Laser Melting*. Metallurgical and Materials Transactions a-Physical Metallurgy and Materials Science, 2011. **42A**(10): p. 3190-3199.
99. Lenders, S., et al., *On the mechanical behaviour of titanium alloy TiAl6V4 manufactured by selective laser melting: Fatigue resistance and crack growth performance*. International Journal of Fatigue, 2013. **48**: p. 300-307.
100. Strizak, J.P., et al., *Fatigue properties of type 316LN stainless steel in air and mercury*. Journal of Nuclear Materials, 2005. **343**(1-3): p. 134-144.
101. Puchi-Cabrera, E.S., et al., *On the fatigue behavior of an AISI 316L stainless steel coated with a PVD TiN deposit*. Surface and Coatings Technology, 2004. **182**(2-3): p. 276-286.
102. Stoffregen, H.A., K. Butterweck, and E. Abele, *FATIGUE ANALYSIS IN SELECTIVE LASER MELTING: REVIEW AND INVESTIGATION OF THIN-WALLED ACTUATOR HOUSINGS*.
103. Wu, J.-H. and C.-K. Lin, *Tensile and fatigue properties of 17-4 PH stainless steel at high temperatures*. Metallurgical and materials transactions A, 2002. **33**(6): p. 1715-1724.
104. Arola, D. and C. Williams, *Estimating the fatigue stress concentration factor of machined surfaces*. International Journal of fatigue, 2002. **24**(9): p. 923-930.

105. Spierings, A.B., T.L. Starr, and K. Wegener, *Fatigue performance of additive manufactured metallic parts*. Rapid Prototyping Journal, 2013. **19**(2): p. 88-94.
106. Yasa, E. and J.P. Kruth, *Microstructural investigation of Selective Laser Melting 316L stainless steel parts exposed to laser re-melting*. Procedia Engineering, 2011. **19**: p. 389-395.
107. Gu, D., et al., *Selective laser melting of in-situ TiC/Ti 5 Si 3 composites with novel reinforcement architecture and elevated performance*. Surface and Coatings Technology, 2011. **205**(10): p. 3285-3292.
108. Hedberg, Y.S., et al., *In vitro biocompatibility of CoCrMo dental alloys fabricated by selective laser melting*. Dental materials, 2014. **30**(5): p. 525-534.
109. de Wild, M., et al., *Damping of selective-laser-melted NiTi for medical implants*. Journal of Materials Engineering and Performance, 2014. **23**(7): p. 2614-2619.
110. Gu, D. and W. Meiners, *Microstructure characteristics and formation mechanisms of in situ WC cemented carbide based hardmetals prepared by Selective Laser Melting*. Materials Science and Engineering a-Structural Materials Properties Microstructure and Processing, 2010. **527**(29-30): p. 7585-7592.
111. Kumar, S. and J.-P. Kruth, *Wear performance of SLS/SLM materials*. Advanced Engineering Materials, 2008. **10**(8): p. 750-753.
112. Gu, D., et al., *Densification behavior, microstructure evolution, and wear performance of selective laser melting processed commercially pure titanium*. Acta Materialia, 2012. **60**(9): p. 3849-3860.
113. Yasa, E., et al. *Microstructure and mechanical properties of maraging steel 300 after Selective Laser Melting*. in *Solid Freeform Fabrication Symposium Proceedings*. 2010.
114. Committee, A.I.H., *ASM handbook: Heat treating, Volume 4*. 1991, United States of America: ASM International.
115. Zhou, X., et al., *Textures formed in a CoCrMo alloy by selective laser melting*. Journal of Alloys and Compounds, 2015. **631**: p. 153-164.
116. Wen, S., et al., *Effect of molten pool boundaries on the mechanical properties of selective laser melting parts*. Journal of Materials Processing Technology, 2014. **214**(11): p. 2660-2667.
117. Gu, D. and Y. Shen, *Balling phenomena in direct laser sintering of stainless steel powder: Metallurgical mechanisms and control methods*. Materials & Design, 2009. **30**(8): p. 2903-2910.
118. Saada, G., *Hall-Petch revisited*. Materials Science and Engineering a-Structural Materials Properties Microstructure and Processing, 2005. **400**: p. 146-149.
119. Gu, D.D., et al., *Bulk-form TiCx/Ti nanocomposites with controlled nanostructure prepared by a new method: selective laser melting*. Journal of Physics D-Applied Physics, 2010. **43**(29): p. 7.
120. Gu, D.D., H.Q. Wang, and G.Q. Zhang, *Selective Laser Melting Additive Manufacturing of Ti-Based Nanocomposites: The Role of Nanopowder*. Metallurgical and Materials Transactions a-Physical Metallurgy and Materials Science, 2014. **45A**(1): p. 464-476.

121. Amato, K.N., et al., *Microstructures and mechanical behavior of Inconel 718 fabricated by selective laser melting*. Acta Materialia, 2012. **60**(5): p. 2229-2239.
122. Song, B., et al., *Fabrication and microstructure characterization of selective laser - melted FeAl intermetallic parts*. Surface and Coatings Technology, 2012. **206**(22): p. 4704-4709.
123. Thijs, L., et al., *Fine-structured aluminium products with controllable texture by selective laser melting of pre-alloyed AlSi10Mg powder*. Acta Materialia, 2013. **61**(5): p. 1809-1819.
124. Thijs, L., et al., *A study of the microstructural evolution during selective laser melting of Ti-6Al-4V*. Acta Materialia, 2010. **58**(9): p. 3303-3312.
125. Yadroitsev, I., et al., *Strategy of manufacturing components with designed internal structure by selective laser melting of metallic powder*. Applied Surface Science, 2007. **254**(4): p. 980-983.
126. Simchi, A. and H. Pohl, *Effects of laser sintering processing parameters on the microstructure and densification of iron powder*. Materials Science and Engineering a-Structural Materials Properties Microstructure and Processing, 2003. **359**(1-2): p. 119-128.
127. Simchi, A., F. Petzoldt, and H. Pohl, *Direct metal laser sintering: Material considerations and mechanisms of particle bonding*. International Journal of Powder Metallurgy, 2001. **37**(2): p. 49-61.
128. Gu, D.D., et al., *Selective Laser Melting of in-situ TiC/Ti5Si3 composites with novel reinforcement architecture and elevated performance*. Surface & Coatings Technology, 2011. **205**(10): p. 3285-3292.
129. Wu, W., et al., *Investigation on processing of ASTM A131 Eh36 high tensile strength steel using selective laser melting*. Virtual and Physical Prototyping, 2015. **10**(4): p. 187-193.
130. Gu, H., et al. *Influences of energy density on porosity and microstructure of selective laser melted 17-4PH stainless steel*. in *Proceedings of Solid Freeform Fabrication Symposium*. 2013.
131. Kruth, J.-P., et al., *Selective laser melting of iron-based powder*. Journal of materials processing technology, 2004. **149**(1-3): p. 616-622.
132. Kruth, J.-P., et al. *Part and material properties in selective laser melting of metals*. in *Proceedings of the 16th International Symposium on Electromachining (ISEM XVI)*. 2010. SHANGHAI JIAO TONG UNIV PRESS.
133. Liu, Z., et al. *A preliminary investigation on selective laser melting of M2 high speed steel*. in *5th International Conference on Advanced Research and Rapid Prototyping, Leiria, Portugal*. 2011.
134. Mertens, R., et al., *Optimization of scan strategies in selective laser melting of aluminum parts with downfacing areas*. Journal of Manufacturing Science and Engineering, 2014. **136**(6).
135. Casalino, G., et al., *Experimental investigation and statistical optimisation of the selective laser melting process of a maraging steel*. Optics & Laser Technology, 2015. **65**: p. 151-158.
136. Mutua, J., et al., *Optimization of selective laser melting parameters and influence of post heat treatment on microstructure and mechanical properties of maraging steel*. Materials & Design, 2018. **139**: p. 486-497.
137. Seede, R., et al., *An ultra-high strength martensitic steel fabricated using selective laser melting additive manufacturing: Densification,*

- microstructure, and mechanical properties*. Acta Materialia, 2020. **186**: p. 199-214.
138. Maamoun, A.H., et al., *The effect of selective laser melting process parameters on the microstructure and mechanical properties of Al6061 and AlSi10Mg alloys*. Materials, 2019. **12**(1): p. 12.
 139. Zhang, P., et al., *Twin structure of the lath martensite in low carbon steel*. Progress in Natural Science: Materials International, 2016. **26**(2): p. 169-172.
 140. Zhang, M., et al., *An investigation into the aging behavior of CoCrMo alloys fabricated by selective laser melting*. Journal of Alloys and Compounds, 2018. **750**: p. 878-886.
 141. Murr, L.E., et al., *Microstructures and properties of 17-4 PH stainless steel fabricated by selective laser melting*. Journal of Materials Research and Technology, 2012. **1**(3): p. 167-177.
 142. Song, B., et al., *Process parameter selection for selective laser melting of Ti6Al4V based on temperature distribution simulation and experimental sintering*. The International Journal of Advanced Manufacturing Technology, 2012. **61**(9-12): p. 967-974.
 143. Cherry, J., et al., *Investigation into the effect of process parameters on microstructural and physical properties of 316L stainless steel parts by selective laser melting*. The International Journal of Advanced Manufacturing Technology, 2015. **76**(5-8): p. 869-879.
 144. Kurgan, N., *Effect of porosity and density on the mechanical and microstructural properties of sintered 316L stainless steel implant materials*. Materials & Design, 2014. **55**: p. 235-241.
 145. Gülsoy, H., S. Özbek, and T. Baykara, *Microstructural and mechanical properties of injection moulded gas and water atomised 17-4 PH stainless steel powder*. Powder metallurgy, 2007. **50**(2): p. 120-126.
 146. Kempen, K., et al., *Microstructure and mechanical properties of Selective Laser Melted 18Ni-300 steel*. Physics Procedia, 2011. **12**: p. 255-263.
 147. Liu, Z.H., et al. *Microstructural investigation of M2 high speed steel produced by selective laser melting: microstructural investigation of M2 high speed steel*. in *Photonics and Optoelectronics (SOPO), 2012 Symposium on*. 2012. IEEE.
 148. Penha, R.N., et al., *Tempering of Steels[1]*, in *Steel Heat Treating Fundamentals and Processes*, J.L. Dossett and G.E. Totten, Editors. 2013, ASM International. p. 0.
 149. Randelius, M., *Influence of microstructure on fatigue and ductility properties of tool steels*. 2008.
 150. Canale, L.C., et al., *A historical overview of steel tempering parameters*. International Journal of Microstructure and Materials Properties, 2008. **3**(4-5): p. 474-525.
 151. Zhao, L.J., et al., *Below-Ms austempering to obtain refined bainitic structure and enhanced mechanical properties in low-C high-Si/Al steels*. Scripta Materialia, 2016. **112**: p. 96-100.
 152. Zhang, Z., et al., *Comprehensive effects of placement orientation and scanning angle on mechanical properties and behavior of 316L stainless steel based on the selective laser melting process*. Journal of Alloys and Compounds, 2019. **791**: p. 166-175.

153. Alsalla, H.H., C. Smith, and L. Hao, *Effect of build orientation on the surface quality, microstructure and mechanical properties of selective laser melting 316L stainless steel*. Rapid Prototyping Journal, 2018. **24**(1): p. 9-17.
154. Wang, X., et al., *Crystallographic-orientation-dependent tensile behaviours of stainless steel 316L fabricated by laser powder bed fusion*. Materials Science and Engineering: A, 2019. **766**: p. 138395.
155. Sun, Y., et al., *Fracture morphologies of advanced high strength steel during deformation*. Acta Metallurgica Sinica (English Letters), 2014. **27**(1): p. 101-106.
156. Das, A. and S. Tarafder, *Geometry of dimples and its correlation with mechanical properties in austenitic stainless steel*. Vol. 59. 2008. 1014-1017.
157. Gong, H., et al., *Influence of defects on mechanical properties of Ti-6Al-4V components produced by selective laser melting and electron beam melting*. Materials & Design, 2015. **86**: p. 545-554.
158. Brueckner-Foit, A., et al., *On the role of internal defects in the fatigue damage process of a cast Al-Si-Cu alloy*. Procedia Structural Integrity, 2017. **7**: p. 36-43.
159. Murakami, Y. and M. Endo, *Effects of defects, inclusions and inhomogeneities on fatigue strength*. International Journal of Fatigue, 1994. **16**(3): p. 163-182.
160. Fleck, N.A. and R.A. Smith, *Effect of Density on Tensile Strength, Fracture Toughness, and Fatigue Crack Propagation Behaviour of Sintered Steel*. Powder Metallurgy, 1981. **24**(3): p. 121-125.
161. Craeghs, T., et al. *Online quality control of selective laser melting*. in *Proceedings of the Solid Freeform Fabrication Symposium, Austin, TX*. 2011.
162. Kasperovich, G., et al., *Correlation between porosity and processing parameters in TiAl6V4 produced by selective laser melting*. Materials & Design, 2016. **105**: p. 160-170.
163. Callister, W.D., *Materials science and engineering*. Vol. 5. John Wiley & Sons NY.
164. Li, W., et al., *Effect of heat treatment on AlSi10Mg alloy fabricated by selective laser melting: Microstructure evolution, mechanical properties and fracture mechanism*. Materials Science and Engineering: A, 2016. **663**: p. 116-125.
165. Prashanth, K., et al., *Microstructure and mechanical properties of Al-12Si produced by selective laser melting: Effect of heat treatment*. Materials Science and Engineering: A, 2014. **590**: p. 153-160.
166. Attar, H., et al., *Manufacture by selective laser melting and mechanical behavior of commercially pure titanium*. Materials Science and Engineering: A, 2014. **593**: p. 170-177.
167. Krauss, G., *Martensite in steel: strength and structure*. Materials Science and Engineering: A, 1999. **273-275**: p. 40-57.
168. Song, J., et al., *Effect of heat treatment on microstructure and mechanical behaviours of 18Ni-300 maraging steel manufactured by selective laser melting*. Optics & Laser Technology, 2019. **120**: p. 105725.
169. Larimian, T., et al., *Effect of energy density and scanning strategy on densification, microstructure and mechanical properties of 316L stainless*

- steel processed via selective laser melting*. Materials Science and Engineering: A, 2020. **770**: p. 138455.
170. Dzugan, J., et al., *Effects of thickness and orientation on the small scale fracture behaviour of additively manufactured Ti-6Al-4V*. Materials Characterization, 2018. **143**: p. 94-109.
171. Jeon, J.M., et al., *Effects of microstructure and internal defects on mechanical anisotropy and asymmetry of selective laser-melted 316L austenitic stainless steel*. Materials Science and Engineering: A, 2019. **763**: p. 138152.
172. Ouyang, D., N. Li, and L. Liu, *Structural heterogeneity in 3D printed Zr-based bulk metallic glass by selective laser melting*. Journal of Alloys and Compounds, 2018. **740**: p. 603-609.

Appendix A – List of all data

Heat Treatment (°C)	Yield Strength (MPa)					
	Tensile Test Coupons (Machined)					
	1st	2nd	3rd	Max	Min	Avg
Nil	1010	990	1089	1089	990	1029.7
205	999	978	1010	1010	978	995.7
315	956	934	990	990	934	960.0
425	969	978	993	993	969	980.0
540	965	950	987	987	950	967.3
650	636	620	680	680	620	645.3
800	385	401	360	401	360	382.0

Heat Treatment (°C)	Yield Strength (MPa)					
	Tensile Test Coupons (As-Built)					
	1st	2nd	3rd	Max	Min	Avg
Nil	967	980	950	980	950	965.6667
205	970	998	948	998	948	972
315	896	903	903	903	896	900.6667
425	965	962	930	965	930	952.3333
540	952	940	910	952	910	934
650	670	650	690	690	650	670
800	344	360	320	360	320	341.3333

Heat Treatment (°C)	Ultimate Tensile Strength (MPa)					
	Tensile Test Coupons (Machined)					
	1st	2nd	3rd	Max	Min	Avg
Nil	1051	1020	1090	1090	1020	1053.667
205	1040	1051	1080	1080	1040	1057
315	1003	1010	1010	1010	1003	1007.667
425	994	980	990	994	980	988
540	990	950	1023	1023	950	987.6667
650	722	740	740	740	722	734
800	526	550	490	550	490	522

Heat Treatment (°C)	Ultimate Tensile Strength (MPa)					
	Tensile Test Coupons (As-Built)					
	1st	2nd	3rd	Max	Min	Avg
Nil	1021	1001	1114	1114	1001	1045.333
205	1017	1030	1030	1030	1017	1025.667
315	906	870	910	910	870	895.3333

425	994	982	1003	1003	982	993
540	976	970	986	986	970	977.3333
650	733	730	745	745	730	736
800	442	451	450	451	442	447.6667

Heat Treatment (°C)	Impact Test Temperature, 0 °C					
	Charpy Test Coupons (Notch Up)					
	1st	2nd	3rd	Max	Min	Avg
Nil	28	30	27	30	27	28.33333
205	28	27	27	28	27	27.33333
315	28	27	28	28	27	27.66667
425	28	29	29	29	28	28.66667
540	36	35	36	36	35	35.66667
650	31	29	38	38	29	32.66667
800	56	53	60	60	53	56.33333

Heat Treatment (°C)	Impact Test Temperature, 0 °C					
	Charpy Test Coupons (Notch Side)					
	1st	2nd	3rd	Max	Min	Avg
Nil	28	29	28	29	28	28.33333
205	31	30	30	31	30	30.33333
315	25	30	26	30	25	27
425	28	29	28	29	28	28.33333
540	21	26	29	29	21	25.33333
650	37	39	40	40	37	38.66667
800	84	80	86	86	80	83.33333

Heat Treatment (°C)	Impact Test Temperature, - 40 °C					
	Charpy Test Coupons (Notch Up)					
	1st	2nd	3rd	Max	Min	Avg
Nil	24	25	25	25	24	24.66667
205	26	27	26	27	26	26.33333
315	24	25	25	25	24	24.66667
425	21	22	22	22	21	21.66667
540	26	30	27	30	26	27.66667
650	33	34	33	34	33	33.33333
800	47	50	48	50	47	48.33333

	Impact Test Temperature, - 40 °C					
	Charpy Test Coupons (Notch Side)					

Heat Treatment (°C)	1st	2nd	3rd	Max	Min	Avg
Nil	24	26	25	26	24	25
205	28	27	29	29	27	28
315	29	31	28	31	28	29.33333
425	23	25	24	25	23	24
540	29	26	29	29	26	28
650	35	36	36	36	35	35.66667
800	50	48	49	50	48	49

Heat Treatment (°C)	Elongation (%)					
	Tensile Test Coupons (Machined)					
	1st	2nd	3rd	Max	Min	Avg
Nil	3	3.7	3.1	3.7	3	3.266667
205	6	5.2	6.3	6.3	5.2	5.833333
315	4	4.8	4.1	4.8	4	4.3
425	6	6.6	6.1	6.6	6	6.233333
540	5	5.9	4.7	5.9	4.7	5.2
650	12	12.8	12.2	12.8	12	12.33333
800	25	24.8	26	26	24.8	25.26667

Heat Treatment (°C)	Elongation (%)					
	Tensile Test Coupons (As-Built)					
	1st	2nd	3rd	Max	Min	Avg
Nil	4	4.1	5	5	4	4.366667
205	3.6	4	3.3	4	3.3	3.633333
315	2.2	2.5	3.8	3.8	2.2	2.833333
425	4	4.3	5	5	4	4.433333
540	5.8	6.1	5.2	6.1	5.2	5.7
650	9.8	11	9.4	11	9.4	10.06667
800	29	27.9	30.1	30.1	27.9	29

Heat Treatment (°C)	Yield Strength (MPa)					
	Tensile Test Coupons (Z)					
	1st	2nd	3rd	Max	Min	Avg
Nil	765	748	787	787	748	766.7
205	620	595	639	639	595	618.0
315	590	642	566	642	566	599.3
425	676	650	637	676	637	654.3
540	727	787	684	787	684	732.7
650	630	633	624	633	624	629.0

800	310	288	336	336	288	311.3
-----	-----	-----	-----	-----	-----	-------

Heat Treatment (°C)	Yield Strength (MPa)					
	Tensile Test Coupons (45)					
	1st	2nd	3rd	Max	Min	Avg
Nil	1032	933	1068	1068	933	1011
205	1030	991	1061	1061	991	1027.333
315	999	1051	1060	1060	999	1036.667
425	946	880	944	946	880	923.3333
540	1000	946	1074	1074	946	1006.667
650	780	727	770	780	727	759
800	387	373	420	420	373	393.3333

Heat Treatment (°C)	Ultimate Tensile Strength (MPa)					
	Tensile Test Coupons (Z)					
	1st	2nd	3rd	Max	Min	Avg
Nil	804	743	778	804	743	775
205	696	688	739	739	688	707.6667
315	617	600	626	626	600	614.3333
425	716	775	743	775	716	744.6667
540	795	732	717	795	717	748
650	682	729	632	729	632	681
800	341	312	348	348	312	333.6667

Heat Treatment (°C)	Ultimate Tensile Strength (MPa)					
	Tensile Test Coupons (45)					
	1st	2nd	3rd	Max	Min	Avg
Nil	1036	1086	1039	1086	1036	1053.667
205	1044	959	949	1044	949	984
315	1008	1011	923	1011	923	980.6667
425	990	898	892	990	892	926.6667
540	1013	1031	1104	1104	1013	1049.333
650	836	898	771	898	771	835
800	492	473	531	531	473	498.6667

Heat Treatment (°C)	Impact Test Temperature, 0 °C					
	Charpy Test Coupons (45)					
	1st	2nd	3rd	Max	Min	Avg
Nil	48	46	45	48	45	46.33333
205	48	49	49	49	48	48.66667

315	51	48	44	51	44	47.66667
425	50	48	46	50	46	48
540	49	47	48	49	47	48
650	60	65	67	67	60	64
800	84	85	98	98	84	89

Heat Treatment (°C)	Impact Test Temperature, 0 °C					
	Charpy Test Coupons (Notch Side)					
	1st	2nd	3rd	Max	Min	Avg
Nil	28	29	28	29	28	28.33333
205	31	30	30	31	30	30.33333
315	25	30	26	30	25	27
425	28	29	28	29	28	28.33333
540	21	26	29	29	21	25.33333
650	37	39	40	40	37	38.66667
800	84	80	86	86	80	83.33333

Heat Treatment (°C)	Impact Test Temperature, - 40 °C					
	Charpy Test Coupons (45)					
	1st	2nd	3rd	Max	Min	Avg
Nil	52	40	42	52	40	44.66667
205	54	44	40	54	40	46
315	60	52	43	60	43	51.66667
425	56.25	43.10204	44	56.25	43.10204	47.78401
540	53.08333	40.86957	44.8	53.08333	40.86957	46.25097
650	65	60	62.53333	65	60	62.51111
800	91	85	91.46667	91.46667	85	89.15556

Heat Treatment (°C)	Impact Test Temperature, - 40 °C					
	Charpy Test Coupons (Notch Side)					
	1st	2nd	3rd	Max	Min	Avg
Nil	24	26	25	26	24	25
205	28	27	29	29	27	28
315	29	31	28	31	28	29.33333
425	23	25	24	25	23	24
540	29	26	29	29	26	28
650	35	36	36	36	35	35.66667
800	50	48	49	50	48	49

	Elongation (%)
--	----------------

Heat Treatment (°C)	Tensile Test Coupons (Z)					
	1st	2nd	3rd	Max	Min	Avg
Nil	5	5.1	5.2	5.2	5	5.1
205	5	5.2	4.5	5.2	4.5	4.9
315	2	2.0	2.2	2.2	2	2.066667
425	6	6.5	6.1	6.5	6	6.2
540	5	4.6	4.5	5	4.5	4.7
650	5	4.9	5.3	5.3	4.9	5.066667
800	8	8.1	7.9	8.1	7.9	8

Heat Treatment (°C)	Elongation (%)					
	Tensile Test Coupons (45)					
	1st	2nd	3rd	Max	Min	Avg
Nil	13	13.3	13.3	13.3	13	13.2
205	12	12.5	12.3	12.5	12	12.26667
315	15	15.4	14.1	15.4	14.1	14.83333
425	12	12.4	11.8	12.4	11.8	12.06667
540	16	16.6	16.1	16.6	16	16.23333
650	23	22.4	24.4	24.4	22.4	23.26667
800	38	37.5	36.4	38	36.4	37.3

Heat Treatment (°C)	Yield Strength (MPa)						Min	Avg
	Vickers hardness (Test coupons)							
	1st	2nd	3rd	4th	5th	Max	Min	Avg
Nil	349.5	359.8	357.4	341	353.7	359.8	341	352.3
205	368.6	359.3	362.4	396.9	373.4	396.9	359.3	372.1
315	356.7	350.4	354.9	352.4	348.1	356.7	348.1	352.5
425	363.9	360.9	331	358.1	361.2	363.9	331	355.0
540	358	370.3	365.5	376.2	374.8	376.2	358	369.0
650	261.8	249.3	255.9	237.8	252.9	261.8	237.8	251.5
800	205.7	201.9	194.2	194.9	203.6	205.7	194.2	200.1

Sample location on node	Yield Strength (MPa)						Min	Avg
	Vickers hardness (Scaled model)							
	1st	2nd	3rd	4th	5th	Max	Min	Avg
1	349.7	349.7	380	331.3	332.6	380	331.3	348.7
2	334.4	373.5	358.2	398.5	323	398.5	323	357.5